A finite element study of the human cranium; The impact of morphological variation on biting performance

María Viviana Toro Ibacache

PhD in Medical Sciences

The University of Hull and the University of York

Hull York Medical School

December 2013

Abstract

This thesis investigated the relationship between craniofacial morphology and masticatory mechanics using finite element analysis (FEA). Chapter 1 is a literature review of the relevant background: bone mechanics, jaw-elevator muscle anatomy, imaging techniques, FEA and geometric morphometrics.

The second, third and fourth chapters comprise experimental work aiming to provide a framework for FE model construction and loading. The second chapter aimed to validate the method for FE model building and assess the sensitivity of models to simplifications. Models with simplified bone anatomy and resolution predicted strains close to those measured experimentally. The third chapter assessed the predictability of muscle cross-sectional area (CSA) from bony features. It was found that muscle CSA, an estimator of muscle force, has low predictability. The fourth chapter assessed FE model sensitivity to variations in applied muscle forces. Results showed that a cranial FE model behaved reasonably robustly under variations in the muscle loading regimen.

Chapter 5 uses the conclusions from the previous studies to build FE models of six human crania, including two individuals with artificial deformations of the neurocranium. Despite differences in form and the presence of deformation, all performed similarly during biting, varying mainly in the magnitudes of performance parameters. The main differences related to the form of the maxilla, irrespective of neurocranial deformation. The most orthognatic individuals with the narrowest maxilla showed the most distinctive deformation during incisor and molar bites, and achieved the greatest bite force efficiency. However, bite forces were similar among individuals irrespective of the presence of artificial deformation. This appears to relate to the preservation of normal dental occlusion, which in turn maintains similar loading and so morphogenesis of the mid face. Altogether, the results of this thesis show that FEA is reliable in comparing masticatory system functioning and point to how variations in morphology impact skeletal performance.

Table of contents

List of figures

List of tables

Acknowledgments

I would like to thank my supervisor, Professor Paul O'Higgins, for guiding me in the last years, and most importantly, for doing it with patience and generosity, and for always offering a word of advice.

To Dr Germán Manríquez Soto (Santiago de Chile), main researcher of the ANILLO ACT-96 Project, who co-supervised Chapter 5 of this thesis and financed part of it. I also thank Dr Manríquez my previous steps in science, as one of my DDS tutors and as my MSc tutor, and for his mentoring that led me to do my PhD with Professor Paul O'Higgins.

To the Dean of Facultad de Odontología de la Universidad de Chile, Professor Jorge Gamonal Aravena, for the support and encouragement. To Hospital Clínico Universidad de Chile and Víctor Zapata Muñoz, for providing the data used in most of this thesis.

I thank colleagues in England: Professor Chris Klingenberg (Manchester), for discussions about geometric morphometrics, science and many other hours of friendly talks and pints. To Dr Laura Fitton (York), who kindly helped me in several ways during my PhD and was a loyal friend in good and difficult times. I also would like to thank Professor John Currey and Dr Samuel Cobb, who were part of my training advisory panel and with whom I had inspiring discussions in and out of TAP meetings.

I am grateful to Hull colleagues and staff: Dr Peter Bazira, Rachel Cunningham, Professor Michael Fagan and Sue Taft. Also to Roxana Freeman and Gill Pulpher from HYMS staff.

To my friends in England. Alphabetically, Hester Baverstock, Dr Phil Cox, Dr Beatrice Demarchi, Dr Jason Dunn, Antonio García, Dr Flora Gröning, Clare Harrison, Dr Miguel Prôa, Karen Swan. To more recent colleagues and friends: Annabelle and Charles Eager, Ricardo Godinho, Andrew McIntosh, Phil Morris, and Nathan Scott-Johnston. To my friends in Chile. The support of my family has been essential and I would like to thank all of them: María, Waldo, Leni, Josefa, Andrés, Graciela, Carlos Hugo, Erika, Günter and Boris.

My last words of gratitude go to Kornelius Kupczik, for the endless patience, support and love. For walking by my side and inspiring me on the way.

Dedicado a mi familia, con el mismo amor que a mí me entregan.

An meine Familie, mit all der Liebe, die sie mir geben.

Author's declaration

I confirm that this work is original and that if any passage(s) or diagram(s) have been copied from academic papers, books, the internet or any other sources these are clearly identified by the use of quotation marks and the reference(s) is fully cited. I certify that, other than where indicated, this is my own work and does not breach the regulations of HYMS, the University of Hull or the University of York regarding plagiarism or academic conduct in examinations. I have read the HYMS Code of Practice on Academic Misconduct, and state that this piece of work is my own and does not contain any unacknowledged work from any other sources.

Chapter 1 : Introduction and literature review

1.1. Introduction

Morphological variations among and within mammal species are the result of interactions between the genetic and epigenetic processes that drive development and evolution. Such variations can lead to functional adaptations (Alberch, 1980; Klingenberg et al., 2010). Variations in the morphology of the different parts of the skull arise during development. The skull is modular, each module is related to the several functions of the head; these modules become integrated during development (Martínez-Abadías et al., 2012). The integration of developing modules occurs in a way that allows for compensation when deficiencies appear in some of them, thus maintaining overall function (Lieberman, 2011). This integration is in large part believed to occur through the action of loading of the skull during e.g. masticatory system functioning, with subsequent strains leading to skeletal adaptation.

The skull of modern humans is distinctive morphologically among primate species, and several of these distinctive human characteristics, such as a vertically inclined face, the chin, small teeth and canines, small masticatory muscles, relate to the masticatory apparatus (Aiello et al., 1990; Lieberman, 2011). Biomechanical analyses of the masticatory system have been undertaken to explore the functional differences that result from such anatomical differences and vice versa. However, the extent to which morphological variations within species affect skull biomechanics, and particularly mastication, is not completely known and yet essential to understand the role of skull anatomy in the ætiology of several diseases, dysfunctions and disorders affecting masticatory muscles, teeth, bones and joints. In these cases the study of the mechanical performance of the skull under masticatory loadings with state-of-the-art methods such as finite element analysis (FEA) has considerable potential, for example, in clinical research and practice. The results of this type of analysis depend on the sets of input variables, both anatomical and material-related, which are specific for each structure under study (Rayfield, 2007; Kupczik, 2008). Questions that might be asked are: How do intraspecific variations affect the mechanical performance of the skull? Can we build a reliable FE model of the human masticatory system? Answering these specific questions is relevant to the general aim of the present work; to study the relationship between variations in form and masticatory system function in the human skull. The aim is to use the state-of-the-art techniques of finite element analysis and geometric morphometrics combined with classical ones such as anatomical dissection, imaging and three-dimensional reconstruction techniques as detailed in each chapter to investigate this question.

In the first part of this thesis, a literature review is presented with information about bone biomechanics, masticatory muscle anatomy and methods used so far to study masticatory biomechanics. The theoretical background of the most relevant methods used in this work will be reviewed: clinical imaging, finite element analysis and geometric morphometrics.

The general hypothesis being tested is that there is no relationship between cranial morphology and parameters of biting performance. The second part of this thesis contains the experimental work developed to test this hypothesis. First, the validation study of a human cranial FE model is presented. Then, two studies assess the impacts of estimating and varying muscle force parameters in FEA, addressing both biological and technical questions. Finally, and considering the results of the previous studies, the general hypothesis is tested by assessing the relationship between differences in cranial morphology and cranial performance under simulated biting using combined FEA and geometric morphometric analysis. The second part is organised as four chapters with the following aims: (1) to compare with experimental data, the predicted strains of an FE model of a human cranium; (2) to assess the predictability of masticatory muscle forces (via muscle cross-sectional area) from skull morphology in a modern human sample; (3) to assess the effects of varying the relative magnitudes of the jaw-elevator muscles on FEA results; and (4) to compare the functioning of human crania showing normal morphological variations and artificially induced large deformations.

The final part of this thesis presents the general conclusions derived from the chapters in the second part.

1.2. Bone morphology and biomechanics

The relationship between bone form and its function has been acknowledged for centuries. According to Koch (1917), the earliest mention of this is credited to Galileo (1638) on his studies of beam mechanics. The same author reviews the descriptive work of several anatomists during the 18th and 19th centuries, most of them based on lower limb bones, especially the femur, discussing the significance of their structure. The idea has remained until today and is relevant in different areas. For example, in paleontology and bioarchaeology, the assumption that bone morphology reflects its loading history is one of the bases of the study of bone remains (Demes, 1987; Spencer and Demes, 1993; Ruff et al., 2006). In orthopaedics, the assessment and control of muscular function is key for the diagnosis and successful correction of bone dysmorphosis (Kiliaridis et al., 1989; Delaire, 1997).

The adaptation of bone to a certain function implies changes in rates and locations of bony tissue deposition and resorption in a relatively predictable way according to its loading history. This idea began to become a paradigm in the 19th Century with the work of Julius Wolff (1892), and it has undergone modifications based on the new evidence of the genetic control of bone development (Slemenda et al., 1991; Karsenty, 1999; Olsen et al., 2000). Today it is widely accepted that bone morphology is the result of both genetic and epigenetic factors (Prentice, 2001; Lovejoy et al., 2003; Pearson and Lieberman, 2004; Ruff et al., 2006). The general mechanisms by which function modifies bone morphology relate to the direct forces generated by muscles inserted on the bone (Scott, 1957; Moss, 1962; DiGirolamo et al., 2013), and to the loads generated by the action itself, such as the bearing of body mass or the reaction force on teeth during biting (Yoshikawa et al., 1994; Gross et al., 2001; Milne and O'Higgins, 2012). Melvin Moss, based on previous work of Cornelis van der Klaaw (1948-1952) stated that skull development is the result of the functional demands of related soft tissues and *functional matrices* (i.e. the group of tissues and spaces related to a particular function; Moss, 1962; Moss, 1968; Moss, 1997) . In this model, skeletal muscles (acting through 'periosteal matrices') are responsible for regulating the histologically observable, active growth processes leading to skeletal tissue adaptations: deposition, resorption and maintenance (Moss, 1997). Harold Frost (1987) focused on the importance of the mechanism (which Frost called the 'mechanostat') that regulates bone mass according to its mechanical loading. In the *mechanostat proposal*, bone strains derived from loadings induce or reduce bone formation, changing bone morphology in such a way that the new loading conditions produce bone strains within the range of bone mass maintenance. The fundamental idea shared by all authors, that bone morphology is regulated by its functional demands, gives rise to the strategy of studying bone growth and adaptation in relation to mechanical loading.

1.2.1. Mechanical response to loading: bone as a material

Although the seminal work of Wolff, Moss and Frost has been continuously revisited (Cowin, 2001; Pearson and Lieberman, 2004; Ruff et al., 2006; Barak et al., 2011), they share fundamental ideas that are widely used by bone biologists and anatomists. First, that in healthy organisms, bone tissue is deposited and resorbed to achieve an optimum balance between strength and weight. Second, bone trabeculae tend to line up with the directions of the stresses that they experience. Third, regulatory mechanisms act in relation to the first two phenomena; mechanical forces acting upon bone tissues, stimulate bone physiological responses and so, adaptation (Wolff, 1892; Moss, 1962; Frost, 1987; Moss, 1997).

The mechanisms of modification of bone morphology through loading can be studied at several levels. In general, a loaded bone deforms at a microscopic level, stimulating the cells and transducing the information into a biochemical signal that regulates bone formation and resorption. This process, further detailed below, will modify or maintain bone morphology at a macroscopic level in a way that, in general terms, depends on the locations, timings and magnitudes of stresses and strains produced in the tissue (Currey, 2006; Huang and Ogawa, 2010; Lieberman, 2011). The stress and strain in a structure under load are calculated as follows:

Stress (σ). The stress reflects the intensity of a force (F) acting across an area (A). It is measured in Pascals (newtons/m^2 or Pa).

$$\sigma = F / A$$

Every force acting on a structure is a vector with three orthogonal components; there is one component perpendicular to the plane that produces *normal stress* and two others that produce *shear stress.*

Strain (ε). *Normal strains* are proportional changes in dimensions (L) under a certain force. Strain is dimensionless.

$$\varepsilon = \Delta L / L$$

Shear strains change the angle between two imaginary lines in the material that are originally at right angles. The angle is measured in radians (γ).

Principal strains are the maximum strains acting on the principal planes of a point where only normal strains act and there are no shear strains. The highest values (*maximum principal strains* or *ε1*) are commonly 'tensile strains' and the lowest values (*minimum principal strains* or *ε3*), 'compressive strains' although in some circumstances both may be compressive or tensile (e.g. both strains are tensile in the skin of a balloon when inflated). *Von Mises strains* are often used to compare strains among structures, and they are calculated from principal strains.

$$\text{Von Mises } \varepsilon = (\varepsilon 1-\varepsilon 2)^2 + (\varepsilon 2-\varepsilon 3)^2 + (\varepsilon 3-\varepsilon 1)^2$$

The material properties of a tissue determine the way it behaves under stress. The degree of stiffness and flexibility of bone, or elasticity, is expressed as the modulus of elasticity or *Young's modulus* (*E*). It is the stress/strain ratio, which behaves linearly in most of elastic materials. The elasticity modulus is expressed in Pascals (Pa), and a high value is associated with stiff materials. Bone stiffness relates mainly to the proportion of mineral content and its volume fraction (Currey, 1988; Currey, 2003). Under load bone behaves as a linearly elastic material, and when loading is beyond physiological norms it reaches a yield point where stresses do not increase while strains keep rising, leading to plastic deformation before it breaks (Currey, 2006; Lieberman, 2011). This relationship is usually depicted as a stress-strain (or load-deformation) curve (Figure 1.1)

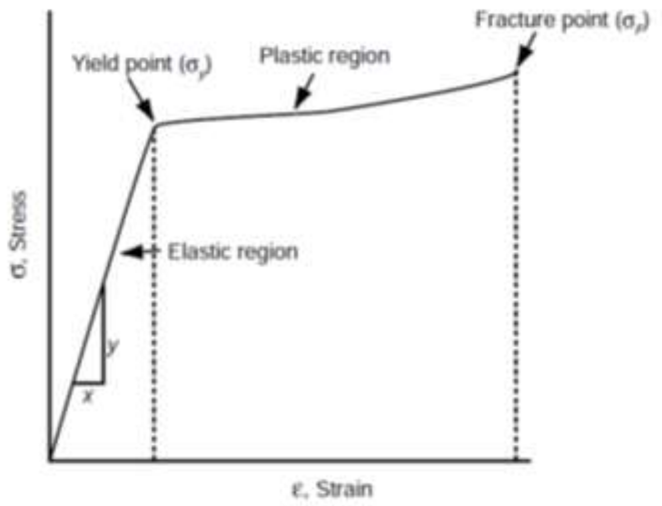

Figure 1.1. Relationship between stress and strain in an elastic material. Relationship between stress and strain in an elastic material. Within the elastic region the relationship between stress and strain is linear. At the yield point the deformation becomes plastic until the point of fracture. From Lieberman (2011).

As a consequence of the point of application of force and its direction, the bone can undergo compression, tension, bending or shearing, causing different patterns of structural deformation. This deformation is then translated to a tissue level, where bone cells sense the mechanical signal and react via deposition and resorption. Areas of bone deposition and resorption can ultimately increase overall resistance to deformation (Figure 1.2).

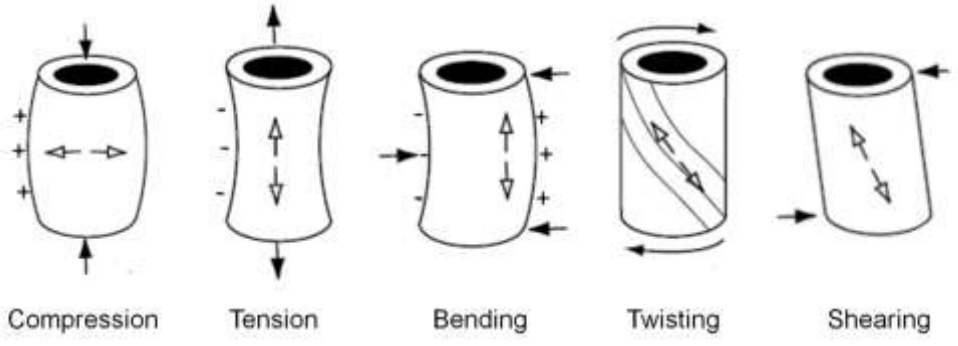

Figure 1.2. Different types of stress regimes. Solid arrows indicate direction of applied forces and hollow arrows indicate directions of tension. Bone resistance to deformation can be increased by deposition (+) and resorption (–). Adapted from Lieberman (2011).

1.2.2. Bone response to loading: mechanoreception and mechanotransduction

Under physiological conditions, bone deposition and resorption are complementary dynamic processes that maintain bone morphology and its structural and metabolic function. This processs takes place in temporary anatomical structures known as basic multicellular units (BMU; Frost, 1973). The BMU is formed by elements in continual replacement: osteoblasts in the front of bone deposition and osteoclasts in the front of resorption, vessels for blood supply and connective tissue. The lifespan of the active cellular component in the BMU is variable, about 12 days for osteoclasts and from a few to 100 days for osteoblasts in humans (Jilka, 2003). Experimentally, it has been observed that cellular responses to applied loads include osteoblast proliferation and reorientation within tissue, synthesis of DNA, collagen, glycosaminoglicans such as hyaluronan and chondroitin-6-sulphate (Hall, 2005). Diminished bone loading induces osteocyte hypoxia and osteoclast proliferation (Chen et al., 2010).

Bone cell activity varies depending on the loading regimen. For example, underloaded bone associated with muscle paralysis or disuse experiences resorption (Rubin et al., 2001; Warner et al., 2006; Poliachik et al., 2010). At the same time, a bone is said to be ‘adapted’ to a certain function when structurally it is able to withstand the loads produced without reaching its failure point. This ability to withstand loads depends on, among other things, bone morphology and bone mass (Turner, 1998; Pearson and Lieberman, 2004; Witzel et al., 2004). The loads imposed by a subject’s normal physical activity leave the rate of bone resorption and deposition in a dynamic equilibrium, and when loads rise above the range caused by normal activity, bone formation rate is increased (Frost, 1987). In the primate skull, areas of high bone density that are also highly strained during biting, such as the zygomatic arch, the nasal notch and the lateral border of the orbital opening, provide examples of bone mass regulation via loading (Hylander and Johnson, 1997; Gross et al., 2001; Witzel et al., 2004; Ross et al., 2011).

Bone cells desensitise rapidly to mechanical stimulation, and so intermittent loading has been shown to induce bone formation more effectively (Duncan and Turner, 1995; Huang and Ogawa, 2010). Particularly, formation is enhanced when the load on bone causes peak absolute strains of 1000 $\mu\varepsilon$ (Rubin and Lanyon, 1985; Duncan and Turner, 1995; Moss, 1997), this occurs at a rate that increases proportionally with frequencies over 0.5 Hz (Turner et al., 1994). Repetitive high strains lead to fatigue microdamage beyond a threshold of 3000 $\mu\varepsilon$, and this stimulates remodelling in normal human bone tissue (Carter and Caler, 1985). However, the application of high-frequency low strains in the order of 200 με is shown to have an anabolic effect on the femur and spine in humans (Rubin et al., 2004). *In vivo* facial recordings during biting in *Macaca* show that the zygomatic arch achieves strains in the range of 500-1400 με (Hylander and Johnson, 1997; Ross et al., 2005; Ross et al., 2011), and the postorbital bar, about 500 με (Ross et al., 2005; Ross et al., 2011). Furthermore, under tetanic contraction of the temporalis muscle, the parasagittal region of the vault reaches up to 700 με also during experiments in *Macaca* (Behrents et al., 1978). In humans *in vivo* strain measurement is impractical, and so only *in vitro* measurements (Gröning et al., 2009; Szwedowski et al., 2011) or *in silico* predictions by methods such as finite element analysis of the cranium (Wroe et al., 2010; Jansen van Rensburg et al., 2012) and the mandible (Gröning et al., 2011b) are available. In all these cases, peak facial strains reach between 300 and 1000 με.

At the cellular level, bone response to loading is the result of an extracellular process that stimulates the cell (mechanoreception) and an intracellular signalling process (mechanotransduction) that ends in the activation and response of the effector cell (Duncan and Turner, 1995; Moss, 1997; Ethier and Simmons, 2007). The characteristics of these processes are now presented.

1.2.2.1. Mechanoreception

Loaded bone experiences stresses and strains. When these reach threshold levels they stimulate sensory cells, producing a response that is transmitted within the bone tissue, among osteocytes that are organised as a network (Moss, 1997). Bone-lining inactive osteoblasts and particularly osteocytes act as sensory cells in the system, whilst the active osteoblasts and osteoclasts are the main effectors (Duncan and Turner, 1995; Huang and Ogawa, 2010). Mechanoreceptors are located in the plasma membrane. Among the proposed mechanisms involved in the process, possibly acting in parallel, are:

Mechanical processes. They are mediated mainly by membrane proteins such as integrins and transient protein complexes such as focal adhesions that link the extracellular matrix (ECM) to the cytoskeleton (Ivaska, 2012). Tissue under compression or tension causes the respective type of deformation in the sensory cells. When tension and compression are combined during bending, a gradient of interstitial fluid is generated from the area in compression to that in tension causing shear stress on cells (Figure 1.3; Duncan and

Turner, 1995) and electrokinetic phenomena as described further below. Strained cells alter their cytoskeleton, changing the physical properties of the cell, activating other cell receptors, regulating molecular events within the cell (Hall, 2005; Ethier and Simmons, 2007; Huang and Ogawa, 2010).

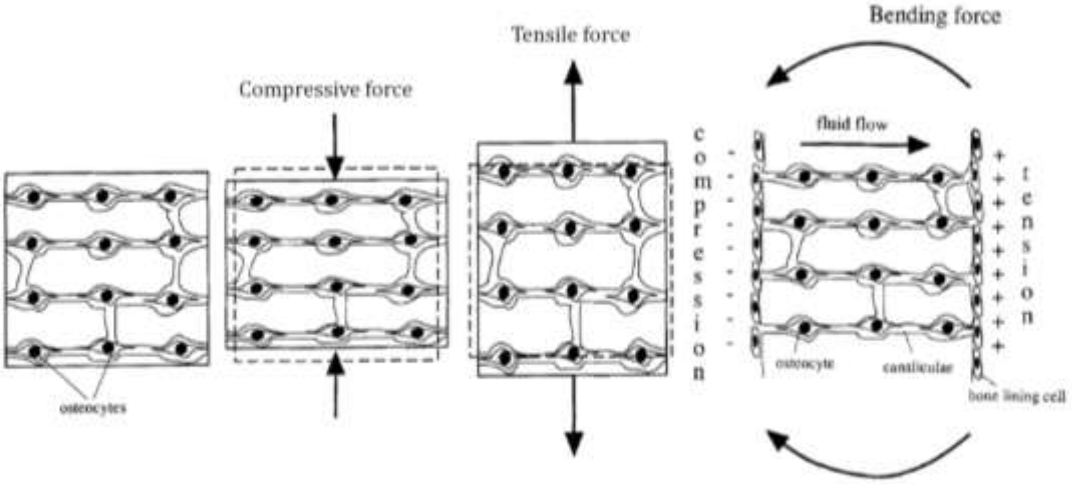

Figure 1.3. Bone deformation. Representation of tissue deformation under compression, tension and bending, causing biaxial cell deformation or compression-to-tension gradient in the interstitial fluids through bone canaliculi. Adapted from Duncan and Turner (1995).

Stretch-activated ion channels. These are membrane proteins that allow the diffusion of inorganic ions that participate in cell metabolism. How mechanical stimuli activate channels is not completely clear. It has been proposed that the deformation under load of the plasma membrane or the cytoskeleton, by proximity or established connections, alters the structure of the ion channel, activating or deactivating it (Moss, 1997; Ethier and Simmons, 2007).

Electrical processes. The membranes of bone cells can be depolarised and hyperpolarised by the movement of ions in the extracellular fluid, which causes changes in the activity of voltage-activated ions (Duncan and Turner, 1995; Moss, 1997). These action potentials can be transmitted through gap junctions to the other cells (Moss, 1997). Additionally, it has been shown that osteoclast migration can be induced with electric fields of 0.1 and 1 V/mm (Ferrier et al., 1986), a range that would be similar to that produced in bone during normal muscle activity (Moss, 1997).

Cell-surface receptor proteins. These are receptors linked to membrane proteins that respond to molecules. They respond to mechanical signals and transduce them in a similar way as stretch-activated ion channels, changing their configuration when the cell is deformed under load. This process is mediated by the plasma membrane, the cytoskeleton and focal adhesions (Ethier and Simmons, 2007)

1.2.2.2. Mechanotransduction

Loads deform the cell membrane and cytoskeleton of the receptor cells in bone tissue. At an intracellular level, the signal transduction to induce changes in cell metabolism is mediated mainly by the cytoskeleton, whose deformation has an effect on connected organelles and molecules. Cytoskeleton deformation may lead to the movement of organelles or changes in the nucleus, affecting gene expression. It also may have an effect on the regulatory proteins attached to it, causing structural changes that affect their kinetic behaviour and biochemical activity (Figure 1.4). Among described second messengers mediating the signal transduction are calcium ions, cyclic adenosine monophosphate, inositol phosphates, kinases related to the integrin pathway, prosteoglandins, nitric oxide, β-cathenins, adenosine triphosphate, insulin-like growth factors, bone morphogenetic proteins and hormone-receptor pathways (Duncan and Turner, 1995; Huang and Ogawa, 2010).

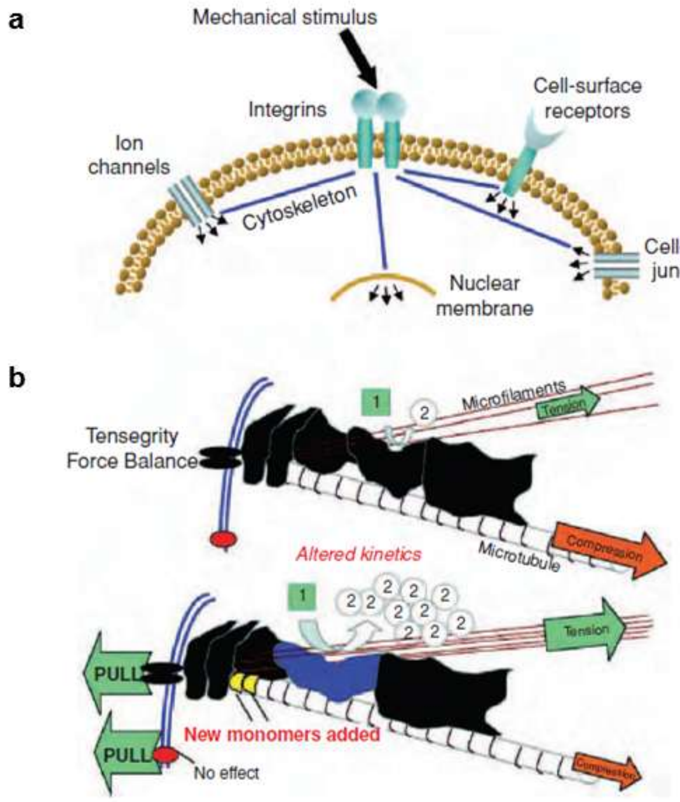

Figure 1.4. Mechanoreception and mechanotransduction systems schematic. (a) Mechanoreceptors and their associated intracellular signalling pathways. (b) The cytoskeleton as a transductor: under load, the immobilized proteins (in black) are deformed, changing protein kinetics and converting more substrate (1) into product (2). From Ethier and Simmons (2007).

1.2.2.3. Effector cell response

The osteocyte or bone-lining cell produces paracrine factors such as insulin-like growth factors and prostaglandins, that recruit and activate the effector cells, i.e. osteoblast and osteoclasts (Duncan and Turner, 1995). These respond via gene expression, RNA transcription, protein secretion, cell shape and mobility, resulting in bone matrix deposition and/or resorption (Ethier and Simmons, 2007). Microscopically, osteoclasts erode resorption lacunae, which after 30-40 days are refilled by the action of osteoblasts (Eriksen, 2010).

The primary response of bone cells to mechanical loading via mechanoreception and mechanotransduction is a process regulated by other factors such as local cytokines, growth factors and systemic hormones (particularly parathyroid and oestrogen), which may be altered during the course of systemic pathologies. Variations in bone response to loading among individuals are also genetically controlled. It has been shown that in mice with mutations associated with different long bone cross-sectional areas, bone mineral densities and material properties show differences in their osteogenic strain thresholds, bone formation rates and osteocyte lacuna populations, in ways that are not predictable on the basis of mechanical function and that the authors propose to be regulated genetically (Robling and Turner, 2002).

1.2.3. Concluding remarks

Bone morphology is the result of several processes among which functional loading is key. Loads induce tissue responses in terms of bone resorption and deposition in a more or less predictable way, according to the direction of applied force, bone material properties and geometry. This structural behaviour is the motivation for stress and strain analyses of bones under load. Although direct measurement of strains is an established approach, FEA has recently become common in studies of primate masticatory biomechanics (Preuschoft and Witzel, 2002; Witzel et al., 2004; Kupczik et al., 2009; Strait et al., 2009; Wroe et al., 2010; Gröning et al., 2011b). Among other advantages over direct measurement, FEA offers a virtual work-environment that is suitable for working with fossils, ancient material and living humans.

1.3. Jaw-elevator muscles: Anatomy and function

Masticatory muscle activity impacts on skull morphogenesis since bone adaptation to functional demands plays a key role in modulating growth (Moss, 1962; McNamara, 1975). The masticatory muscles are innervated by the mandibular division of the trigeminal nerve. Their origin is on the cranium and insertion on the mandible, and so they move the mandible relative to the cranium with a fulcrum at the temporomandibular joint (TMJ). The temporalis, masseter and medial pterygoid muscles (Figure 1.5) are jaw elevators. All these plus the jaw-opening muscles are paired. The medial pterygoid also contributes largely to lateral movements when contracting asymmetrically. The lateral pterygoid, mylohyoid and the anterior portions of the digastric muscles are jaw depressors, and the first of these is the main actor in lateral movements of the jaw.

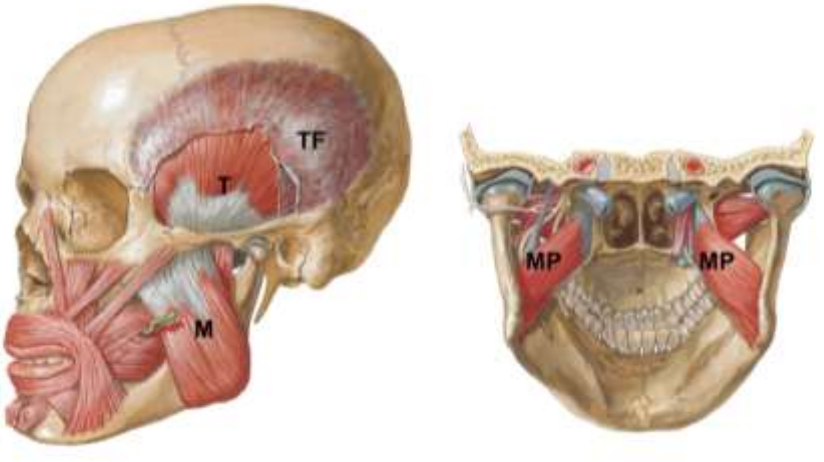

Figure 1.5. Illustration of masticatory muscles *in situ*. Lateral (left) and postero-inferior (right) views. T=temporalis, TF=temporalis fascia, M=masseter and MP=medial pterygoid muscles. Adapted from Netter (2006).

1.3.1. Skeletal muscle structure

Skeletal muscle fibres are the basic cellular units that generate muscle force. Their structure is depicted in Figure 1.6. The general mechanism by which a muscle fibre creates tension is by binding of two fibre proteins: actin and myosin during the cross-bridge cycle. During muscle contraction, the neural impulse reaches the motor end-plate. The muscle fibre is then depolarized producing a response called the action potential (AP). The AP spreads over the fibre bi-directionally reversing cell polarity through ionic movement across the membrane, activating calcium channels of the membrane that interact with the sarcoplasmic reticulum, which release calcium. In the sarcomere (Figure 1.6), actin's myosin binding sites are normally covered by tropomyosin and troponin, and they are uncovered during contraction due to binding of calcium with troponin. About thirteen types of myosin have been described in humans and this diversity plays a key role in regulating the cross-bridge cycle, and therefore, muscle contraction (Sweeney and Houdusse, 2010).

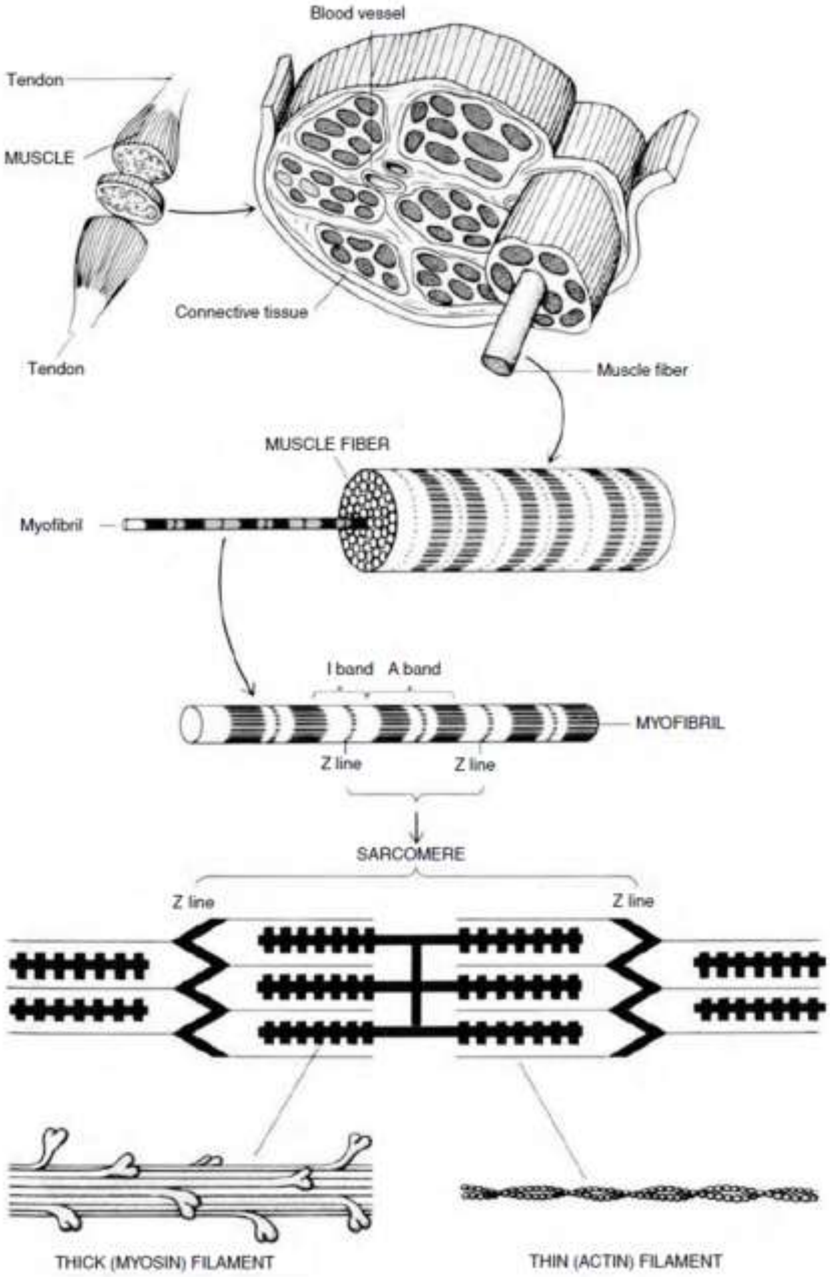

Figure 1.6. Basic micro- and macrostructure of skeletal muscles. From Ethier and Simmons (2007).

1.3.2. Jaw-elevator muscle structure

Histologically jaw-elevator muscles show some differences from the other muscles of the body in composition, structure and distribution of muscle fibre types (Eriksson and Thornell, 1983; Stål et al., 1994). Fibre typing is based on myosin structure, which is formed by light- and heavy-chain polypeptids. Depending on the heavy chain (MyHC) isoform, skeletal muscle fibres have been classified into 'slow' type I and 'fast' type II fibres. Each has subtypes, and also 'hybrid' fibres are found that contain more than one isoform of MyHC (Korfage et al., 2005; Grünheid et al., 2009). Human jaw-closing muscles in general are composed of more or less similar proportions of type I and II fibres but distributed differently among muscle portions, suggesting task-related specialisations of these (Eriksson and Thornell, 1983; Korfage et al., 2005; Grünheid et al., 2009; Österlund et al., 2011). Moreover, some MyHC isoforms in masticatory muscle fibres differ from those in postcranial skeletal muscles (Sciote and Morris, 2000; Grünheid et al., 2009). Variations in masticatory muscle composition are also found among primates, with human muscles containing the type II fibre with the smallest cross-sectional area (CSA; Sciote and Morris, 2000; Stedman et al., 2004), and lacking in the 'super fast' type IIM fibre subtype (Sciote and Morris, 2000).

The jaw-elevator muscles of adult humans also show particular MyHC isoforms such as developmental (fœtal-MyHC) and cardiac (α-cardiac-MyHC) myosins that are usually present in hybrid fibres and have contractile properties intermediate between those of 'pure' fibres (Grünheid et al., 2009). From a functional perspective, the diversity of fibre-types shown by masticatory muscles gives them the potential for muscle adaptation *in vivo* (Korfage et al., 2005) and also phylogenetic plasticity (Hoh, 2002). Another characteristic of the masticatory muscles is that fibres are controlled by specific motor units located in specific regions of the muscle, and do not intermingle with others, as it happens in limb muscles (Grünheid et al., 2009). All of these features allow masticatory muscles to perform slow, tonic contractions and controlled movements of the jaw. The particular combination of morphofunctional features in the jaw-elevators optimises function while minimizing energy use, which makes mastication a highly efficient process (Korfage et al, 2005).

In the masticatory system, muscle force and consequently bone loading change naturally under physiological conditions. The ageing process includes neuro-degenerative changes, producing muscle atrophy with a decrease in fibre and consequently muscle cross-sectional area (Newton et al., 1993; Grünheid et al., 2009). Furthermore, with increasing age there is a decrease in type I fibres and an increase in type II and hybrid fibres, particularly those expressing developmental MyHC isoforms. The consequence of these changes is the development of more atrophic muscles with a narrow range of contraction velocities (Grünheid et al., 2009). Similar modifications in muscle characteristics have been observed with changes in food consistency. In animal experiments, soft diets produce a decrease in the cross-sectional area of most fibre types in the masseter muscle (Kitagawa et al., 2004), as well changes in the proportions of myosin isoforms towards faster types (Saito et al., 2002). Variations in skull morphology have also been associated with variations in muscle anatomy, particularly muscle CSA and so force (Weijs and Hillen, 1986; Hannam and Wood, 1989; van Spronsen et al., 1991; van Spronsen et al., 1992). At a histological level, individuals with vertically elongated faces have been associated with a higher proportion of type I fibres and shorter faces with type II fibres (Rowlerson et al., 2005; Grünheid et al., 2009; Sciote et al., 2012). As mentioned at the beginning of this literature review a decrease in muscle force is associated with a decrease in bone strains during muscle function. The bone reacts by increasing its resorption rate particularly in the cancellous part (Frost, 1997; Rubin et al., 2002) with a consequent decrease in bone strength.

Another relevant aspect of the functional anatomy of muscle is the arrangement of fibres with respect to the muscle axis, or *pennation*. In jaw-elevator muscles the fibres attach obliquely to inner aponeuroses. Pennation gives masticatory muscles the possibility of increasing the number of muscle fibres and hence CSA in a limited space, thus increasing muscle tension or intrinsic muscle strength (Figure 1.7; Hannam and McMillan, 1994; Ethier and Simmons, 2007). The inclined fibres rotate about their origins, causing the translation of the aponeurosis to which they are attached. Narrow angles between the muscle fibre and the tendon lead to larger movements of the latter and vice versa. In the jaw-elevator muscles, this angle varies between 12° and 17° (van Eijden et al., 1997)

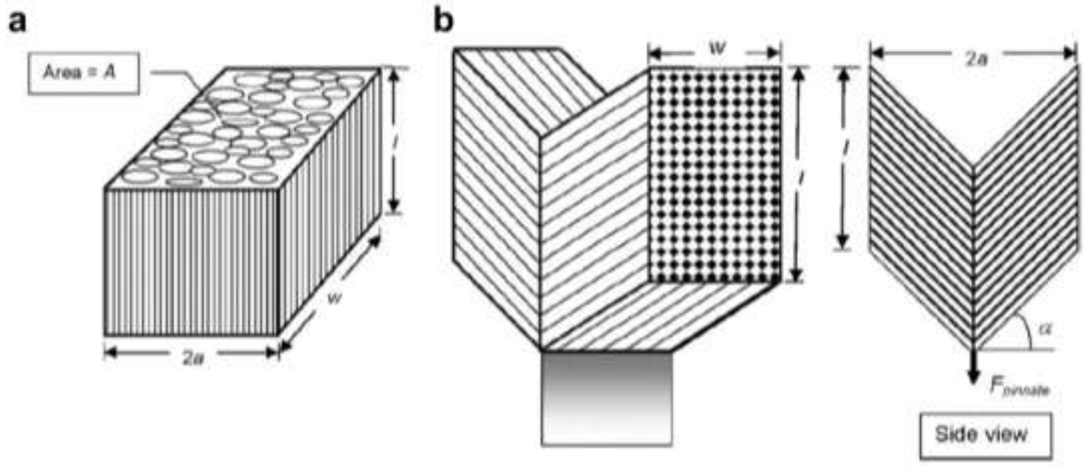

Figure 1.7. Muscle fibre organisation diagram. (a) Parallel fibre muscle, where force is the product of muscle intrinsic strength and CSA (*A*). In pennate muscles (b), force is the product of intrinsic strength, CSA (from *wl*) and the cosine of the fibre inclination angle (90°-α). Adapted from Ethier and Simmons (2007).

The anatomy of the three masticatory muscles emphasising the most relevant aspects for biomechanical modelling is presented next.

1.3.3. Temporalis muscle anatomy

The temporalis (Figure 1.8) is a pennate muscle formed by two main portions: the anterior (orbital) and the posterior (temporal) portion (Gaudy et al., 2002), laterally covered by a fascia with its own particular anatomy and function. A zygo-mandibular muscle and other deep muscle bundles are also described as part of the temporal muscle.

Anterior (orbital) portion of the temporalis muscle. The origin is on the temporal surface of the temporal bone and the greater wing and the infratemporal crest of the sphenoid bone. A deep aponeurosis is found extending from the infratemporal crest to the tendon, to which the fleshy body attaches. This tendon inserts onto the temporal ridge and anterior border of the mandibular ramus, and on the supero-medial aspect of the ramus. At its most anterior part, a variable amount of fatty tissue separates the flesh from the bone. From a frontal view, the anterior temporalis is a bipennate muscle with a larger CSA than the posterior portion (Hannam and McMillan, 1994; van Eijden et al., 1997). The vertical fibres of the anterior temporalis are more frequently activated compared to the posterior portion in motor tasks where the jaws are within a common range of functional proximity (Korfage et al., 2005). This portion has been described as possessing an approximately equal proportion of fibres of types I and II (Eriksson and Thornell, 1983). Korfage et al. (2005), on the other hand, characterise the anterior temporalis as having predominantly type I fibres.

Posterior (temporal) portion of the temporalis muscle. Two main subportions of the posterior portion have been described. The most posterior subportion has fibres inserted onto the anterior border of the articular disc of the temporomandibular joint (Gaudy et al., 2002). The common insertion tendon reaches the coronoid process of the mandible, covering its lateral aspect partially and its medial aspect entirely. The posterior portion of the temporalis muscle has a small CSA (Hannam and McMillan, 1994), it is less pennate than the anterior portion (van Eijden et al., 1997) and shows a higher proportion of a subtype of type II fibres than the anterior portion of the muscle (Eriksson and Thornell, 1983).

The temporal fascia. In the temporal fossa, the fascia inserts along the superior temporal line. At the supraorbital margin, it splits into a thin superficial layer and a deeper, thicker and more fibrous layer. Some lateral fibres of the temporal muscle originate in the upper portion of the fascia. It has been suggested that it could play a role as the mechanical counterpart of the masseter on the zygomatic arch in *Macaca*, reducing downward deflection of and hence strains within the zygomatic arch (Curtis et al., 2011). A deeper fascia has also been described, medial to the deeper fascicles of the temporal muscle and tendon, which continues forward with the buccinator fascia (Gaughran, 1957).

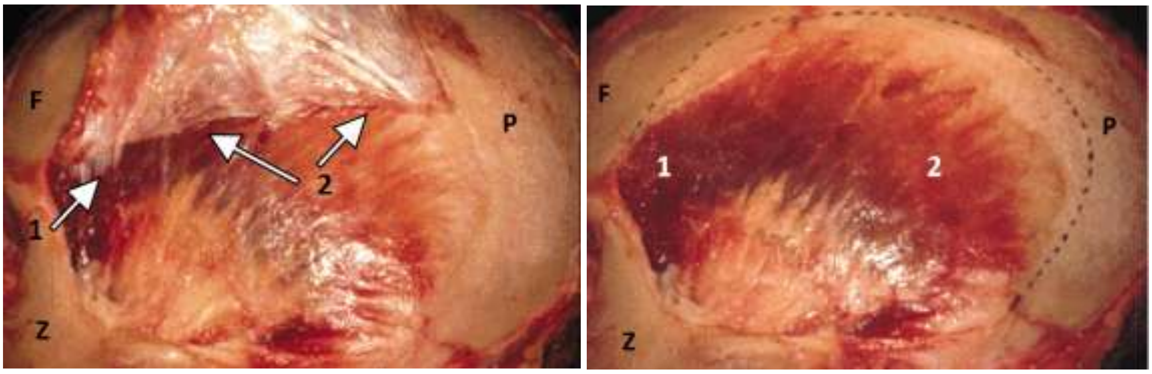

Figure 1.8. Dissection of the human temporalis muscle. Left: temporalis fascia lifted to show the muscle attachments to its medial face (arrows). Right: (1) anterior and (2) posterior portions of the temporalis muscle, with the superior insertion of the temporalis fascia (dotted line). F=frontal bone; P=parietal bone; Z=zygomatic bone. Adapted from Gaudy et al. (2002).

Among masticatory muscles, the temporal muscle as a whole has the highest CSA on magnetic resonance images (MRIs) (Weijs and Hillen, 1984), the longest fibres, the largest physiological CSA (PCSA, the CSA of all muscle fibres at a specified muscle length; Weijs and Hillen, 1984) and the highest mass of contractile tissue (van Eijden et al., 1997). It also shows the longest moment arm and, due to the differences between its portions, the direction of the temporalis muscle force is more vertically than horizontally aligned (Hylander, 1975).

1.3.4. Masseter muscle anatomy

The masseter (Figure 1.9) is a multipennate muscle with several intramuscular septa, formed by three main layers or portions: the superficial, intermediate and the deep masseter (Hannam and McMillan, 1994; Gaudy et al., 2000).

Superficial masseter. It is formed by two sublayers with their tendinous origin in the zygomatic arch, giving way to the fleshy body at the opposite end that attaches onto the mandibular angle. The fibres of the superficial masseter are longer than those of the deeper portions (Hannam and McMillan, 1994).

Intermediate masseter. It is oriented perpendicular to the occlusal plane and is formed by a musculo-aponeurotic layer whose origin is on the zygomatic arch and the zygomatic bone. This gives way to a fleshy portion that inserts onto the lateral face of the mandibular ramus.

Deep masseter. It is oriented mostly vertically and is divided into an anterior and a posterior part by the masseteric neurovascular bundle. The fleshy parts originate in the zygomatic arch, and its tendons insert onto the lateral aspect of the mandibular ramus. The architecture of this and the intermediate portion are more variable, but they have been described as fan-shaped (Hannam and McMillan, 1994).

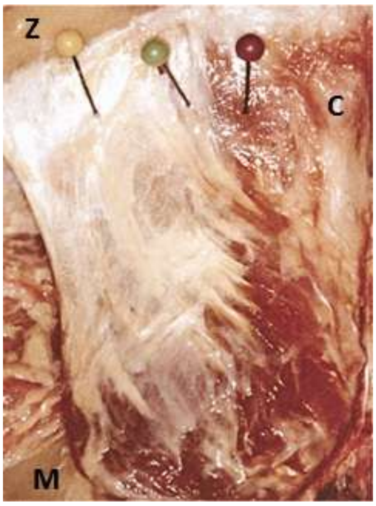

Figure 1.9. Dissection of the human masseter muscle. The three layers are shown: superficial (yellow pin), intermediate (green pin) and deep (red pin). Z=zygomatic bone; C=condyle of the mandible; M=body of the mandible. Adapted from Gaudy et al. (2000).

Although anatomically the masseter muscle is formed by a superficial and two deeper portions, functionally it shows a division similar to the temporalis muscle with an anterior and posterior part. The anterior part has a longer moment arm than the posterior; for this reason a more frequent activation of this portion during jaw closing would be expected as occurs with the anterior temporalis (Korfage et al., 2005). It comprises mainly type I muscle fibres plus slow isoforms of type II fibres, developmental isoforms of both fast and slow fibres, and developmental cardiac-type myosin with each fibre showing unique combinations of MyHC isoforms (Stål et al., 1994; Österlund et al., 2011).

1.3.5. Medial pterygoid muscle anatomy

The medial pterygoid muscle is relatively small, with an internal architecture similar to the masseter muscle, but with shorter fibres. The numerous inner tendons (Schumacher, 1961; Hannam and McMillan, 1994; van Eijden et al., 1997) give the muscle the highest degree of pennation among masticatory muscles. Nevertheless, this muscle has the lowest PCSA (van Eijden et al., 1997). The medial pterygoid muscle shows a multilayered organisation (El Haddioui et al., 2007) and two main portions can be recognised. The more anterior fibres of the muscle originate in the lowest and most lateral portion of the pterygoid fossa and the tuberosity of the maxilla, while the more posterior arise in the highest and most medial part of the same fossa. The fibres are directed infero-posteriorly- and laterally, attaching to the inferior portion of the medial face of the mandible (Figure 1.10; van Eijden et al., 1995; van Eijden et al, 1997) . The small area of origin combined with a wide insertion area results in several muscle fibre and thus force directions. This suggests some versatility in medial pterygoid action likely related to stabilization of jaw motion (Hannam and McMillan, 1994).

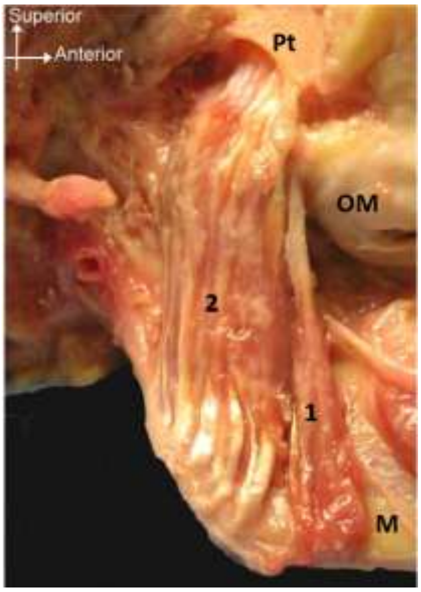

Figure 1.10. Medial pterygoid muscle. Medial view showing (1) anterior and (2) posterior muscle portion. Pt=medial wing of the pterygoid process; OM=maxillary oral mucosa; M=body of the mandible. Adapted from El-Haddioui et al. (2007).

1.3.4. Concluding remarks

The jaw-elevators are muscles with a cranial origin and mandibular insertion that close the jaws during contraction. Compared to other skeletal muscles, the jaw-elevators show a particular combination of structural and functional features such as variable proportions of fibre types, mysosin isoforms, activation timings, degrees of pennation and fibre orientations. These characteristics make the jaw-elevator muscles versatile and adaptable to changes in masticatory function (e.g. changes in diet, loss of teeth, aging).

Jaw-elevator muscles act on the bone they insert into by directly generating strains during contraction. They also define the lever arms during biting and hence, they define the loads that are ultimately transmitted from teeth during biting. Their role in masticatory mechanics is crucial, and therefore the potential consequences of variations in muscle morphology and activity need to be taken into account when modelling masticatory function.

1.4. Modelling the human skull: the available tools

The biomechanics of the masticatory system in terms of bite forces, joint reaction forces and bone strains/stresses is of interest in fields such as anthropology and medicine. In the former, these variables are proposed to reflect feeding capability and are of interest in relation to adaptations to feeding and how they change during evolution and development (Demes, 1987; Spencer and Demes, 1993; Kupczik et al., 2009; Strait et al., 2009). In medicine, variation in biomechanics among individuals is of importance in the diagnosis and treatment planning of facial dysmorphism and masticatory dysfunction (Pruim et al., 1980; Hagberg, 1987; García-Morales et al., 2003; van Spronsen, 2010). Studying masticatory biomechanics by means of graphical and mathematical representations is a common choice among researchers. In general terms, modelling the human skull requires (1) adequate representation of the anatomy under study, which is usually obtained from imaging methods, (2) functional parameters such as bite force, muscle activation patterns, kinematic data, etc, and (3) an analysis algorithm, usually using specialist programs such as finite element analysis packages.

To achieve the aims of this thesis, finite element models of the human cranium simulating biting will be developed. A literature review of relevant topics for understanding the method is presented next. First is an introduction to past and current methods for biomechanical modelling. This is followed by a review of three-dimensional medical imaging methods for anatomical data acquisition. Finally, finite element analysis and geometric morphometrics are presented. Geometric morphometric tools are used here to compare the results from finite element analysis, as well as for analyses of shape or form variation in the different chapters of this thesis.

1.4.1. Biomechanical models of the human skull

The use of mathematical and physical tools for studying masticatory system functioning is not new. Representations of the jaw acting as a lever have been widely used for studying masticatory biomechanics in humans. This approach has been criticised due to the implicit oversimplification of such a representation. However, authors agree that in general terms the jaws act as follows: (1) the centre of rotation of the mandible is located close to the condyle; that (2) with moderate or greater unilateral bite forces the balancing TMJ produces a higher reaction force; and that (3) different combinations of anatomical features can perform masticatory system tasks with equal biomechanical efficiency (Hylander, 1975; Koolstra et al., 1988; Spencer, 1998; Raadsheer et al., 1999; O'Connor et al., 2005).

With the development of computer technology, the use of complex 3D models of the human masticatory system has become more frequent. These have provided more detailed information about variables of interest such as bite forces, joint reaction forces and muscle forces and activitations (Koolstra et al., 1988; Langenbach and Hannam, 1999; Sellers and Crompton, 2004). Among current methods of biomechanical modelling, finite element analysis (FEA) is an engineering technique that has become widely used to predict the structural behaviour of an organism in terms of stress and strain as explained below, and recently to predict muscle activity (Röhrle and Pullan, 2007; Röhrle et al., 2012). In relation to bite force, TMJ reaction force, and muscle force and activity, results of studies using both 2D and 3D models show generally consistent results. It is accepted that the human masticatory system is highly efficient compared to other extant and extinct primates, producing a relatively high bite force using low muscle forces (O'Connor et al., 2005; Wroe et al., 2010). Finite element analyses of bone under load, for example, have shown that overall stress in different skull parts caused by mastication is lower when compared to other hominoids (Wroe et al., 2010; Gröning et al., 2011b). The finite element method, which is the basic method for biomechanical analysis in this thesis, is more extensively described below.

The building of mechanical models to understand masticatory system functioning is a relatively new approach, still under development. The biomechanical complexity of masticatory function is not likely to be fully reproduced, nor are models able to be fully validated with current technology. Computer-based 3D models of the human skull, although they have provided significantly new information, are difficult to build and fully validate because of physical and ethical constraints that make it impossible to obtain certain *in vivo* data required for building and validation such as muscle forces, bone stresses and strains and joint reaction forces. However, models generally produce biologically plausible results when their performance is compared with available *in vivo* data and as such are increasingly used.

1.4.2. Building the structure for biomechanical analysis: three-dimensional imaging techniques

Reconstruction is the first step in building models simulating masticatory system functioning, such as FEA. Advances in computational technologies facilitate sophisticated and high resolution 3D digital reconstruction.

Cross-sectional medical imaging techniques such as CT and MRI are commonly used to visualise the anatomy of an organism, and have been significantly refined since their introduction in the 1970s (Fishman et al., 1991). Subsequently, methods for virtual 3D reconstruction of high resolution anatomical cross-sectional images were developed. Accurate representation of the anatomy under study depends on factors like the method used to map the organism (CT or MRI), image resolution and the approach to tissue labelling and segmentation from surrounding structures. Hence, the reconstruction method has to be selected depending on the object of interest and the aims of the study.

1.4.2.1. Computed tomography (CT)

Computed tomography as well as MRI, provides the raw image of the anatomy under study from which a digital 3D reconstruction is undertaken. This reconstruction is then used to create the FE model. The basic principle underlying CT is the same as for traditional radiography: differential absorption of X-rays. The X-ray source and detectors are synchronously rotated through one complete revolution around the individual, generating one-dimensional projections from several angles which are then used to reconstruct the different planes of the organism (Smith and Webb, 2010). Current equipment (e.g. multichannel, multidetector or multislice helical CT) incorporates an array of small-sized detectors along the axial axis, increasing imaging efficiency and allowing the creation of thin image slices. Reduced slice thickness means that high resolution images can be created improving multiplanar reconstruction and volume rendering, providing detailed visualisation of planes other than the axial (Douglas-Akinwande et al., 2006; Smith and Webb, 2010).

Computed tomography and bone reconstruction techniques are among the most used approaches for skull FE modelling (Kupczik et al., 2009; Wroe et al., 2010; Gröning et al., 2011b; Fitton et al., 2012). However, the use of ionising radiation limits the use of CT in living humans. In these cases, magnetic resonance imaging is a potential alternative for the production of 3D reconstructions.

1.4.2.2. Magnetic resonance imaging (MRI)

Magnetic resonance imaging provides a spatial map of the hydrogen nuclei (water and lipid) in different tissues. It works by placing the organism in a superconducting magnet (1-3 Tesla) and a radiofrequency coil. Under the effect of the superconducting magnet the hydrogen in tissue is in a dynamic energetic equilibrium. The resulting net magnetisation of hydrogen atoms within each voxel is represented using a grey scale image. This net magnetisation cannot be directly measured, and so is estimated indirectly by disturbing the equilibrium using radiofrequency waves, and the magnetic field produced by the hydrogen under disturbance (Suetens, 2009). To generate the 3D image, a series of linear magnetic field gradients are superimposed. This causes the hydrogen in different locations to be excited at different rates, information that is translated into positional data (Suetens, 2009; Smith and Webb, 2011).

With strong magnetic fields and modern scanners high definition of soft tissues is achievable, however bone cannot be directly visualised, which poses some difficulties when aiming for 3D bone reconstruction. The price of MRI is high compared to CT, and it involves the subject spending a long time inside a closed scanner. However, no ionizing radiation is used, and the only known negative effects relate to patients with metallic implants that interact with the magnetic field.

1.4.2.3. Three-dimensional reconstruction by image segmentation

Once the volume data of the anatomical structure is produced by the imaging method, classification of the tissues represented in each voxel (segmentation) followed by projection of the classified volume data are undertaken (Fishman et al., 1991). Classification by image segmentation works by partitioning an image into non-overlapping, constituent regions that are homogeneous with respect to some characteristic such as light intensity in CT or depth value in MRI (Pal and Pal, 1993; Pham et al., 2000). Image resolution is crucial, and low image resolution can cause several tissues to be represented in the same voxel thus blurring tissue boundaries. One of the most common segmentation methods in skull biomechanics involves the use of grey-level thresholds to differentiate tissues. The threshold level used to determine the boundaries between two tissues needs to be chosen or calculated, A commonly used approach assigns this threshold the mean of the two grey levels on either side of the interface. This is known as the half maximum height (HMH) criterion (Figure 1.11; Spoor et al., 1993) .

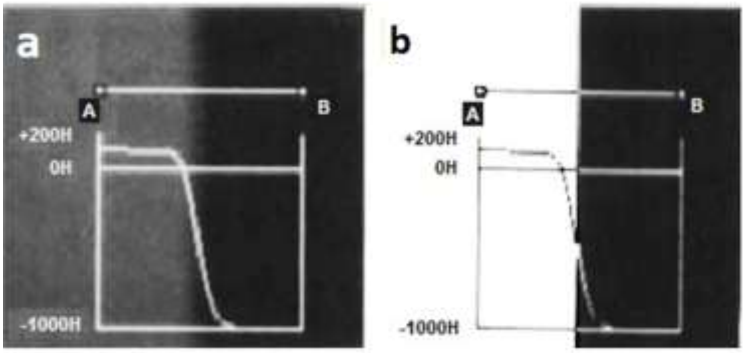

Figure 1.11. Computed tomography image showing the grey-level gradual change in a plexiglass-air interface. (a) Between points A (plexiglass) and B (air), grey levels go from 130 to -1000H, with a blurred boundary. (b) The actual interface is located where defined by the HMH. Adapted from Spoor et al. (1993).

The use of grey-level thresholds is well established for CT-based volume reconstruction (Figure 1.12). Semi-automated methods for bone segmentation from medical MRI, on the other hand, are not in common use in biomechanical modelling. Bone signal intensity is low for labelling and the resolution of MRI is low compared to CT (Schmid and Magnenat-Thalmann, 2008), which may lead to anatomical inaccuracies. An alternative to overcome the lack of boundary homogeneity is a manual segmentation approach based on boundary tracing, where the observer is guided by expert knowledge of the anatomy (Clarke et al., 1995).

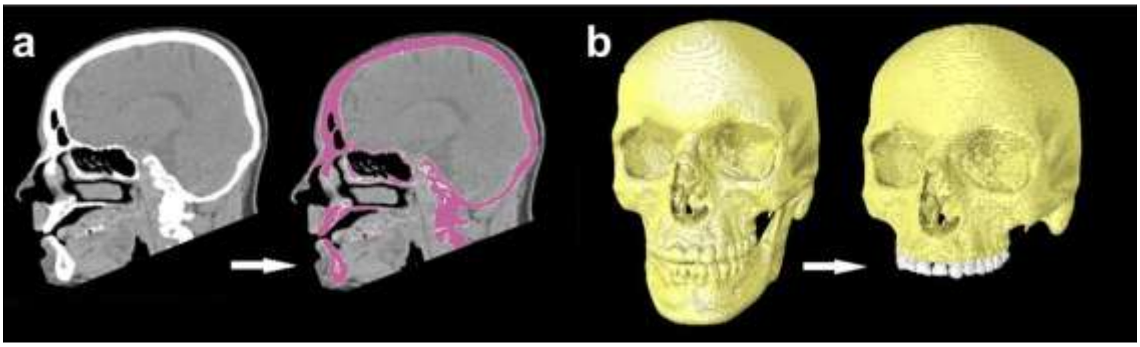

Figure 1.12. Three-dimensional reconstruction of a human cranium from CT image data. (a) Grey level-based segmentation of the hard tissues (in purple). A (b) volume data of all the hard tissues in the head is generated. With further processing, the maxillary teeth and the mandible have been labelled separately, and the mandible deleted from the final volume data in order to create the model of a cranium.

Three-dimensional reconstruction of anatomical structures is a fundamental step in preparing a model for 3D FEA. Advances in both imaging methods and graphics programs have led to the construction of virtual models of sub-millimetre resolution of complex structures such as the vertebrate skull. The choice of the best method of imaging and segmentation depends on the aims of the study, but other constraints related to costs and ethical use of imaging methods in living individuals also impact on study design. Given the spectrum of possibilities, differences in the resulting virtual model can potentially affect the mechanical behaviour of the structure in FEA. Validation and sensitivity studies are then crucial to understand the effects of different reconstruction decisions and achieve accurate and reliable results

1.4.3. Finite element analysis and the study of skull biomechanics

Finite element analysis is an engineering technique used in biomechanics for reconstructing the mechanical performance of a biological structure under loading in terms of stress, strain and deformation. This was initially developed in the first half of the twentieth century with the work of Alexander Hrenikoff (1941) and Richard Courant (1943). Since the seventies and with advances in computer technology that make implementation feasible, FEA has been increasingly applied in biology offering new insights in biomechanics of the human musculoskeletal system. With this new approach limitations related to classic experimental techniques such as brittle coating of surfaces, photo-stress techniques and strain-gauge measurements are avoided (Brekelmans et al., 1972). However the issue of validity arises with simulation, this is considered further below in the Finite Element Analysis section.

The earliest applications to the study of organisms concerned orthopaedics, in part due to rapidly growing interest in joint replacement and trauma. Since 1973 FEA has been increasingly applied to the study of skull bones and human masticatory function in different fields of craniofacial research such as dentistry or evolutionary anatomy (Gupta et al., 1973; Knoell, 1977; Hart et al., 1992; Koolstra and van Eijden, 2005; Kupczik et al., 2009; Wroe et al., 2010; Gröning et al., 2011b). The functional basis of the evolution of anatomical traits of other vertebrates has also been studied with FEA (Dumont et al., 2005; Rayfield, 2005; Moazen et al., 2009), making this still developing technique one of the preferred methods for studying cranial biomechanics.

The use of FEA in skull research has provided a more comprehensive understanding of cranial skeletal performance during biting. In primates it has been observed that the main concentrations of stresses and strains during biting are associated with muscle attachments and bite points. In particular, the masseter muscle has been shown to markedly strain the zygomatic arch (Kupczik et al., 2007; Curtis et al., 2011; Fitton et al., 2012), which has led to discussion of the role of the temporal fasciae in limiting deformation of this structure (Curtis et al., 2011). Tooth loading results in concentrations of strains in the areas of compact tissue surrounding facial cavities forming the 'facial buttresses' (Donat et al., 1998; Linnau et al., 2003); that is, the maxillary bone forming the nasal notch, its frontal process during incisor biting, and the zygomatic and frontal process of the maxilla during molar biting (Gross et al., 2001; Witzel et al., 2004; Kupczik et al., 2009; Fitton et al., 2012; Jansen van Rensburg et al., 2012). This detailed information on cranial behaviour during biting arises mainly from applications of the FE method which are detailed below.

1.4.3.1. The finite element method in mechanical analyses

Finite element analysis can be undertaken for uni-, bi- or three-dimensional (1D, 2D and 3D respectively) structures. The method comprises three main steps: pre-processing, solution and post-processing.

Pre-processing. This consists of the virtual recreation of the structure under study. 3D anatomical structures obtained from CT scans by segmentation methods using image processing programs (e.g. Amira$^{\copyright}$and Avizo$^{\copyright}$, by Visualization Sciences Group, Burlington, USA; Mimics$^{\copyright}$, by Materialise, Leuven, Belgium) have been used in FEA since 1980 (as reported by Keyak et al., 1990) and are widely used nowadays. The geometry of the structure is then transformed from a continuum into a mesh comprising a finite number of discrete subregions called elements that are connected at nodal points. The geometry and locations of nodes that define the element (Figure 1.13) have an effect on the solution and, depending on the method employed, the element type and node number can be selected by the operator according to the needs of the study. Although increasing element number and complexity tends to provide more accurate results, it makes the model more complex to solve and computationally more expensive (Bright and Rayfield, 2011).

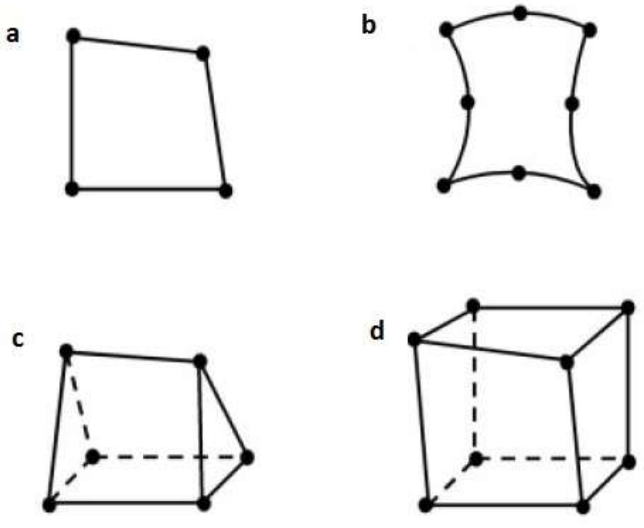

Figure 1.13. Examples of element types. Based on their dimensionality they can be 1D, 2D (a and b) or 3D (c and d). Based on the locations of nodes (black dots), their behaviour under loading can be represented by linear or polynomial functions (a and b type of elements respectively). Adapted from Richmond et al. (2005).

Other methods of mesh generation aim to simplify element manipulation with programs that transform the voxels directly from CT scans or MRI into volumetric elements (e.g. Vox-FE; the Simpleware$^{©}$ package, Exeter, UK). After the mesh has been created, the material properties of the body have to be specified. When bone is modelled as linearly elastic and isotropic homogeneously throughout the structure, a single Young's modulus of elasticity and one Poisson's ratio (i.e. the transverse strain in relation to the longitudinal strain of a material) are used. If not, several other properties can be considered and allocated heterogenously throughout the model, such as the shear modulus, nonlinear elasticity and viscoelasticity as well as different elastic moduli and Poisson's ratios. As with element complexity, the more heterogeneous mechanical properties are, the more computationally complex the model building and solution become. Finally, the boundary conditions of the model describing kinematic constraints and loading conditions must be defined. This requires the user's knowledge of the anatomy and physiology of the organism under study. Kinematic constraints are used to prevent rigid displacement of the body. Loads such as muscle forces have to be defined in terms of points of application, magnitudes and directions. Accurate recreation of boundary conditions is essential to obtain a model response that is close to reality. The pre-processing stage is fundamental to achieving reliably functioning simulations that fulfil the aims of the study, and it requires a considerable amount of work and careful planning by the operator (Fagan, 1992; Richmond et al., 2005; Rayfield, 2007; Kupczik, 2008).

Solution. The second step consists of the solution of the system equations, given the pre-defined mechanical properties and boundary conditions. Nodal displacements are calculated and from them, the strains and stress in the structure.

Post-processing. In the final stage results are displayed either numerically or graphically by means of contour plots that represent the intensity of variables such as displacement and strain (Figure 1.14). Typically, displacements are used to calculate strains, and stresses are calculated from strain and the elasticity modulus. Contour plots can be used to depict the relative locations of high and low magnitudes of the parameter (e.g. principal strain) under study, thus providing a visual display the spatial distribution of magnitudes over the surface. Additionally, animations that represent the deformation of the body under loading can be used (Fagan, 1992; Richmond et al., 2005; Zienkiewicz et al., 2005).

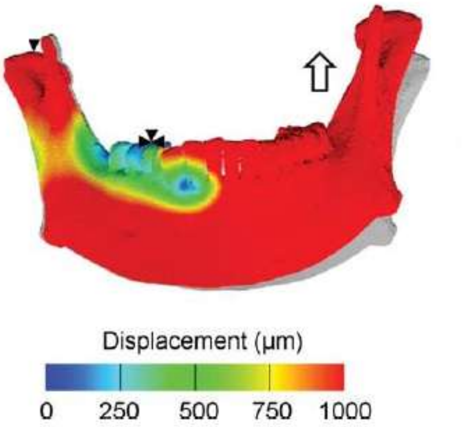

Figure 1.14. Finite element analysis of a human mandible showing the location and intensity of node displacement and overall deformation under unilateral premolar load. The grey outline represents the unloaded mandibular morphology, the black arrowheads represent the constraints and the hollow arrows, the direction of the displacement in the left side of the mandible. Adapted from Gröning et al. (2011b).

1.4.3.2. Building FE models: Factors affecting model accuracy

The use of FEA to elucidate functional aspects of biological structures has raised questions related to the robustness and accuracy of the method. The mechanical performance of the structure under analysis depends mainly on three factors: geometry, material properties and boundary conditions, each defined by the operator. To date reproducing completely a complex structure like the skull is nearly, if not completely, impossible. Simplifications in geometry, material properties and boundary conditions are needed. Validation and sensitivity analyses are then needed to assess (1) the extent to which FEA results accurately predict the structure's performance under experimental conditions, and (2) how varying model variables such as geometry, loads, constraints and material properties impact model performance. These two types of analyses are closely related; model sensitivity to variations can be compared to experimentally measured strains. Obtaining accurate FEA results improves the interpretation of the underlying biological phenomena (Rayfield, 2007; Dumont et al., 2009; Anderson et al., 2012).

Bone anatomy. In the case of the virtual representation of an anatomical structure, questions arise regarding errors introduced by the method of 3D reconstruction. The omission of detail such as internal bone anatomy offers advantages such as saving of pre-processing time and facilitates reconstruction of hypothetical anatomies. Parr et al. (2012) found that modelling internal cavities in the varanoid mandible had an impact on FEA results, showing not surprisingly higher strains and bending magnitudes compared to the same mandibles modelled in a 'solid' way. However, strain distributions remained similar. These results are particularly relevant when the aim is to generate different specimens by means of warping, which is potentially useful for rapid model building and so increasing sample size. Warping can be used to reconstruct incomplete structures by adjusting the anatomy of a complete specimen to fit and replace missing parts in another or to create hypothetical anatomies to test different functional hypotheses (Sigal et al., 2008; O'Higgins et al., 2011; Parr et al., 2012). In complex structures like the primate skull, the internal anatomy cannot be warped by means of morphometric methods due to the need for an excessive number of landmarks to reliably represent internal features. In addition any such warping of internal features would likely result in internal architecture that does not accurately represent the anatomy that would be found in reality because internal architecture is plastic and adapts to *in vivo* loads; warping from one specimen to another cannot take account of such adaptive changes. Using reliable solid meshes is also of interest in cases where the volume data come from image data where the detailed bone anatomy is not observable such as in MRIs or in low-resolution medical CTs.

Articular soft tissues. Other sensitivity studies have assessed the mechanical effect of modelling the soft tissues between articular surfaces in the vertebrate skull. Structures like ligaments and fibrocartilage are of functional significance but pose methodological problems, due to their complex properties and difficulties in defining their anatomy with the available tools. Among articular soft tissues, the effect of modelling periodontal ligament has received special attention. Panagiatopoulou et al. (2011) after comparing strain values in key points of a macaque mandible, concluded that the presence and properties of the periodontal ligament affect the strain values in the local alveolar bone, but do not have an effect on the mechanical behaviour of the macaque mandible as a whole. In contrast, using combined FEA and geometric morphometrics, Gröning et al. (2011a) showed that the deformation of a human mandible changes considerably when the periodontal ligament is included or its properties change. Other authors using partial 2D FE models of human teeth and alveolar bone (Middleton et al., 1996; Rees, 2001) suggested an important role of the periodontal ligament in modulating the strains developed in adjacent tissues. Wood et al. (2011) showed in the cranial model of a capuchin monkey that the effect of including and varying the periodontal ligament characteristics is localised to the alveolar area, and it does not affect the overall mechanical response. Thus, the effects of including or excluding the periodontal ligament are yet unclear. Perhaps the cranium is less sensitive than the mandible to presence or absence of periodontal ligament because it is stiffer overall.

The presence of cranial sutures is another subject of interest in FEA sensitivity analyses. Differences in strain magnitudes and distributions were found when sutures are assigned lower stiffness in an isotropic bone model of a crocodile mandible (Reed et al., 2011). The presence of sutures causes higher and less homogeneous strains in the FE model of a *Sphenodon* reptile when compared with a model with fused sutures (Curtis et al., 2013). In macaques, inclusion of the zygomatico-temporal suture resulted in strain patterns closer to those obtained from *in vitro* experiments using strain gauges (Kupczik et al., 2007). Similarly, using speckle interferometry to measure surface strains, local variations in strain were obtained when additional facial sutures were included in the same macaque model (Fitton et al., 2009). On the other hand, Bright (2012) found that including facial sutures in the pig cranium increased the differences in strains from those obtained *in vitro*. Moreover, including cranial sutures in a macaque skull showed a small effect on the strain distributions in areas distant from the sutures, and bite force was not affected (Wang et al., 2010). The same authors ran a similar experiment using static and dynamic bite simulations and found a small overall effect of including sutures in the FE model (Wang et al., 2012). The authors of the last two studies conclude that the omission or fusion of sutures is a reasonable modelling approximation in crania with anatomical characteristics comparable to those of the macaque.

Mechanical properties and muscle loads. As with anatomical details, fully reproducing the mechanical properties of the different structures is not always possible. Kupzcik et al. (2007) observed that the most accurate FEA results were achieved using elasticity modulus obtained directly from nanoindentation in the specimen under study rather than from the literature. In a very complete study, Strait et al. (2005) tested in macaque skulls the effects of different sets of elastic properties: isotropic using data from the literature; average isotropic properties obtained from different parts of the same specimen; using different isotropic properties for each part of the skull; and using orthotropic properties for the face alone. Results differed to some degree, and the last model obtained results that were closest to those obtained *in vivo* using strain gauges. It was concluded by the authors that the decision to simplify the material properties of a specimen relates to the degree of accuracy needed. In a complementary study using the same specimens, Ross et al. (2005) assessed the effects of varying muscle loads, concluding that muscle force magnitude has a larger effect than muscle recruitment pattern. Fitton et al. (2012) also studied the effect of different muscle activation patterns on a macaque cranium model under different biting tasks. Using GM methods for model performance comparison, the authors concluded that variation due to biting point location outweighed that due to different patterns of muscle activation.

Validation of FEA results. Validating FEA input variables and results is more difficult than carrying out sensitivity analyses. This because *in vivo* validation studies raise practical and ethical problems for data acquisition. For example, mechanical testing of tissues to obtain input parameters for FEA would imply the use of invasive procedures for sample collection. A reasonable alternative for data collection is the use of post-mortem material, which poses several problems, including the difficulty of adequately loading and constraining the part such that physiological conditions are simulated and the issue of potential tissue alterations due to decomposition or drying during storage and preservation procedures (De Clerck et al., 1990; Kupczik et al., 2007). In many cases the validation of FEA-predicted strains is simply not possible, as in the study of rare species or of fossils which not only are structurally damaged, but also have undergone alterations in material properties during fossilisation. However, studies comparing predicted versus experimental strains in vertebrate skulls using different approaches have shown that, in general, FEA is a reliable tool for predicting bone strains. Among methods for validation by comparison with measured strain, the use of strain gauges attached to surface is one of the most used (Remmler et al., 1998; Metzger et al., 2005; Kupczik et al., 2007; Rayfield, 2011). A recognised disadvantage of this method is the limited size and number of measurement when using gauges (Hack and Schumacher, 2007; Gröning et al., 2009). A relatively new method, speckle laser interferometry, uses full-field, non-contact laser measurement of microscopic deformation (Yang et al., 2007), offering large areas of measurement and easier manipulation of bone samples compared to strain gauge methods (Gröning et al., 2009). Hence, speckle laser interferometry has become one of the most used methods for FEA validation in the vertebrate skull (Verrue et al., 2001; Gröning et al., 2009; Bright and Gröning, 2011; Panagiotopoulou et al., 2011).

Although there is no consensus on which characteristics of FE models yield accuracy while allowing simplification, all the above mentioned studies concur in that the decisions in FE modelling have to be guided by the questions to be answered. If the effects on the results due to variations in the input parameters are such that they change interpretation, then additional analyses or a different approach to the problem should be considered.

1.4.3.3. Interpretation of FEA results

Loaded bone undergoes elastic and/or plastic deformation. Local deformation (strain) is useful in assessing parameters such as the risk of fracture, which could be considered as a measurement of adaptation or could be a way to predict other biological phenomena such as remodelling (Currey, 2006; O'Higgins et al., 2011). However, when the aim is to compare the mechanical responses of different organisms to a load, an important question arises. The deformation of a structure under load is directly related to its size and shape. Comparability of models with differences in size and shape for biological interpretation of adaptive processes has been a topic of discussion in the last few years (Dumont et al., 2009; O'Higgins et al., 2011; Weber et al., 2011; Milne and O'Higgins, 2012).

Dumont et al. (2009) proposed that comparability problems related to size differences might be overcome by appropriate scaling of models or strains.. Shape differences render comparison of performance among models difficult. This is because it is not possible to match every surface point between models. In these cases, the use of anatomical landmarks for comparing strain/stress is one of the proposed methods (O'Higgins et al., 2011; Parr et al., 2012; O'Higgins and Milne, 2013). Over the last few years, an additional method has been proposed to compare the mechanical performance of a biological structure under loading; since strains represent localized deformation and hence, morphological changes, the large scale deformations can be compared directly among different structures under the 'same' loading (or between different loadings in the same structure) using Procrustes form (Cox et al., 2011) and size and shape analysis (Milne and O'Higgins, 2012; O'Higgins et al., 2012; O'Higgins and Milne, 2013). This approach, detailed further in the Geometric Morphometrics section, aims to quantify and characterise differences in large scale deformation resulting from applied loads using anatomical landmarks and multivariate statistics. However, while equivalent anatomical landmarks might be located on different bones, it is not possible to match every point (or in practical terms, finite element nodes) when comparing structures that differ in shape (O'Higgins et al., 2011).

Changes in overall model size and shape do not directly relate to mechanically interesting parameters such as strains, or strain energy (but see Bookstein 2012 for strains in beams). However, the modes of deformation are of interest in themselves and any differences in deformation indicate differences in performance because the strains cannot be the same among models if they differ in large scale deformation. This justifies the use of landmark-based analyses of large scale deformation, using geometric morphometric tools to compare changes in size and shape due to loading.

1.4.4. Geometric morphometrics and the study of skull shape

Geometric morphometrics (GM) is a statistical framework used to study size and shape variation and covariation with other variables (Bookstein, 1991; Dryden and Mardia, 1998). Geometric morphometric methods produce variables representing the size and shape of a configuration of landmarks that are suitable for subsequent multivariate analysis. The major development of GM occurred in the second half of the twentieth century with the work of Sneath (1967), Kendall (1977; 1984), Bookstein (1984), Goodall (1991), Dryden and Mardia (1993), Kent (1994) among others, that laid down the mathematical and statistical framework. Geometric morphometrics based on Cartesian landmark coordinates and Procrustes superimposition methods (detailed below) is the most widespread method for size and shape analysis, and it is one of the approaches used in this thesis. This method retains the geometric information of the landmark configuration (representing morphology) throughout the analytical process (O'Higgins, 2000; Slice, 2007; Mitteroecker and Gunz, 2009), allowing for visualization of results in terms of differences in the sizes and shapes of configurations. The well understood and well behaved statistical characteristics as well as the ability to visualise results have made GM a widely used method in biology, in areas such as evolutionary anatomy (Skinner et al., 2008; Gunz, 2012), developmental anatomy (Strand Viðarsdóttir et al., 2002; Bastir et al., 2006) and clinical research (Halazonetis, 2004; Bugaighis et al., 2010). In these studies GM is used to localize and quantify morphological changes deriving from evolution, development or medical conditions. As noted previously, GM has very recently been combined with the displacements arising from FEA to quantify and compare the structural deformation produced by loads (Gröning et al., 2011a; Milne and O'Higgins, 2012), a method that is further described at the end of this chapter.

A GM analysis consists of three fundamental steps: landmark data acquisition, Procrustes fitting and tangent projection to derive size and shape variables, followed by multivariate analysis.

Landmark data. The selection and acquisition of landmarks is a fundamental step in GM. An ideal data configuration should contain enough equivalent landmarks to capture the aspects of geometry of interest for the object under study. The process of landmarking should be reliably repeatable to minimise the effect of measurement error (Oxnard and O'Higgins, 2009; Zelditch et al., 2012). There are two main methods for landmark acquisition: directly from the object using 3D digitisers and virtually using specialist programs to view and landmark surfaces or volumes, such as might be derived by image segmentation. The latter is the method used in this thesis for data acquisition.

Procrustes fit. Once the landmark configuration is obtained, nuisance parameters due to differences in location and rotation are dealt with by centring and rotating. Size differences are removed by scaling the landmark configurations. This is a least-squares approach that generates shape variables describing the landmark configuration: the *Procrustes coordinates*. The differences in shape among individuals are described by the distances between them in the multidimensional shape space (Kendall, 1984) in which configurations of landmarks are represented as points. The Procrustes fit produces shape variables (the Procrustes coordinates) and a geometric size variable or *centroid size*, calculated as the square root of the sum of the squared distance of each landmark from the configuration geometric centroid (Zelditch et al., 2012).

When both size and shape are of interest, as is the case for the analysis of developmental changes or allometry, the Procrustes coordinates can be augmented by the natural logarithm of centroid size (Mitteroecker and Gunz, 2009). The logging avoids size differences being given undue weight relative to shape. The set of shape variables plus the natural logarithm of centroid size are collectively known as *form* variables. Alternatively, where size changes have a direct physical meaning, such as in the study of changes in size and shape and shape (in morphometrics referred to as deformations) arising from FEA, the scaling step can be omitted from the Procrustes analysis (O'Higgins et al., 2012). This preserves the linear scaling relationship between loading and changes in size and shape, resulting in *size and shape* variables (Dryden and Mardia, 1998) which can be used for subsequent analyses.

Data projection. Mathematically, Kendall's shape space corresponds to a manifold whose dimensions are determined by the number of landmarks and the number of landmark coordinates (Kent, 1994). When shape differences are large, distributions in this space are not immediately amenable to linear statistical methods for their analysis. The use of projection methods onto a Euclidean tangent space enables linear multivariate statistical methods to be used for subsequent analyses (O'Higgins, 2000; Slice, 2007; Mitteroecker and Gunz, 2009). This Euclidian space is tangent to Kendall's shape space (at the point of the mean configuration, and differences in the positions of points representing the shapes of landmark configurations in the space indicate differences in shape. Data projection can be omitted if variation is small enough that the curvature of the portion of shape space in which the data lie is negligible. (Mitteroecker and Gunz, 2009). In this case, distances in the shape space between Procrustes coordinates represent differences in shape and are used directly as shape variables for analyses.

In Procrustes size and shape analysis of FEA deformations we deal with extremely small changes in size and shape, lying scattered above and below Kendall's shape manifold surface according to size (Zelditch et al., 2012), the data are not confined to a manifold and so tangent projection is not undertaken.

As mentioned above, one of the main advantages of GM is the retention of the geometry of the landmark configuration throughout the analysis, allowing visualisation of size and shape differences. The use of transformation grids to represent shape change or difference in a single diagram is well established. Transformation grids derive from D'Arcy Thompson's (1942) use of Cartesian grids to represent morphological differences. Current algorithms for mapping homologous points between individuals are mainly based on work by Sneath (1967) and Bookstein (1989). The former used cubic splines and the latter *thin-plate splines* (TPS) as the function to smoothly map the space between landmarks from a reference configuration to the target form. The reference shape usually has a regular grid drawn over (2D) or within (3D) it. Its vertices are mapped into the space of the target configuration using 2 (2D) or 3 (3D) thin-plate splines. The resulting deformed grid aids interpretation of the overall and localized shape differences between the starting and target configurations. This method is also used for 3D surface warping where the TPS function is applied to the vertices of triangles that define the surface, the pixels of an image or voxels of volume data. Examples of the use of the TPS function for visualisation of size and shape differences or for surface warping are shown in Figure 1.15.

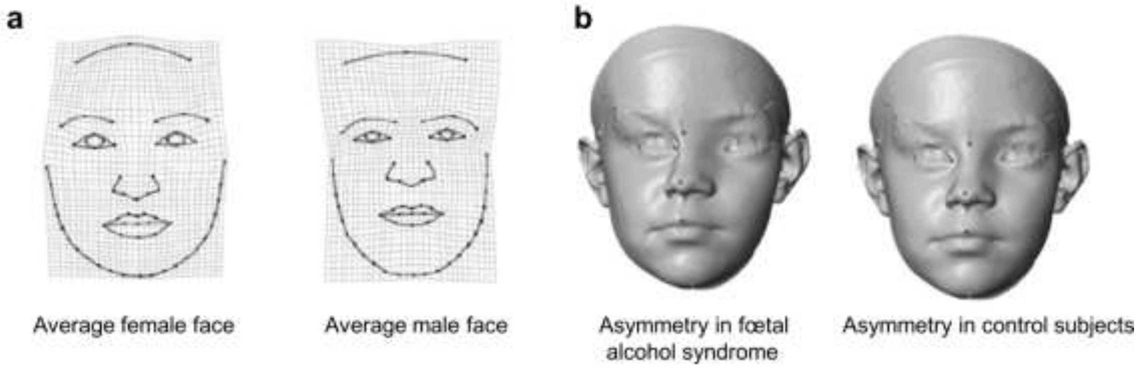

Figure 1.15. Thin-plate splines function for visualisation. (a) Shape differences between a female and male face using 2D transformation grids. From Fink et al. (2005). (b) Shape differences between the faces of children with and without prenatal alcohol exposure, expressed in terms of directional asymmetry (Klingenberg et al., 2010).

The TPS function for warping 3D surfaces can also be used in building virtual reconstructions. An incomplete anatomical structure can be estimated from another complete surface using homologous landmarks on the partial and complete surfaces to warp the relevant part of the complete onto the partial structure (Figure 1.16). With little modification, the same approach can be used to modify the form of an FE model, allowing experimentation with the aim of e.g. assessing the effects of anatomical variation on FE results.

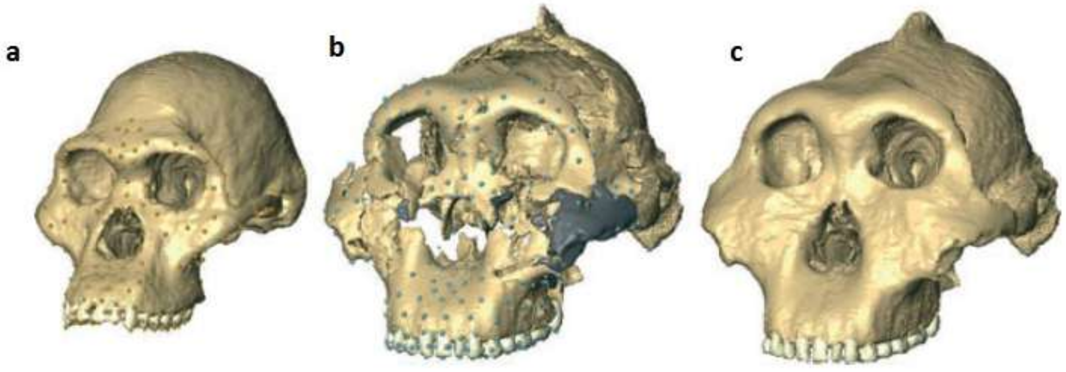

Figure 1.16. The TPS function used for cranial reconstruction. (a) The surface of a reconstructed *Australopitecus africanus* is warped to reconstruct (c) *Australopitecus boisei*, using (b) 325 reference landmarks taken from the incomplete cranium, partially reconstructed via mirror imaging (in grey). From O'Higgins et al. (2012).

The statistical analysis of shape or form variables can be undertaken using multivariate methods according to the aim of the study. Among the most widespread methods that are used in this thesis are:

Principal components analysis (PCA). The covariance matrix of Procrustes coordinates of a sample can be studied using PCA to derive orthogonal linear combinations of the original variables that summarise sample variability, reducing dimensionality (Slice, 2007). Principal components analysis lacks a priori assumptions, and so its results can unveil relationships between individuals based solely on their patterns of morphological variation. Natural group structures, developmental and/or allometric vectors and outliers may be observed. In FEA, PCA of Procrustes size and shape variables has been proposed as a method to compare deformations due to loading either between individuals, or within individuals under different loading scenarios. This is possible since a loaded structure deforms, and the overall size and shape changes can be captured using landmarks followed by GM analysis of size and shape variables (Figure 1.17; O'Higgins et al., 2011; 2012).

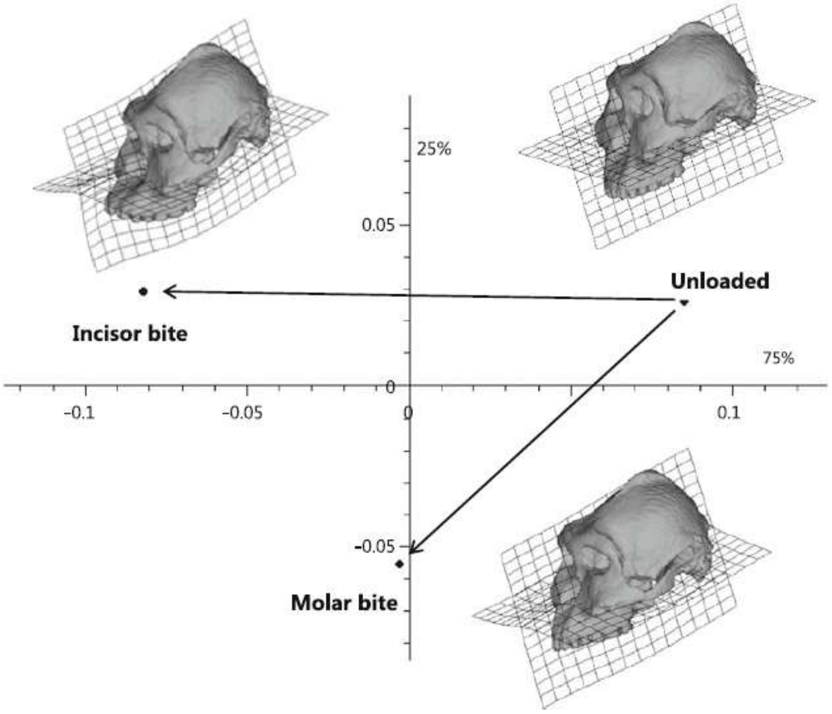

Figure 1.17. Principal components analysis of size and shape variables describing the deformation of an australopithecine cranium under incisor and molar loads. From O'Higgins et al. (2012).

Multivariate regression. Computes the relationship between a set of dependent variables and one or more independent variables. In GM studies it is commonly used to assess the predictability of shape or form (as dependent variables) from other continuous variables such as metric traits or ecological data (the independent variables). One of the most common uses of this method is to investigate allometry, by regressing shape variables against the natural logarithm of centroid size (Slice, 2007).

Partial least squares analysis (PLS). PLS assesses the association between two sets of variables from the same individuals. These variables can be two blocks of shape or form variables, or one block of shape or form variables, and another of continuous ones. PLS extracts linear combinations of the two sets of variables that best account for the pattern of association across the sets (Rohlf and Corti, 2000). Unlike regression analysis, PLS treats both variables symmetrically without assuming dependence of one variable on another.

The methods mentioned above are among the most commonly used in GM studies. Depending on the aim of the study, shape and form variables can also be analysed using other approaches such as discriminant analysis, canonical variate analyses, multivariate analysis of variance, etc (Hennessy and Stringer, 2002; Penin et al., 2002; Harvati, 2003; Klingenberg et al., 2010).

1.4.5. Concluding remarks

Finite element models are useful to predict the skull response to masticatory loading in terms of bite and reaction forces, bone deformation, stresses and strains. In craniofacial research, they are useful to understand how cranial form has adapted during evolution; the relationship between masticatory function and cranial morphogenesis; and how altered morphologies impact masticatory function and vice versa.

Among mechanical modelling techniques, FEA has become increasingly used to relate bone strains and stresses during biting to function and ecology. Geometric morphometrics offers the possibility of quantifying and characterising FEA results in terms of deformation and relating these deformations to other variables. Since both methods are still under development, the validity of FEA alone or in combination with GM to interpret biological phenomena is still being studied. However, series of validation and sensitivity studies have shown that FEA is in general a reliable method whose limitations should be acknowledged for each studied case. Both FEA and GM are extensively used in this thesis to test hypotheses concerning the relationship between skull morphology and masticatory function.

Chapter 2 : Validation of a voxel-based finite element model of a human cranium using digital speckle interferometry

2.1. Introduction

The second chapter of this thesis describes the validation of a finite element model of the human cranium. By comparing the strains predicted by a series of models with the strains measured on the actual cranium loaded experimentally, the aim is to validate the method used to build finite element models of the human cranium in the following chapters of this thesis.

Finite element analysis (FEA) is a numerical technique for predicting the mechanical performance of a system (Zienkiewicz et al., 2005) that has been applied in bone research to assess the tissue response under functional or experimental loads. In the skull, bone under masticatory load experiences strains and stresses whose distribution (relative locations of high and low strains evident in e.g. contour maps) and magnitude can be interpreted in terms of variables such as ecology, diet and phylogeny (Rayfield, 2007; O'Higgins et al., 2012). Thus, FEA of the skull has become a common method to study factors underlying primate development (Kupczik et al., 2009; Ross et al., 2011), evolution (Strait et al., 2009; Wroe et al., 2010; Gröning et al., 2011b) and masticatory system physiology (Gross et al., 2001; Koolstra and Tanaka, 2009).

It is important to know the degree of error in the predictions of the FEA before using the model to address biological questions. The results of an FEA depend on model geometry, material properties, applied loads and kinematic constraints. Full reproduction of these characteristics in a model of a complex structure like the primate cranium is currently impossible and thus simplification is necessary. However care is needed; it is key to assess the validity of the FE model and how each simplification impacts on model performance.

The main approaches to validating FE models of the primate skull include the comparison of predicted strains with those measured *in vivo* (Strait et al., 2005; Ross et al., 2011), and with strains resulting from loading cadaveric material (Marinescu et al., 2005; Kupczik et al., 2007; Gröning et al., 2009). To date, only one study has validated a hybrid mesh-based model of a human cranium. This used 13 gauges to measure the strains over a cadaveric cranium (Szwedowski et al., 2011). In their study, the authors induced strains by simulating a non-physiological block-bite of the left half of the upper dental arch. The authors performed analyses showing that the mesh with the most detailed cortical bone reconstruction and material properties correlated best with the experimental data.

The validation of an FE model is subject-specific and involves a great deal of effort. Thus it is simply not feasible in studies comparing many models to carry out validations of each. This limitation is not only due to the time and effort required but also to the availability of specimens that can undergo direct strain measurement. The situation is particularly severe if *in vivo* strains are to be gathered for validation. Further, it is impossible to carry out validation of FE models based on fossils. A practical solution is to validate one or a limited number of models in detail and to carry out sensitivity analyses of modelling approaches. Sensitivity analyses are an important complement to validation studies. These are used to assess the impact of simplification approaches in model construction. The knowledge gained can guide subsequent model building and so increase reliability and confidence in the results.

Among simplification approaches, it is common to omit structures that are not practical to reproduce such as some muscles, fasciae and the periodontal ligament (Wang et al., 2010; Curtis et al., 2011; Gröning et al., 2011a; Wood et al., 2011). The material properties of bone tissue are complex and vary throughout the skull (Robbins and Wood, 1969; McElhaney et al., 1970; Dechow et al., 1993), thus in FE models bone is usually allocated homogeneous and isotropic material properties obtained from the literature or the specimen itself (Strait et al., 2005; Kupczik et al., 2007). Cancellous bone is often modelled as a bulk material because trabeculae in the cancellous bone are not distinguishable even in micro CTs with sub millimetre resolution (Gröning et al., 2012). Moreover, increasing CT resolution brings with it severe issues with regard to the work involved in manual segmentation and the requirements of computing power in relation model complexity.

A common simplification also made in FE models of the primate skull is the use of static muscle loads, usually based on estimates from bony proxies or the literature. It is common to apply maximal muscle forces simultaneously (Ross et al., 2005; Fitton et al., 2012; Gröning et al., 2012) but that rarely occurs in reality (van Eijden, 1990; Blanksma and van Eijden, 1995; Langenbach and van Eijden, 2001; Shi et al., 2012). The effect of this simplification of loading will be assessed later in this thesis.

This chapter combines validation and sensitivity analyses of a single cadaveric cranium to provide a frame of reference for the construction of further models of the human cranium. Five voxel-based FE models of the same human cranium were built varying their anatomy and resolution. The cranium was represented either using different materials for cortical and cancellous bone or using a single material with the properties of cortical bone. Structures poorly represented in CT images because of the constraints in resolution, such as the inner sinus walls were omitted or fully reconstructed following anatomical principles. Model resolution was increased by reducing the sizes of voxel (and thus elements) and so increasing their number. To validate the FE models, the strains and bite forces predicted by each model were compared with those measured experimentally in the actual specimen. Model sensitivity was assessed by comparing the FEA results among models built using different approaches to simplification of model geometry and varying resolution.

Experimental strains were measured using an optical technique called digital speckle pattern interferometry (DSPI; Yang and Ettemeyer, 2003; Yang et al, 2007). This approach has previously been used to validate FE models of human and macaque mandibles (Gröning et al., 2009; Panagiotopoulou et al., 2011). In contrast with the point measurements provided by strain gauges, it measures strains over large areas. Bite force is another parameter of interest in masticatory performance (Pruim et al., 1980; Demes and Creel, 1988; Korioth et al., 1997; O'Connor et al., 2005). It can be estimated from reaction forces taken from the model at the bite point. Predicted bite forces were compared with experimentally measured reaction forces at the incisor.

The following hypotheses were tested:

Hypothesis 1 (H1): There are no differences in distribution, magnitude and direction between the strains predicted by FE models built using different segmentation approaches and those measured experimentally

Hypothesis 2 (H2): There are no differences between the bite forces predicted by FE models built using different segmentation approaches and those measured experimentally.

Model sensitivity to variations in modelling decisions was additionally assessed in terms of changes in model size and shape due to loading. These changes were compared using landmarks followed by a Procrustes size and shape analysis (Milne and O'Higgins, 2012; O'Higgins and Milne, 2013). The following hypothesis was tested:

Hypothesis 3 (H3): Finite element models of the same skull built using different segmentation approaches predict the same modes of large scale deformation.

2.2. Materials and Methods

2.2.1. Sample

The cadaveric head of a 74 year old man from the repository of the Centre for Anatomical and Human Sciences (Hull York Medical School, UK) was used in this study. The subject signed consent for experimental anatomical studies when he donated his remains and ethical approval was obtained from the HYMS ethics committee by Professor Paul O'Higgins. All experimental work was carried out in accordance with the Human Tissue Act (2004) and Hull York Medical School protocols for the handling and storage of cadaveric material.

The cadaver had been embalmed two years prior to this study using a modified version of the University of Bristol embalming fluid formulation (1.4% formaldehyde and 70% ethanol, Vickers Laboratories Ltd., Pudsey, UK). The head was CT scanned at the York Teaching Hospital (York, UK) with a Siemens 16-channel multidetector CT scanner equipped with a STRATON tube (Siemens Somatom Sensation 16, Siemens Healthcare, Erlangen, Germany). Voxel size was 0.48 x 0.48 x 0.7 mm. Initial reconstruction of images was performed using a specialist system (Syngo Multimodality workplace, Siemens Healthcare, Erlangen, Germany) to ensure adequate field of view and image quality. The image stacks were then exported as DICOM files for detailed segmentation and reconstruction as described further below.

2.2.2. *In vitro* strain measurement

The selected head was skeletonised by dissection, removing the soft tissues and the periosteum taking precautions not to damage the bone surface (Figure 2.1).

[redacted] [redacted]

Figure 2.1. Dissection of the cadaveric head. (a) From left to right, the starting condition of the head and the removal of soft tissues; (b) frontal; and lateral views of the cranium after removing soft tissues.

The experimental setup (Figure 2.2a) was designed to load the cranium in a way that (1) generates facial strains comparable to those reported in previous experimental and FEA studies simulating incisor bites (Hylander et al., 1991; Gross et al., 2001; Kupczik et al., 2009; Ross et al., 2011; Szwedowski et al., 2011); that (2) could be fully controlled during experiments; and that (3) is reproducible in the FE model.

Loading. The head was placed in a vertical position, constrained at both mastoid processes and the left central incisor. Compressive vertical forces were applied to the midplane of the frontal squama, 13 mm anterior to bregma using a universal material testing machine with a 1 kN load cell (Lloyd's EZ50, Ametek-Lloyd Instruments Inc., Sussex, UK). The load was applied in 11 steps of 50 N to achieve a final load of 550 N. Stability of the cranium after each step was assessed by continually checking that increases in the reaction force at the constrained border of the left central incisor scaled linearly with increasing loads. This reaction force was measured using a strain meter equipped with a 5 kN load cell (Omega DP25B-S, Omega Engineering Inc., Stamford, USA) previously calibrated applying known compressive loads with the Lloyd's testing machine described above. Additionally, the position of the loading point on the cranium was marked with a pen to control the position of the load on the cranium, thus ensuring comparability among loading experiments. The experiment was repeated several times per measured area (infraorbital region and frontal process of the maxilla). After initial evaluation, data from several experimental rounds were dismissed due to evidence of system instability. Five stable experimental rounds were achieved for the infraorbital region and four for the frontal process of the maxilla.

Full-field surface strain measurement. Full-field surface strains were measured using DSPI. Digital (or electronic) speckle pattern interferometry (DSPI and ESPI respectively) are optical non-contact full-field techniques for measuring the microscopic deformation and calculating the surface displacements and strains (as well as stresses if Young's modulus is known) of an object under load. ESPI and DSPI differ in that, ESPI uses analogue electronics and DSPI uses digital electronics (Creath and Slettemoen, 1985). The process starts with the illumination of the surface using laser beams that reflect from the object surface and recombine with a reference beam to generate an interference pattern (*speckle interferogram*) that is recorded with a CCD (charge coupled device) camera. The deformation of the object under load changes the phase of the speckle interferogram, and the difference between the starting and following interferograms results in a fringe pattern. The noise in the fringes is reduced via phase shifting that images the speckles in each interferogram and calculates a quantitative phase map that encodes the magnitudes and directions of surface deformation. This information is then used to calculate the displacements and consequently strains. In a complex curved surface like the human cranium, characterisation of surface topography is required since the coordinate system in the plane images has to be projected onto the surface contour for spatial accuracy. In the DSPI system used in this study, surface characterisation is done using a system similar to that for strain measurement but the phase change is given by the curvatures and the ways they reflect moving illuminating beams. Once contours are computed, the deformation components of the object relative to the sensor coordinate system are calculated and the principal strains on the surface are determined from normal and shear strains (Yang and Ettemeyer, 2003; Yang et al., 2007).

As mentioned above, the regions selected for strain measurement in this study were the left infraorbital region and the frontal process of the maxilla, since both show high strains in FEAs of simulated incisor bites in primates (Gross et al., 2001; Kupczik et al., 2009; Fitton et al., 2012). The DSPI system used was a Q-100 DSPI system (DANTEC Dynamics

GmbH, Ulm, Germany). This system provides a maximum field of view (FOV) of 25 x 33 mm^2. The measured surfaces were covered with a thin layer of white spray (DIFFU-THERM developer BAB-BCB, Technische Chemie KG, Herten, Germany) to prevent surface reflection of ambient light. The Q-100 sensor was glued to the boundaries of the treated surface using an acrylic-based adhesive (X60, HBM Inc., Darmstadt, Germany). Surface characterisation, phase calculation and deformation estimation (Figure 2.2b) were made using the Istra Q-100 (v.2.7, DANTEC Dynamics GmbH, Ulm, Germany). Maximum (ε1) and minimum (ε3) principal strain magnitudes, plus 2D and 3D colour-coded strain contour plots (representing strain distributions, i.e. relative locations of high and low strain) were exported and used for comparison with FEA results.

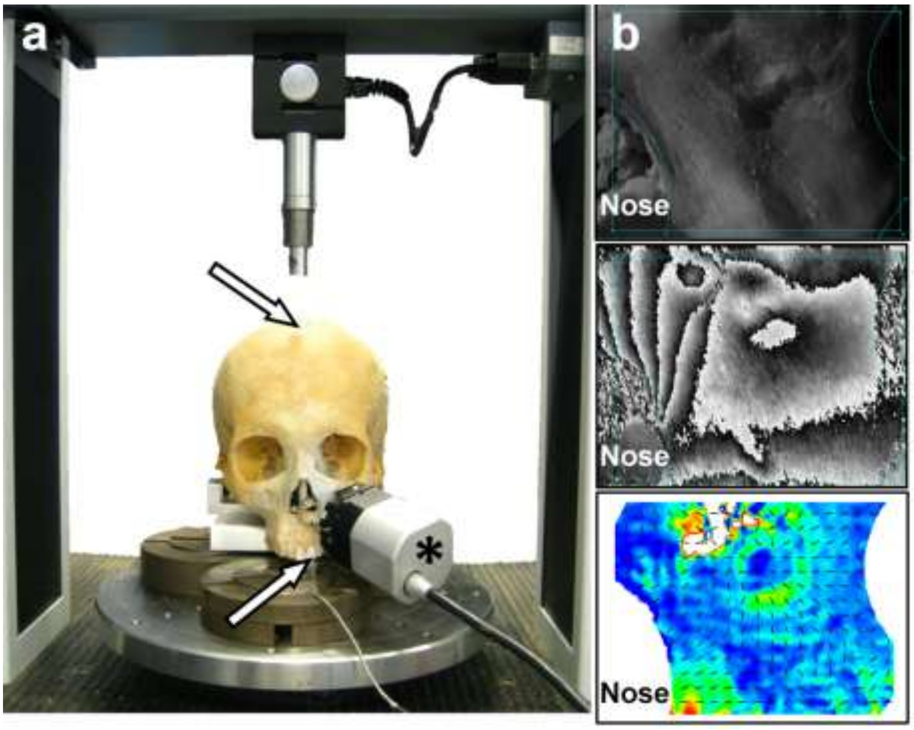

Figure 2.2. Experimental strain measurement. (a) Vertical compressive load applied to the calvarium (upper arrow) simulating a left central incisor bite (lower arrow). The cranium was constrained vertically at both mastoid processes. The asterisk shows the DSPI sensor attached to the infraorbital region. (b) DSPI-based surface strain measurement, where the unstrained surface (upper image) provides a speckle interferogram that changes under load. The change is quantified in a phase map (middle image). Surface strains are calculated from 3D displacements, and expressed as colour-coded strain contour plots and strain vector orientations (lower image). The position of the nose is shown for reference

2.2.3. Finite element analysis

The volume data of the cranium used in this study was obtained from the CT images through a combined approach of thresholding and manual segmentation of bone and teeth using the visualisation program Avizo (v.7.0.1, Visualization Sciences Group, Burlington, USA).

2.2.3.1. Finite element model under experimental loading

To assess the impact of anatomical simplifications and model resolution, different models were built. To assess the impact of omitting cancellous bone reconstruction, one model was built using only cortical bone whereas the remaining models have a cortical shell with cancellous bone below the fronto-zygomatic suture level. The cancellous bone was defined as a bulk material of much lower modulus than cortical bone, and it represent about 10.50% of the model volume (see Table 2.1 for details). To assess the impact of omitting the inner walls of the frontal, ethmoidal, sphenoidal and maxillary sinuses during model construction, which are thinner than a voxel and so prone to being poorly represented in the CT, their anatomies were fully reconstructed manually or left as assigned by grey level threshold. To assess the effect of model resolution two models with different voxel sizes were created via resampling; one is low (voxel size=0.48 mm) and the other high (voxel size=0.35 mm) resolution. Once segmented, anatomical details were manually refined in each model where needed (thus varying the number of voxels and so elements among models, see Table 2.1). In all cases, teeth were modelled as one material with a higher elastic modulus (*E*) than bone.

The volume data were resampled to produce isometric voxels. Subsequently, data were exported as BMP stacks and converted into FE meshes of eight-noded linear cubic elements by direct voxel conversion. Model pre- and postprocessing were performed using the custom FEA program VOX-FE (Fagan et al., 2007; Liu et al., 2012).

In all models cortical bone, cancellous bone and teeth were allocated homogeneous linearly elastic and isotropic (*E*=17 GPa; Poisson's ratio=0.3) material properties as in prior validated models of human and macaque crania (Kupczik et al., 2007; Szwedowski et al., 2011) and the human mandible (Gröning et al., 2009). For cancellous bone, an *E* of 56 MPa was assigned (Misch et al., 1999). An *E* of 50 GPa was assigned to teeth, this being approximately the mean of the large range of values found in the literature for enamel and dentine (Meredith et al., 1996; Barak et al., 2009; Benazzi et al., 2012).

The material properties of cortical bone are particularly important in relation to overall model stiffness (Marinescu et al., 2005; Strait et al., 2005). For this reason material properties of the cadaveric cranium were directly measured before settling on a suitable value. Two samples were collected, one from the specimen's maxillary tuberosity and the other from the zygomatic arch to avoid damaging the facial skeleton in case further validation loadings were necessary. *E* was measured using a nano-hardness tester with a Berkovitch diamond indenter (CSM Instruments S.A., Peseux, Switzerland) following the protocol in Kupczik et al. (2007). The mean value was 16.3±3.7 GPa for the tuberosity and 21.9±2.7 GPa for the zygomatic arch. Since these values lie within the range used in the literature for models of the human cranium (Horgan and Gilchrist, 2003; Wroe et al., 2010; Jansen van Rensburg et al., 2012), the common value of 17 GPa was assigned to cortical bone (Kupczik et al., 2009; Gröning et al., 2011b; Fitton et al., 2012).

The characteristics of each model are detailed in Table 2.1 and their features depicted in Figure 2.3.

Table 2.1. Finite element models description.

Model	Voxel size (mm)	No. of elements	Materials	Material volume		Features
				mm^3	%	
Model 1	0.48 x 0.48 x 0.48	4,028,201	Cortical bone	448,482.28	97.96	Full manual reconstruction of sinus bony walls.
			Teeth	9,316.64	2.04	
Model 2	0.48 x 0.48 x 0.48	3,324,738	Cortical bone	327,607.88	86.70	Partial (threshold based) reconstruction of inner sinus bony walls.
			Cancellous bone	40,923.63	10.83	
			Teeth	9,316.75	2.47	
Model 3	0.48 x 0.48 x 0.48	3,502,427	Cortical bone	347,760.47	87.37	Full manual reconstruction of sinus bony walls.
			Cancellous bone	40,967.38	10.29	
			Teeth	9,316.75	2.34	
Model 4	0.35 x 0.35 x 0.35	8,809,110	Cortical bone	326,740.44	86.72	Like Model 2.
			Cancellous bone	40,733.73	10.81	
			Teeth	9,285.66	2.46	
Model 5	0.35 x 0.35 x 0.35	9,232,754	Cortical bone	344,845.72	87.33	Like Model 3.
			Cancellous bone	40,748.40	10.32	
			Teeth	9,285.53	2.35	

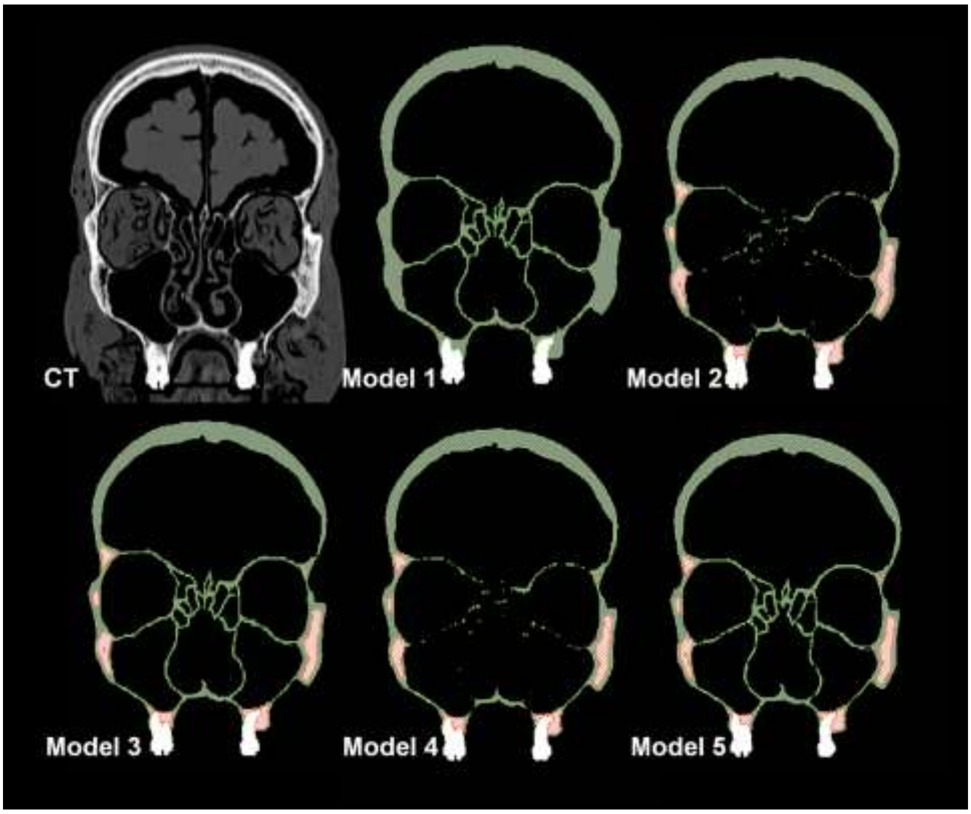

Figure 2.3. Coronal section of the original CT and the FE models showing the results produced by different segmentations. In the models green represents cortical bone, red represents cancellous bone and white represents teeth.

The points of compressive force application and cranial support were replicated in the model using a vertical constraint for the tooth, and three-axis constraints at each mastoid process. In the experiment the mastoids were constrained in the vertical direction by the platform on which they rested and they were able to move with some resistance in the horizontal plane. The decision to use three axes of constraint for the mastoids in the models was based on a prior sensitivity analysis showing that other combinations of (fewer) constraints resulted in rigid-body motion of the model.

2.2.4. Comparison of cranial and model performance

2.2.4.1. Measured vs. predicted strains

Comparisons of DSPI and FEA results are summarised in Figure 2.4. The procedure comprised three main steps: (1) matching the FOV of the DSPI with the area of interest of the FE model, (2) data extraction and (3) analysis. The comparison protocol for strain distribution, magnitude and direction is detailed below:

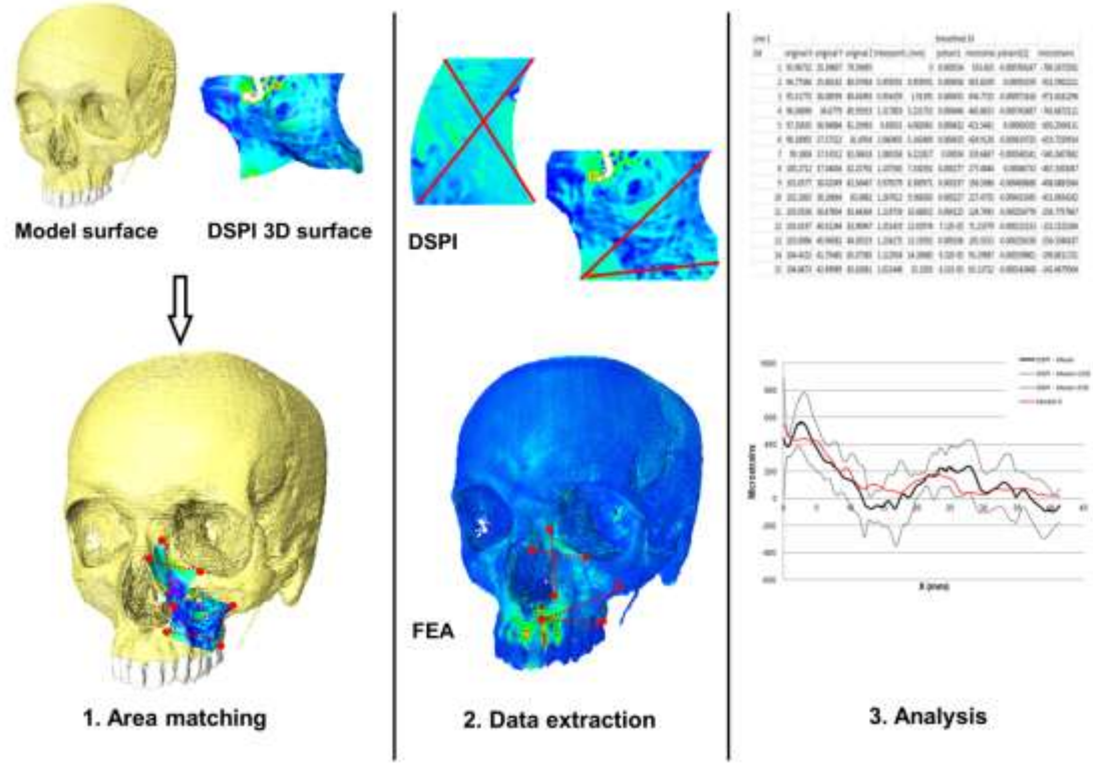

Figure 2.4. Comparison of measured vs. predicted strains. During area matching, the FOV of the DSPI is mapped on the FE model surface using landmarks (in red). Data are extracted from lines in the DSPI and from landmarks replicating the DSPI-lines in the FE model. During analysis, strains per line are tabulated and plotted; DSPI (grey) and FE model (red) line.

Strain distribution. To compare strain distributions, similar colours were mapped to equivalent strain ranges from DSPI and FEA. However, the Istra Q-100 depicts areas with lower values than the lowest limit of the scale in purple whereas in VOX-FE these remain the same colour (blue). The DSPI measured surface geometry was exported as a Virtual Reality Modeling Language (VRML) file and visualised in 3D using Avizo. The surface of the cranium extracted from CT was loaded into the same scene. The DSPI surface was then manually translated to best fit the cranium surface guided by anatomical structures and high magnification photographs of the skull surface (area matching in Figure 2.4). Best-fit was assessed by two observers (MV Toro Ibacache and P O'Higgins). The locations of the vertices of the DSPI surfaces on the CT-derived cranial surface were saved as x, y, z coordinates in Avizo in order to preserve the positioning of sampling points among models.

Strain magnitudes. Data extraction from DSPI is only possible from the 2D output that ignores surface curvature, i.e. the third dimension is projected into the plane as in photography. As will be discussed later, this impacts on the distances among surface patches represented by pixels and so on the resulting plots of strains. Two straight lines in this plane (lines 1 and 2) were traced across the infraorbital and two across the frontal process fields of view (FOV; lines 3 and 4) using the vertices of the FOVs to optimise replicability of measurement. Strain magnitudes at each point of the line were extracted and smoothed by once-averaging of single adjacent points on either side to reduce noise. To extract corresponding data from the 3D surface of the FE model, landmarks were placed on the model surface forming a line between the vertices of the DSPI's FOVs (data extraction in Figure 2.4). Lines comprising 37 (line 1), 30 (line 2), 28 (line 3) and 33 (line 4) landmarks were traced in Avizo. These lines replicate the lines traced on the DSPI FOVs but in 3D, over the surface of the FE model. Strain values were smoothed in VOX-FE by once-averaging of neighbouring voxels in order to reduce strain fluctuations due to voxellation (Liu et al., 2012). After strain smoothing, predicted strain magnitudes at each of the landmarks were extracted for further analysis.

Strain values were sampled from the starting point along equivalent traced lines on the DSPI and VOX-FE outputs, at equivalent Euclidean distances between DSPI sampling points and VOX-FE landmarks. However because the former are 2D and the latter 3D there are unavoidable discrepancies in the computed lengths of equivalent lines, particularly over highly curved surface regions. Thus, as expected when the lengths of the traced lines are calculated between the starting and ending points all the (2D) DSPI lines are shorter than those from (3D) VOX-FE (Table 2.2).

Table 2.2. Total length of sampled lines.

Data origin	Length (mm)			
	Line 1	Line 2	Line 3	Line 4
DSPI, all (x,y) coordinates	44.52	26.79	36.05	39.63
DSPI, first and last (x,y) coordinates	33.79	25.93	27.82	29.97
VOX-FE, all (x,y,z) coordinates	41.36	33.98	30.56	33.14

A further source of error arises when computing the lengths of lines traced using DSPI program. Because of pixellation, unless a line is oriented parallel to one side of the FOV, the x and y coordinates of sampling points trace a stepped path. This results in an overestimate of line length (Figure 2.5).

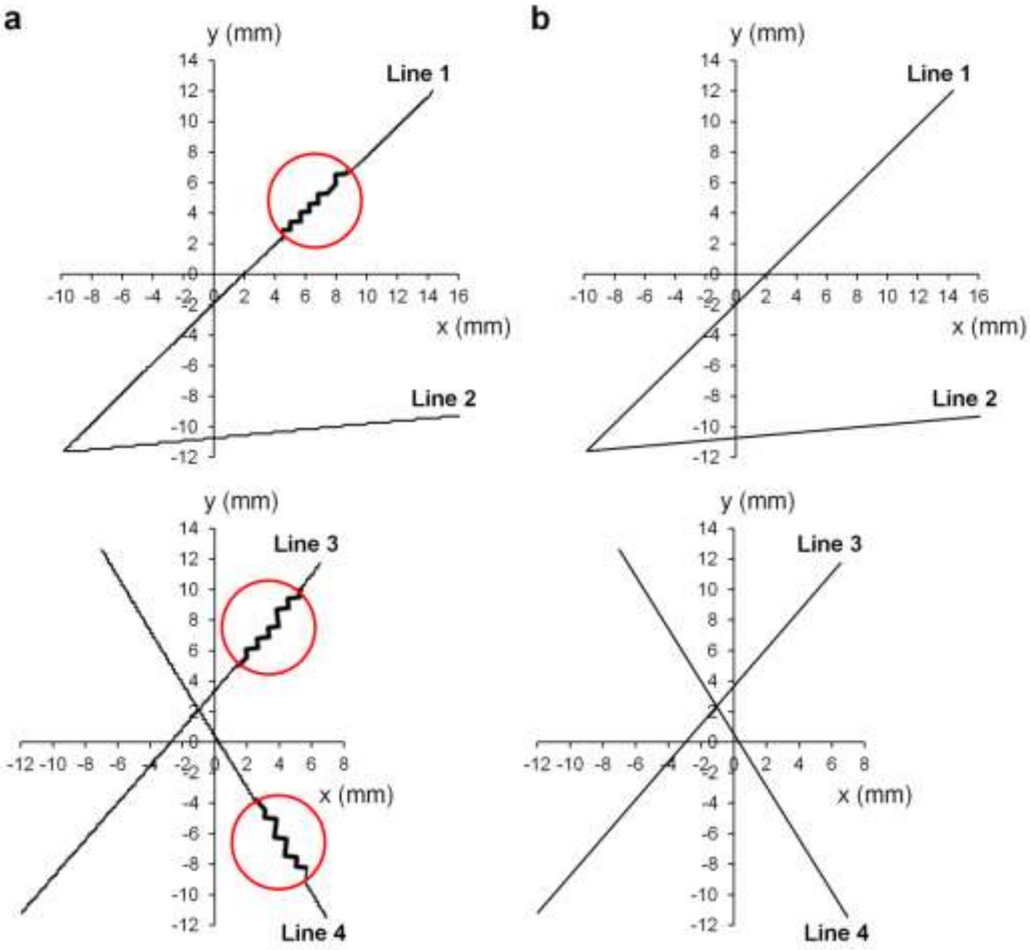

Figure 2.5. Discrepancies in the lengths of homologous DSPI lines. (a) Lines traced between pixels. Red circles show a 250% zoom the steps in the line. (b) Straight lines between the first and last x,y coordinates are shorter because they show no stepping.

Strain directions. Both the Istra Q-100 (DSPI) and VOX-FE allow visualisation of strain directions in 2D and 3D, respectively. To avoid crowding the image with lines representing strain vectors, these were drawn at every fourth node in Models 1, 2 and 3 and every eighth in Models 4 and 5 for the areas of interest.

2.2.4.2. Experimental and predicted bite force

As explained above in *in vitro* strain measurement, the reaction force at the incisor was measured during the cranial loading using a strain meter equipped with a 5 kN load cell (Omega DP25B-S, Omega Engineering Inc., Stamford, USA). Predicted bite force was obtained from the output of the FEAs performed in this study and compared among models. The bite force in the FE models is the total reaction force at the incisor constraints.

2.2.4.2. Large scale model deformation.

Large scale model deformations resulting from applied loads were compared through Procrustes size and shape analyses based on 51 craniofacial landmarks (described in Table 2.3) from a landmark set used throughout this thesis (see Chapter 3 for further details). During Procrustes size and shape analysis, coordinates are rotated and translated but not scaled as in a full Procrustes fit. This preserves the changes in model size as well as shape due to loading. The resulting size and shape coordinates are then submitted to principal components analysis (PCA; Fitton et al., 2012; O'Higgins et al., 2012). Visualisation of shape changes used the surface corresponding to Model 1, warped to the mean unloaded configuration before further warping to model deformations. Two orthogonal grids (one in the analysis of facial deformation, as explained further in the results) were drawn over the mean landmark configuration, and warped with the surface.

Table 2.3. Landmarks used in the study of large scale model deformation.

No.	Symbol	Name	Definition
1	V	Vertex	Highest point of the calvarium.
2	N	Nasion	Intersection between frontonasal and internasal suture.
3	ANS	Anterior Nasal Spine	Tip of the anterior nasal spine.
4	Pr	Prosthion	Most buccal and occlusal point of the interalveolar septum between central incisors.
5	Oc	Occiput	Most posterior point of the neurocranium.
6&20	SoT	Supraorbital Torus	Most anterior point of supraorbital ridge.
7&21	InfO	Infraorbitale	Most inferior point of the infraorbital ridge.
8&22	NNot	Nasal Notch	Most lateral part of the nasal aperture.
9&23	M1	First Molar	Most buccal and mesial point of M1 and alveolar process junction. If absent, landmark is in the lowest most buccal point of the interalveolar septum between the second premolar and the next present molar.
10&24	M3	Last Molar	Last point of the dental arch, located at the most buccal and distal point on the last present molar and alveolar process junction .
11&25	ZM	Zygo-maxillar	Most inferior point of the zygo-maxillary suture.
12&26	FZ	Fronto-zygomatic	Most lateral point of the fronto-zygomatic suture.
13&27	FTZ	Fronto-temporal angle	Point of intersection between the frontal and temporal processes of the zygomatic bone.
14&28	ZAl	Zygomatic Arch lateral	Most lateral point of the zygomatic arch.
15&29	ZRp	Zygomatic Root posterior	Most posterior-superior point of the intersection zygomatic root and the squama of the temporal bone.
16&30	ZRa	Zygomatic Root anterior	Most anterior point of the intersection between the zygomatic root and the squama of the temporal bone.
17&31	ZAm	Zygomatic Arch medial	Most lateral point on the inner face of the zygomatic arch.
18&32	ItC	Infratemporal Crest	Most medial point of the infratemporal crest.
19&33	Eu	Eurion	Most lateral point of the neurocranium.
34&37	aTemOr	Anterior Temporal origin	Most anterior point of origin of the temporal muscle on the temporal line.
35&38	sTemOr	Superior Temporal origin	Most superior point of origin of the temporal muscle on the temporal line.
36&39	pTemOr	Posterior Temporal origin	Most posterior point of origin of the temporal muscle on the temporal line.
40&43	aMassOr	Anterior Masseter origin	Most anterior point of origin of the masseter muscle on the zygomatic arch.
41&44	pMassOr	Posterior Masseter origin	Most posterior point of origin of the masseter muscle on the zygomatic arch.
42&45	midMassOr	Mid-Masseter origin	Midpoint along the origin area of the masseter muscle on the zygomatic arch.
46&49	sPtOr	Superior Pterygoid origin	Most superior point of origin of medial pterygoid muscle on the pterygoid fossa.
47&50	iPtOr	Inferior Pterygoid origin	Most inferior point of origin of medial pterygoid muscle on the pterygoid fossa.
48&51	midPtOr	Mid-Pterygoid origin	Midpoint along the origin area of the medial pterygoid muscle on the pterygoid fossa.

2.2.5. Measurement error.

The error associated with data extraction from both DSPI and FEA results was assessed by repeating the extraction (line tracing in the DSPI output and landmark placement in the VOX-FE output) of lines 1 and 3 on three different days. Data were processed as explained in 2.2.4.1. The errors introduced during different extraction sessions were assessed using plots of strain vs. position along the traced line. These are shown in Figure 2.6 where it is evident that from DSPI errors are very small, with the repeated tracings of each line nearly overlapping. From FEA the situation is similar but there are moderately larger differences between tracings. In both cases the error appears small.

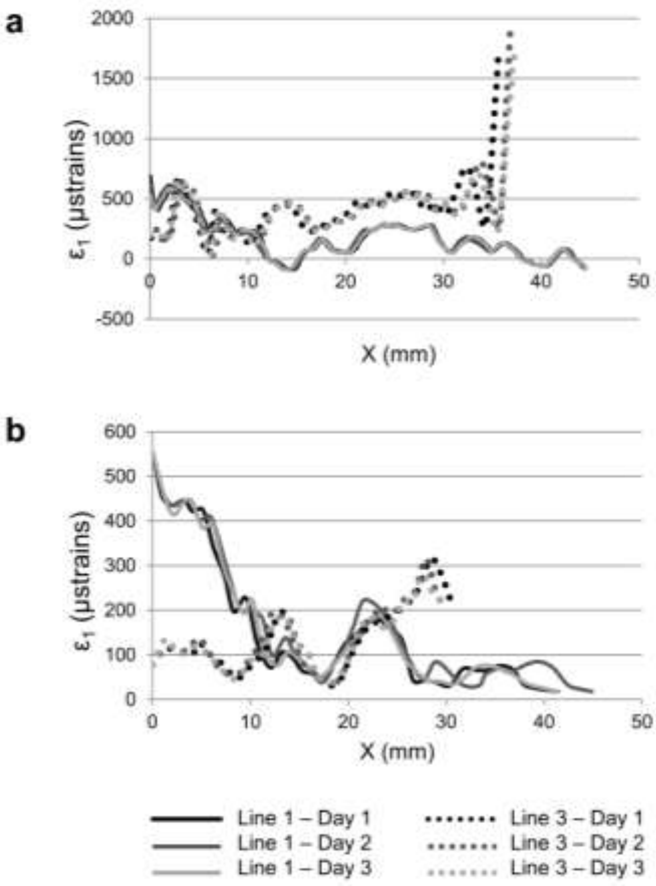

Figure 2.6. Intraobserver error in (a) DSPI and (b) FEA.

2.3. Results

The results are presented below in relation to each hypothesis.

H1: There are no differences in distribution, magnitude and direction between the strains predicted by FE models built using different segmentation approaches and those measured experimentally

Strain distribution. In general, the strains predicted by the FEAs of different models differ in magnitude but show similar distributions in the contour maps and similar principal strain directions, as reported later. The most marked differences among models relate to overall model stiffness that increases as cancellous bone is replaced by cortical bone and sinus walls are reconstructed. As noted earlier, the locations of regions of relatively high and low strains remain similar (Figure 2.7). This similarity is most evident when ranges of the strain contour plots in the stiffest models, i.e. Model 1 (no cancellous bone), and Models 3 and 5 (with reconstructed inner walls of paranasal cavities) are adjusted to match the remaining models (Figure 2.8).

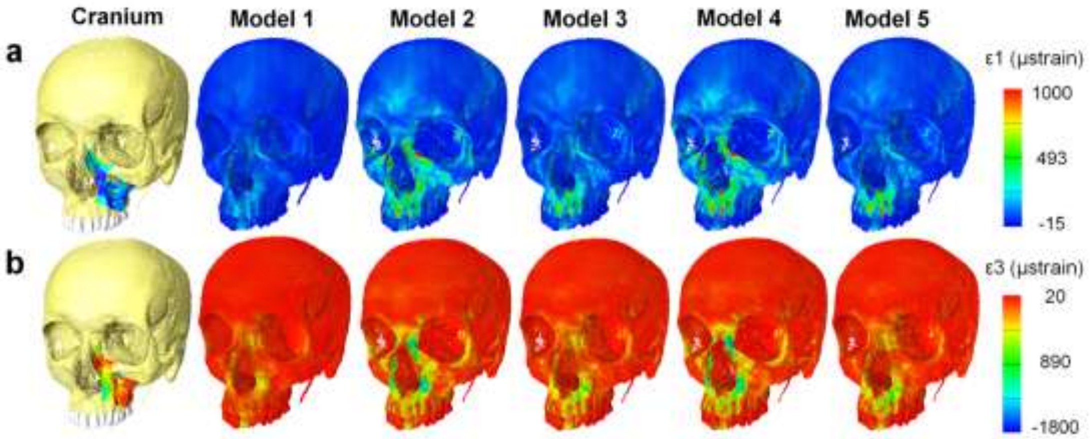

Figure 2.7. Strain controur plots showing (a) ε1 and (b) ε3 strain contours. In the DSPI results superimposed on the cranium, purple represents areas with values below the lower limit of the scale.

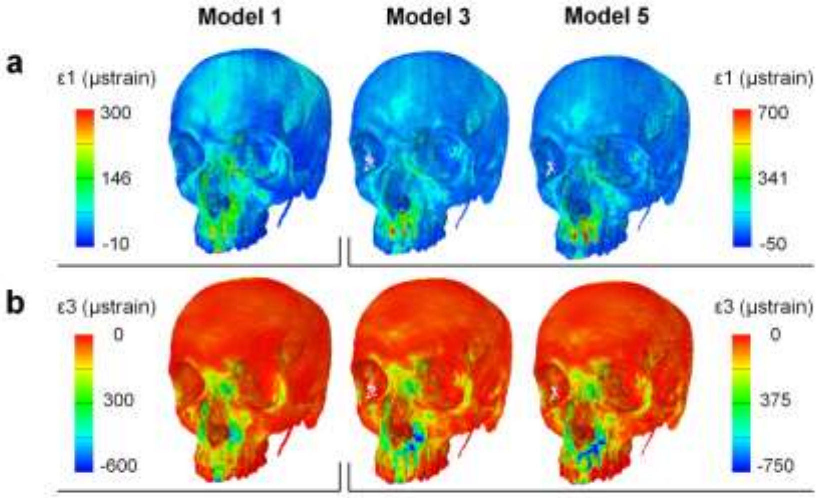

Figure 2.8. Strain contour plots of models 1, 3 and 5 showing (a) ε1 and (b) ε3 strain distributions. The ranges of the strain contour plots have been adjusted to best match among models.

Strain magnitudes. The main effect of representing regions of cancellous bone as cortical, and reconstructing sinus walls is to increase model stiffness. Model 1 shows strains about three times lower than the experimental results and the strains predicted for the other models (Figures 2.9 and 2.10). Overall, models 2 to 5 showed similar strain magnitudes. Models 2 and 4 (with incompletely reconstructed sinus walls) show higher peaks in ε3 values in lines 3 and 4 the (frontal process of the maxilla; Figure 2.10). Model resolution over the range assessed in this study does not have an effect on strain magnitude.

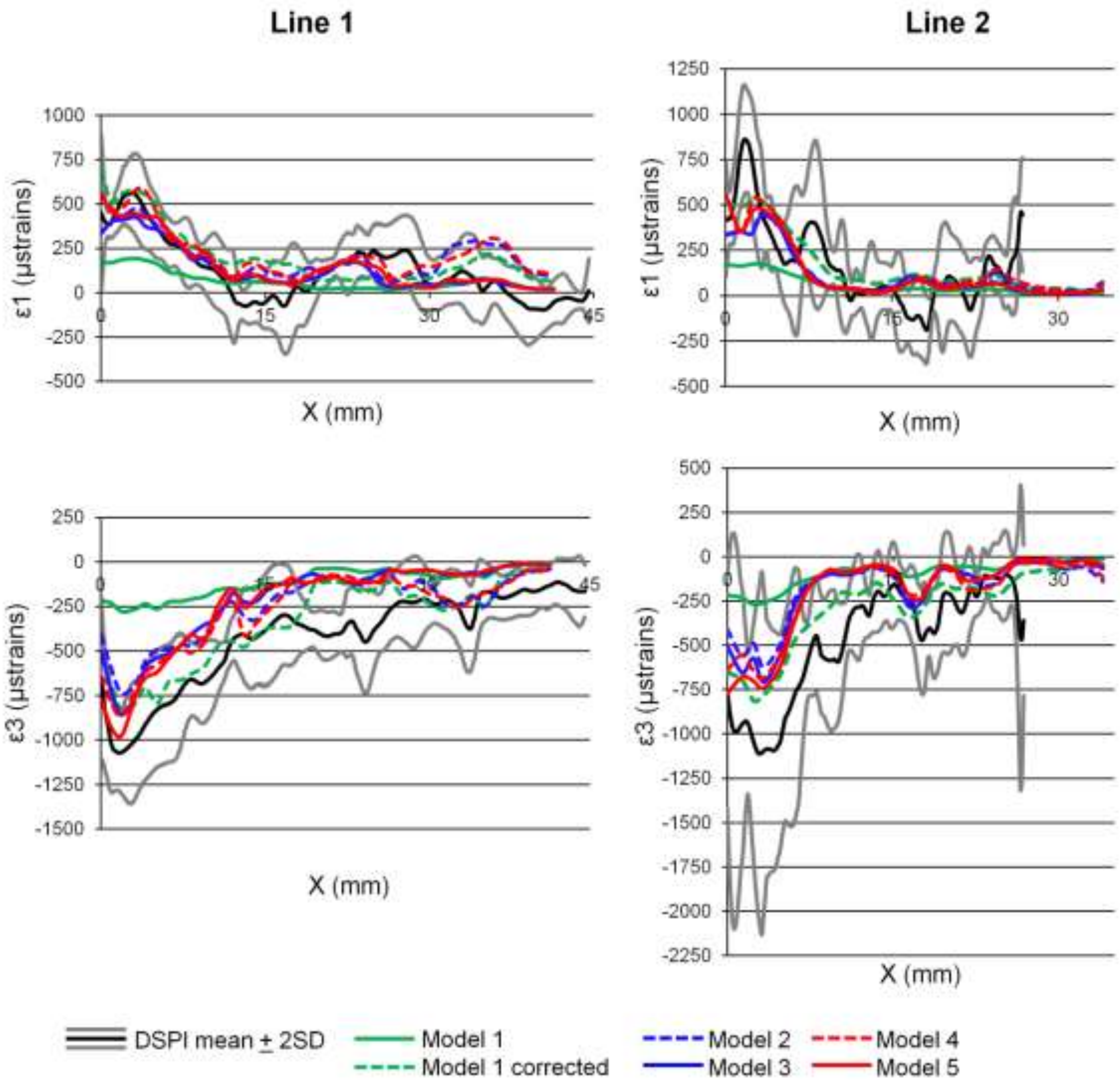

Figure 2.9. Experimental vs. predicted strain magnitudes across the infraorbital region. Strains in model 1 are shown by a solid green line, the dotted line 'corrected', shows the strains multiplied by three which approximately corrects for increased model stiffness due to infilled cancellous bone.

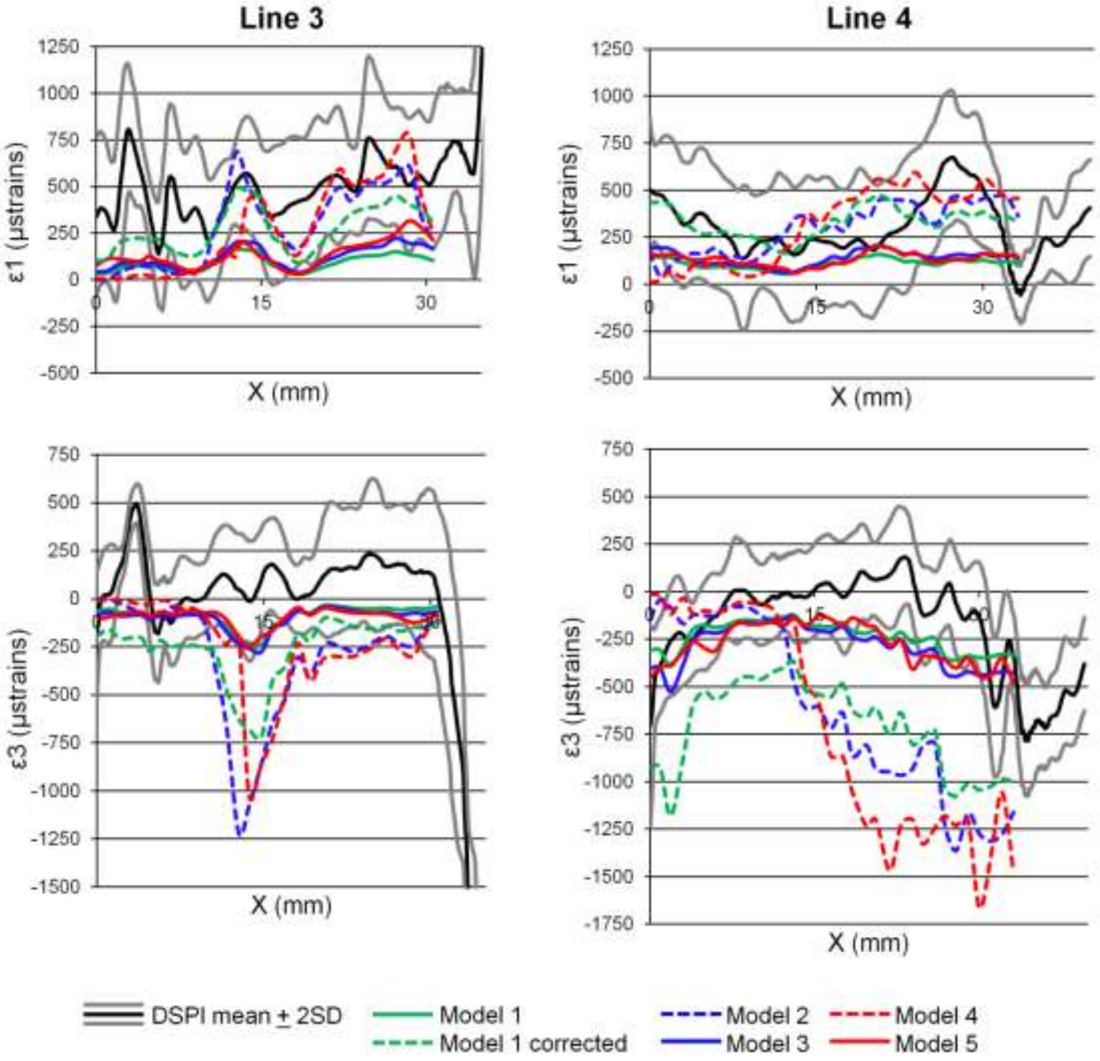

Figure 2.10. Experimental vs. predicted strain magnitudes across the frontal process of the maxilla excluding the peak values at the ends of lines 3. Strains in model 1 are shown by a solid green line, the dotted line 'corrected', shows the strains multiplied by three which approximately corrects for increased model stiffness due to infilled cancellous bone.

Strain vectors. The directions of the principal strain vectors are very similar among models and between the models and the DSPI measured strains (Figure 2.11 and 2.12). This is evident, despite the differences in the ways strain vectors are displayed in the DSPI and VOX-FE outputs. Thus, VOX-FE displays vector directions and magnitudes while DSPI displays only direction.

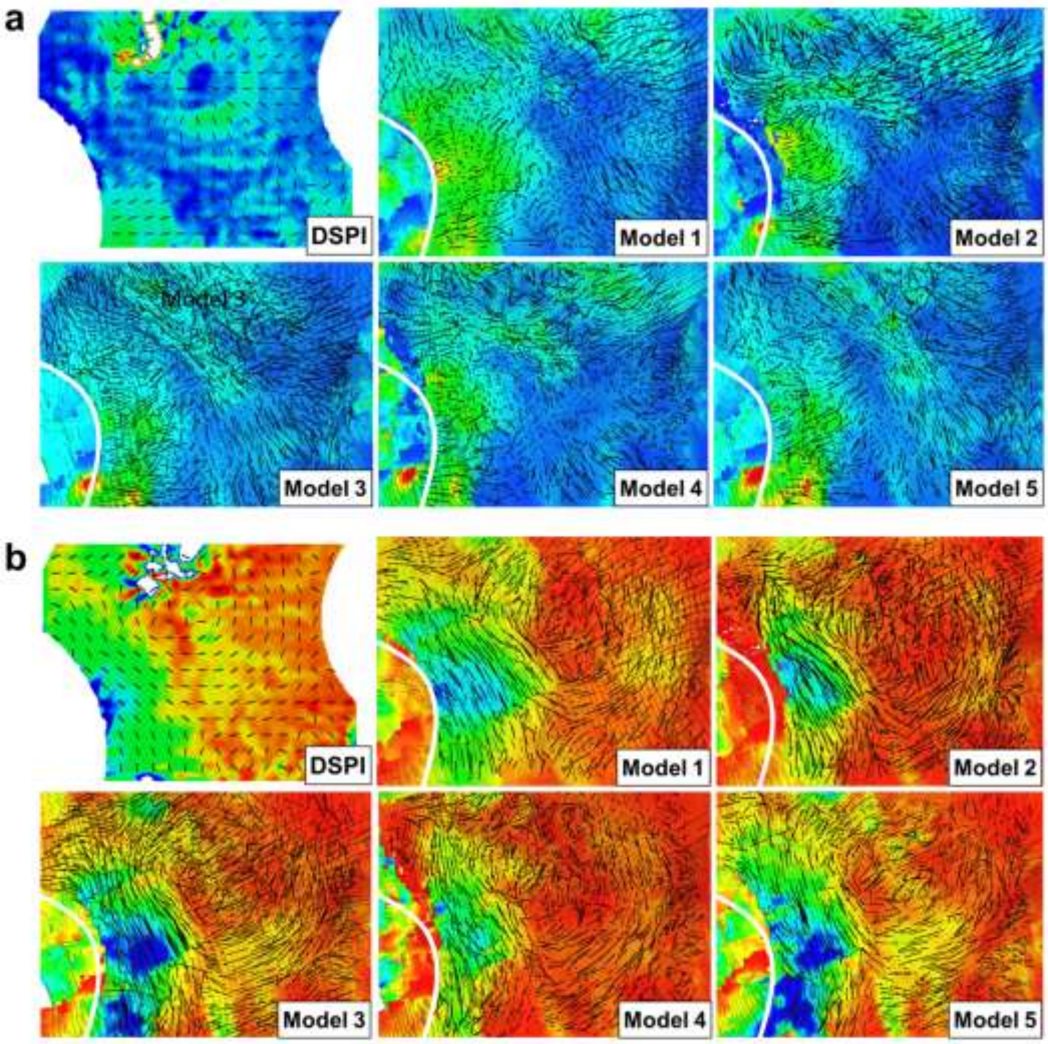

Figure 2.11. Experimental vs. predicted vectors of in the infraorbital region. (a) Principal strains 1 and (b) principal strains 3. To best match contours and to facilitate the identification of corresponding regions, vector magnitudes in the FEA outputs and ranges of each strain contour plot have been independently adjusted.

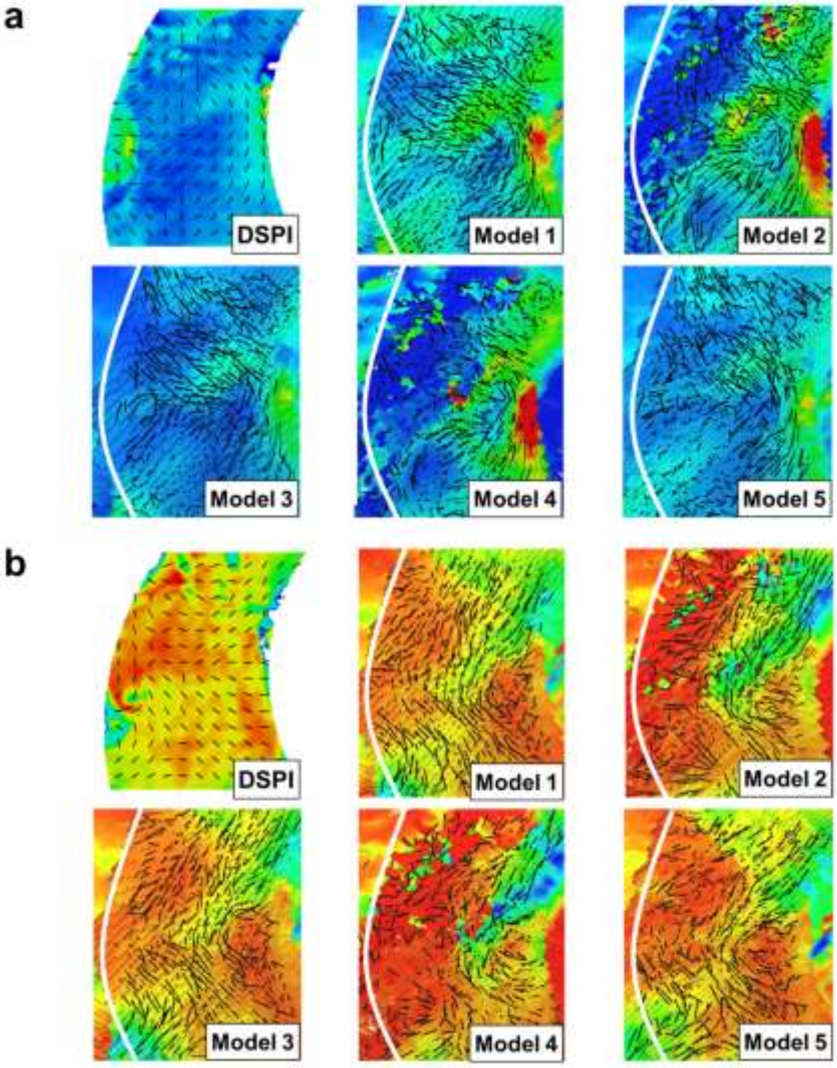

Figure 2.12. Experimental vs. predicted vectors in the frontal process of the maxilla. To best match contours and to facilitate the identification of corresponding regions, vector magnitudes in the FEA outputs and ranges of each strain contour plot have been independently adjusted.

H2: There are no differences between the bite forces predicted by FE models built using different segmentation approaches and those measured experimentally.

Bite force varied little among models despite the differences in model geometry. The bite forces produced by all models were larger than the reaction forces at the incisors measured during the experiment by 23-27% (Table 2.4).

Table 2.4. Experimental and predicted bite forces.

	Experiment (average ± SD)	Model 1	Model 2	Model 3	Model 4	Model 5
Reaction force at incisors (N)	176.84 ± 9.44	223.6	224.1	224.2	219	219.2
Difference from experimental reaction force (±%)	-	+26.46	+26.74	+26.77	+23.83	+23.93

H3: Finite element models of the same skull built using different segmentation approaches predict the same modes of large scale deformation.

The PCA of size and shape variables from the entire landmark set (listed in Table 2.3) confirms many of the findings from the analyses of strains. Model deformations are represented by lines connecting the loaded and unloaded models (Figure 2.13). Large scale deformations generally consist of dorso-ventral bending of the maxilla mainly at the level of the nasal notch. The deformation of Models 1, 3 and 5 is virtually the same, varying only in magnitude. Models 2 and 4 deform to greater degree and in subtly different ways, with more compression of the nasal aperture and lateral displacement of the maxilla at the mid to upper parts of the nasal margins. They also deform more asymmetrically than the other models. The PCA was repeated using only the facial landmarks in order to focus on deformation of the face. The results are consistent with those using the complete landmark configuration (Figure 2.14).

The magnitudes of model deformation are very small. As such, to aid visualisation the warpings in figure 2.13 and 2.14 were magnified 200 times.

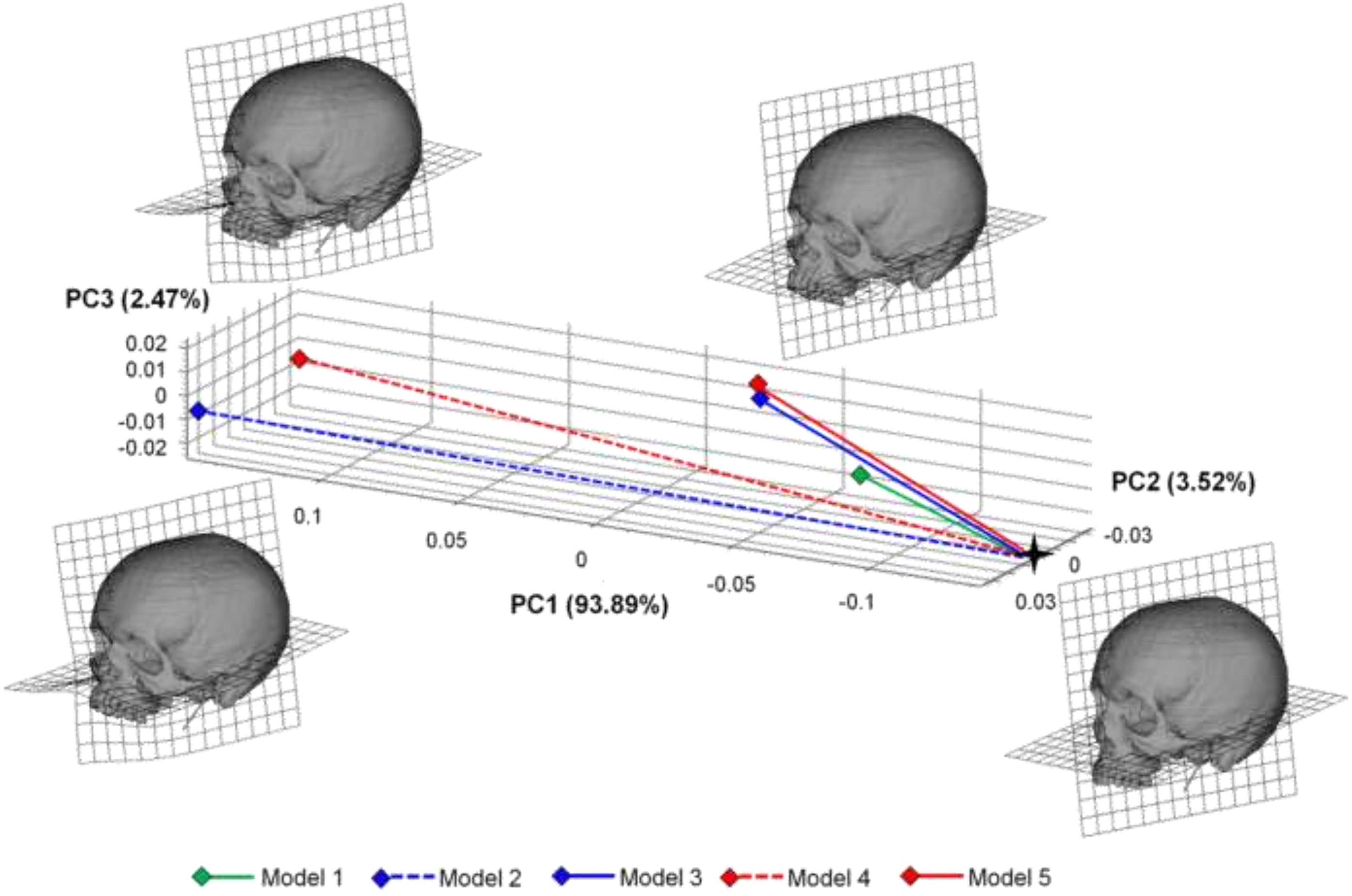

Figure 2.13. Principal components analysis of size and shape variables from the full landmark set in Table 2.3 representing deformation of Models 1 to 5 under a simulated incisor bite. The black star represents the unloaded cranium. Deformations are magnified 200 times to facilitate visualisation.

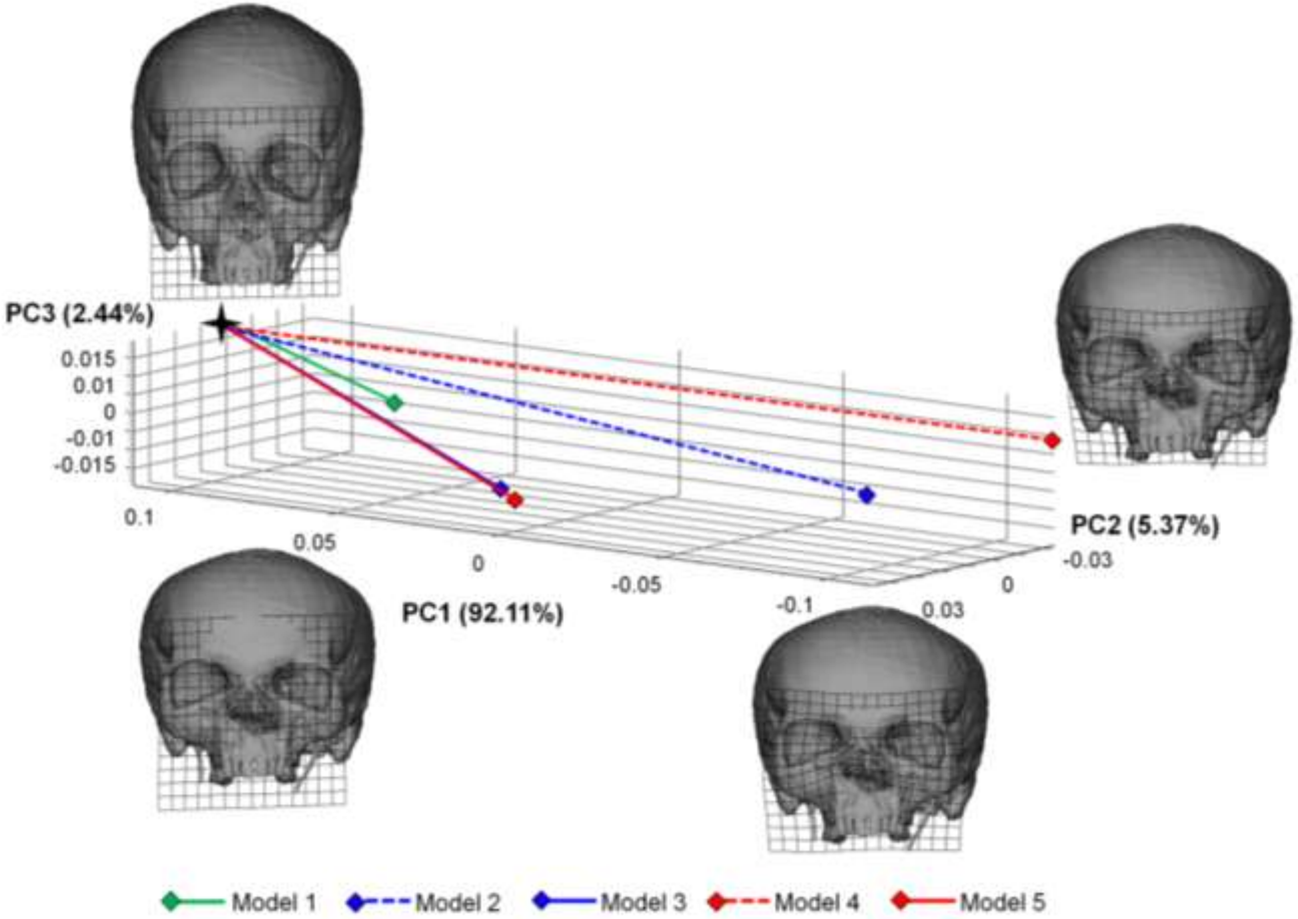

Figure 2.14. Principal components analysis of facial landmarks of Models 1 to 5 under a simulated incisor bite. The black star represents the unloaded cranium. Deformations are magnified 200 times to facilitate visualisation.

2.4. Discussion

The aim of the present study was to validate and assess the sensitivity of FE models of a human cranium to variations in anatomical accuracy and model resolution. For this, a human cranium was loaded experimentally, simulating a bite at the left upper incisor and the resulting strains and reaction force at the incisor were measured. These were then compared to the strains and bite forces predicted by FE models built using different simplification approaches: presence or absence of cancellous bone and inner sinus walls, and high or low resolution. It was hypothesised that there were no differences in strains and bite forces predicted by FE models and those measured experimentally. These were assessed in terms of magnitudes, and for strains, contours and principal strain vector orientations.

Model sensitivity to varying construction approaches was further assessed by comparing their resulting large scale deformations. The hypothesis was that all models predict the same modes of large scale deformation.

The hypotheses were falsified for all models to the extent that while they all deformed similarly to the experimentally loaded cranium, but they did not produce the same results. Thus, the models performed with varying accuracy in terms of strain magnitudes, contours, vectors and bite force. The degree of accuracy depends on model stiffness and the extent of reconstruction of inner sinus walls. In general, it is recommended to represent cortical bone as well as reconstructing internal nasal anatomy, as it leads to more accurate results than when omitted, but how important this accuracy is depends of the aim of the study. This is discussed further below.

Measured vs. predicted strains

This study used a voxel-based approach for FE mesh generation that is fast and automated, facilitating the process of model construction (Keyak et al., 1990; Lengsfeld et al., 1998). The results show that, irrespective of model geometry and resolution, the FE models predict strain distributions that are similar to those measured in the cranium under experimental loading. The main differences were in strain magnitudes; the results from models with cortical and cancellous bone represented separately were the closest to measured values. Among these models, those with careful reconstruction of sinus walls showed the best overall fit to experimental data. This is expected; anatomically more accurate FE models behave more similarly to the real cranium under experimental loadings than simplified models (Marinescu et al., 2005; Strait et al., 2005; Kupczik et al., 2007). In the frontal process of the maxilla, ε1 strains of Models 2 and 4 better match the experimental strains than the remaining models, but ε3 strains differ from the experimental range (Figure 2.15). This reflects an issue in model building where the sinus walls are thinner than the width of a voxel. By excluding the walls, the model is more flexible, for ε1 this results in a closer match but for ε3 a worse match than if the walls are reconstructed. This problem of how to represent very thin structures with low resolution models has no clear solution. However the models with reconstructed sinus walls generally perform more reliably than those without and so the approach that is followed in the remainder of the thesis is to reconstruct bony walls even when they are thinner than a voxel.

In the model without separate representation of cancellous bone, strains were three to four times lower than in the more detailed models. Thus, not including cancellous bone as a low modulus distinct material increases model stiffness, with surface strain distributions in the contour maps remaining approximately consistent among all models with reconstructed sinus walls. These results support the use of the simplification approaches depicted here when relative rather than absolute magnitudes of strains are of interest since they have a limited impact on strain contours. Moreover, model resolution over the limited range assessed here, has no appreciable effect on model performance. However, Gröning et al. (2009) showed in a voxel-based FE model of a mandible that an increase of three times in voxel size of the original CT (a reduction of model resolution by a factor of three) reduces model accuracy. Hence, the present findings of a negligible effect of model resolution should be considered to indicate that, whilst small variations in the range assessed here have had little impact, larger variations might be more significant. This remains to be assessed.

These findings are of importance in FEA studies where accurate representation of cancellous bone or sinus walls is not possible such as in fossils or damaged archaeological material or where the construction of high resolution models is impractical. Since there was no CT scan with a higher resolution available, increasing model resolution in this study was achieved mainly by increasing element number and by anatomical representation of thin structures such as the sinus walls even when their thickness is smaller than voxel (element) size.

The effect of another parameter of importance in FEA, material properties, was not considered in this study although it is known that cranial skeletal material properties are heterogeneous (McElhaney et al., 1970; Dechow et al., 1993; Peterson and Dechow, 2003; Schwartz-Dabney and Dechow, 2003), the use of linearly elastic, isotropic material properties of bone homogeneously throughout the skull is common in FEA (Kupczik et al., 2009; Wroe et al., 2010; Bright and Gröning, 2011; Gröning et al., 2012). Using heterogeneous material properties improved model accuracy in a study by Strait et al. (2005). This required a large amount of preliminary work in mapping and representing heterogeneity and it considerably increased model complexity and computation to achieve a solution. However, several validation and sensitivity analyses support the use of simplified, homogeneous, material properties throughout the skull, since such models achieved results reasonably close to experimental data (Strait et al., 2005; Kupczik et al., 2007; Gröning et al., 2009; Szwedowski et al., 2011). The findings of the present study also support the use of linearly elastic, isotropic and homogeneous material properties for the cranium and teeth, given the good concordance between predicted and measured strain contours and large scale deformations when the sinus walls are represented.

Considering these results, model construction using simplification approaches that preserve sinus wall anatomy, such as those described here, should not impact greatly on reliability. However, model limitations should be evaluated against the aims of the study. Variations in both measured and predicted strains suggest a low reliability of FEA in cases where accurate estimates of strain magnitude are of importance. On the other hand, if relative strain magnitudes are relevant, then reasonably accurate FE model geometries (i.e. including sinus walls) should perform reasonably well. But, how well requires experimental data for assessment. Indeed a finding of this work is that to achieve reliable prediction of strain magnitudes is much harder (and less likely without experimental data to guide model refinement) than to estimate relative strains and large scale deformations.

Predicted bite force

Model sensitivity to simplification is low in terms of resulting bite force. The closest values of bite force to the experimentally measured ones (but only marginally so) were obtained by the highest resolution models and the most dissimilar, by the model without cancellous bone. However the models all performed very similarly, with differences in reaction force at the incisor less than 2% with respect to the mean predicted bite force. This said, on average the models overestimate bite force by 23-27% with respect to values found in experimental loadings. Thus, bite forces are overestimated by all models and different model simplifications have little effect on the degree of overestimation. This calls for caution in studies where bite force prediction is central.

Large scale model deformation

In terms of large scale deformation, model sensitivity is higher to how the sinus walls are reconstructed than to the presence of cancellous bone or model resolution. Thus the three models (Models 1, 3 and 5) with reconstructed sinus walls deform very similarly, differing mainly in the magnitude of deformation (length of vector connecting unloaded and loaded models). These models deform differently to models in which the sinus walls are omitted (Models 2 and 4). These models have a higher degree and somewhat different mode of dorso-ventral maxillary bending. This contrasts with the effect of not representing cancellous bone as a separate material, where the major impact is on the magnitude rather than mode of deformation. Model resolution when varied over the range assessed in this study has little effect.

It should be borne in mind that large scale deformations offer quite different insights into model performance than stresses and strains. The former can be used to compute strains (if every node in the FE model is treated as landmark) and so differences in modes of large scale deformation imply different strain contours, while differences in magnitudes imply similar contours but different magnitudes of strains. Strains and stress are relevant to prediction of failure/fracture and possibly, remodelling activity. In contrast, Procrustes size and shape analyses of large scale deformations describe general features of deformation such as dorso-ventral bending or twisting (O'Higgins et al., 2012).

2.5. Conclusion

By comparing the strains predicted by a series of FE models of the human cranium with those measured experimentally in the actual specimen, the impact of different modelling simplifications on predicted deformations was assessed. The hypothesis that there are no differences in strains predicted by the FE models and those measured experimentally in the cranium was not falsified. Thus the model built with only cortical bone and teeth showed strain magnitudes that were three to four times lower than the experimental cranium but the mode of deformation was largely unaltered. Omitting sinus walls led to alterations in modes and magnitudes of deformation.

The second hypothesis, that there are no differences in bite force predicted by the FE models and those measured experimentally, was falsified in that all models achieved substantially higher bite forces than the experimentally loaded cranium. However, among models the differences in predicted bite forces were less than 2% of the mean.

The third hypothesis, that FE models predict the same modes of large scale deformation, was not falsified. The effects are mainly on magnitude of deformation where model geometry is consistent. Modes of deformation are less sensitive to how cancellous bone is represented and model resolution than to variations in sinus wall representation. Thus, simplifications of cancellous bone anatomy have an impact on magnitude rather than mode of deformation while under representation of very thin bony structures such as are found in the sinus walls impacts on both mode and magnitude of deformation. These findings will guide subsequent model building in later chapters of this thesis.

Chapter 3 : Can muscle cross-sectional area be predicted from skull morphology?

3.1. Introduction

The present chapter comprises two studies examining different aspects of the relationship between muscle force and skull morphology. First, the predictability of muscle cross-sectional area (CSA) from bone morphology is assessed by comparing CSA values measured on computed tomography (CT) images with the values estimated using bony proxies. Second, the association between skull shape and muscle CSA is assessed using geometric morphometric tools.

The first study is relevant for mechanical analyses of the masticatory system such as those used in this thesis. The second study is important to understand how skull form covaries with jaw-elevator muscle force, in order to understand the factors underlying human masticatory mechanics.

Estimating muscle CSA for biomechanical analyses

Muscle force can be estimated from physiological cross-sectional area. Physiological cross-sectional area (PCSA) is defined as the total cross-sectional area (CSA) of all muscle fibres at a specified muscle length, and the muscle force equals the product of PCSA and the intrinsic strength of the muscle (Weijs and Hillen, 1985a; Koolstra et al., 1988; O'Connor et al., 2005). In studies involving humans it is not straightforward to obtain muscle data; skeletal collections lack soft tissues and ethical and supply issues limit access to cadaveric material. Dissection room specimens are often available only after they have been used for teaching and so are often too damaged to perform direct muscle force estimation (Koolstra et al., 1988; van Eijden et al., 1997; Antón, 1999). Computed tomography or magnetic resonance imaging can lead to direct measurement of CSA (Weijs and Hillen, 1986; Hannam and Wood, 1989; van Spronsen et al., 1992), which has been shown to correlate with PCSA in jaw-elevator muscles (Weijs and Hillen, 1984). However, when muscles are absent, as is the case in studies based on skeletal specimens, bony proxies are commonly used to estimate CSA (Antón, 1990; O'Connor et al., 2005; Wroe et al., 2010).

Muscle force estimation from bony features is particularly relevant in fossils or in relation to museum skeletal collections. Such estimation has frequently been carried out in relation to fossil hominins with the aim of inferring diet and ecology from masticatory mechanics (Demes, 1987; Spencer and Demes, 1993; Antón, 1996; O'Connor et al., 2005; Wroe et al., 2010). However, PCSAs of jaw-elevator muscles have shown low predictability from bony proxies in macaques (Antón, 1999). The same author studied this relationship in ten human cadavers, showing a lack of correlation between masseter and medial pterygoid bone attachment areas and PCSAs, and a low relationship between the latter and the antero-posterior length of the temporal fossa at the level of the zygomatic arch (Antón, 1994). To date, no further predictability studies in humans have been performed.

Muscle CSA and its relationship with skull shape

Muscle forces and skeletal morphology are related through the process of bone remodelling. During contraction, muscles directly strain the bone where they insert and apply loads as well as impacting on strains elsewhere during load-bearing functions (Scott, 1957; Moss, 1962; Yoshikawa et al., 1994; Milne and O'Higgins, 2012; DiGirolamo et al., 2013). Mechanical models of the human masticatory system (Hylander, 1975; Gingerich, 1979; Koolstra et al., 1988; Spencer, 1998; Röhrle and Pullan, 2007) have shown that jaw-elevator muscles play a key role in the generation of reaction force at the temporomandibular joints (TMJs) and the magnitude of bite force. The same studies demonstrated that, because of lever mechanics, forces produced during mastication are also influenced by anatomical features such as the relative positions of the TMJs, muscle insertions and dental morphology.

It has been shown in macaques that individuals with longer mandibular bodies have larger PCSAs. This, has been interpreted as an adaptation to maintain bite force; when the bite force lever arm increases, muscle force also increases (Antón, 1999). This relationship has also been found in humans using muscle CSA (Weijs and Hillen, 1986; Hannam and Wood, 1989). Significant correlations have also been found between measures of facial width and the CSA of the medial pterygoid (Hannam and Wood, 1989; van Spronsen et al., 1992), the temporalis muscle and most markedly, the masseter muscles (Weijs and Hillen, 1986; Hannam and Wood, 1989; van Spronsen et al., 1991; van Spronsen et al., 1992; Raadsheer et al., 1999).

Aims and hypotheses

In light of the uncertainties surrounding estimation of muscle areas from bony proxies, something that needs to be done for archaeological crania later in this thesis, one aim of this chapter is to reassess the relationships between masticatory muscle CSAs and the bony proxies used to estimate them. This forms the subject of the first study in this chapter. A second aim is to assess relationships between muscle CSAs and aspects of skull form. In part this is to investigate the possibility that skull form might provide additional information relevant to estimating muscle CSA, but it also is an interesting topic of investigation in its own right.

The aim of the first study is to assess the predictability of CSA from bony features. Two sets of variables are investigated with regard to their ability to predict CSA: (1) the areas enclosed by muscle markings on cranial bones (referred to as muscle areas) and (2) skull sizes. The following hypothesis is tested:

Hypothesis 1 (H1): There is no relationship between muscle CSAs, muscle areas estimated using bony features, and skull size.

The aim of the second study is to assess the association between skull shape and muscle CSA. In contrast to previous studies this analysis uses geometric morphometric methods (O'Higgins and Dryden, 1993; Slice, 2007; Mitteroecker and Gunz, 2009) to assess associations between cranial shape and masticatory muscle CSAs. The following hypothesis is tested:

Hypothesis 2 (H2): There is no association between skull shape and masticatory muscle CSAs.

If falsified, H1 would suggest that estimating muscle CSA from bony proxies is a reliable approach where direct measurement is impractical. If H2 is falsified this will provide interesting insights into how skull features relate to muscle force and vice versa. Such a relationship might provide an opportunity to improve muscle force estimation by incorporating data on skull shape.

3.2. Materials and Methods

3.2.1. Sample

The CT scans of 20 adult individuals, 11 women (aged 29 to 86 years) and nine men (aged 38 to 72 years) were used in this study (described in Table A.1 in Appendix). The individuals were without skull deformities or orthognathic surgery, and had full or almost-full dentitions. The CT images were provided by the Teaching Hospital of the University of Chile (Hospital Clínico de la Universidad de Chile, Santiago de Chile) under their ethics protocol for the use of patient data. The images were obtained for prior medical reasons, unrelated to this study using a Siemens 64-channel multidetector CT scanner equipped with a STRATON tube (Siemens Somatom Sensation 64, Siemens Healthcare, Erlangen, Germany). The CTs were taken with jaws closed, which is important because it allows landmarking of cranium and mandible in the knowledge that the dentition is always in or very close to occlusion. Clenching is unlikely to have happened during imaging; the imaging protocol dictates that patients are asked not to do it. However, this cannot be ruled out. Further, the extent of anatomical coverage in the CTs differs among patients, and most of the sample lacks a complete mandible. The primary reconstruction of images was performed using ad hoc program (Syngo Multimodality Workplace, Siemens Healthcare, Erlangen, Germany). Average voxel size was 0.43 x 0.43 x 1 mm. The image stacks were exported as DICOM files for their use in this study.

Three-dimensional (3D) skull morphologies were reconstructed from the CT stacks using Avizo (v.7.0.1, Visualization Sciences Group, Burlington, USA). Semi-automated segmentation of CTs based on grey-level thresholds to separate bone from surrounding tissues and air was undertaken as described below. Additionally, manual segmentation was performed where needed. A surface file was generated for each individual and exported for shape analysis.

3.2.2. Data acquisition

3.2.2.1. Skull shape and centroid size

Skull geometry and centroid size were captured using 59 landmarks. Forty-one landmarks are well defined anatomically. The remaining 18 represent the cranial origins of the temporalis, masseter and medial pterygoid muscles. The latter are less well defined. It is conceivable that these 18 landmarks are not reliably measured and so, add 'noise' (=error) to the analysis. To assess their impact, a preliminary principal components analysis (PCA) of shape variables (Procrustes coordinates as explained below) was performed using both the 41 and 59 landmark configurations. The resulting PCAs are very similar, except for reflected y-axes (Figure 3.1). Thus, these 18 landmarks are included in subsequent analyses because they provide data on muscle attachment areas and facilitate visualisation of results. The 59 landmark list is described in Table 3.1 and shown in Figure 3.2. Further analyses focussed on facial morphology and used a subset of 43 landmarks (see Table 3.1).

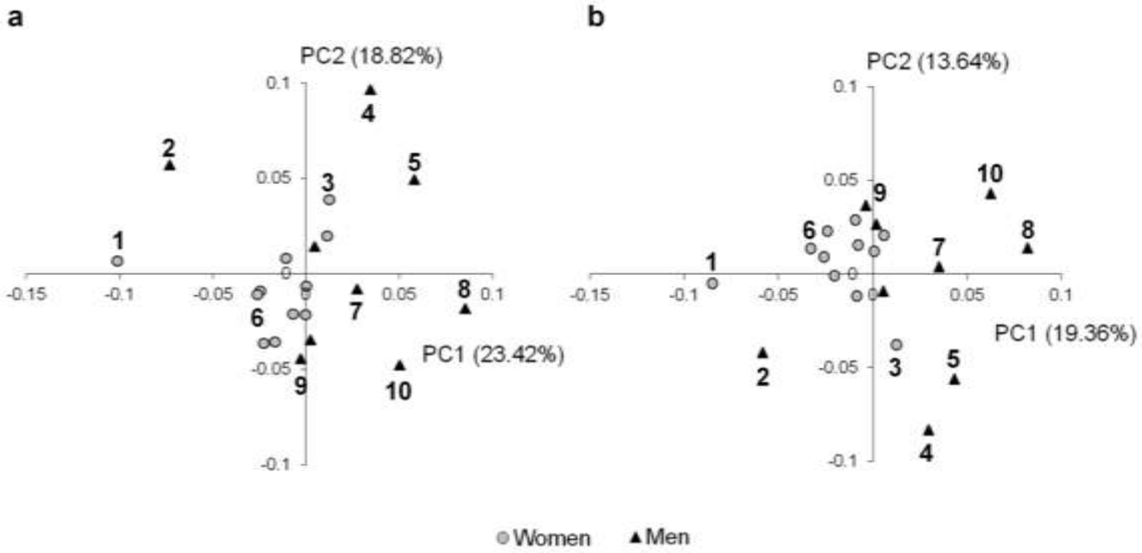

Figure 3.1. The impact of including landmarks representing muscle attachments. (a) Variation in skull shape using 41 landmarks. (b) Variation in skull shape using 59 landmarks. The ten individuals with the most different shape from the mean are labelled to facilitate comparison of the PC plots.

Only the shape of the superior part of the mandibular ramus was represented by landmarks due to the absence of the mandibular body and angle in most of the sample. Digitisation of landmarks as well as the PCA of Procrustes coordinates were performed using the EVAN toolbox (v.1.62, www.evan-society.org).

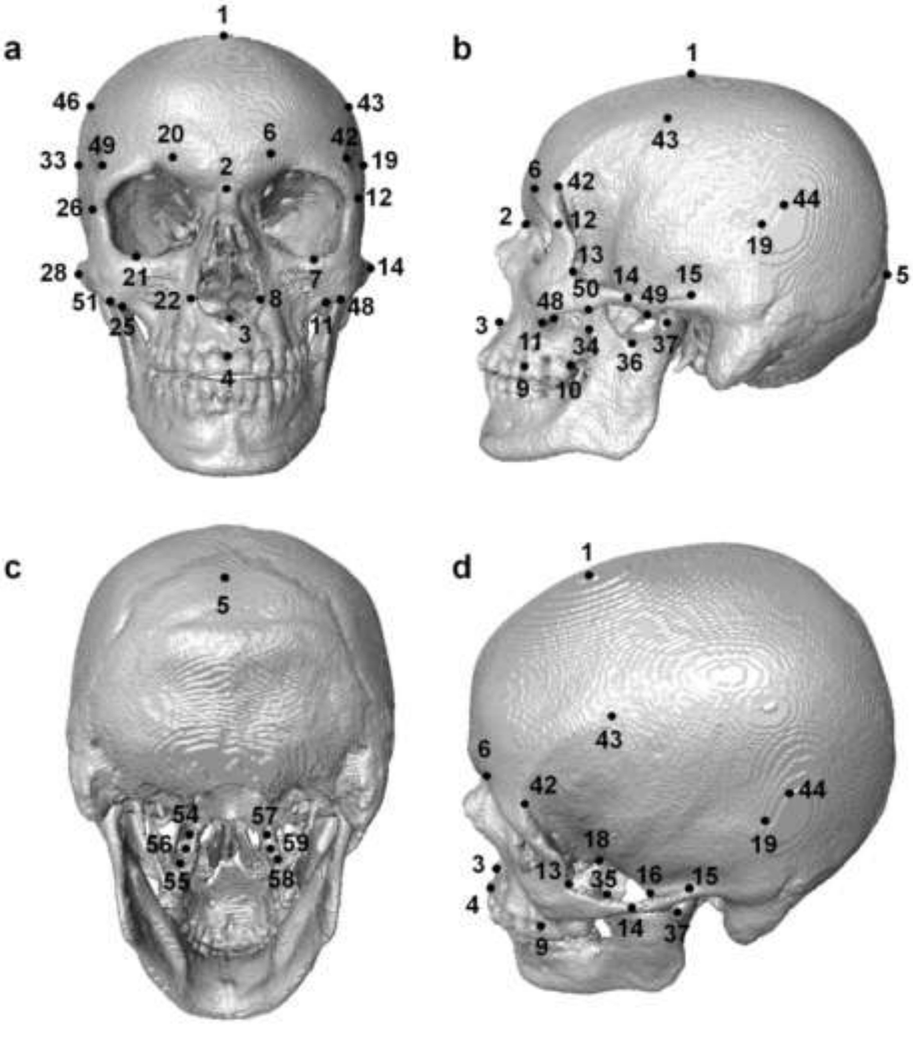

Figure 3.2. Positions of the landmarks listed in Table 3.1. (a) frontal view, (b) lateral view, (c) infero-posterior view and (d) latero-superior view. Landmarks were not placed on the mandibular angle and body due to their absence in most of the CTs.

Table 3.1. Selected skull landmarks. Facial landmarks shown with asterisk.

Structure	No.	Symbol	Name	Definition
Cranium	1	V	Vertex	Highest point of the calvarium.
	2	N	Nasion*	Intersection between frontonasal and internasal sutures.
	3	ANS	Anterior Nasal Spine*	Tip of the anterior nasal spine.
	4	Pr	Prosthion*	Most buccal and occlusal point of the interalveolar septum between central incisors.
	5	Oc	Occiput	Most posterior point of the neurocranium.
	6&20	SoT	Supraorbital Torus*	Most anterior point of the supraorbital ridge.
	7&21	InfO	Infraorbitale*	Most inferior point of the infraorbital ridge.
	8&22	NNot	Nasal Notch*	Most lateral part of the nasal aperture.
	9&23	M1	First Molar*	Most buccal and mesial point of M1 and alveolar process junction. If absent, the landmark is placed in the lowest most buccal point of the interalveolar septum between the second premolar and the next present molar.
	10&24	M3	Last Molar*	Last point of the dental arch, located at the most buccal and distal point on the last present molar and alveolar process junction.
	11&25	ZM	Zygo-maxillar*	Most inferior point of the zygo-maxillary suture.
	12&26	FZ	Fronto-zygomatic*	Most lateral point of the fronto-zygomatic suture.
	13&27	FTZ	Fronto-temporal angle*	Point at the intersection between frontal and temporal processes of the zygomatic bone.
	14&28	ZAl	Zygomatic Arch lateral*	Most lateral point of the zygomatic arch.
	15&29	ZRp	Zygomatic Root posterior	Most posterior-superior point of the intersection between the zygomatic root and the squama of temporal bone.
	16&30	ZRa	Zygomatic Root anterior	Most anterior point of the intersection between the zygomatic root and the squama of temporal bone.
	17&31	ZAm	Zygomatic Arch medial	Most lateral point on the inner face of the zygomatic arch.
	18&32	ItC	Infratemporal Crest	Most medial point of the infratemporal crest.
	19&33	Eu	Eurion	Most lateral point of the neurocranium.
Mandible	34&38	CPa	Coronoid Process anterior*	Most anterior point of the coronoid process.
	35&39	CPs	Coronoid Process superior*	Most superior point of the coronoid process.
	36&40	ManNot	Mandibular Notch*	Most inferior point of the mandibular notch.
	37&41	Co	Condyle*	Most lateral point of the condyle.
Muscle origin/ Insertion	42&45	aTemOr	Anterior Temporal origin*	Most anterior point of origin of the temporal muscle on the temporal line.
	43&46	sTemOr	Superior Temporal origin	Most superior point of origin of the temporal muscle on the temporal line.
	44&47	pTemOr	Posterior Temporal origin	Most posterior point of origin of the temporal muscle on the temporal line.
	48&51	aMassOr	Anterior Masseter origin*	Most anterior point of origin of the masseter muscle on the zygomatic arch.
	49&52	pMassOr	Posterior Masseter origin*	Most posterior point of origin of the masseter muscle on the zygomatic arch.
	50&53	midMassOr	Mid-Masseter origin*	Midpoint along the area of area of origin of the masseter muscle on the zygomatic arch.
	54&57	sPtOr	Superior Pterygoid origin*	Most superior point of origin of medial pterygoid muscle on the pterygoid fossa.
	55&58	iPtOr	Inferior Pterygoid origin*	Most inferior point of origin of medial pterygoid muscle on the pterygoid fossa.
	56&59	midPtOr	Mid-Pterygoid origin*	Midpoint along the area of origin of the medial pterygoid muscle on the pterygoid fossa.

Segmentation and measurement error

Since the skulls used in this study are reconstructed from CT scans and then landmarked, the effects of error introduced by segmentation of the CT images, and by the landmarking procedure are assessed separately.

Segmentation of CT image data based on grey level thresholds is a common technique for reconstructing the 3D anatomy of hard tissues (Skinner et al., 2008; Benazzi et al., 2009; Neubauer et al., 2009; Bright, 2012). The threshold defines the tissue boundaries, and different choices of threshold will result in different reconstructions, with potential effects on subsequent morphometric analyses. One of the most widely used methods to determine the segmentation threshold is to use the half maximum height (HMH) criterion; the mean of the grey levels on either side of the interface (Spoor et al., 1993). In applying the HMH criterion, different thresholding values may be used for different anatomical regions to take account of variations in e.g. bone radio-opacity. Thus, this segmentation approach can be time-consuming when applied to a large sample of volume data. A faster, alternative approach is to select a threshold on the basis of visual assessment; choosing the value that appears to perform best in segmenting bones throughout the CT stack.

In order to assess the impacts of these different approaches, a sensitivity analysis was performed, to assess the errors introduced by the different thresholding and segmentation approaches. The CT datasets of two women (29 and 61 years old) and two men (38 and 72 years old) were segmented twice. The differences in resulting reconstructions were assessed using landmark data. Landmarking itself is error prone and so, to control for this source of error each segmented cranium was landmarked five times on five different days.

HMH criterion. The average grey threshold level was calculated in ten different facial regions per individual. This was done using grey level curve values obtained with ImageJ (v.1.44p, Wayne Rasband, National Institutes of Health, USA).

Observed best-threshold criterion. The threshold for bone labelling was selected based on the best fit to bone observed in the CT images. Compared to the HMH criterion this method is considerably less time consuming.

Five unilateral facial landmarks over the infraorbital and zygomatic regions were used to assess error: N, ANS, M1, InfO and FTZ (previously described in Table 3.1). Facial landmarks were chosen because the face is the main focus of interest in the present study. Each individual was segmented twice, once using each segmentation approach. As noted above, each surface was then landmarked five times over five different days.

Shape variation was assessed using geometric morphometric tools. Procrustes fit was followed by PCA of Procrustes coordinates (O'Higgins, 2000; Slice, 2007; Mitteroecker and Gunz, 2009) using EVAN toolbox. The PC scores were then used as variables in a two-way non-parametric multivariate analysis of variance (NPMANOVA; Anderson, 2001) to assess the effects of segmentation method and landmarking. The PC plot is shown in Figure 3.3. Although considerable variation due to landmarking is present, the points representing each individual remain in separate clusters. Thus the errors are smaller than differences among individuals. The NPMANOVA, after 9999 permutations, showed that none of the effects nor their interaction was significant (segmentation method: F=0.32 df=1,30 p=0.8; landmark placement: F=0.13 df=4,30 p=0.8 ; interaction: F=0.1 df=4,30 p=1). Based on these results, threshold-segmentation using observed best-fit, introduces no greater error than landmarking and is faster to apply than HMH. Thus, the best fit criterion was used throughout this thesis. The NPMANOVA of PCA scores was performed with PAST (Hammer et al., 2012).

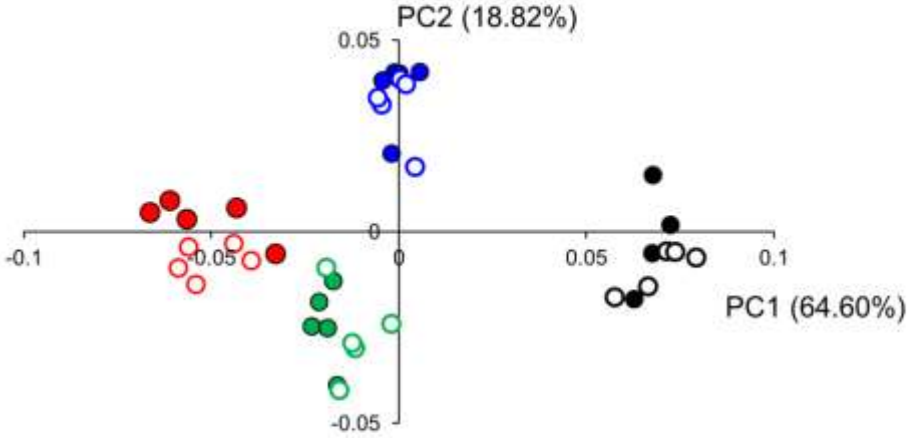

Figure 3.3. Effect of segmentation approach and landmarking. Each individual is represented by a different colour. Surfaces generated by observed best-fit threshold segmentation are represented by hollow symbols.

3.2.2.2. Measurement of jaw-elevator muscle CSAs

The procedure used to estimate the CSAs of jaw-elevator muscles from CT scans was based on that of Weijs and Hillen (1984):

CSA of the temporalis muscle. The CSA of the temporalis muscle was estimated by reference to the Frankfurt Plane (FP), which passes through left infraorbitale, and left and right porion. Weijs and Hillen (1984), in a sample of human cranial MRI scans found that the largest temporalis muscle CSAs are found in planes that lie 4-16 mm above and parallel to the FP (mean 10 mm). Because skulls vary in size it was decided not to estimate CSA using a sectioning plane at fixed distance above FP. Instead, the sectioning plane used in this study was standardised to pass through the most medial point of the infratemporal crest. This is identifiable on all specimens and lies well within the region where Weijs and Hillen (1984) found CSA to vary little (4-16 mm above FP). The CSA was estimated as the average of the muscle cross sectional areas in this sectioning plane and in the two planes (~1 mm thick) immediately above it (Figure 3.4a and b).

CSA of the masseter and medial pterygoid muscles. For the masseter and medial pterygoid muscles, the sectioning plane was defined to lie at the level of the lingula and to be parallel to the anterior-most part of the infero-posterior borders of the zygomatic bones on both sides. (Weijs and Hillen, 1984) found the largest CSAs of both muscles to lie 25 mm above the mandibular angle. Further, they noted that CSA is largely unchanged in planes oriented as in this study over distances ranging between 12 and 30 mm from the zygomatic bone. In the present sample, the mandibular angle could not always be used due to its absence in CT scans. However, the lingula was identifiable in all scans and lies within the range of distances from the zygomatic where CSA changes little (Weijs and Hillen, 1984). The lingula was therefore chosen as the reference level for the sectioning plane in this study. Masseter and medial pterygoid CSAs were estimated by averaging CSAs from the sectioning plane the single planes (~1 mm thick) that lie above and below it (Figure 3.4c-e.).

To control for the error associated with the definition of muscle contours, muscle CSA in each slide was measured three times and the values averaged.

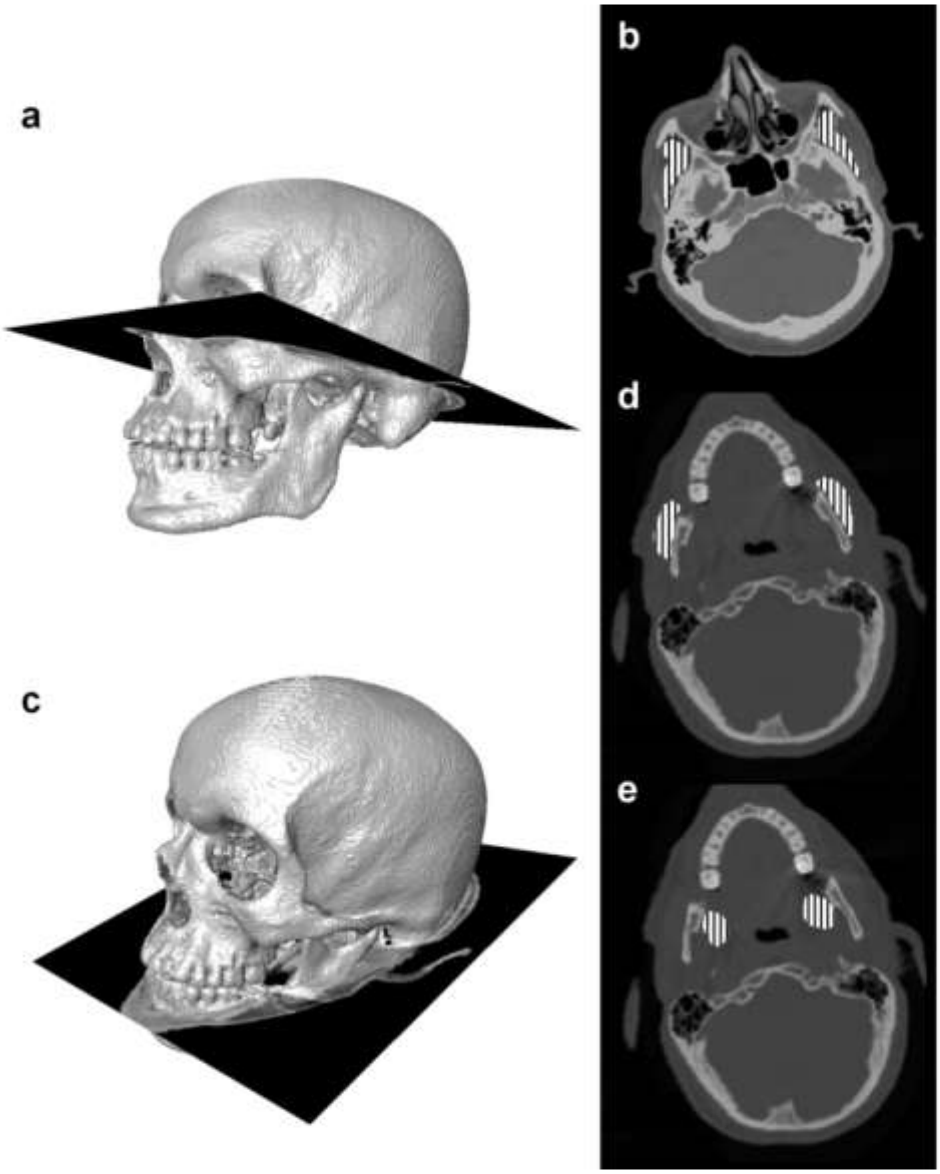

Figure 3.4. Selected planes used to measure cross-sectional areas of jaw-elevator muscles. (a) Plane for (b) temporal muscles, (c) plane for (d) masseter and (e) medial pterygoid muscles.

3.2.2.3. Estimation of muscle areas from bony proxies

The method used to estimate the CSA of jaw-elevator muscles from muscle proxies, is based on O'Connor et al. (2005) and Antón (1999). These estimates are not true cross-sectional areas and are referred to as 'muscle areas' in the following text.

Temporalis area. Corresponds to the area enclosed by the temporal fossa at the zygomatic arch in a plane parallel to the FP. The vertical position of this plane was chosen to be at the level where bony boundaries are most complete. This minimised the need to estimate them when measuring areas in this section (Figure 3.5a and b).

Masseter area. This is calculated as the product of the length of the masseter origin on the zygomatic arch and the width of the muscle. The width of the muscle is estimated as the medio-lateral distance between the lateral face of the mandibular ramus, and the lateral edge of the zygomatic arch projected onto the FP (Figure 3.5c and d). Due to the lack of complete mandibles in most of the sample the base of the lingula projected onto the lateral surface of the mandibular ramus was used as the medial point used to estimate masseter width (Figure 3.5d).

Medial pterygoid area. The bony surface of the medial pterygoid muscle insertion onto the mandible was often missing in the CT scans and so area could not be estimated reliably. Hence this muscle was not included in the analysis.

To control for error, the masseter area was estimated from bony proxies three times in each individual and averaged. The temporalis area was estimated once in each individual because it is an automatic calculation based almost completely on boundaries defined a priori by the surrounding bone.

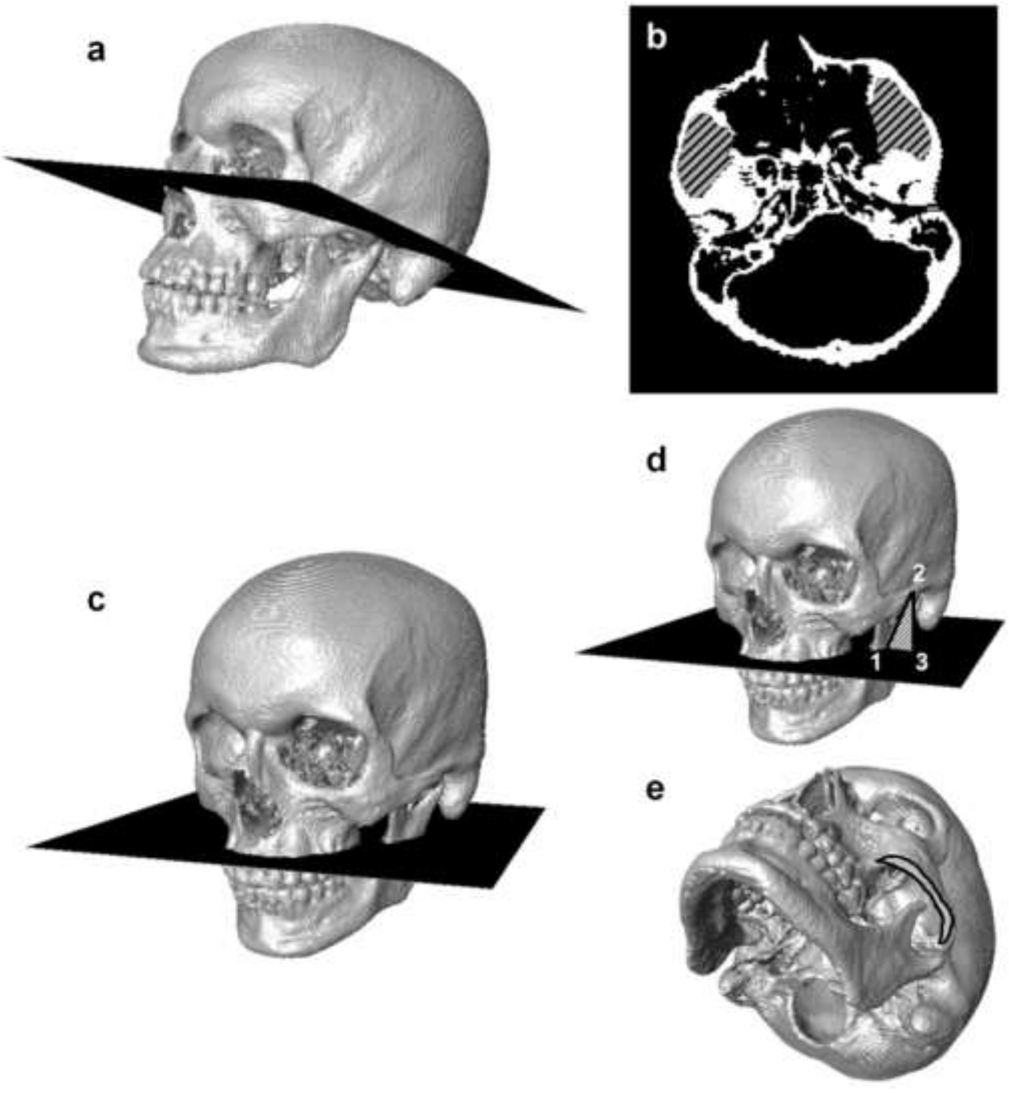

Figure 3.5. Selected planes used to estimate muscle areas from bone anatomy. (a) Plane for measurement of (b) temporalis area, (c) reference plane for masseter area, estimated as the product of the width and the length of the masseter origin. (d) The ‘width’ of the masseter area was defined as the medio-lateral distance from point 1 at the lateral surface of the mandibular ramus to point 3 which is projected vertically from the lateral edge of the zygomatic arch (point 2) onto the Frankfurt plane. (e) The ‘length’ of the master origin was measured along the muscle scar on the zygomatic arch (highlighted area).

3.2.3. Analyses

3.2.3.1. Predictability of muscle CSA from muscle areas on bone and skull size

A preliminary ANOVA showed no significant effect of side (i.e. left/right asymmetry) on the data (Table 3.3). Hence the CSAs and muscle areas corresponding to the right side of the head were used. After Bonferroni correction, only sex had a significant interaction with facial size; therefore sexes were pooled in the study.

As a first step the square roots of CSAs and estimated muscle areas were calculated. These were used in subsequent analyses as were raw values of centroid size. This ensured the dimensions of all variables were the same; mm. The normality of muscle CSAs and muscle areas (as square roots) and centroid sizes using a Shapiro-Wilks test with a significance level of 0.05.

The first hypothesis, that there is no relationship between muscle CSAs, muscle areas estimated using bony features, and skull size, was tested through a series of analyses. First, a t-test was used to assess the difference between directly measured square roots of both CSAs and estimated muscle areas. Second, Pearson's correlation (r) between the same sets of data was computed. Finally, the proportions of muscle CSA variance explained (R^2) by the square roots of estimated muscle areas and skull centroid sizes were computed.

All the analyses above were performed using PAST.

3.2.3.2. Association between skull shape and CSA of jaw-elevator muscles

Prior to testing the second hypothesis of this chapter (H2), the effects of confounding factors that also impact on skull shape variation were assessed. Subsequently, an exploratory analysis of sample morphological variation was performed. Finally, H2 was tested using GM tools for statistical analysis and visualisation of shape changes. Visualisation of shape changes used the surface corresponding to one of the individuals in the sample (Male, 43 years old), warped to the mean configuration before further warping to the target. Grids were drawn over the mean landmark configuration, and warped with the surface.

Confounding factors: The effects of asymmetry and sex on shape variation

The skull shows a degree of asymmetry which is irrelevant to this study and might add 'noise'. It was therefore decided to remove asymmetry by reflected relabeling followed by averaging of the original and reflected landmarks (Corti et al., 2001). After GPA, PCAs of both original and symmetrised skulls and faces were performed to compare patterns of shape variation. In both cases, the PC plots are very similar (Figure 3.6), suggesting asymmetry is not a significant factor impacting on patterns of skull variation. These analyses were performed using the EVAN toolbox. For convenience (particularly for the use of symmetric shapes and muscle data) the symmetrised data were used in subsequent analyses of this chapter.

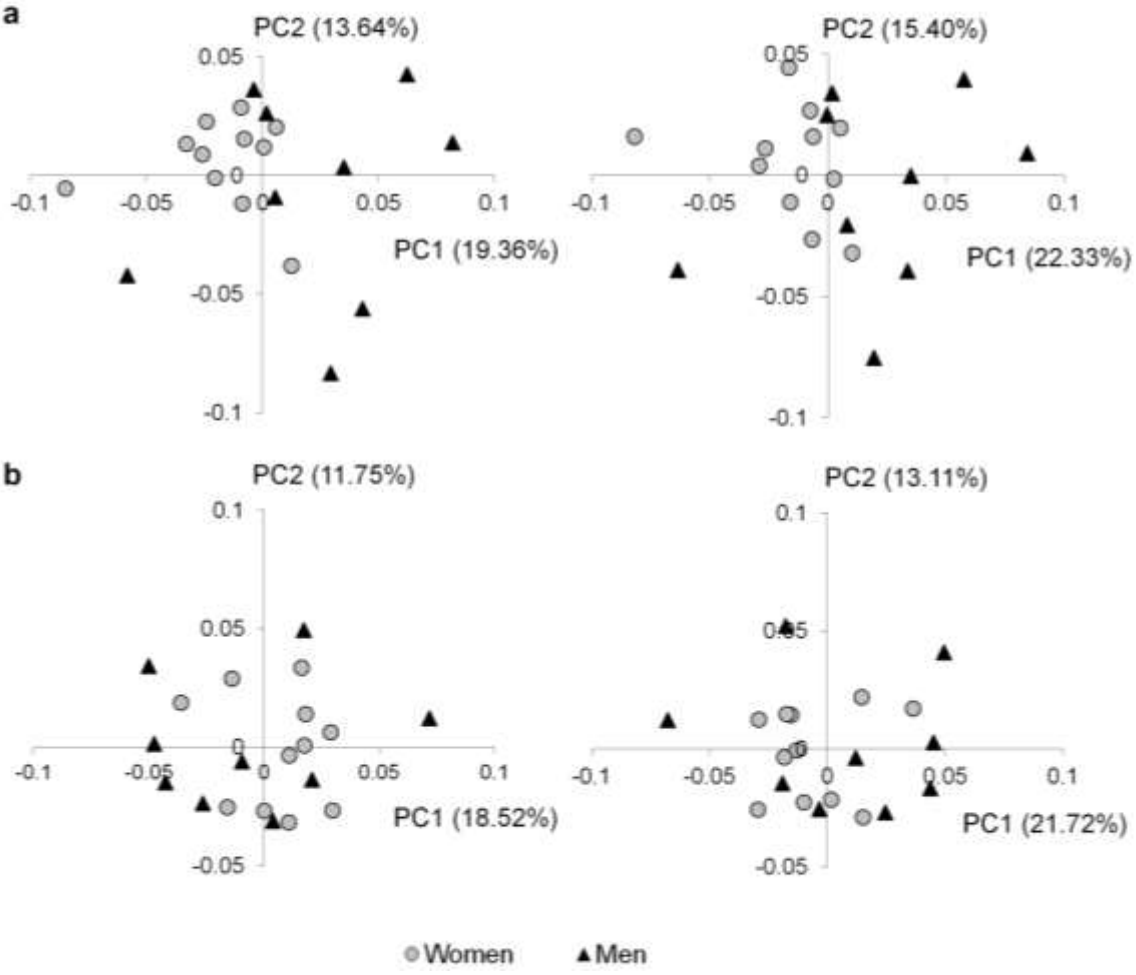

Figure 3.6. Effect of sample symmetrisation. PC plots showing (a) skull and (b) face shape variation among original (left) and symmetrised (right) landmark configurations.

Sexual dimorphism in skull shape was assessed using discriminant analysis (MorphoJ v.1.05c, Klingenberg, 2011). The analysis showed that this sample is not sexually dimorphic (T^2_{skull}=0.07; T^2_{face}=0.6). Thus data are pooled in subsequent cranial shape analyses.

Skull shape variation

Geometric morphometric analyses of skull and face landmark configurations were used to explore patterns of shape variation. These analyses also allowed the identification of individuals at the extremes of shape variation, used in Chapter 5 to study the relationship between cranial form and the mechanical performance of the craniofacial skeleton during biting simulations. After full Procrustes fit, PCA of shape coordinates was performed (O'Higgins, 2000; Slice, 2007; Mitteroecker and Gunz, 2009) using the EVAN toolbox.

Relationship between jaw-elevator muscle CSA and skull shape

Hypothesis 2, that there is no association between skull shape and masticatory muscle CSAs., was formally tested using partial-least squares (PLS) and multivariate regression analyses. The PLS method finds pairs of axes, called singular warps, for each set (block) of variables through singular value decomposition of the among block covariance matrix. Like principal components, the first axis is constructed such that it explains the largest possible proportion of among block covariance with successive orthogonal axes accounting for diminishing proportions (Rohlf and Corti, 2000). Muscle variables correspond to the averaged left and right muscle CSAs of temporalis, masseter, and medial pterygoid. Two sets of PLS analyses were undertaken. Each set was computed using either cranial or facial landmark data. In the first, the muscle block of data comprised the square roots of muscle CSAs and the second, proportions of total muscle CSA accounted for by each muscle. The first PLS therefore assesses the association between absolute muscle CSAs (and so maximum forces) and skull or face shape while the second considers relative CSAs.

The proportions of covariance explained by the first pair of singular warps (one being shape, the other muscle CSA) were computed and correlations between individual scores on them were used as measures of association between the two blocks. Additionally, multivariate regression was used to assess skull and face shape predictability from muscle CSAs or CSA proportions. A permutation test of 1,000 rounds was used. The association between skull and face shape and muscle data was visualised through surface warping.

Besides PLS, the RV coefficient which is a multivariate generalization of the squared Pearson correlation coefficient (Escoufier, 1973; Klingenberg, 2009) was also used to assess associations. It does not allow visualisation as in PLS. The above analyses were undertaken using the EVAN toolbox and MorphoJ.

3.3. Results

3.3.1. Descriptive statistics of muscle data

Table 3.2 presents descriptive statistics for skull and face centroid sizes, masticatory muscle CSAs, CSA proportions and muscle areas estimated from bony proxies. As mentioned in materials and methods, the effects of sex and side were assessed using ANOVA. The significance level of 0.05 after Bonferroni correction becomes 0.05/10=0.005. As such only the association between facial size and sex is significant (p=0.003). Given the small sample size, the analyses were repeated using the non-parametric Kruskal-Wallis test, giving the same results.

Table 3.2. Descriptive statistics. F=female, M=male, SD=standard deviation. Significant p-value after Bonferroni correction are shown in bold.

Variable	Sex	N	Mean ± SD			Effects (F-test)			
			Centroid Size	Left	Right	Sex	p-value	Side	p-value
Skull Centroid Size (mm)	F	11	491.2 ± 14.2	-	-	4.84	0.04	-	-
	M	9	504.8 ± 13	-	-				
Face Centroid Size (mm)	F	11	329.3 ± 9.7	-	-	12.04	**0.003**	-	-
	M	9	344.3 ± 9.5	-	-				
Temporalis CSA (mm^2)	F	11	-	475.8 ± 58.6	517 ± 66	2.62	0.11	0.05	0.82
	M	9	-	488.5 ± 44.5	511.6 ± 80.6				
Temporalis Proportion (%)	F	11	-	39.8 ± 4.1	40.7 ± 3.8	3.35	0.07	0.11	0.74
	M	9	-	38.3 ± 1.91	38.1 ± 3.4				
Temporalis Area (mm^2)	F	11	-	804.2 ± 94.9	798.1 ± 153.7	<0.001	0.98	0.16	0.69
	M	9	-	815.4 ± 153.8	823.8 ± 148.5				
Masseter CSA (mm^2)	F	11	-	422.8 ± 73.8	432.2 ± 85.3	6.34	0.02	0.09	0.76
	M	9	-	488.6 ± 67.4	494.1 ± 90.4				
Masseter Proportion (%)	F	11	-	35.1 ± 2.9	35.5 ± 3.4	1.37	0.25	0.17	0.68
	M	9	-	36.2 ± 2.8	36.6 ± 2.9				
Masseter Area (mm^2)	F	11	-	715.2 ± 80.1	783.3 ± 138.4	6.32	0.02	1.05	0.31
	M	9	-	729.9 ± 134.1	850.2 ± 113.5				
Medial Pterygoid CSA (mm^2)	F	11	-	302.3 ± 64.7	289.8 ± 63.4	5.68	0.02	0.21	0.65
	M	9	-	344.5 ± 53.6	339 ± 60				
Medial Pterygoid Proportion (%)	F	11	-	25.1 ± 3.5	23.9 ± 3.8	0.85	0.36	0.60	0.44
	M	9	-	25.5 ± 2.1	25.3 ± 2.4				

3.3.2. Predictability of muscle CSA from bony proxies and skull size

The accuracy of predictions of muscle CSAs from bony proxies was explored by comparing the means of measured CSAs and estimated muscle areas, assessing the correlation between them and computing regressions of muscle CSAs on estimated areas to assess their predictability from muscle areas. The results are summarised in Table 3.3. The medians of CSAs and estimated muscle areas are significantly different in both the temporalis and masseter for both males and females. After Bonferroni correction (significant p-value 0.05/6=0.008), only the association between temporalis muscle CSA and estimated temporalis areas is significant as assessed by the Pearson correlation coefficient. Predictability of true CSA from estimated muscle area, as assessed by regression, was generally poor, with the highest values of explained covariance (R^2) where correlation coefficients are largest. Plotted data are shown in Figures 3.7 and 3.8.

Table 3.3. Relationship between muscle CSA, estimated muscle area and skull centroid size. Data are from the right side of the head. Significant p-values after Bonferroni correction are shown in bold.

Muscle	Variables X vs. Y	Means.		Correlation		Regression	
		t	p-value	r	p-value	F(x)	R2
Temporalis	Muscle area vs. CSA	9.63	**<0.001**	0.66	**0.001**	y=0.37x+11.81	0.45
	Centroid size vs. CSA	-	-	0.58	0.008	y=0.05x-4.31	0.33
	Centroid size vs. Muscle area	-	-	0.25	0.28	y=0.04x+7.32	0.06
Masseter	Muscle area vs. CSA	9	**<0.001**	0.073	0.76	y=0.06x+19.58	0.01
	Centroid size vs. CSA	-	-	0.51	0.02	y=0.07x-14.37	0.26
	Centroid size vs. Muscle area	-	-	0.56	0.01	y=0.09x-17.51	0.31

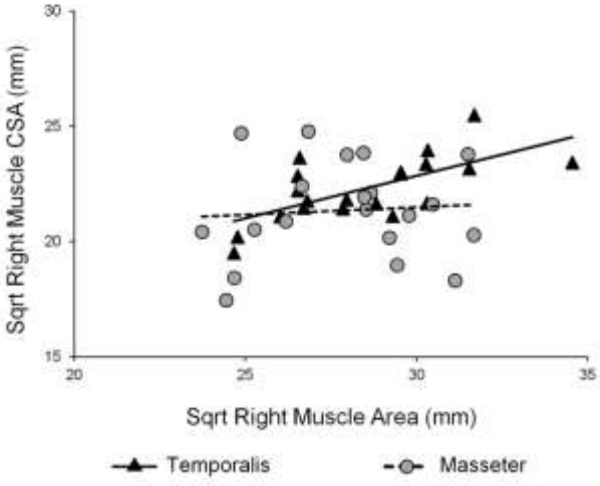

Figure 3.7. Relationships between actual muscle CSAs and estimated muscle areas. The regression lines are shown for each muscle.

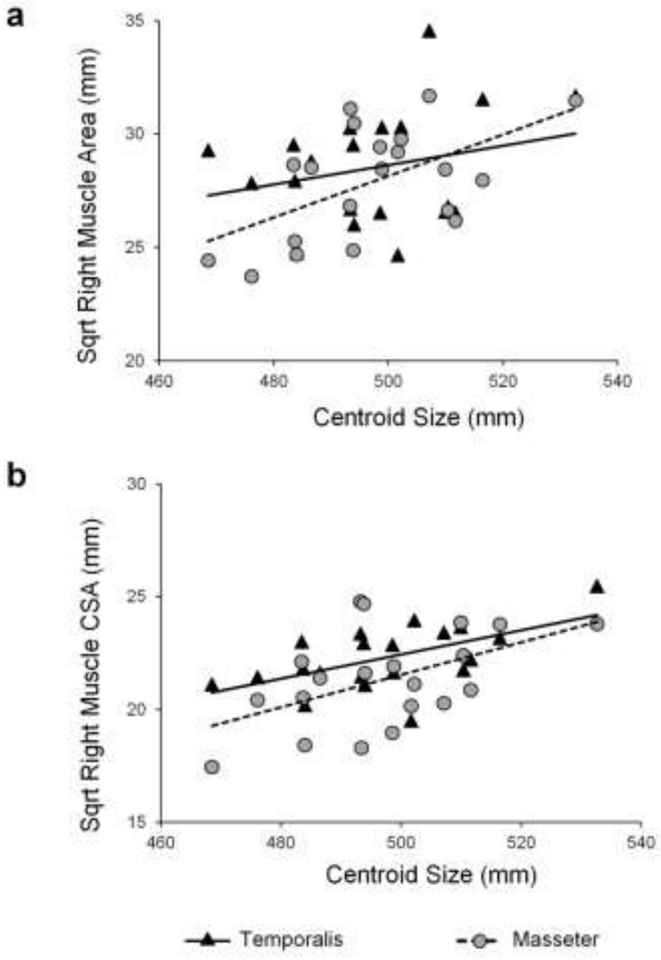

Figure 3.8. Relationships between (a) actual muscle CSAs, (b) estimated muscle areas and skull centroid size. The regression lines are shown for each muscle.

3.3.3. Skull shape variation

In the PCAs of shape, PC1 and PC2 account for 22.34% and 15.4% = 37.74% of skull shape variance, and 21.72% and 13.11% = 34.83% of face shape variance. Thus there is no single strong vector of variation. The male and female distributions overlap almost completely and males appear slightly more variable than females in the plots of Figures 3.9 and 3.10, respectively. In the skull, the first two principal components relate to co-variations in both neurocranial and facial proportions (i.e. they are both narrow and tall or wide and long in the insets; Figure 3.9). In the face, the first two PCs relate to combinations of vertically long or wide faces and more or less prognathic maxillae (Figure 3.10).

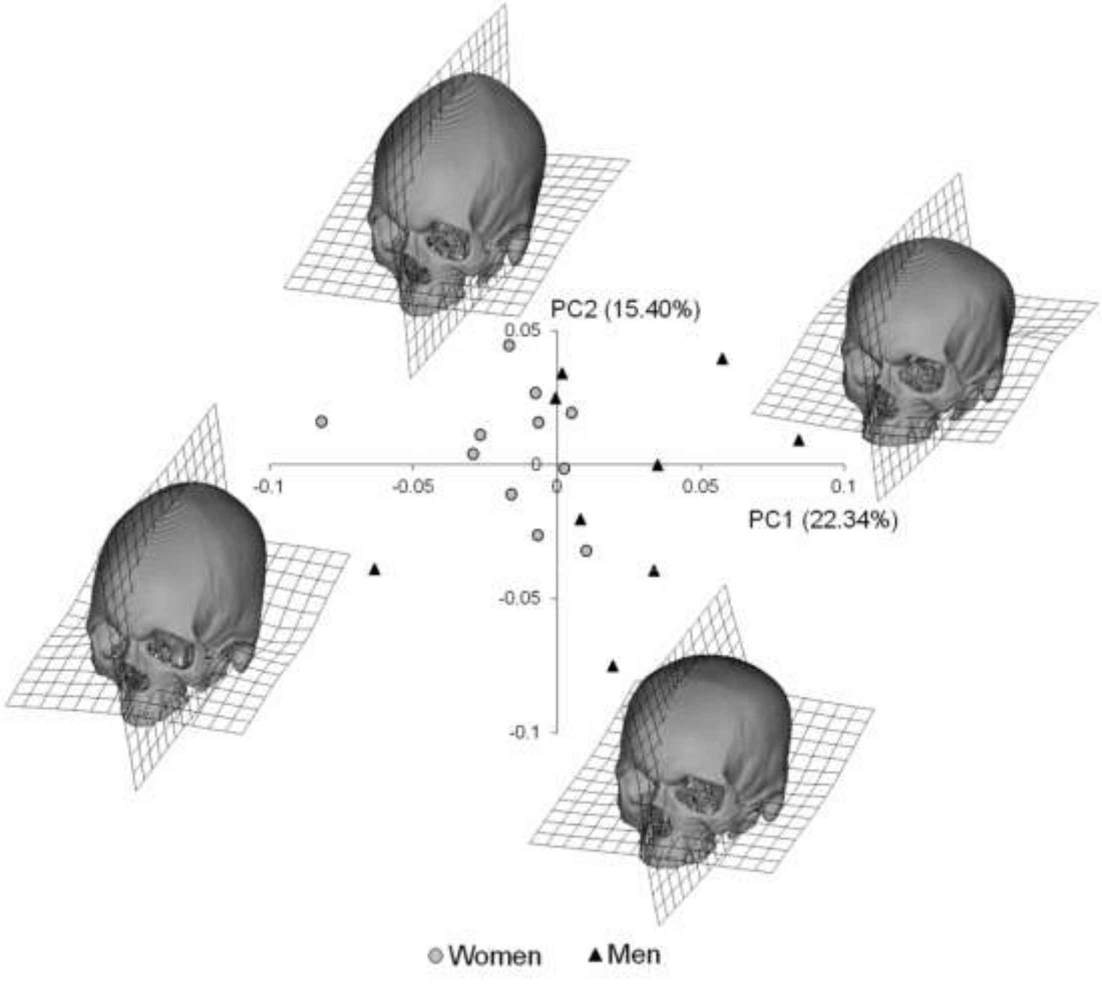

Figure 3.9. Principal components analysis of skull shape coordinates. Visualisations of variation represented by each PC are shown as warped surfaces and transformation grids at their positive and negative extremes. Warpings are with respect to the mean and have been magnified 1.5 times to improve visualisation.

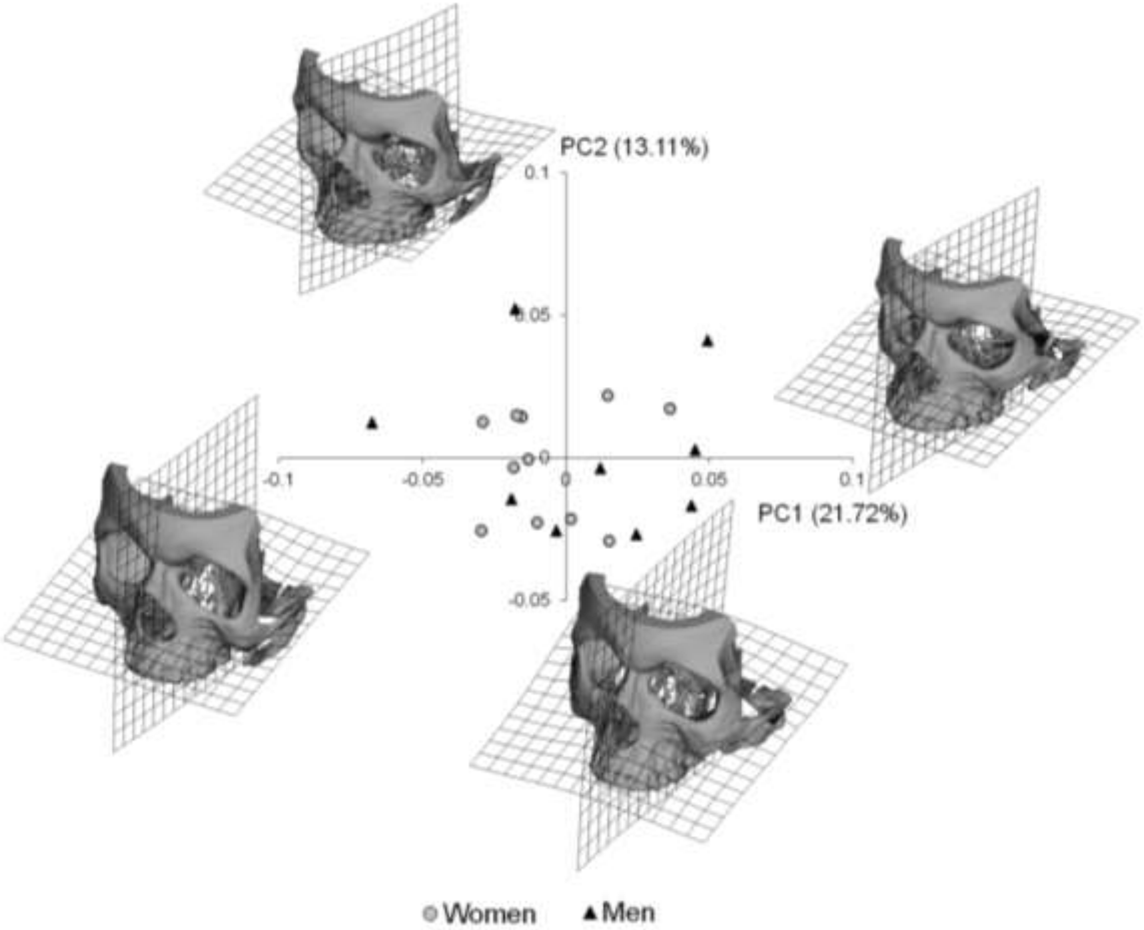

Figure 3.10. Principal components analysis of face shape coordinates. Visualisations of variation represented by each PC are shown as warped surfaces and transformation grids at their positive and negative extremes. Warpings are with respect to the mean and have been magnified three times to improve visualisation.

3.3.4. Associations between skull shape and jaw-elevator muscle CSAs and proportions

Two-block PLS analyses examined the associations between muscle CSAs, proportions of total muscle CSA and skull or face shape. The CSAs and proportions were entered singly into the analyses as one 'block' of data and the shape coordinates for the sample as the other block. As expected, given that one block contains only one variable, the PLS analyses resulted in one singular value (SV) explaining 100% of the covariance of CSA with skull or face shape. The RV coefficient was also calculated as a measure of association between these blocks.

Temporalis proportion showed the strongest association with both skull and face shape. The correlation among first singular warps (SW1) was the highest found for the face (r=0.81). The RV coefficients for skull (RV=0.22) and face (RV=0.29) shape with temporalis proportion were the largest found. Temporalis proportion also explained the greatest (yet quite small) proportions of the total variance of skull ($R^2=0.075$; i.e. 7.5% of the total variance) and face ($R^2=0.095$; i.e. 9.5% of the total variance) shape. Only the relationship between temporalis proportion and face shape was statistically significant at the $p<0.05$ level (Table 3.4), but not after Bonferroni correction (p-value 0.05/12=0.004).

Table 3.4. Relationship between skull and face shape and masticatory muscle CSAs (as the squared root of the CSA values) and proportions of total muscle CSA

Variable	Structure	SV	% of total covariance	PLS		RV	p-value	Regression	
				correlation (r)	p-value			R^2	p-value
Temporalis	Skull	0.025	100	0.76	0.37	0.16	0.37	0.056	0.37
CSA	Face	0.024	100	0.67	0.09	0.23	0.09	0.076	0.09
Masseter	Skull	0.029	100	0.60	0.87	0.10	0.87	0.034	0.87
CSA	Face	0.025	100	0.76	0.79	0.12	0.79	0.039	0.79
Medial Pt.	Skull	0.033	100	0.72	0.37	0.16	0.37	0.056	0.37
CSA	Face	0.027	100	0.78	0.32	0.18	0.32	0.057	0.33
Temporalis	Skull	0.036	100	0.71	0.12	0.22	0.12	0.075	0.11
Proportion	Face	0.033	100	0.81	0.02	0.29	0.02	0.095	0.02
Masseter	Skull	0.020	100	0.61	0.90	0.09	0.90	0.032	0.90
Proportion	Face	0.018	100	0.68	0.75	0.12	0.75	0.040	0.77
Medial Pt.	Skull	0.030	100	0.68	0.36	0.17	0.36	0.057	0.35
Proportion	Face	0.027	100	0.71	0.19	0.20	0.19	0.065	0.19

Morphologically, the SW1 of skull shape against temporalis muscle CSA expressed as a proportion of total muscle CSA indicates that a large temporalis proportion is associated with a relatively antero-posteriorly elongated neurocranium and mandibular ramus, wider face and less prognathic maxilla compared to those individuals with small temporalis proportions (Figure 3.11). The transformation grids show large deformations in the lateral aspects of the neurocranium. These reflect shifts in the relative positions of the Eurion (most lateral point of the neurocranium) with respect to the landmarks representing temporalis attachment.

When only facial landmarks are considered, the results parallel those of the skull. Large temporalis proportions are associated with a relatively narrower, less prognathic, vertically shorter maxilla, and an antero-posteriorly elongated mandibular ramus and a low-set coronoid process when compared to small temporalis proportions (Figure 3.12).

As noted above these apparent associations, although anatomically appealing in that they indicate shape covariations with temporalis proportions that involve the temporalis attachment to the vault, they are not significant after Bonferroni correction so should be treated with due caution.

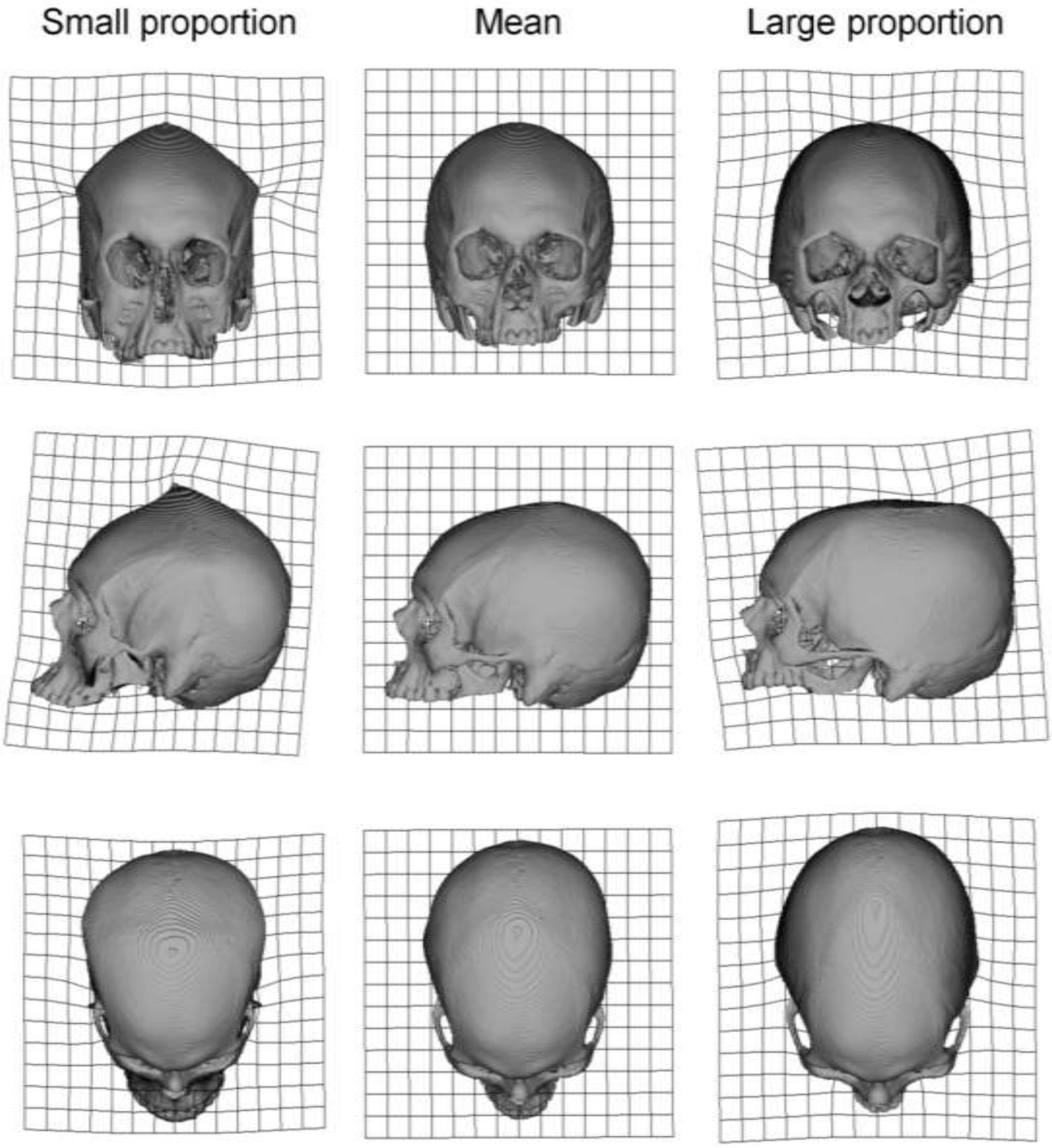

Figure 3.11. Association between skull shape and temporalis muscle proportion. Warpings of skull shape on SW1. Individuals with a large temporalis proportion show an antero-posteriorly elongated neurocranium and mandibular ramus and a vertically shorter face. Surface warpings have been magnified three times to improve visualisation.

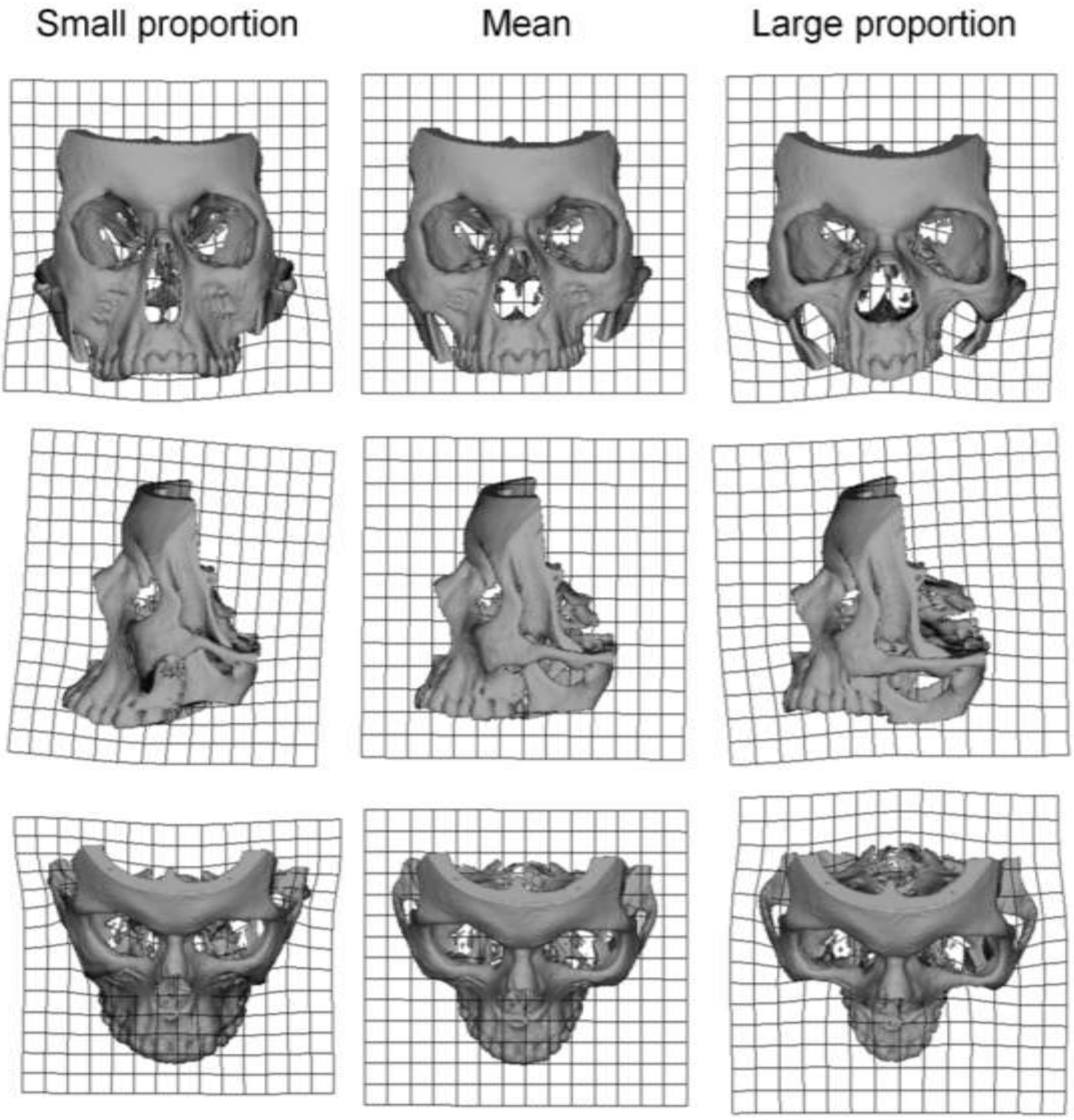

Figure 3.12. Association between face shape and temporalis muscle proportion. Warpings of facial shape on SW1. In individuals with large temporalis proportion, the maxilla is narrower and less prognathic than in individuals with a small temporalis proportion. In the mandible, the coronoid process is less prominent and in a low position in individuals with large temporalis proportion. Surface warpings have been magnified three times to improve visualisation.

3.4. Discussion

The present chapter comprises two studies assessing aspects of the relationship between skull shape and muscle force: (1) the predictability of muscle CSA from bony features, and (2) the association between skull shape and muscle CSA. The first study is needed in light of the uncertainties surrounding estimation of muscle area from bony proxies (Antón, 1994; Antón, 1999), which is common in biomechanical analyses of fossils or museum material (Demes and Creel, 1988; O'Connor et al., 2005; Wroe et al., 2010) and which needs to be done for the archaeological crania in Chapter 5 of this thesis. The second study assesses the association between muscle CSA and skull form. In part this is to investigate the possibility that cranial form might provide additional information relevant to estimating muscle CSA, but it is also an interesting topic of investigation in its own right.

The first study tested the hypothesis that there is no relationship between muscle CSAs, muscle areas estimated using bony features, and skull size. This hypothesis was falsified only for the correlation between temporalis CSA and area on bone (Table 3.3). The second study tested the hypothesis that there is no association between skull shape and masticatory muscle CSAs. None of the tested relationships falsified this null hypothesis after Bonferroni correction. Variations in temporalis muscle CSA with facial shape show the strongest association, significant as a single test but not overall. These findings are further discussed below.

The CSAs of jaw-masticatory muscles and their predictability from bony proxies and skull size

Average CSAs lie within the range of published data based on medical images (Weijs and Hillen, 1985b; Hannam and Wood, 1989; van Spronsen et al., 1989).

The findings of this study indicate that the relationship between muscle CSAs and areas estimated from bony proxies is weak and not significant except for the temporalis muscle. This might be due to the small sample size. Alternatively it might indicate that the use of bony proxies is not a reliable approach to estimating masticatory muscle CSAs in humans. This is in agreement with the findings of Antón (1994) who found a low correlation between masseter PCSA and the area estimated from bony proxies in cadavers. However, in the same study, the author found a low predictability of the temporalis PCSA from the antero-posterior length of the temporal fossa at the zygomatic arch.

There is also a weak relationship between skull size and both muscle CSA and muscle area. This is in agreement with Weijs and Hillen (1986); they found the highest correlations between CSAs and isolated facial metric traits rather than those related to general size.

Despite the degree of correlation, the comparison of means showed that both temporalis and masseter CSAs are largely overestimated by muscle areas estimated from bony proxies. Methodologically, the fact that this sample did not have a controlled degree of jaw-clenching may also explain the lack of correlation and overestimation of the masseter (Kiliaridis and Kälebo, 1991), which unlike the temporalis functions in an anatomical region with fewer surrounding structures (and is thus less constrained).

In conclusion, the results of this study suggest that, although the temporalis CSA correlates significantly with the area estimated using bony proxies, jaw-elevator muscle CSAs cannot be reliably estimated from them. Larger samples and the inclusion of the medial pterygoid muscles are desired to reach more conclusive results. The low predictability of muscle force from bony proxies calls for studies assessing the impact of variations in muscle force on mechanical analyses of fossils and archaeological material. This topic is addressed in Chapter 4 of this thesis.

Association between skull and face shape and muscle CSA

The second study of this chapter failed to show any significant association between skull or facial shape and muscle CSAs or proportional CSAs. This despite apparently significant associations for the single test of temporalis (Table 3.4). Indeed the RV coefficient suggests that temporalis CSA as a proportion of total CSA explains 7.5% of total skull and 9.5% of total facial variance. However, Bonferroni correction renders these associations insignificant. This means that a future study should examine a larger sample and probably carry out fewer, better targeted tests of association focusing on the temporalis.

Despite this lack of significance there is a weak relationship between temporalis muscle CSA and skull and face shape that is at least consistent with the anatomy of this muscle and the space required to accommodate it. Thus, among jaw-elevators, the temporalis muscle has the largest CSA (Weijs and Hillen, 1984), the longest fibres, the largest PCSA and the largest mass of contractile tissue (van Eijden et al., 1997). It therefore has the greatest potential impact on bone morphology by producing the highest strains at both mandibular insertion and bite points. The albeit insignificant association found in this study between temporalis CSA as a proportion of total masticatory muscle CSA and facial shape, namely that large temporalis proportions are associated with a relatively narrower, less prognathic, vertically shorter maxilla and vice versa, is in agreement with previous studies using linear morphometrics. Thus, Weijs and Hillen (1986) have also noted that temporalis and masseter CSA appear to be related to facial width. They also concluded that there is no general size effect ('large skull, large muscle') on muscle CSA (but see Figure 3.13 and Table 3.3 which suggest this may not be true; albeit weakly). With regard to the converse, that a relatively small temporalis CSA is associated with a vertically elongated skull, van Spronsen (2010) noted such an association and suggested by way of explanation that the muscles in long faced individuals show a lower intrinsic strength produced by a high proportion of slow-twitch type I muscle fibres.

In individuals with a large temporalis proportion, medio-lateral and antero-posterior enlargement of the inferior opening of the temporal fossa, as is suggested but not confirmed by this study, may provide space for a large temporalis muscle CSA. The low position of the coronoid process and consequent more vertical orientation of the temporalis has been suggested to increase mechanical efficiency in the human masticatory system in Nicholson and Harvati (2006). In the present study, the maxilla in individuals with a large temporalis proportion tends to narrow and shorten vertically. There are few and inconclusive studies addressing the mechanical impact of variations in maxillary width on masticatory mechanics. In women, a wide dental arch has been noted to be associated with a (medio-laterally) thicker masseter (Kiliaridis et al., 2003), whereas no relationship between bite force and dental arch width was found in pre-adolescents (Sonnesen and Bakke, 2005).

3.5. Conclusion

The present study has shown that, in general, there is a weak relationship between aspects of skull form and muscle force. The first hypothesis that there is no relationship between measured muscle CSA and the estimated values using bony proxies could not be falsified except for a significant correlation between temporalis CSA and its muscle area estimated from bony proxies. These findings are of significance for mechanical studies of the masticatory system in fossils or archaeological material where muscle force cannot be directly measured. They mean that bony proxies cannot be used to predict muscle CSAs with any reliability and that muscle areas on bone largely overestimate muscle CSAs but in an inconsistent way. This begs the question of the impact of errors in estimation of CSA. If FEA models simulating biting in human crania are very sensitive to applied muscle forces it may be imposible to carry out reliable FEAs where CSA is not known (i.e. in fossils or archaeological material). Sensitivity analyses are needed to assess this, and such analyses are the subject of the next chapter.

The second hypothesis was that there is no association between skull shape and muscle CSA. This was not falsified. Among all jaw-elevator muscles the proportion of temporalis CSA showed the strongest association with skull, and particularly, facial shape but this failed to reach statistical significance. Large temporalis proportions may be associated with a relatively narrower, less prognathic, vertically shorter maxilla and a low-set coronoid process but more targeted studies are required to confirm this.

Chapter 4 : The effects of varying jaw-elevator muscle forces on a finite element model of a human cranium

4.1. Introduction

Movement of the mandible during jaw closing depends on muscle action. Thus, muscle force is a parameter that has to be considered in any mechanical analysis of the human masticatory system. The fourth chapter of this thesis studies the effects of varying the relative force magnitudes among jaw-elevator muscles on a finite element model of a human cranium. This is relevant to understanding the effects of using estimates of muscle forces in cases where the actual information is not available as in fossils, museum material or living individuals without complete data on muscle CSAs or activations, such as in Chapter 5 of this thesis.

It is generally agreed that in simple terms, the human jaw functions as a lever (Hylander, 1975; Koolstra et al., 1988; Spencer, 1998) with the temporomandibular joint (TMJ) acting as a fulcrum, the bite point as the resistance and the muscle force as the load. The bite force is then the resultant of the muscle force magnitude and the morphology of muscle and bite lever arms. Finite element analysis (FEA) is often used to predict the mechanical response (deformation) of the skull to both muscle and bite forces. Stresses and strains are computed from the displacements of FE nodes to quantify local deformations. These parameters are then commonly investigated in relation to evolutionary (Strait et al., 2009; Wroe et al., 2010), developmental (Kupczik et al., 2009) and physiological or pathological processes and adaptations (Tanne et al., 1988; Gross et al., 2001; Koolstra and Tanaka, 2009).

Since a reliable FEA simulation depends on accurate geometry and boundary conditions (Fagan, 1992; Richmond et al., 2005; Kupczik, 2008), anatomically and functionally accurate models should, in theory, work better than simplified models. However, current methods for FE model construction cannot fully reproduce the details of skull morphology. Hence it is common to simplify anatomy, loads, and constraints. In many cases actual muscle forces, TMJ reaction forces, material properties of bone throughout the cranium, fasciae and other tissues are extremely difficult or impossible to obtain. Chapter 2 of this thesis focused on the validation of simplification approaches commonly used in anatomical reconstruction of cranial models. In Chapter 3, low to zero predictability of muscle force magnitude from bone anatomy was found. This means that in many cases where FEA might be applied key details of muscle forces cannot be estimated with any reliability. In consequence it becomes important to know how sensitive model performance is to variations in applied muscle forces. Thus, the present chapter aims to assess the effects of simplifying muscle forces and so, cranial loading conditions. Extreme variants of muscle loading were applied to an FE model of a human cranium and the effects on cranial deformation were assessed.

Many sensitivity analyses have been carried out in relation to cranial FEA of biting simulations in vertebrates. These have mainly focused in the effects of omitting soft tissues such as sutures and the periodontal ligament or on the effects of varying the mechanical properties of bone (Strait et al., 2005; Kupczik et al., 2007; Wood et al., 2011; Bright, 2012). Only two have assessed the effects of varying muscle parameters (Ross et al., 2005; Fitton et al., 2012).

The maximum contractile force of a muscle can be estimated using anatomical and chemical dissection methods for the measurement of muscle mass and fibre length to estimate muscle's physiological cross-sectional area (van Eijden et al., 1997; Antón, 1999). This method is impractical for ethical reasons in living, and impossible in fossil, humans. It is possible using human cadaveric material but the findings would be applicable only to a model of that individual. In living individuals, the cross-sectional areas (CSA) of jaw-elevator muscles obtained from medical images have been proposed as a reasonable estimator of the potential maximum force of pennate muscles (Weijs and Hillen, 1985a; Weijs and Hillen, 1986; Koolstra et al., 1988; van Spronsen et al., 1991).

The magnitude of force actually produced by a muscle during a certain task can be estimated using electromyography (EMG) to scale performance parameters, e.g. the maximum force that the muscle can produce (Manns et al., 1979; Reaz et al., 2006). This approach uses the EMG activity of a muscle generating maximum force to estimate the force produced during a sub-maximum bite by scaling according to the EMG activity recorded during the maximal bite (Hagberg et al., 1985; Ueda et al., 1998; Farella et al., 2009). When maximum muscle forces are calculated from muscle PCSAs, the EMG activity is used to scale the force magnitudes produced under a certain task (Ross et al., 2005). The EMG activity of masticatory muscles has a complex relationship with bite force as muscles shorten, although during isometric contraction a linear relationship can be generally found (Prum et al., 1978; Hagberg et al., 1985; Wang et al., 2000). Moreover, a relationship has been found between EMG activity and skull morphology (Miralles et al., 1991; Ueda et al., 1998; Farias Gomes et al., 2010), and activity and biting task (Stohler, 1986). In relation to biting tasks, a symmetric pattern of activation has been observed during maximum intercuspidation (Ferrario et al., 2000; Schindler et al., 2005), unilateral food crushing (Spencer, 1998) and isometric bites (van Eijden, 1990) but not during complete, consecutive mastication cycles (Stohler, 1986). Additionally, Farella et al. (2009) found changing patterns of muscle activation over time under maximum and sub-maximum sustained unilateral bites. The potential effects on FE models of the human cranium of varying muscle forces have not yet been explored, and this is of particular interest when actual muscle forces and activation patterns are not available such as in the studies of Chapter 5 of this thesis.

The following hypothesis was tested:

Hypothesis 1 (H1): varying the relative magnitudes of muscle forces during the same biting task has no effect on FEA results in terms of strain distribution and magnitudes, bite force, TMJ reaction force and large scale model deformation.

To test this hypothesis, several combinations of muscle forces representing different muscle activations were simulated while skull and muscle anatomy, tissue material properties and the kinematic constraints of the model were kept constant. It is to be expected from Hooke's law that local principal strains and large scale deformations will scale linearly (i.e. vary linearly in magnitude not mode of deformation) with applied load magnitude (O'Higgins and Milne, 2013). Thus the hypothesis is erected principally to investigate modes of deformation rather than magnitudes.

4. 2. Materials and Method

4.2.1. Sample

An FE model of the cranium of a male human aged 43, with full dentition, was used in this study. This model was built from the medical CT of a patient of the Teaching Hospital of the University of Chile (Hospital Clínico de la Universidad de Chile, Santiago de Chile) under their ethics protocol for the use of patient data. The images were taken in life for medical reasons before the beginning of this study using a Siemens 64-channel multidetector CT scanner equipped with a STRATON tube (Siemens Somatom Sensation 64, Siemens Healthcare, Erlangen, Germany). The CT was included in the sample used in Chapter 3 of this thesis. The primary reconstruction of images was performed using specialist program (Syngo Multimodality Workplace, Siemens Healthcare, Erlangen, Germany). Voxel size was 0.44 x 0.44 x 1 mm. The image stacks were exported for use in this study as DICOM files. The 3D skull morphology was reconstructed from the CT volume stack using Avizo (v.7.0.1, Visualization Sciences Group, Burlington, USA). Semi-automated segmentation of CTs based on grey level thresholds was used to separate bone from surrounding tissues and air. Manual segmentation was performed where needed. Craniofacial sinuses were preserved but cortical and cancellous bone were not segmented as distinct tissues, rather the bone was treated as a solid whole with the material properties of cortical bone; an approach justified by the results of Chapter 2.

4.2.2. Muscle forces

Static bites were simulated at the central incisors (I1) and at the left or right first molars (M1). The maximum muscle forces from the temporal, masseter and medial pterygoid muscles were estimated from their CSAs using the protocol explained in Chapter 3 and the formula Force = CSA x 37 N/cm^2, where the latter is the magnitude of intrinsic muscle strength for human masticatory muscles (Weijs and Hillen, 1985a; O'Connor et al., 2005). The values are presented in Table 4.1.

Table 4.1. Estimated values of CSA and maximum forces of jaw-elevator muscles.

Muscle	CSA (cm^2)		Muscle force (N)	
	Left	Right	Left	Right
Temporalis	4.54	4.61	168.02	170.67
Masseter	3.62	3.35	134.06	124.01
Medial Pterygoid	3.35	3.18	124.01	117.49

4.2.2.1. Muscle force variations

Before carrying out the assessment of the impact of different loading scenarios on FE model performance two sensitivity analyses were undertaken. In the first, the results of applying maximal forces based on estimated CSAs, which are asymmetric (Table 4.1), were compared with identical biting simulations using symmetric muscle forces (average of left and right applied to both sides). In the second, the strain maps resulting from bites on left and right M1 were assessed in order to check that bites on different sides produce results that are mirror images of each other.

To test H1, loadcases simulating different muscle activation levels for each bite point were made by scaling maximum muscle forces (Ross et al., 2005; Fitton et al., 2012). Since it is impractical to reproduce all possible combinations of muscle activations, three main patterns were used, based on EMG studies of individuals performing different biting tasks: bilaterally homogeneous activations during both symmetric and asymmetric bites (van Eijden, 1990; Spencer, 1998); asymmetric activations during unilateral tasks (Blanksma and van Eijden, 1995); and varying levels of muscle activition (among muscles) under both symmetric and asymmetric bites (Vitti and Basmajian, 1977; Moore et al., 1988; van Eijden, 1990; Blanksma and van Eijden, 1995; Farella et al., 2009).

Homogeneously activated muscles. Muscle force activations were simulated by simultaneously applying maximum forces scaled to 100%, 50% or 25% during both I1 and M1 bites.

Asymmetrically activated muscles. During M1 bites, each working side muscle is 100% activated. On the balancing side, the maximum forces of all muscles were to 75%, 50% or 25% activated.

Heterogeneously activated muscles. In simulated I1 biting, the maximum forces of the temporalis, masseter and medial pterygoid were bilaterally activated in the ratio of 50%:100%:100%, and then 25%:100%:100%. During unilateral M1 biting simulations, a constant recruitment of 50% for all balancing side muscle forces was used. Two separate sets of working side forces were applied in the following activation ratios: temporalis: masseter: medial pterygoid = 50%:100%:100% and 25%:100%:100%.

4.2.3. Finite element analyses

The volume data generated by CT segmentation were resampled to an isometric voxel size of 0.44 mm, exported as BMP stacks and converted into an FE mesh of 6,306,181 eight-noded cubic elements by direct voxel conversion. Based on the approach used in Chapter 2 of this thesis, fixed Young's moduli of 17 GPa for bone and 50 GPa for teeth were used, both with a Poisson's ratio of 0.3.

Each loaded model was kinematically constrained at the most anterior and superior parts of both mandibular fossae in the x, y and z axes. Vertical constraints on the incisal border of both I1 and on the occlusal face of left and right M1 were applied separately, simulating bite points. The choice of axes of constraint was based on prior experiments in which these constraints were reduced (e.g. TMJ constrained in x and y only) with the result that the model rotated when loaded. Thus the chosen constraints were the minimum required to fix the model in space. Left and right M1 bites were used to control for possible effects of asymmetries in bone morphology and muscle attachment. Muscle origins and insertions were reproduced in the model based on the original CT image in which muscles were clearly visible.

Loadcases 1 to 9 (homogeneously activated muscles). For each bite point the muscle forces were bilaterally scaled to 100%, 50% or 25%. Since maximum muscle forces were estimated from their CSAs and these are not necessarily symmetrical, for each of these loadcases, an additional loadcase was created using identical magnitudes of muscle forces on each side (the mean of left and right forces). This is relevant in cases where unilateral or left-right average reference values of maximum muscle force are used.

Loadcases 10 to 15 (asymmetrically activated muscles). Each M1 bite was simulated with 100% muscle force on the working side, and 75%, 50% or 25% on the balancing side.

Loadcases 16 and 17 (heterogeneously activated muscles). I1 bite with bilaterally applied muscle forces of 50% or 25% of the maximum temporalis force and 100% for the masseter and the medial pterygoid muscles.

Loadcases 18 to 21 (heterogeneously activated muscles). For each M1 bite the muscle forces applied on the balancing side were scaled to 50%. For the working side, a muscle force was used of 50% or 25% for the temporalis, and a 100% for the masseter and the medial pterygoid muscles.

Model pre- and postprocessing were performed using the custom FEA program VOX-FE (Fagan et al., 2007; Liu et al., 2012).

4.2.4. Comparison of mechanical performance among loadcases

To test H1 the following performance parameters were used: strain distribution and magnitudes, bite forces and TMJ reaction forces. Procrustes size and shape analysis was also undertaken, to compare large scale deformations among loadcases.

Strain distribution and magnitudes. These were assessed using strain contour plots, representing the spatial distribution of regions of high and low strains and their magnitudes.

Bite forces and TMJ reaction forces. Bite and TMJ reaction forces were calculated by summing the forces predicted by the FEA at each constrained node. Force magnitudes were plotted against applied muscle forces to assess the relationships between these variables.

Large scale model deformation. As in Chapter 2, the patterns of cranial deformation resulting from applied loads were assessed using Procrustes size and shape analyses based on a configuration of 51 craniofacial landmarks (listed in Table 4.2) representing the form of the cranium and facial structures normally strained during biting (Demes, 1987; Gross et al., 2001; Kupczik et al., 2009; Ross et al., 2011). The Procrustes size and shape analysis consists of rotation and translation but not scaling of the landmark coordinates of the original, unloaded cranium and the coordinates from the deformed, loaded crania, followed by principal components analysis (PCA) of the new coordinates (Fitton et al., 2012; O'Higgins et al., 2012). In order to assess the impact of zygomatic arch deflection on the analysis of large scale deformations the size and shape analysis was repeated using a subset of 43 landmarks, excluding those located in the zygomatic arch (ZAl, ZAm, pMassOr, midMassOr).

The analysis of large scale deformation was performed using the EVAN toolbox (v.1.62, www.evan-society.org).

Table 4.2. Landmarks used in the study of large scale cranial deformation. Zygomatic arch landmarks excluded are indicated by an asterisk (*).

No.	Symbol	Name	Definition
1	V	Vertex	Highest point on the calvarium.
2	N	Nasion	Intersection between frontonasal and internasal sutures.
3	ANS	Anterior Nasal Spine	Tip of the anterior nasal spine.
4	Pr	Prosthion	Most buccal and occlusal point of the interalveolar septum between central incisors.
5	Oc	Occiput	Most posterior point of the neurocranium.
6&20	SoT	Supraorbital Torus	Most anterior point of the supraorbital ridge.
7&21	InfO	Infraorbitale	Most inferior point of the infraorbital ridge.
8&22	NNot	Nasal Notch	Most lateral point of the nasal aperture.
9&23	M1	First Molar	Most buccal and mesial point of M1and alveolar process junction. If absent, the landmark is in the lowest most buccal point of the interalveolar septum between the second premolar and the next present molar.
10&24	LM	Last Molar	Last point of the dental arch, located at the most buccal and distal point on the last present molar and alveolar process junction.
11&25	ZM	Zygo-maxillar	Most inferior point of the zygo-maxillary suture.
12&26	FZ	Fronto-zygomatic	Most lateral point of the fronto-zygomatic suture.
13&27	FTZ	Fronto-temporal angle	Point at the intersection between frontal and temporal processes of the zygomatic bone.
14&28	ZAl	Lateral zygomatic Arch*	Most lateral point on the zygomatic arch.
15&29	ZRp	Zygomatic Root posterior	Most posterior-superior point of the intersection between the zygomatic root and the squama of temporal bone.
16&30	ZRa	Zygomatic Root anterior	Most anterior point of the intersection between the zygomatic root and the squama of temporal bone.
17&31	ZAm	Zygomatic Arch medial*	Most lateral point on the inner face of the zygomatic arch.
18&32	ItC	Infratemporal Crest	Most medial point of the infratemporal crest.
19&33	Eu	Eurion	Most lateral point of the neurocranium.
34&37	aTemOr	Anterior Temporalis origin	Most anterior point of origin of the temporal muscle on the temporal line.
35&38	sTemOr	Superior Temporalis origin	Most superior point of origin of the temporal muscle on the temporal line.
36&39	pTemOr	Posterior Temporalis origin	Most posterior point of origin of the temporal muscle on the temporal line.
40&43	aMassOr	Anterior Masseteric origin	Most anterior point of origin of the masseter muscle on the zygomatic arch.
41&44	pMassOr	Posterior Masseteric origin*	Most posterior point of origin of the masseter muscle on the zygomatic arch.
42&45	midMassOr	Mid-Masseteric origin*	Midpoint along the origin area of the masseter muscle on the zygomatic arch.
46&49	sPtOr	Superior Pterygoid origin	Most superior point of origin of medial pterygoid muscle on the pterygoid fossa.
47&50	iPtOr	Inferior Pterygoid origin	Most inferior point of origin of medial pterygoid muscle on the pterygoid fossa.
48&51	midPtOr	Mid-Pterygoid origin	Midpoint of the area of origin of the medial pterygoid muscle on the pterygoid fossa.

4.3. Results

Before considering the results in relation to H1 two small sensitivity analyses are reported. In the first, the results of applying maximum forces based on estimated CSAs, which are asymmetric (Table 4.1), are compared with identical biting simulations using identical left-right muscle forces (average of left and right applied to both sides). Compared to the loadcases based on the estimated maximum muscle forces, the perfectly symmetric loadcases predicted virtually identical strain distributions and magnitudes, bite forces and TMJ reaction forces, and large scale deformation (see below). In the second sensitivity analysis, bites on left and right M1 resulted in strain contour maps that are almost perfect mirror images of each other. As such, only the strain distribution and magnitudes under left M1 bites are considered further.

The results are presented below.

4.3.1. Strain distribution and magnitudes

For each simulated bite the strain contour maps arising from different loadcases show differences in strain magnitudes and much less so in distribution. Thus where strains are predicted to be relatively high or low differs little among simulations but the average strain magnitude does differ.

The highest strains are found in the regions of masseter and medial pterygoid attachment, and in the facial regions close to the bite point. That is, the maxillary bone at the nasal notch and the frontal process during incisor bites, and the zygomatic and frontal process of the maxilla during molar bites.

During I1 biting simulations, strains decrease from maximum values of >200 $\mu\varepsilon$ to 100-200 $\mu\varepsilon$ in the face, zygomatic arch and mandibular fossae as the magnitude of total applied muscle force decreases. However, their distribution hardly varies, irrespective of the pattern of muscle activation (Figure 4.1). The same situation occurs in the face during unilateral M1 bites. However, in the mandibular fossa the strain magnitudes differ in the relationship between left and right magnitudes among loadcases. The loadcases with more symmetric total muscle forces, i.e. loadcases 4 to 9 and 18 to 21, predict the highest strains over the mandibular fossa of the balancing side relative to the working side (e.g. in loadcase 4 strains in the fossae exceed 200 με and are larger on the balancing than on the working side; Figure 4.2). This pattern is inverted during the most markedly asymmetric activation patterns (loadcases 11, 12, 14 and 15; Figure 4.2). Thus, during the most asymmetric muscle activation pattern (loadcases 12 and 15), the mandibular fossa of the working side shows a larger area reaching strains over 200 με than the balancing side fossa where most of strains are ~150 με (Figure 4.2).

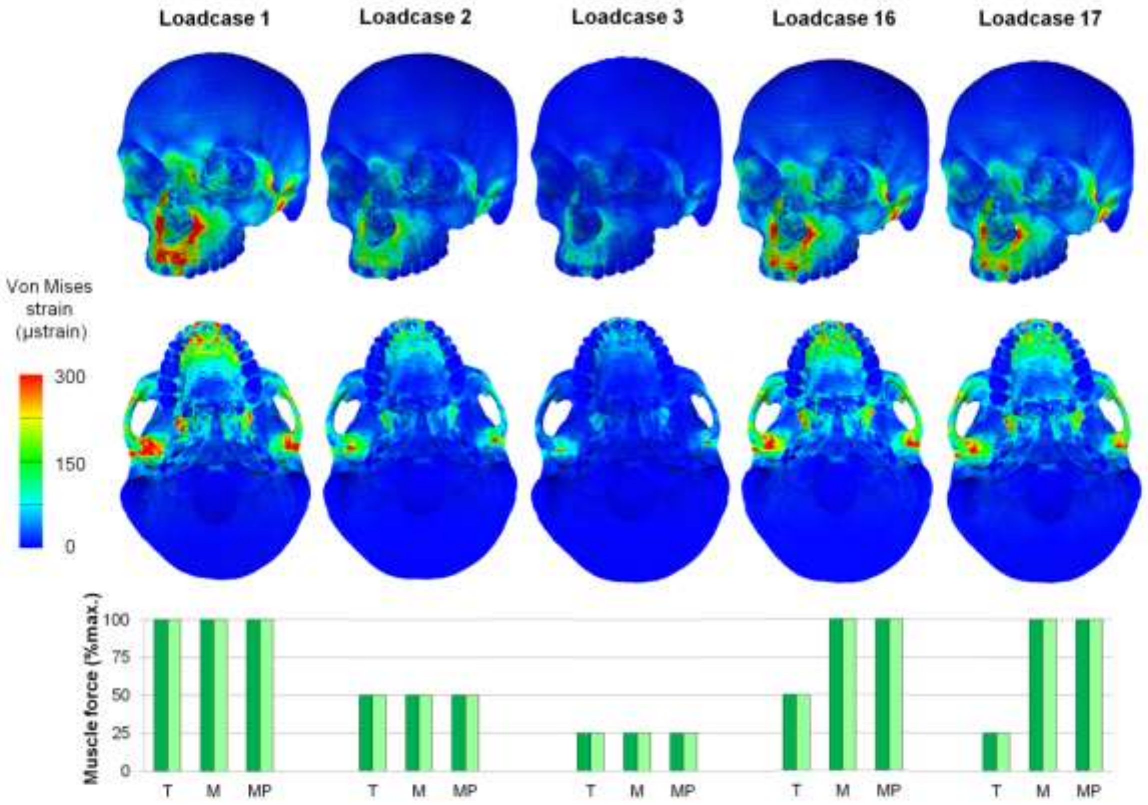

Figure 4.1. Strain contour plots from I1 biting simulations. Loadcases 1, 2 and 3 correspond to homogeneously activated muscles Loadcases 16 and 17 correspond to lower levels of activation of the temporalis (T) compared to masseter (M) and medial pterygoid (MP) muscles. Plots representing the levels of muscle activation of each loadcase are shown: working side, dark green bars; balancing side, light greenbars.

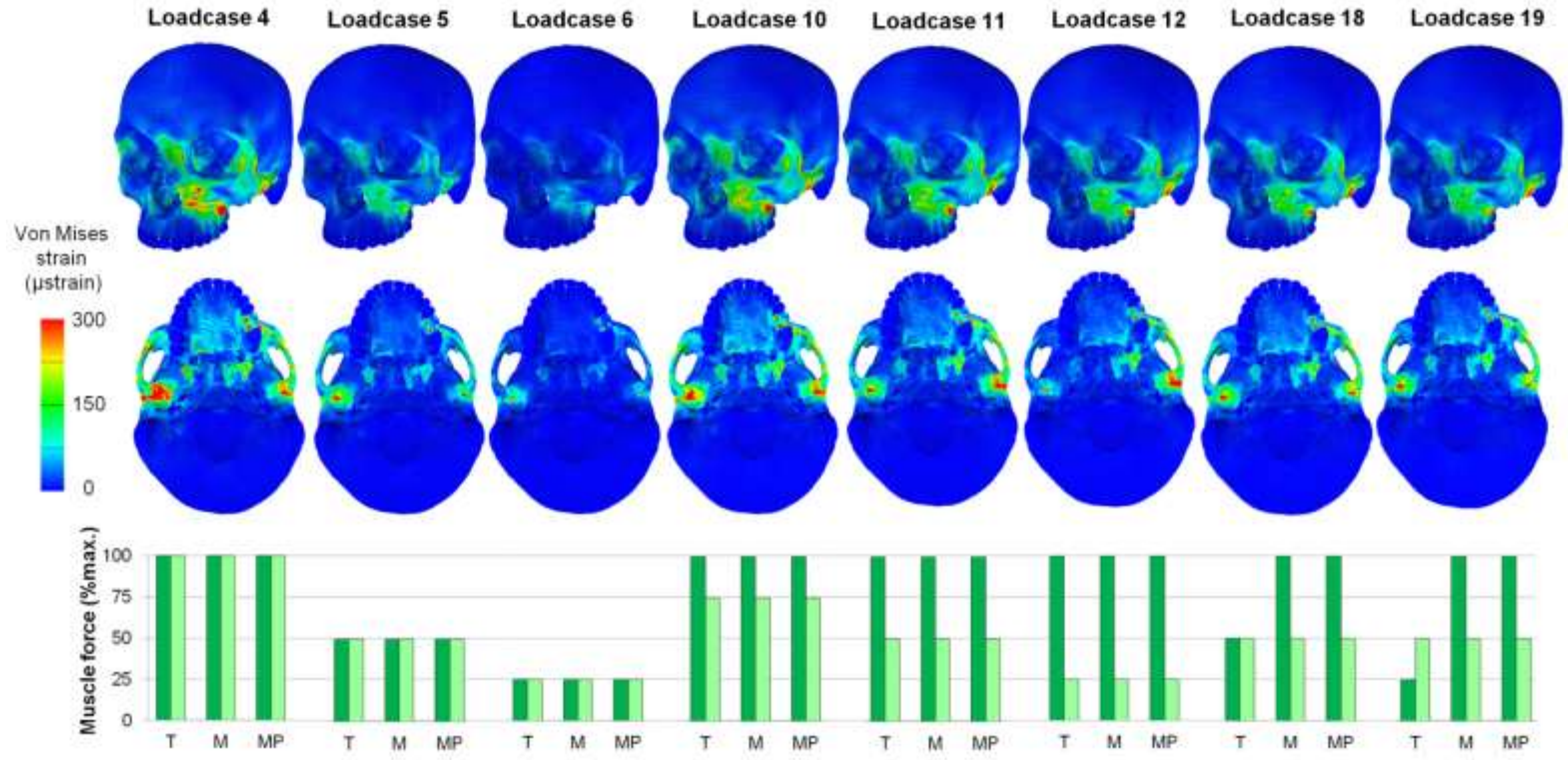

Figure 4.2. Strain contour plots from simulated left M1 bites with different loadcases. Loadcases 4, 5 and 6 correspond to homogeneously activated muscles. Loadcases 10, 11 and 12 correspond to asymmetrically activated muscles. Loadcases 18 and 19 correspond to heterogeneously activated muscles, with temporalis (T) activated to lesser degree than masseter (M) and medial pterygoid (MP) muscles on the working side. Plots representing the levels of muscle activation of each loadcase are shown: working side, dark green bars; balancing side, light green bars.

4.3.2. Bite force and TMJ reaction force

Predicted bite forces and TMJ reaction forces (Table 4.3) are consistent with the results depicted by the strain contour plots. In general, bite force and TMJ reaction forces increase in proportion with total applied muscle force, particularly during I1 bites (loadcases 1 to 3, 16 and 17; Figures 4.3a and 4.5a). During M1 bites, TMJ reaction force is higher on the balancing side than the working side with homogeneously activated muscles (loadcases 4 to 9; Figure 4.3b and c). In contrast, asymmetric (10 to 15; Figure 4.4) and heterogeneously activated loadcases (18 to 21; Figure 4.5b and c) predict lower TMJ forces on the balancing than the working side. This was especially marked with the most asymmetric loadcases (11, 12, 14 and 15; Figure 4.4)

Table 4.3. Bite forces and TMJ reaction forces from different loadcases. S=loadcases with symmetrical, averaged left-right muscle forces, W=working, B=balancing L=left, R=right, T=temporalis, M&MP=masseter and medial pterygoid muscles. The TMJ reaction forces from the working side are marked with an asterisk (*).

Loadcase	Bite point	W / B side muscle activation	Bite force (N)	TMJ reaction force (N)	
				L-TMJ	R-TMJ
Loadcase 1	L- and R-I1	100%	234.29	218.76	254.22
Loadcase 1S	L- and R-I1	100%	234.18	215.39	257.34
Loadcase 2	L- and R-I1	50%	117.15	109.38	127.10
Loadcase 2S	L- and R-I1	50%	117.13	107.22	129.05
Loadcase 3	L- and R-I1	25%	58.60	54.67	63.59
Loadcase 3S	L- and R-I1	25%	58.59	53.60	64.57
Loadcase 4	L-M1	100%	358.91	87.77*	277.53
Loadcase 4S	L-M1	100%	358.75	86.49*	281.12
Loadcase 5	L-M1	50%	179.44	43.89*	138.75
Loadcase 5S	L-M1	50%	179.37	43.25*	140.56
Loadcase 6	L-M1	25%	89.72	21.95*	69.39
Loadcase 6S	L-M1	25%	89.69	21.63*	70.29
Loadcase 7	R-M1	100%	355.09	242.91	128.81*
Loadcase 7S	R-M1	100%	355.03	238.92	130.42*
Loadcase 8	R-M1	50%	177.58	121.48	64.42*
Loadcase 8S	R-M1	50%	177.56	119.48	65.23*
Loadcase 9	R-M1	25%	88.56	61.01	32.36*
Loadcase 9S	R-M1	25%	88.50	60.09	32.83*
Loadcase 10	L-M1	100% / 75%	315.84	110.69*	205.81
Loadcase 11	L-M1	100% / 50%	272.73	135.96*	135.74
Loadcase 12	L-M1	100% / 25%	229.61	162.43*	72.56
Loadcase 13	R-M1	100% / 75%	309.76	174.33	145.76*
Loadcase 14	R-M1	100% / 50%	264.27	106.15	166.17*
Loadcase 15	R-M1	100% / 25%	220.05	39.99	187.86*
Loadcase 16	L- and R-I1	50% (T), 100% (M&MP)	188.74	176.31	195.99
Loadcase 17	L- and R-I1	25% (T), 100% (M&MP)	165.90	161.85	170.76
Loadcase 18	L-M1	50% (T), 100% (M&MP) / 50%	237.59	83.94*	146.09
Loadcase 19	L-M1	25% (T), 100% (M&MP) / 50%	219.99	72.50*	151.36
Loadcase 20	R-M1	50% (T), 100% (M&MP) / 50%	230.02	120.51	102.51*
Loadcase 21	R-M1	25% (T), 100% (M&MP) / 50%	212.79	127.75	77.85*

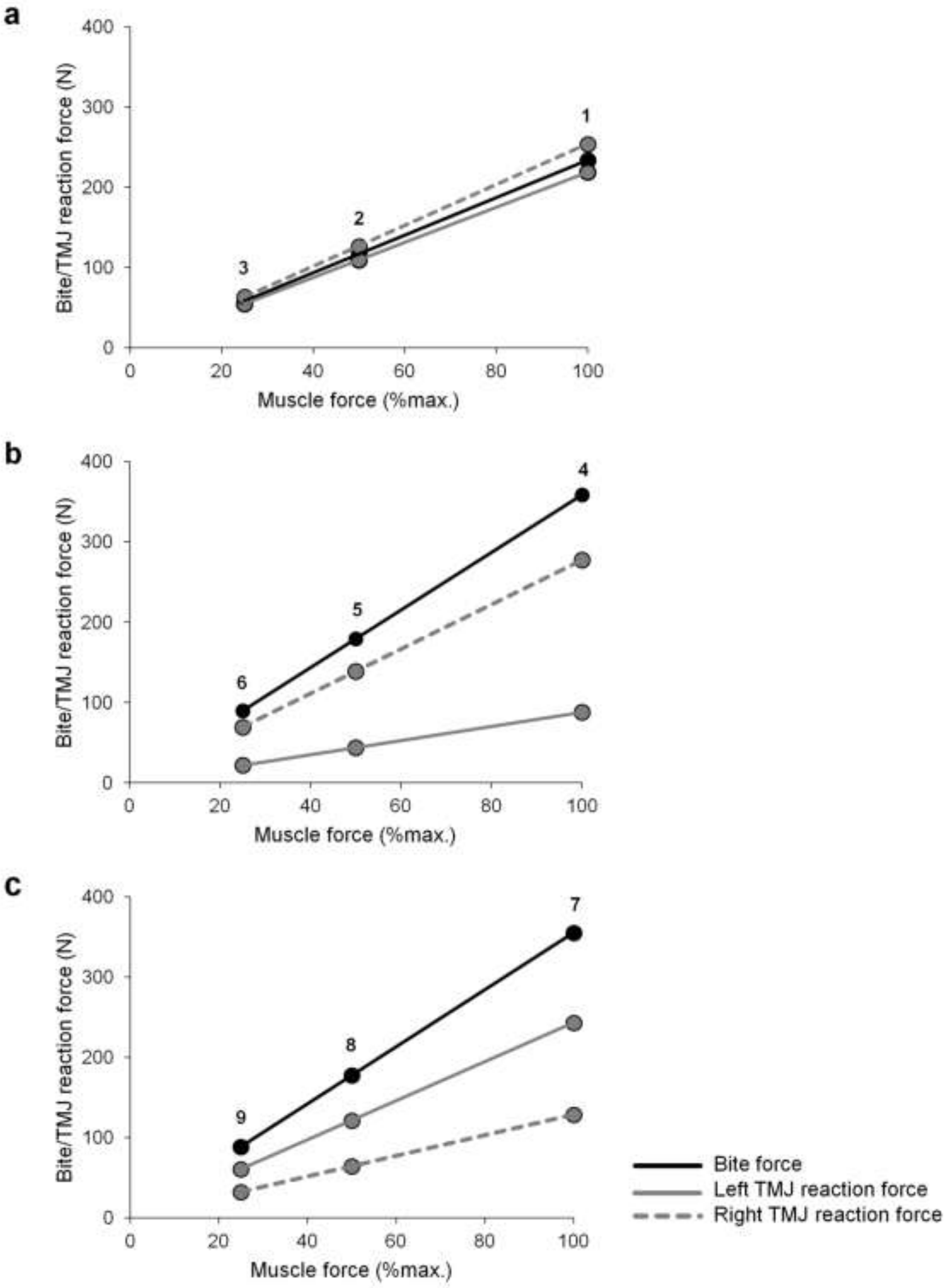

Figure 4.3. Bite forces and TMJ reaction forces in loadcases simulating homogeneously activated muscles. Loadcase number is shown in bold. (a) I1 bites, (b) left M1 bites (working side=left), and (c) right M1 bites (working side=right).

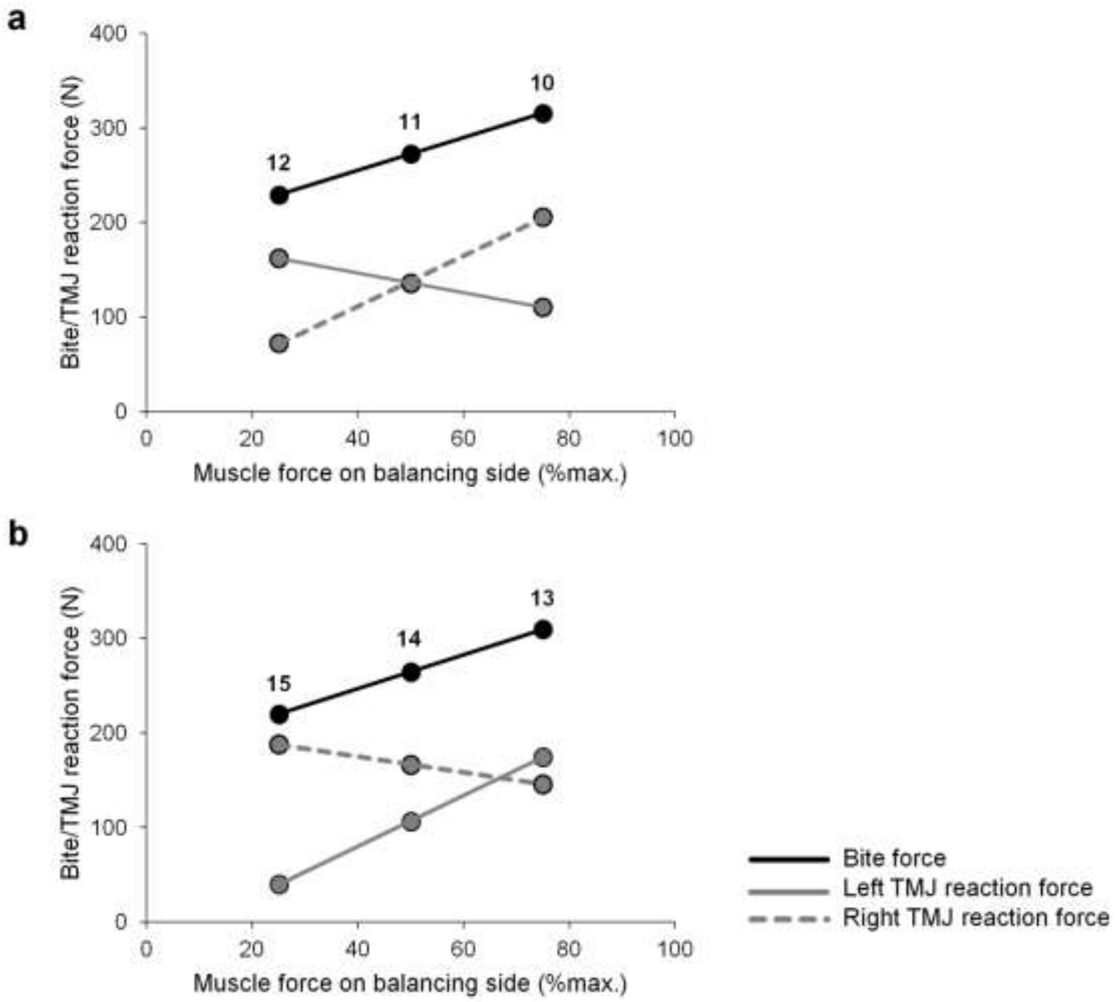

Figure 4.4. Bite forces and TMJ reaction forces in loadcases simulating asymmetrically activated muscles. Loadcase number is shown in bold. (a) Left M1 bite (working side=left), (b) right M1 bite (working side=right).

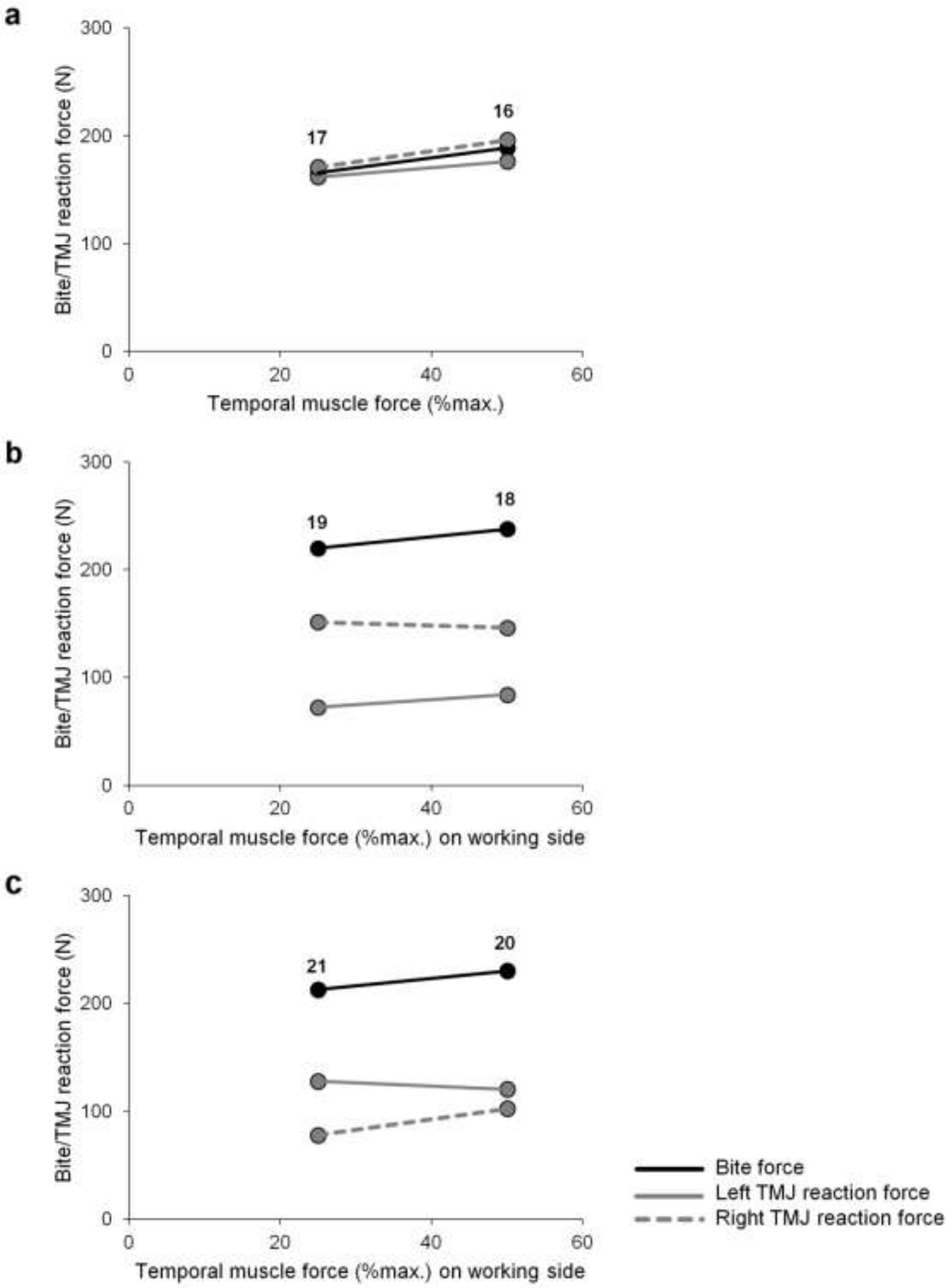

Figure 4.5. Bite forces and TMJ reaction forces in loadcases simulating heterogeneously activated muscles. Loadcase number is shown in bold. (a) I1 bites, (b) left M1 bites (working side=left), and (c) right M1 bites (working side=right).

4.3.3. Large scale deformation

The Procrustes size and shape PCAs of cranial deformations resulting from FEA distinguished three different vectors of deformation, one for each bite point. These are represented as lines connecting the unloaded model and the loadcases for each bite point (Figure 4.6). Differences in loadcase have a very small effect compared to the differences due to changes in bite point.

The vectors connecting the unloaded and molar biting simulations are almost symmetrically disposed about the vectors representing incisor bites (Figure 4.6). Thus the large scale deformations arising from left and right M1 bites are almost mirror images of each other, The asymmetry of deformation reflects asymmetry of form. These findings reflect the symmetries and asymmetries of the strain contour maps of mentioned earlier.

The largest degrees of deformation (distances between unloaded and loaded models in the plot) are achieved when muscles are activated homogeneously and maximally, irrespective of the bite point. In both I1 and M1 bites the greatest relative deformations are of the alveolar process near the bite point. With incisor bites the lower face is dorso-ventrally deflected with respect to the upper face and neurocranium. With M1 bites the face undergoes torsion and local deformation above the bite point. The vectors of deformation for the symmetric muscle forces with different activation levels scale exactly in proportion to applied force. As noted earlier, loadcases created using perfectly symmetric muscle forces (left and right average) deform along almost identical vectors as models using their estimated asymmetric force magnitudes (Figure 4.6).

The loadcases simulating asymmetric and heterogeneous muscle activations result in deformations that are different from the homogeneously activated loadcases. However, the vectors for the different muscle loadcases applied to each bite point closely group (Figure 4.6). This indicates small effects in terms of vector direction due to variations in loading relative to the differences due to different bite points. The omission of zygomatic arch landmarks has a small effect on the PCA of FEA results. The main effect is that the vectors from all muscle activation patterns more nearly overlap (Figure 4.7). This indicates that deformations of the zygomatic arch accounted for a substantial portion of the divergences between vectors representing the same bite point in Figure 4.6.

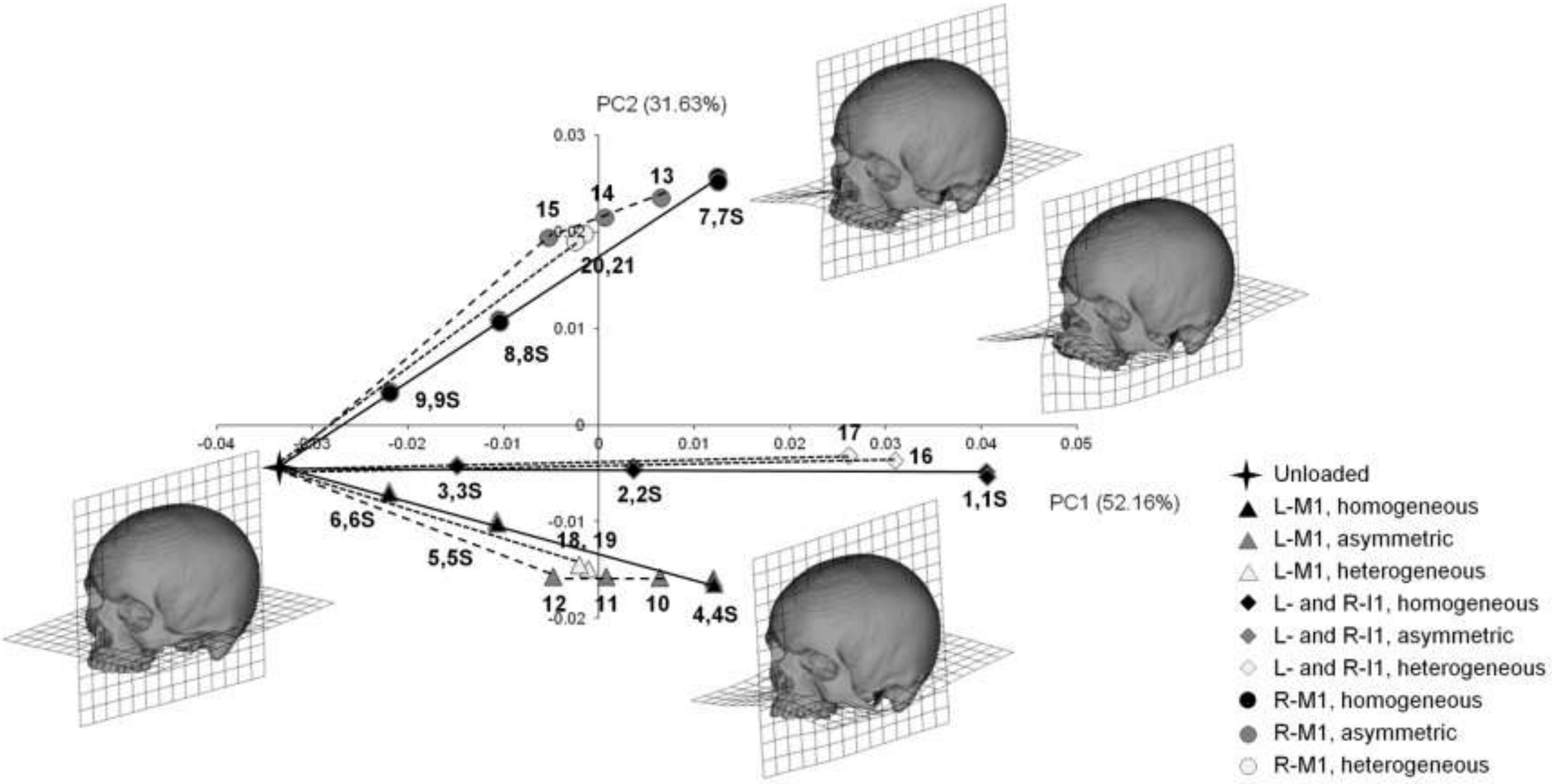

Figure 4.6. Principal components analysis of 51 cranial landmarks on the unloaded model and the same model loaded with different muscle activations. The lines represent the vectors of deformation under each loading regimen. Loadcase numbers are shown in bold. L=left and R=right. The largest deformation for each bite point is shown, magnified 1000 times to improve visualisation.

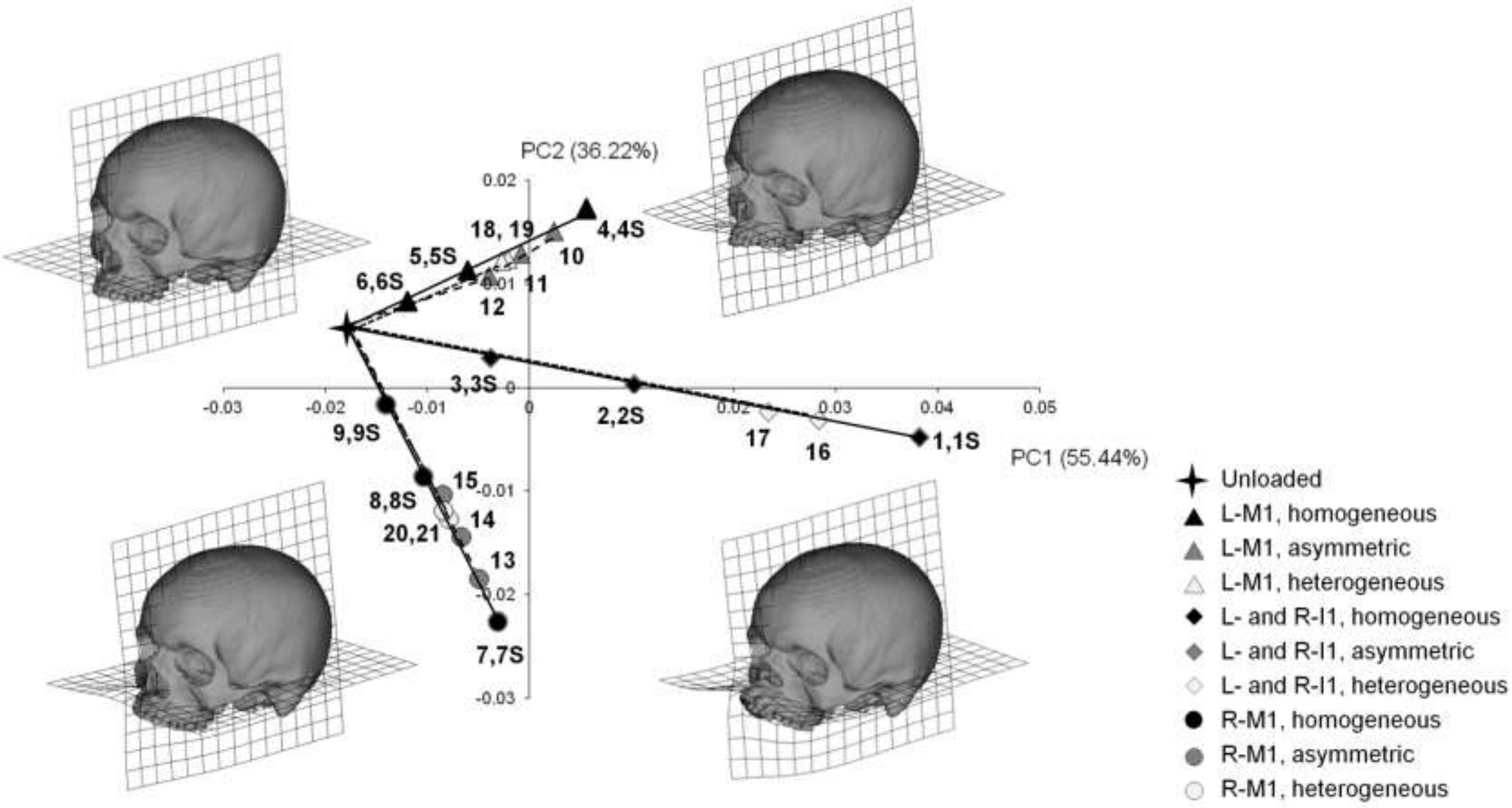

Figure 4.7. Principal components analysis of 43 cranial landmarks on the unloaded model and the same model loaded with different muscle activations. Zygomatic arch landmarks have been omitted. The lines represent the vectors of deformation under each loading regimen. Loadcase numbers are shown in bold. L=left and R=right. The largest deformation for each bite point is shown, magnified 1000 times to improve visualisation.

4.4. Discussion

The present study assessed the effects on FE model performance of varying muscle activations during simulated static incisor and molar bites. This is important because muscle forces are rarely known with any precision and so, simplified or estimated loadings are often applied. Thus maximal muscle forces might be estimated from bony proxies (but see previous chapter for issues in estimation) or by reference to values in the literature. Forces might be applied using 100% maximum activation of all muscles or some more complex muscle activation pattern. The study of this chapter aimed to assess the sensitivity of some aspects of model performance to such variations in muscle activations. The findings are of significance in interpreting the results of the comparative FEAs presented in the next chapter.

The study aimed to test the hypothesis that there is no effect of varying the relative magnitudes of muscle forces during the same biting task on FEA results in terms of strain distribution and magnitude, bite force, TMJ reaction force and large scale model deformation. This hypothesis was not falsified; at least the effects of varying muscle activation pattern are very small everywhere except in the zygomatic arch and the effects of varying magnitudes is to diminish deformation magnitudes. The latter is to be expected in an elastic material. Bite and TMJ reaction force also scale with muscle force.

These results are further discussed below.

Strain distribution and magnitude

Strains are greatest during all simulations in the face in the vicinity of the bite point and where the masseter and medial pterygoid attach. Temporalis, in having a very large attachment area to the large, stiff cranium, does not produce large strains over the vault when it contracts. Thus the major changes in strain maps between muscle activation patterns occur in the regions of the masseter and medial pterygoid attachments.

The results of this study indicate that the greatest impact on facial strains arises because of variations in the total applied muscle force. As expected, strain magnitudes (Figures 4.1 and 4.2) show an approximately linear relationship to total applied muscle force. This is in agreement with the results of Ross et al. (2005) and Fitton et al. (2012) in macaque models and expected as mentioned in the introduction of this chapter.

Varying activation pattern has a small impact on strain distribution. Principally this affects the regions local to the masseter muscle attachment site, causing strains to disproportionately vary in this region according to the force of masseter contraction. This finding of consistent strain distribution under different muscle loading regimens opens up the possibility of performing reliable FEAs of the human cranium using simplified muscle activations; e.g. symmetrical maximum muscle forces. Estimates of these forces can often be obtained from the literature, be estimated for each individual from muscle CSA or even from bony proxies. It is worth to remember that Chapter 3 showed that the last method of estimation is likely to be inaccurate. This inaccuracy will have major impact on strain magnitudes but not on relative facial strains. Thus, if relative rather than absolute strains are of interest, reasonable muscle activation patterns all produce approximately similar results.

The present study varied relative force magnitudes but not muscle orientations because in the present sample, as well as in the different chapters of this thesis, the mandible was present and so muscle attachments to it, and force vectors, are known. Each muscle was considered to have a single vector of action. This was a necessary simplification given the resolution of the CT images; the finer details of muscle anatomy and fibre directions are unknown. It is worth noting in this regard that subdividing e.g. the masseter into different parts with different vectors may introduce significant errors in estimation of the principal vector of muscle action (Röhrle and Pullan, 2007). The effect of varying the directions of muscle force vectors is worth exploring in future studies, especially where only the cranium is available and the position of mandibular muscle insertions has to be estimated.

Bite force and TMJ reaction force

As with strain magnitudes, predicted bite force is, as expected, proportional to total applied muscle force (Table 4.3). The same occurs in TMJ reaction forces during I1 bites. During I1 biting, small asymmetries in TMJ reaction forces can be observed, which is expected given the bilateral asymmetry normally found in skulls.

Temporomandibular joint loading is an important parameter of human masticatory function; an altered load distribution during mastication may result in dysfunction due to morphological changes and an inflammatory response in the articular tissues (McNamara, 1975; Tanaka et al., 2008; Barton, 2012). Temporomandibular joint loading in humans is difficult to estimate due to the impracticability of using direct methods and also because the mathematical models used to predict it have been shown to be highly sensitive to variations in muscle parameters (Throckmorton, 1985; Koolstra et al., 1988). Today, it is generally acknowledged that during unilateral bites the TMJ of the balancing side is more loaded than that of working side (Hylander, 1975; Throckmorton and Throckmorton, 1985; Koolstra and van Eijden, 2005). In this study such differences in loading between working and balancing sides is achieved during symmetric or close to symmetric muscle activations. However, under unilateral bites greater asymmetry (irrespective of heterogeneity) in muscle activations reverses the relationship between TMJ reaction forces at the working and balancing sides (Figure 4.3).

Considering these results, symmetrical maximum muscle forces appear to be a reasonable simplification approach in FEAs of the human cranium when bite force and TMJ reaction force are parameters of interest. The sensitivity of TMJ reaction forces in the FE model to asymmetries in muscle activations calls for further investigation using e.g. multibody dynamic approaches (Curtis, 2011) to better understand the reversal of TMJ reaction forces under asymmetric muscle activations.

Large scale model deformation

As with predicted strains and bite forces, varying muscle activations produces mainly differences in the magnitude rather than mode of large scale model deformation within each bite point. This magnitude relates to the total applied muscle force. This reflects the linear relationship between load and deformation in most elastic materials (as assigned to bone), and is consistent with the findings of O'Higgins and Milne (2013) in femora.

That asymmetric muscle activations principally impact on zygomatic arch deformation is consistent with the findings of (Fitton et al., 2012) who also noted that varying muscle activations mainly led to differences in zygomatic arch deformation. Principally this affects the regions local to the masseter muscle attachment site; ignoring zygomatic landmarks results in vectors of deformation that closely overlap for each bite point, irrespective of muscle activation pattern. This begs the question of whether or not arch deformation is physiological or merely a reflection of inadequate representation of the temporal fascia (Curtis et al., 2011). The present study is uninformative in this regard but for now, it seems sensible to treat the deformation of the arch during biting simulations with caution.

The relationship between variations in muscle force and cranial physiology

The relatively low sensitivity of cranial deformation mode to varying muscle forces may be relevant in understanding how the growing face copes and responds to ontogenetic changes in muscle proportions and lever mechanics. Thus, during ontogeny, cranial bones change their sizes, shapes and relative positions among structures and so bones impact on muscles and TMJs by changing lever arms. However, despite the differences in developmental timing among skull regions (Bastir et al., 2006), a generally consistent vector of ontogenetic shape change is maintained (Strand Viðarsdóttir et al., 2002).

It might be that ontogenetic variations in muscle action and force have a similar lack of impact on strain distribution as it has been observed here when muscle activations are varied. This relative invariance in the relative position of high and low strains could partially explain invariance of ontogenetic shape trajectories and so point to a mechanism whereby the growing cranium is relatively unperturbed by ontogenetic variations in muscle size and action (and so lever arms).

This is also consistent with the mechanical and kinematic redundancy of mammalian mastication noted by several authors (Herring, 1985; van Eijden, 1990; Langenbach and van Eijden, 2001), whereby similar bite forces and bites can be achieved using varying muscle activations. Thus the masticatory system appears to maintain its function in the face of significant perturbations of muscular forces and this may underlie the consistency of craniofacial growth.

4.5. Conclusion

The results of this study show that the main effect on the FE model of a human cranium of varying relative magnitudes of applied muscle forces during biting concerns the scaling of deformation and bite force with total applied muscle force. Varying relative muscle activations has a much smaller effect, principally impacting on the deformation of the zygomatic arch, where masseter attaches. The TMJ reaction forces seem to be sensitive to symmetry of loading of the masticatory system

The hypothesis that varying the relative magnitudes of muscle forces during the same biting task has no effect on FEA results in terms of strain distribution and magnitudes, bite forces, TMJ reaction forces and large scale model deformation was largely not falsified, the exception being relative left and right TMJ reaction forces.

Considering these findings, when relative strain magnitudes among cranial regions are the focus of interest, the use of symmetric maximum muscle forces is a reasonable loading simplification. The total magnitude of applied muscle forces relates to absolute strain and bite force magnitudes. This needs to be borne in mind when comparing principal strain magnitudes and bite forces among models. The results of this study are of relevance in the design of the comparative FEA analyses of the next chapter of this thesis.

Chapter 5 : The relationship between cranial form and masticatory system performance parameters

5.1. Introduction

The previous chapters of this thesis used validation and sensitivity analyses to provide data on how to construct finite element models of the human cranium. Based on what was learnt, the present chapter uses the finite element method to address the biological question driving this thesis: what is the relationship between cranial form and masticatory function?

To assess this, the present study examines local and global deformations (bone strains and Procrustes size and shape analyses) and bite forces among modern and archaeological, artificially deformed crania during simulated biting using finite element analysis (FEA). Finite element analysis is an engineering technique that predicts the mechanical performance of a structure under loads in terms of deformation, stress and strain (Richmond et al., 2005; Zienkiewicz et al., 2005; Rayfield, 2007). This technique has become increasingly used to study the functional consequences of morphological variation in primate development (Kupczik et al., 2009) and evolution (Strait et al., 2009; Wroe et al., 2010; Gröning et al., 2011b). In modern humans, FEA has been used to study the mechanical behaviour of different components of the masticatory system during biting (Gross et al., 2001; Röhrle and Pullan, 2007; Koolstra and Tanaka, 2009). (Jansen van Rensburg et al., 2012) compared the FEA results from two models of the human cranium, one more prognathic than the other, generated using a generic mesh modified to match each cranium through warping (i.e. non-rigid registration). However, no comparative studies using FEA among a series of modern humans have been performed to date.

Thus, the aim of this study is to assess the relationship between cranial form and the mechanical performance of morphologically diverse human crania. The sample varied in the form of both the neurocranium and the face. Form variation can impact bone mechanics in different ways. Different morphologies can show different cross-sectional bone anatomies and hence differ in their resistance to bending (Rubin, 1984; Demes, 1987). Additionally, the relative positions of the jaws, teeth and temporomandibular joints (TMJ) vary among individuals, producing variations in masticatory system lever arms (Spencer, 1998; O'Connor et al., 2005). In the present study, mechanical performance during central incisor (I1) and first molar (M1) bites was compared among morphologically different crania in terms of strain distribution (i.e. the relative location of high and low strains), magnitudes, bite forces and large scale deformations. The central hypothesis is that there is no relationship between cranial form and masticatory system performance parameters.

This central hypothesis was tested using three different loading scenarios of which the specific hypotheses are:

Hypothesis 1 (H1): there are no differences in strain distribution and magnitudes, bite forces, TMJ reaction forces and large scale deformations among models loaded with maximum muscle forces estimated from their individual anatomies (CT scans for living and bony proxies for archaeological individuals).

Hypothesis 2 (H2): there are no differences in strain distribution and magnitudes, bite forces, TMJ reaction forces and large scale deformations among models loaded with identical muscle force magnitudes.

Hypothesis 3 (H3): there are no differences in strain distributions and magnitudes, and large scale deformations among models exerting the same bite force magnitudes.

The intentionally deformed crania used here provide an interesting model to study the relationship between form variation and masticatory function in humans. Intentional cranial deformation dramatically alters neurocranial morphology and also affects facial morphology (Antón, 1989; Kohn et al., 1993; Manríquez et al., 2006; Khonsari et al., 2013). However, there is no evidence that the facial changes affect dental occlusion (Cheverud and Midkiff, 1992; Jimenez et al., 2012); thus function may well be maintained despite the artificially induced alterations of form.

5.2. Materials and Method

5.2.1. Sample

The CTs of six adults were used in this study. Two of them correspond to artificially deformed crania from a pre-Hispanic population of northern Chile. The remaining four come from the sample of modern Chilean individuals used in Chapter 3.

5.2.2.1. Deformed individuals

These crania were selected because of the presence of extreme deformations. These were produced intentionally by the prolonged use of deforming device in the newborn's skull to modify the main vectors of cranial development (Manríquez et al., 2006; Perez, 2007). Previous studies have defined two main deformation patterns: fronto-occipital or antero-posterior and annular (Antón, 1989; Frieß and Baylac, 2003). These are equivalent to crania whose deformation is termed erect and oblique by Manríquez et al. (2006) in a geometric morphometric-based study of a geographically similar sample. For this thesis, two individuals showing each of these deformation types were selected (Figure 5.1):

Deformed oblique. This corresponds to individual L8F1E1 of the collection housed in the archaeological laboratory of the Corporation of Culture and Tourism (Laboratorio Arqueológico Corporación de Cultura y Turismo) of Calama City, Chile. Based on morphoscopic bioanthropological diagnosis of skeletal remains it has been previously sexed as a woman. It was recovered from the cemetery Regimiento Chorrillos (Calama, Chile). Via radiocarbon dating of other anthropological material as well as relative dating, the site was dated around 800 to 200 years BC, a chronological period known as the Formative (Hidalgo et al., 1989; González and Westfall, 2006). This skull possesses full dentition and shows some loss of enamel over the upper incisors.

Deformed erect. This corresponds to individual 31401 from the same collection as the individual above and it was sexed as female using the same criteria. It was recovered from the site of Lasana (Calama, Chile) and dated between the Twelfth and the Fifteenth Centuries A.D. based on relative dating (qualitative assessment of related pottery), this chronological period is known as the Late Intermediary (Hidalgo et al., 1989). This skull suffered post-mortem loss of the upper anterior teeth.

Figure 5.1. Anatomical features of the deformed individuals. Anterior, lateral and inferior views of the CT surfaces of the individuals showing (a) oblique deformation and (b) erect deformation.

5.2.2.2. Individuals within the range of normal morphological variation

For the purposes of this study, rather than include all 20 modern Chilean crania from Chapter 3 in FEA simulations, the four individuals who show the most extreme differences in terms of the first two principal components of shape (Figure 5.2) were selected. This greatly reduces the number of FE models to be built and loaded while accounting for the key modes of variation in the wider sample. These individuals (one woman and three men; Table 5.2) present variations in size and in the degrees to which their faces are vertically elongated or wide and their maxillae are prognathic. Such variations are frequently present in human populations (Bhat and Enlow, 1985).

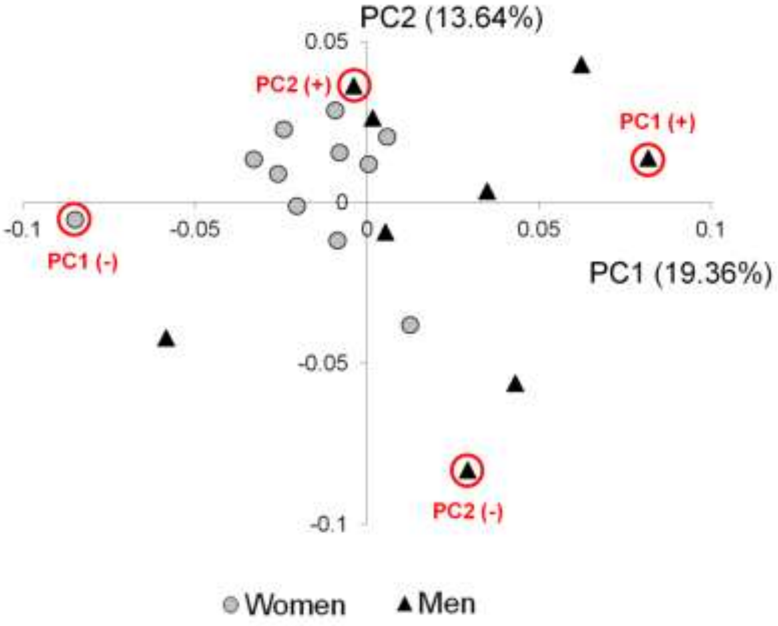

Figure 5.2. Principal component 1 vs. PC2 of shape for the sample in Chapter 3. The red circles show the individuals representing the most extreme variations in shape, who were selected for the present study.

The CTs of the deformed crania were acquired at a private clinic (Centro Médico Resonancia Magnética, Santiago de Chile) in a Philips 16-slice multidetector CT scanner equipped with an MRC tube (Brilliance CT 16-slice, Philips Healthcare, Andover, MA, USA). Voxel size was 0.39 x 0.39 x 0.75 mm. Primary image reconstruction was performed using a specialist system (Brilliance Workspace, Philips Healthcare, Andover, MA, USA). The CTs of the undeformed group were acquired for medical reasons unrelated to this study at the Teaching Hospital of the University of Chile (Hospital Clínico de la Universidad de Chile, Santiago de Chile) and provided under their ethical protocol for the use of patient data. Details of data acquisition are explained in Chapter 3. Average voxel size was 0.43 x 0.43 x 1 mm.

The CT image stacks were exported for their use in this study as DICOM files. The 3D cranial morphologies were reconstructed from the image stack using Avizo (v.7.0.1, Visualisation Sciences Group, Burlington, MA, USA) by applying a combined approach of user-defined grey-density thresholding and manual segmentation editing. Craniofacial sinuses were preserved and cancellous bone was modelled as cortical, a decision based on the results of Chapter 2 (decreases model stiffness almost proportionally, i.e. without marked change of strain distribution in contour maps or directions of principal strain vectors).

During image segmentation, post-mortem dental loss in the deformed-erect individual was corrected by filling the alveoli with tooth material. PC1(-) had premature loss of both upper M1s that were reconstructed by replicating the individual's own upper second molars. PC1(+) had premature loss of the upper right first and second premolars, that were reconstructed by mirroring the homologous teeth of the left side. PC1(-) and PC2(+) required a slight lengthening of both I1s since their medical CT extended only to the upper parts of them. After these corrections the volume data were resampled to achieve isometric voxel sizes. The final 3D reconstructions are shown in Figure 5.3. Note that the deformed erect individual shows very marked asymmetry of the face and that asymmetries are present in all crania to varying degree (as seen in CT scans).

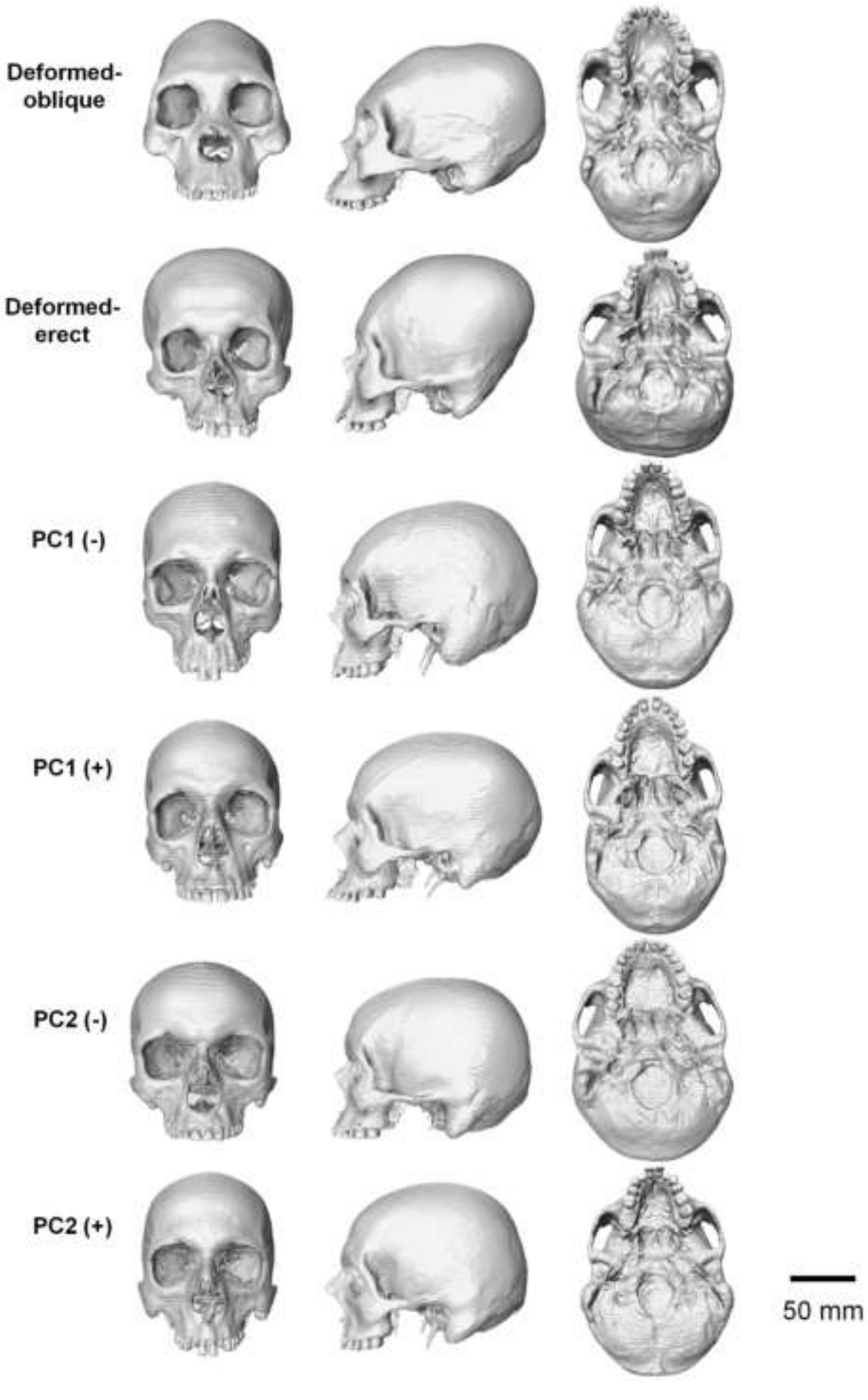

Figure 5.3. Sample. Frontal (left), lateral (middle) and inferior (right) views of the 3D reconstructions.

5.2.2. Muscle forces

The maximum masticatory muscle forces produced by the four living individuals were estimated from their muscle CSAs as explained in Chapter 3. In the case of the deformed individuals, soft tissues are lacking. Chapter 3 showed the low predictability of CSA from muscle areas on bone. However, Chapter 4 showed that the effect of bite point location on facial strains largely outweighs the effects of varying muscle activations, making the use of surrogate values a reasonable option for these cases.

Muscle CSAs do not correlate well with estimates from bony proxies, and in deformed crania the situation may be worse because of deformation of the morphology of the bony features used to estimate CSAs. Therefore, as a first step, therefore the anatomy of the bony proxies in the deformed crania was compared with that of the living, undeformed Chilean skulls using geometric morphometric tools. The aim was to see if these are particularly unusual, requiring particular care in approximating muscle CSAs. In Avizo, five landmarks from the right side of the head were digitised to represent the space available for each muscle's CSA. These were selected from the list of landmarks used throughout this thesis (see analysis of form below). For the temporalis the landmarks used were FTZ, ZRp, ZRa, ZAm and ItC. For the masseter area the selected landmarks were ZAl, aMassOr, pMassOr and midMassOr plus the landmark corresponding to the projection of base of the lingula on the lateral surface of the mandibular ramus. Principal components analyses to assess the morphological variation of each area in the sample were performed in the EVAN toolbox (v.1.62, www.evan-society.org). Landmarks are shown in Figure 5.4.

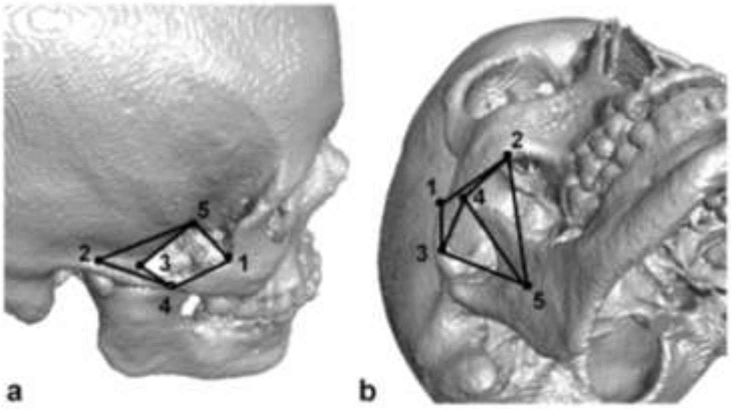

Figure 5.4. Landmarks used for shape analysis of (a) temporalis and (b) masseter muscle areas on bone.

The PCA of shape components of the anatomical features defining muscle areas on bone in the six crania (Figure 5.6) showed that the bony features in the temporal area vary mainly in the degree of transverse expansion/contraction of the regions. The masseter areas were less variable, and the features in the deformed-erect were similar to those in two of the living crania. The main ways in which they vary relate to transverse expansion/contraction. The deformed crania therefore do not present any particular features that would disproportionally impact on CSA estimation.

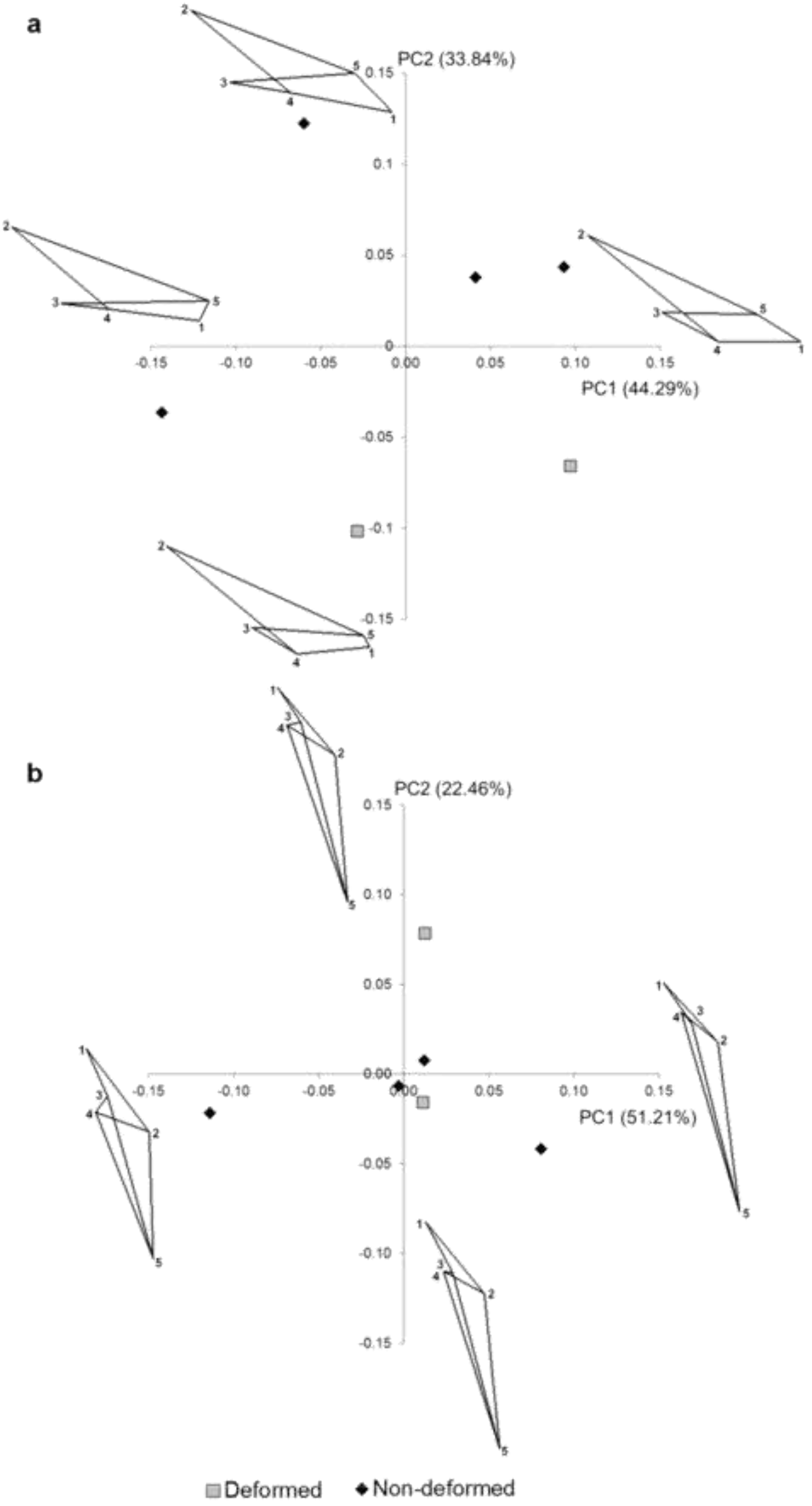

Figure 5.5. Principal components analysis of shape components from a) temporalis area and b) masseter area.

Next, CSAs in the deformed crania were estimated using bony proxies as in chapter 3. Their values lie within (or close to, in the case of left masseter in the deformed oblique) the range of actual CSAs of the non-deformed sample used in Chapter 3 (Table 3.2 in Chapter 3).

Table 5.1. Estimated CSAa in the deformed skulls. Reference values come from actual CSA measurements in the sample of Chapter 3.

	Sex	Left temporalis area (mm^2)	Right temporalis area (mm^2)	Left masseter area (mm^2)	Right masseter area (mm^2)
Deformed-oblique	F?	822.4	810.4	936	729.7
Deformed-erect	F?	738.8	748.4	849	944
Reference	F	804.2 ± 94.9	798.1 ± 153.7	715.2 ± 80.1	783.3 ± 138.4
(mean ± SD)	M	815.4 ± 153.8	823.8 ± 148.5	729.9 ± 134.1	850.2 ± 113.5

As noted above, variations in CSA affect the magnitudes of muscle forces but this has a very limited impact in strain distribution (but more on magnitudes) under different simulated bites (see Chapter 4). Considering this, the findings above and the sex of the deformed crania, it was decided to use average values of temporalis and masseter CSA from the women in Chapter 3 as estimates of muscle forces in the deformed crania. While not assessed in the above analyses because of the lack of a mandible, medial pterygoid force in the deformed crania was also estimated using the mean CSA of the same sample.

5.2.3. Finite element analysis

The 3D volumes were exported as BMP stacks and converted by direct voxel-element conversion into meshes of eight-noded cubic elements. A Young's modulus of 17 GPa was assigned to bone and of 50 GPa to teeth as used in Chapter 2. Both materials were homogeneously modelled as linearly elastic and isotropic with a Poisson's ratio of 0.3. Each model was kinematically constrained at both articular surfaces of the mandibular fossa (simulating a normal human temporomandibular joint) in the x, y and z axes. Constraints in the vertical axis were placed on the incisal border of both I1 and the tip of the four cusps of the left and right M1, simulating common human bite points. The choice of axes of constraint was based on the experiments of Chapter 2. About 15-25 nodes were selected at each constraint, with the aim of reflecting normal loading while keeping the number of constrained nodes small to avoid over-constraining the model. Simulations of both left and right M1 bites aimed to evaluate and account for any effects of cranial asymmetry. While some asymmetry was evident it did not appear severe enough to require separate analyses of bites by side. Only I1 and left M1 simulated bites were considered further.

The characteristics of each model are summarised in Table 5.2.

Table 5.2. Description of FE models.

Individual	Sex	Age (years)	Centroid size (mm)		CT voxel size (mm)	Number of elements	Temporalis force (N)		Masseter force (N)		M. Pterygoid force (N)	
			Cranium	Face			Left	Right	Left	Right	Left	Right
Deformed-oblique	F	Unk.	490.71	230.23	0.39 x 0.39 x 0.75	8,014,205	176	180.8	156.5	159.9	111.7	107.4
Deformed-erect	F	Unk.	512.20	222.41	0.39 x 0.39 x 0.75	9,502,898	176	180.8	156.5	159.9	111.7	107.4
PC1 (-)	F	54	468.53	218.68	0.45 x 0.45 x 1	7,787,812	195.1	202.2	200.4	227.2	121.4	129.8
PC1 (+)	M	46	469.36	221.74	0.43 x 0.43 x 1	7,745,806	188.2	194.9	209	225.7	143	153.6
PC2 (-)	M	43	464.78	217.07	0.44 x 0.44 x 1	6,306,181	168	170.7	134.6	124	124	117.5
PC2 (+)	M	38	469.10	213.34	0.43 x 0.43 x 1	7,007,049	180.4	164.8	193.2	173	115.4	106.6

Muscle origins and insertions were reproduced in the models based on the original CT images for the living sample. Two different loadings were simulated:

Model specific force magnitudes. Maximal muscle forces per individual were calculated from their CSAs (or for deformed crania, the modern Chilean averages) using the equation F = CSA x 37 N/cm^2 where the latter value is the intrinsic muscle strength for human masticatory muscles (see Chapter 4; Weijs and Hillen, 1994) .

Identical force magnitudes. In the above loading scenario each cranium is loaded with estimated maximal physiological masticatory muscle loads. This allows a comparison of estimated maximum bite forces and deformations. An alternative is to compare cranial responses to the same loadcase. This allows a comparison of relative performance with the same muscle force inputs. To do this, the same total muscle force of 2000 N was applied to each model. Each temporalis was assigned a magnitude of 400 N, each masseter 350 N and each medial pterygoid 250 N. These force magnitudes were approximately based on the average proportions of jaw-elevator muscle areas calculated in Chapter 3 in the 20 living Chileans (see Table 3.2 in Chapter 3) but the total force is relatively large.

A third loading scenario, **Identical bite forces**, was also assessed but no further FEAs were needed to produce strain contour plots (the conventional method to depict FEA results, as used throughout this thesis), compute strain magnitudes, or assess large scale deformations for this case. This is because the FE models were assigned linearly elastic properties and, with static loads applied, deformations scale linearly with force. Thus, strain contour colour maps from the model specific loadcases were rescaled according to the ratio between the required (same) bite force and the bite force that was estimated in the original FEA. Likewise strains were scaled and for large scale deformations assessed by Procrustes size and shape analysis (see below) the landmark displacements were scaled according to this ratio. For I1 bites the standard bite force to which each loading scenario was scaled was 350 N (O'Connor et al., 2005) and for M1 bites 700 N (van Eijden, 1991; Waltimo and Könönen, 1993).

5.2.4. Comparison of mechanical performance among crania

5.2.4.1 Preliminary analysis of form

A preliminary landmark-based GM analysis was undertaken to assess form variation in the sample. This is relevant to subsequent interpretation of differences among crania in terms of performance under simulated biting. As in previous chapters, the selected landmarks are the cranial ones used in Chapter 3 (Table 5.3). Form variation was also assessed using a subset of 25 facial landmarks, since the structures directly strained during incisor and molar bites are principally in the face (Gross et al., 2001; Kupczik et al., 2009; Wroe et al., 2010; Fitton et al., 2012). The form analysis consisted of a standard full Procrustes fit, followed by PCA of resulting shape variables plus the logarithm of centroid size (see Chapter 1 for rationale; Mitteroecker and Gunz, 2009) . Visualisation of shape changes used the surface corresponding to one of the individuals in the sample, PC2(-), warped to the mean configuration before further warping to the extremes of axes. Two orthogonal grids were drawn over the mean landmark configuration, and warped with the surface.

Table 5.3. Landmarks for the study of form variation.

No.	Symbol	Name	Definition
1	V	Vertex	Highest point on the calvarium.
2	N	Nasion	Intersection between frontonasal and internasal sutures.
3	ANS	Anterior Nasal Spine	Tip of the anterior nasal spine.
4	Pr	Prosthion	Most buccal and occlusal point of the interalveolar septum between central incisors.
5	Oc	Occiput	Most posterior point of the neurocranium.
6&20	SoT	Supraorbital Torus	Most anterior point of the supraorbital ridge.
7&21	InfO	Infraorbitale	Most inferior point of the infraorbital ridge.
8&22	NNot	Nasal Notch	Most lateral point of the nasal aperture.
9&23	M1	First Molar	Most buccal and mesial point of M1and alveolar process junction. If absent, the landmark is in the lowest most buccal point of the interalveolar septum between the second premolar and the next present molar.
10&24	LM	Last Molar	Last point of the dental arch, located at the most buccal and distal point on the last present molar and alveolar process junction.
11&25	ZM	Zygo-maxillar	Most inferior point of the zygo-maxillary suture.
12&26	FZ	Fronto-zygomatic	Most lateral point of the fronto-zygomatic suture.
13&27	FTZ	Fronto-temporal angle	Point at the intersection between frontal and temporal processes of the zygomatic bone.
14&28	ZAl	Lateral zygomatic Arch	Most lateral point on the zygomatic arch.
15&29	ZRp	Zygomatic Root posterior	Most posterior-superior point of the intersection between the zygomatic root and the squama of temporal bone.
16&30	ZRa	Zygomatic Root anterior	Most anterior point of the intersection between the zygomatic root and the squama of temporal bone.
17&31	ZAm	Zygomatic Arch medial	Most lateral point on the inner face of the zygomatic arch.
18&32	ItC	Infratemporal Crest	Most medial point of the infratemporal crest.
19&33	Eu	Eurion	Most lateral point of the neurocranium.
34&37	aTemOr	Anterior Temporalis origin	Most anterior point of origin of the temporal muscle on the temporal line.
35&38	sTemOr	Superior Temporalis origin	Most superior point of origin of the temporal muscle on the temporal line.
36&39	pTemOr	Posterior Temporalis origin	Most posterior point of origin of the temporal muscle on the temporal line.
40&43	aMassOr	Anterior Masseteric origin	Most anterior point of origin of the masseter muscle on the zygomatic arch.
41&44	pMassOr	Posterior Masseteric origin	Most posterior point of origin of the masseter muscle on the zygomatic arch.
42&45	midMassOr	Mid-Masseteric origin	Midpoint along the origin area of the masseter muscle on the zygomatic arch.
46&49	sPtOr	Superior Pterygoid origin	Most superior point of origin of medial pterygoid muscle on the pterygoid fossa.
47&50	iPtOr	Inferior Pterygoid origin	Most inferior point of origin of medial pterygoid muscle on the pterygoid fossa.
48&51	midPtOr	Mid-Pterygoid origin	Midpoint of the area of origin of the medial pterygoid muscle on the pterygoid fossa.

5.2.4.2. Strain distribution and magnitude

As briefly mentioned earlier, evaluation of FEA results was carried out using colour-coded strain contour plots, a qualitative and a quantitative approach aiming to compare the relative locations of low and high strains (referred to as distribution) and magnitudes of predicted strains. Additionally and as reference, strain magnitudes of each model under each loading condition (Model specific force magnitudes, Identical force magnitudes and Identical bite forces) were extracted from the locations of landmarks in Table 5.3.

5.2.4.3. Bite force and TMJ reaction forces

The reaction forces at the constrained areas (i.e. bite points and TMJ surfaces) predicted by the FEAs were used as estimates of bite and TMJ reaction forces. To compare bite force production efficiency the ratio of bite force/muscle force was calculated for each model (O'Connor et al., 2005) under model specific loadings. For I1 bites, TMJ reaction force was averaged between sides, and for left and right M1 bites the TMJ reaction forces were averaged within working and balancing sides.

5.2.4.4. Large scale model deformation

Resulting model deformation was studied from two perspectives, using geometric morphometric tools. First, the differences in mode of deformation among models were assessed using PCA of Procrustes size and shape variables, as explained below. Subsequently, the association between facial form and model deformation was analysed using partial least squares (PLS).

Differences in deformation mode among models

Geometric morphometric tools have recently been applied to compare FEA results among different morphologies by assessing the changes in size and shape produced by node displacement in the loaded models. The approach by Milne and O'Higgins (2012) was used in this study.

In this study a subset of 43 cranial landmarks from those used in the form analysis (Table 5.3) was used. The landmarks on the zygomatic arch (ZAl, ZAm, pMassOr, midMassOr) were excluded. The zygomatic arch was excluded because of the uncertainties about muscle forces in the artificially deformed crania (see Chapter 4 for rationale). The coordinate data from the unloaded and the loaded crania were submitted to full Procrustes fit. Because differences in cranial shape are very large when compared to the differences due to loading, they would swamp subsequent analyses and so need to be removed from consideration at this stage. Thus, the shape coordinates of the unloaded model were subtracted from those of each loaded one. The resulting residuals were then added to the mean unloaded configuration and rescaled to maintain the ratios of centroid sizes between loaded and unloaded models. The resulting size and shape coordinates are then submitted to PCA. To compare deformations at the same bite forces, the size and shape residuals from the model specific loadcases were scaled according to the ratio between the desired and actual bite forces as described earlier.

The changes in size and shape from the mean, undeformed reference model to I1 and left M1 simulated bites were then visualised using transformation grids and the surface warping tool in the EVAN toolbox.

Association between facial form and model deformation

As mentioned above, since the face is the most strained part of the cranium during biting, the association between facial form and cranial model deformation was studied using a novel approach based on PLS, a method previously used in Chapter 3 of this thesis (see the rationale in Chapter 1 of this thesis). In the present chapter, the two sets of data corresponded to ‘blocks’ of three dimensional coordinates, the first dataset (Block 1) comprised the 25 landmarks describing facial form and the second (Block 2), the 43 landmark data representing cranial model deformation under I1 or left M1 bites. These are the same coordinates used in the Procrustes size and shape PCA of deformations in the previous section. The size and shape data from identical muscle forces were used, since identical muscle forces provide comparability of performance under the same muscle force inputs, thus focussing the analysis on differences in performance due to model form rather than model loadcase.

The PLS method finds pairs of axes called singular warps (SW) depicting associations between the blocks of data through singular value decomposition. The first pair of axes explains the largest proportion of the total covariance between blocks. To visualise the pattern of association described by a pair of singular warps, warpings of the means of each block are used. Transformation grids and the mean surface were warped along each SW using the EVAN toolbox.

While the PLS focuses on the covariance among blocks and the first singular values (SV) usually explain a good proportion of this covariation, it is also of interest to know the proportion of the total variance of form within each block accounted for by covariances with the other block. For each block, this was calculated as the ratio between the variance among the scores on the SW of interest and the total variance represented by the sum of the eigenvalues of each PC axis from the PCA of the corresponding block, i.e. face form (Block 1), and model deformation (Block 2).

5.3. Results

This study assessed cranial performance during simulated biting, under three different loading conditions. After a preliminary analysis of form, the results of each loading experiment are presented and, finally, variations in facial form are related to variations in modes of large scale deformation under incisor and molar bites.

5.3.1. Preliminary analysis of form

The analysis of cranial form shows a clear separation between the non-deformed and the deformed individuals, mainly due to variations in the proportions of the neurocranium (Figure 5.6). The first PC relates to changes in the relative length of the neurocranium and facial prognathism, while PC2 relates to variations in neurocranial and facial width.

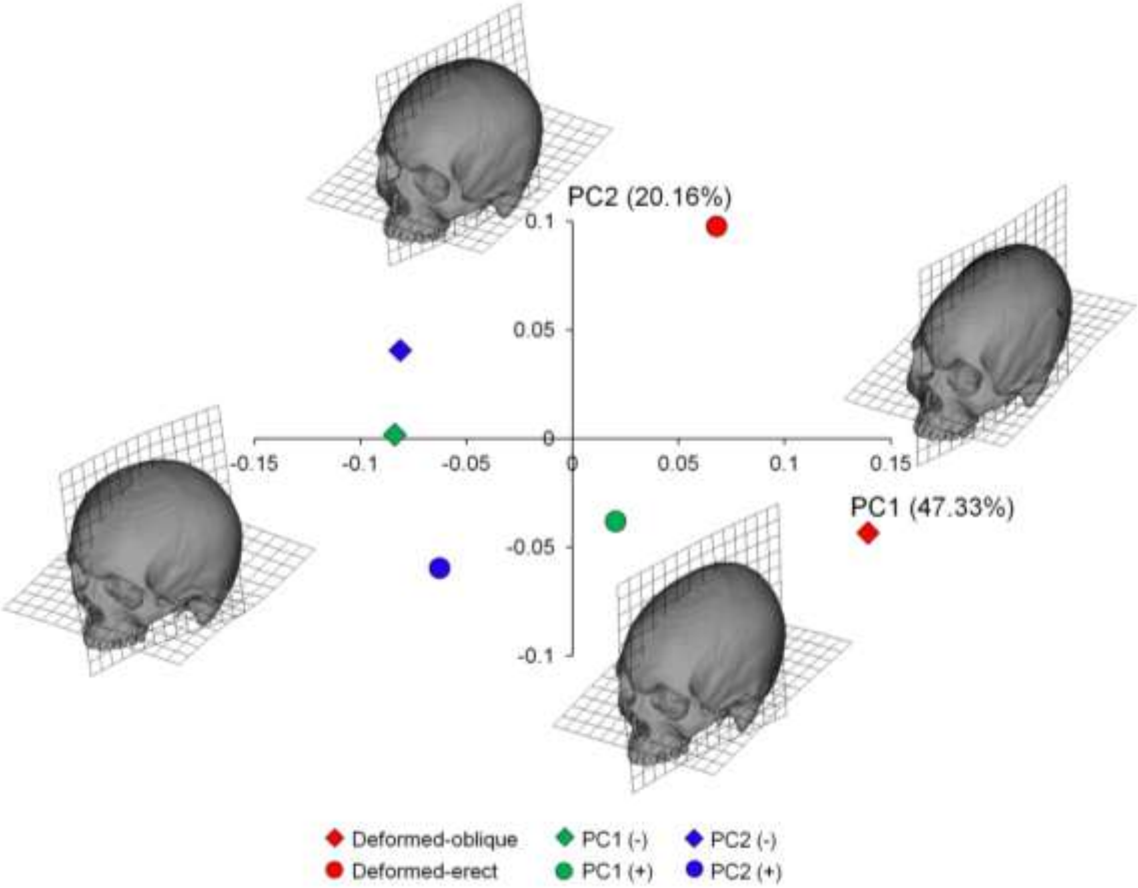

Figure 5.6. Principal components analysis of cranial form components. Aspects of form variation represented by PC1 and PC2 are shown at the extremes of each PC. The degree of warping is not magnified.

The form analysis of the facial landmark configurations alone shows that the main variations are in the degree of prognathism of the maxilla (PC1), overall facial expansion in the antero-posterior and medio-lateral axes (PC2), and in the vertical height and midline convexity of the face (PC3; Figure 5.7). Compared to PC1 and PC2, variation in PC3 shows a large asymmetric component, with the deformed erect individual at one extreme and the deformed oblique at the other.

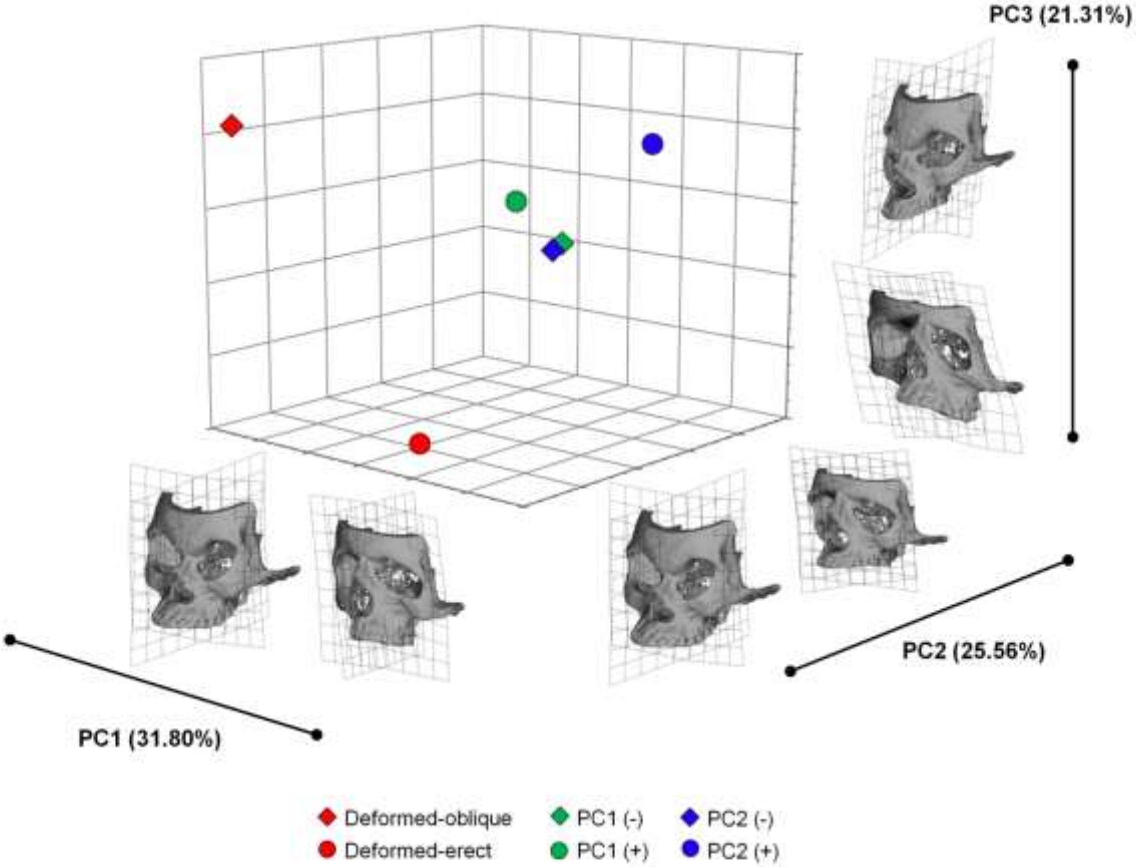

Figure 5.7. Principal components analysis of facial form components. Aspects of form variation represented by PC1, PC2 and PC3 are shown at the extremes of each PC. Warpings are magnified three times to improve visualisation. The scores in each axis range from -0.07 to 0.07 but labels are not shown to avoid crowding the figure.

5.3.2. Strain distribution and magnitudes

The strain magnitudes at each landmark location (Table 5.3) in each model under its specific and identical muscle forces as well as after scaling the specific force strains to identical bite forces are listed in Tables A.2, A.3 and A.4 of Appendix.

FEA results show that the distribution (not magnitudes) of regions of high and low strains in the contour maps is very similar among models and loadcases, irrespective of the presence of artificial deformation. Differences in loading conditions were reflected mainly in the magnitudes of strains. Under model specific muscle forces, the locations of high strains (>150 με) derived from either incisor or molar bites were consistent among models. Highest strains (>200 με) are concentrated over the zygomatic arch in I1 and M1 bites. In the face, during I1 bites the greatest magnitude strains are found in areas related to the bite point; alveolar process, nasal notch, frontal process of the maxilla and anterior palate. Magnitudes, but to lesser degree distributions, differ among individuals. The less prognathic individuals PC1(-) and PC2(+) showed markedly lower values of strain over both vestibular and the palatal aspects of the alveolar process compared to the other individuals, who showed larger areas of strains above 250 με in the same regions (Figure 5.8). The deformed erect individual developed high strains over the cranial base.

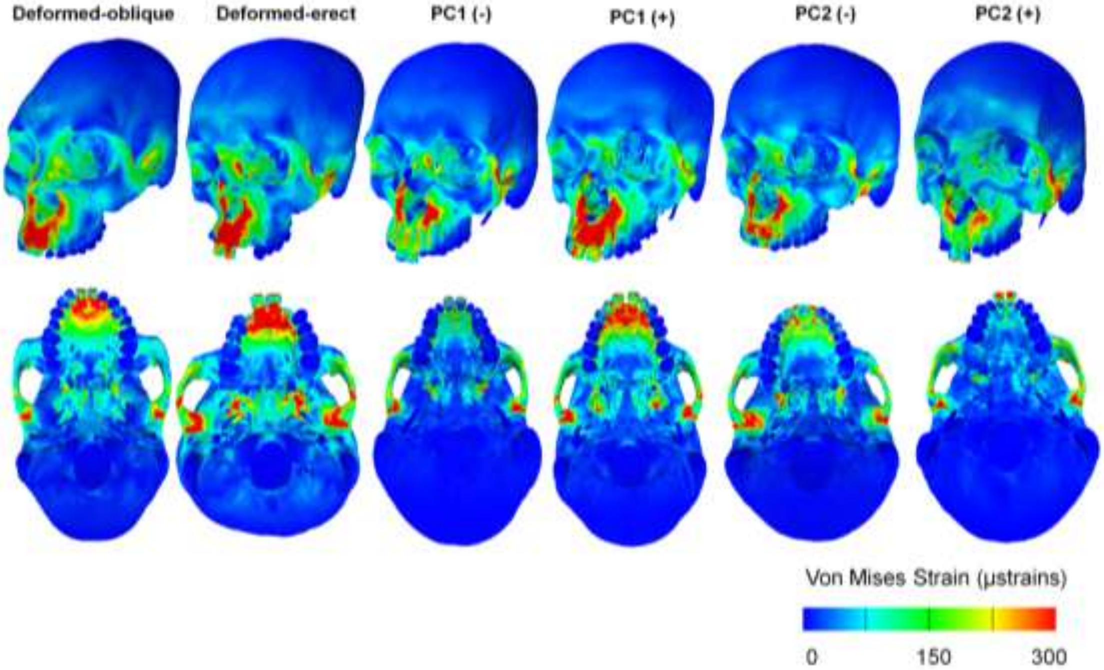

Figure 5.8. Strain contour plots under a bilateral I1 biting simulations with model specific muscle forces. Models of living Chileans were loaded with their own muscle forces estimated from muscle CSAs and the deformed crania with average CSA values from the whole sample of living Chileans.

During M1 bites the highest strains were located over the zygomatic process of the maxilla, the lateral border of the orbital opening and the area between the anterior wall of the maxillary sinus and the nasal notch. Individuals with a broader maxilla, namely both deformed individuals and to lesser degree, PC2(-), show lower peak strain magnitudes (Figure 5.9).

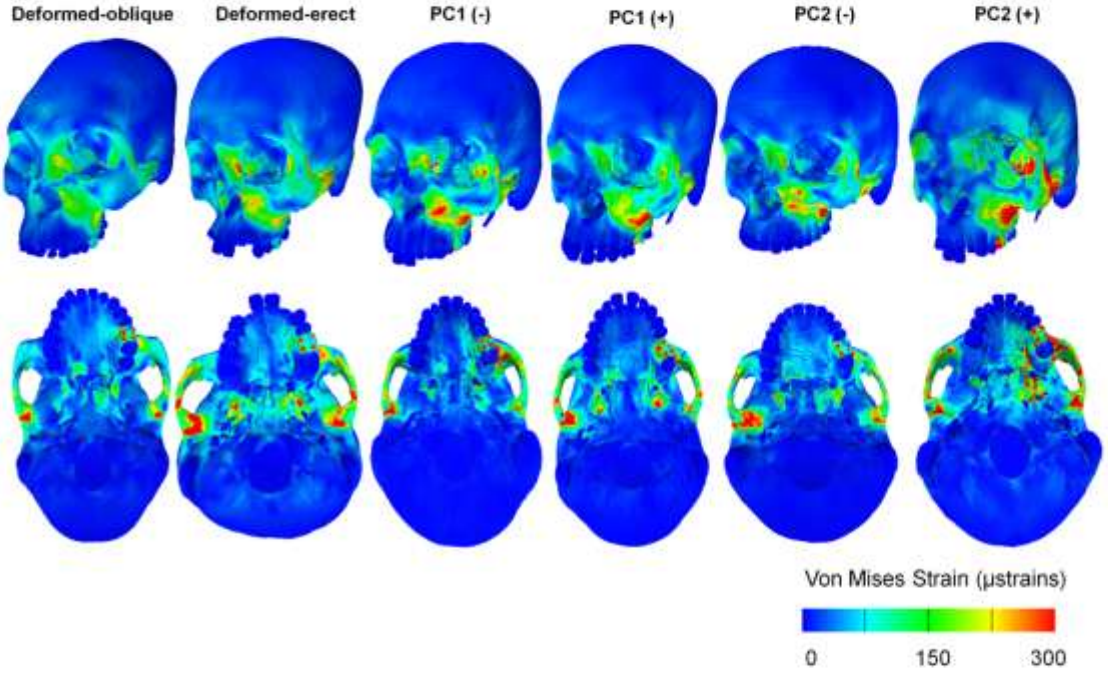

Figure 5.9. Strain contour plots under left M1 biting simulations with model specific muscle forces. Models of living Chileans were loaded with their own muscle forces estimated from muscle CSAs and the deformed crania with average CSA values from the whole sample of living Chileans.

Under identical muscle forces, the applied load is identical between specimens and in every case it is larger than the specific loads applied in the previous experiments. In consequence strain magnitudes are generally higher but the spatial distributions of regions of high and low strain differ little from the above analyses. During I1 bites, under 2000 N of total muscle force the complete frontal region reaches ~150 µε in all the models. This compares with parts of the frontal region reaching strains above 100 µε in the first analyses using model specific forces. In the lower facial areas, larger areas show strains >250 µε, consistent with the increased muscle force. In the palate, the least prognathic individuals, PC1(-) and PC2(+), showed less marked increases in strain magnitudes. These magnitudes remained of the order of ~150 µε but are more widely distributed (Figure 5.10).

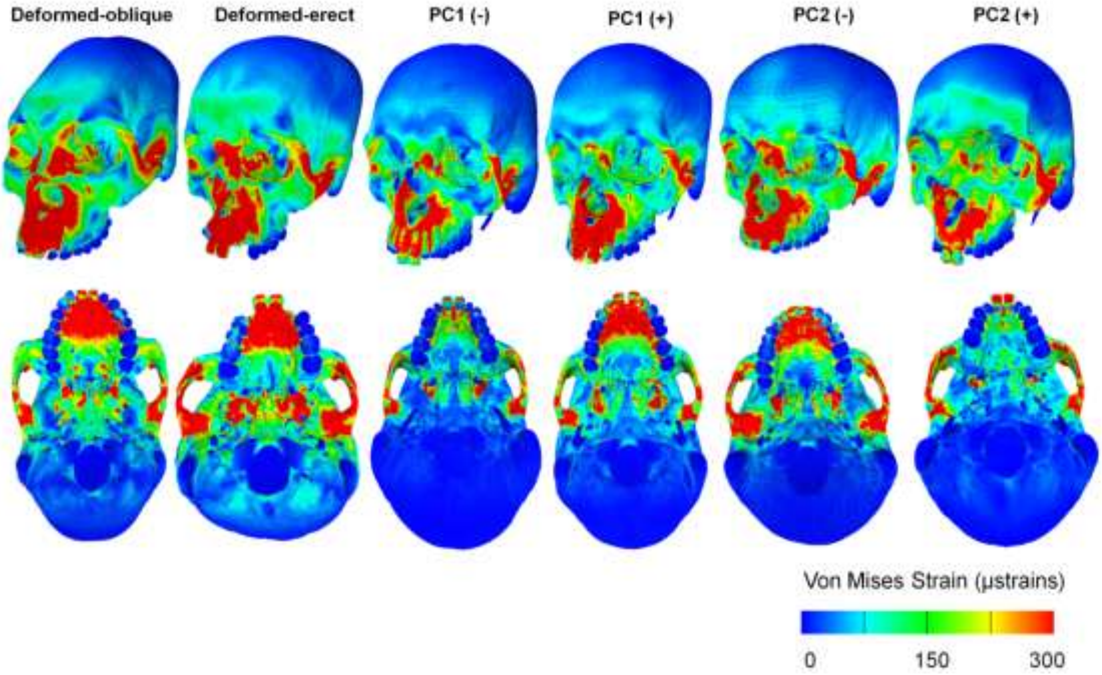

Figure 5.10. Strain contour plots under a I1 biting simulations with models loaded with a total muscle force of 2000 N.

During left M1 bite and with identical muscle forces, strain magnitudes also show an overall rise and are more similar among specimens. The spatial distributions of high and low strains are again very similar between these loading experiments and the earlier ones using specific muscle forces. However, the deformed crania show relatively higher facial strains (~150 με) more homogeneously distributed in the balancing side. Compared to models loaded with their own muscle forces, the extent of facial areas reaching over 250 με is more similar among models (Figure 5.11).

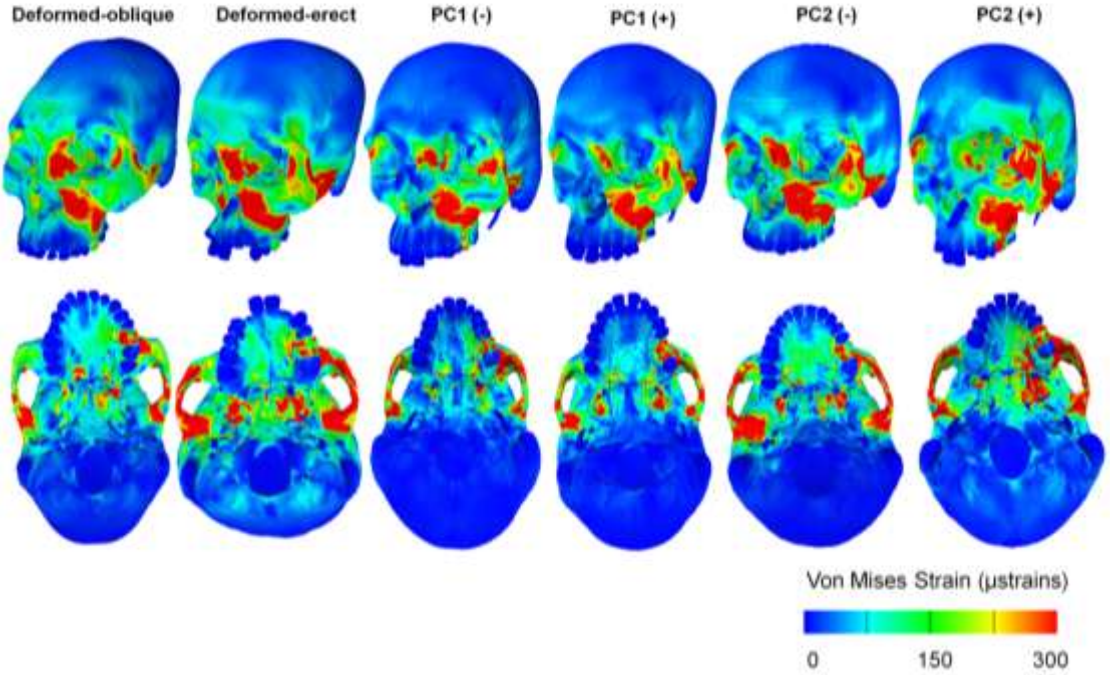

Figure 5.11. Strain contour plots under a left M1 biting simulations with models loaded with a total muscle force of 2000 N.

Under identical I1 and M1 bite forces, the results are consistent with those above from different loading scenarios. That is, strain distributions remain largely unaltered between experiments but strain magnitudes differ (Figures 5.12 and 5.13). The spatial distributions of regions of high and low strain resemble those observed in models loaded with their own muscle forces (Figures 5.8 and 5.9); PC1(-) and PC2(+) show the smallest facial areas with strains over 250 με (red in the figures).

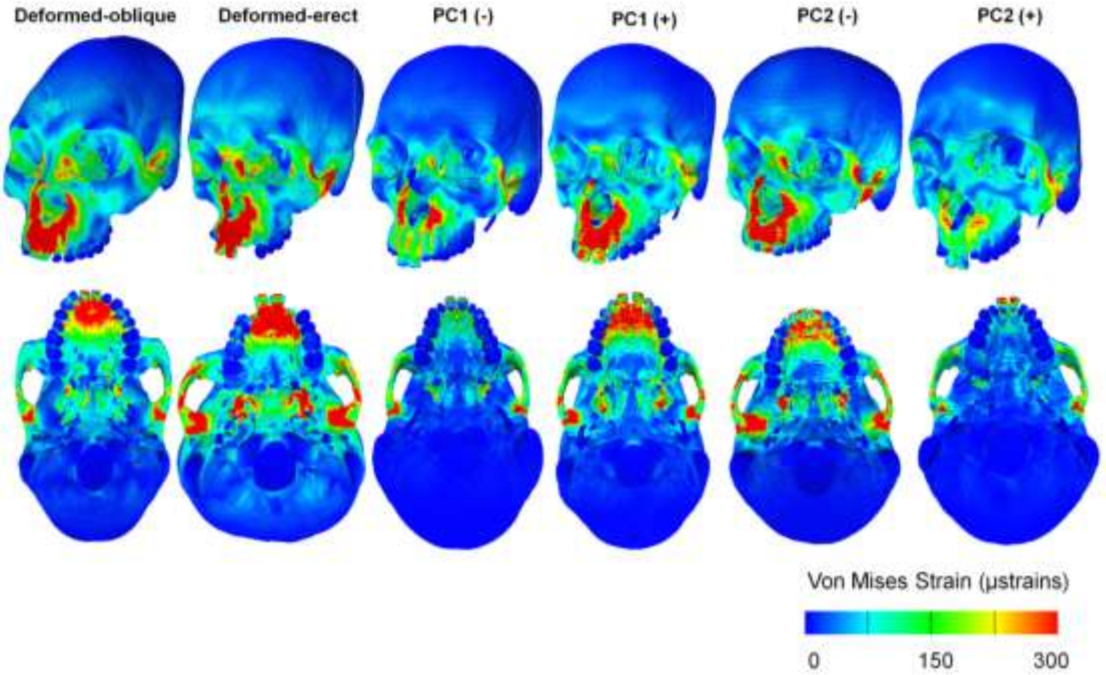

Figure 5.12. Strain contour plots of crania exerting 350 N of bilateral I1 bite force.

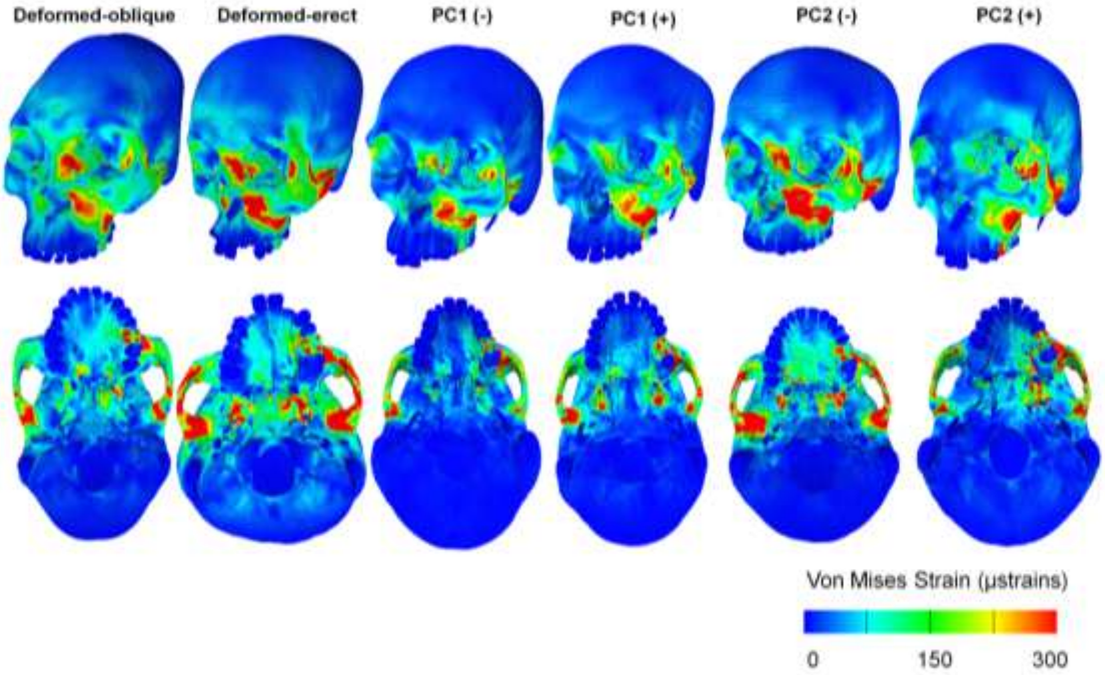

Figure 5.13. Strain contour plots of crania exerting 700 N of left M1 bite force.

5.3.3. Bite force and TMJ reaction force

The resulting bite forces and reaction forces at the TMJs are consistent with the changes in peak strains near bite points and the mandibular fossae under different muscle loadings. The greatest bite forces under identical applied muscle forces and efficiencies (Table 5.4) under specific loading were achieved by the least prognathic individuals with the narrowest maxillae: PC1(-) and PC2(+). Of the deformed crania, the deformed erect shows lower bite force and efficiency (irrespective of the muscle load), and among all models, it is predicted to show the largest TMJ reaction force under identical muscle forces.

Table 5.4. Bite and TMJ reaction forces. BF=bite force; W=working; B=balancing.

Model	Specific loading Bite force (N)		Identical loading Bite force (N)		Specific loading Efficiency (BF/MuscleF)*100		Specific loading Average TMJ reaction force (N)		Identical loading Average TMJ reaction force (N)	
	I1 bite	Average M1 bite	I1 bite	Average M1 bite	I1 bite	Average M1 bite	I1 bite	M1 bite W/B side	I1 bite	M1 bite W/B side
Deformed -oblique	282.96	454.21	632.78	1017.22	31.71	50.90	233.93	106.22 / 264.52	524.03	238.14 /592.41
Deformed -erect	265.28	434.94	592.99	972.36	29.73	48.74	296.13	198.47 / 304.16	664.24	446.13 /682.14
PC1 (-)	358.91	618.69	658.61	1135.64	33.35	57.49	262.75	82.76 / 275.22	482.17	138.28 /504.89
PC1 (+)	301.06	530.08	536.62	945.09	27.02	47.57	310.42	68.55 / 331.84	557.45	113.61 /595.85
PC2 (-)	234.29	357	565.36	860.96	27.93	42.56	236.49	108.29 / 260.22	567.25	257.08 /625.05
PC2 (+)	380.04	603.29	807.41	1281.98	40.72	64.63	216.82	159.59 / 225.97	453.93	313.41 /474.10

5.3.4. Large scale model deformation

5.3.4.1. Differences in deformation mode among models

In the PCA of Procrustes size and shape coordinates, the deformed erect and PC2(+) individuals represent the extremes of the modes of model deformation, although PC2(+) is the most distinctive in performance, particularly in the molar biting simulation. Thus, as expected from the results relating to strain contours and magnitudes, the size and shape analysis of large scale deformations from FEA biting simulations shows that the deformed crania have similar behaviour to the non-deformed individuals. When the differences in deformation between I1 and left M1 bites are represented as a vector connecting these two loadcases in each individual, it can be observed PC2(+), differs most in the relationships between these loadcases irrespective of muscle loading conditions (Figures 5.14, to 5.16).

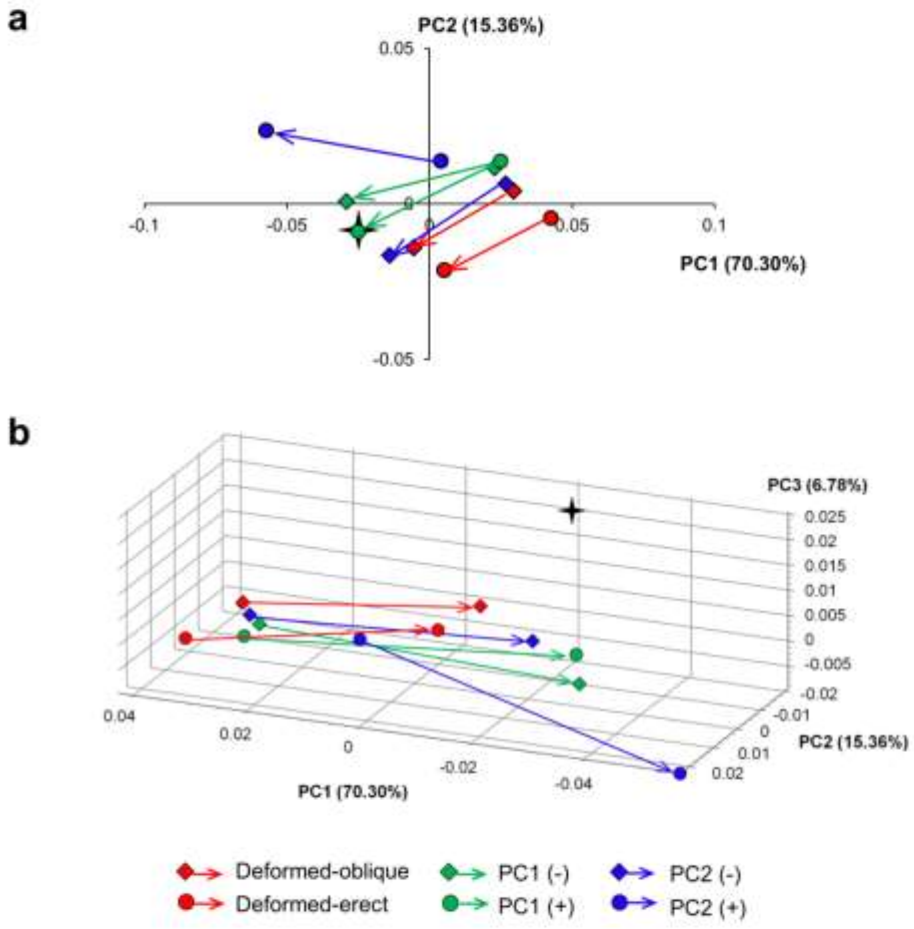

Figure 5.14. Principal components analysis of 43 craniofacial landmarks representing changes in size and shape among FE models loaded with their own muscle forces. a) PC1 vs. PC2, and b) PC1, PC2 and PC3. The star represents the mean undeformed reference model. Arrows represent the vector between I1 (beginning of the arrow) and left M1 (end of the arrow) biting simulations.

Visualisations of size and shape changes arising in each loading scenario showed that loaded crania deform similarly despite varying loading conditions. The main differences are in magnitudes of deformation (Figures 5.17 to 5.19). Within loading conditions, I1 bites produced similar deformations in the models consisting of sagittal, dorso-ventral bending around a horizontal axis located approximately at the upper limit of the alveolar process. The main outlier in the PCAs of size and shape variables is specimen PC2(+), and to a lesser degree, PC1(-) under simulated left M1 biting irrespective of muscle loading scenario. PC2(+) is also an outlier in the PCA of facial form in presenting the most orthognathic, tallest and narrowest face. It shows the greatest degree of maxillary and orbital deformation on the working side with the greatest degree of lateral displacement of the upper face and lateral orbit on the balancing side in Figures 5.17-19. The most marked differences are apparent under identical muscle loadings (Figure 5.18), in agreement with the results observed in the strain contour plots derived from identical loadings (Figure 5.11). In these contour plots, PC2(+) differs from the others in that the region of high strain over the left maxilla extends less anteriorly and superiorly and strains in the lateral orbit are higher.

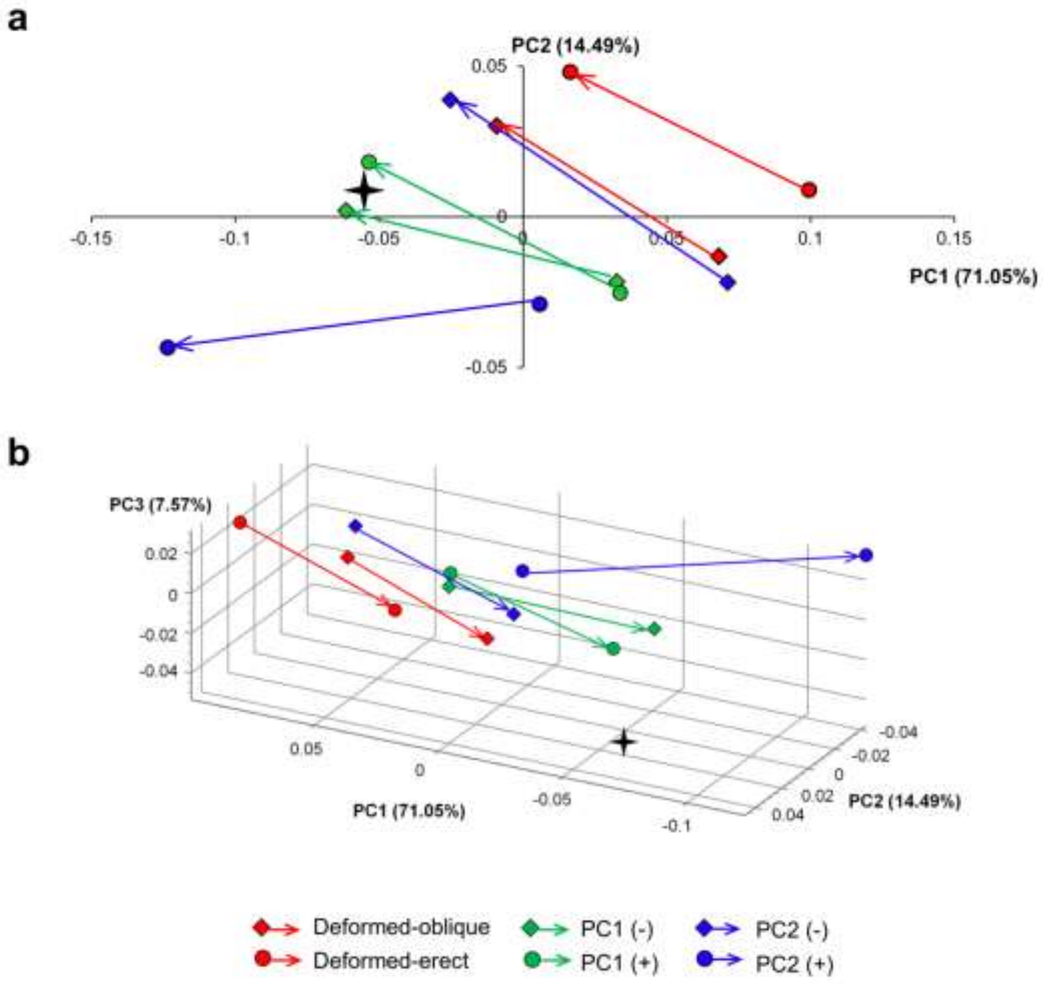

Figure 5.15. Principal components analysis of 43 craniofacial landmarks representing changes in size and shape among FE models loaded with 2000 N of total muscle force. a) PC1 vs. PC2, and b) PC1, PC2 and PC3. The star represents the mean undeformed reference model. Arrows represent the vector between I1 (beginning of the arrow) and left M1 (end of the arrow) biting simulations.

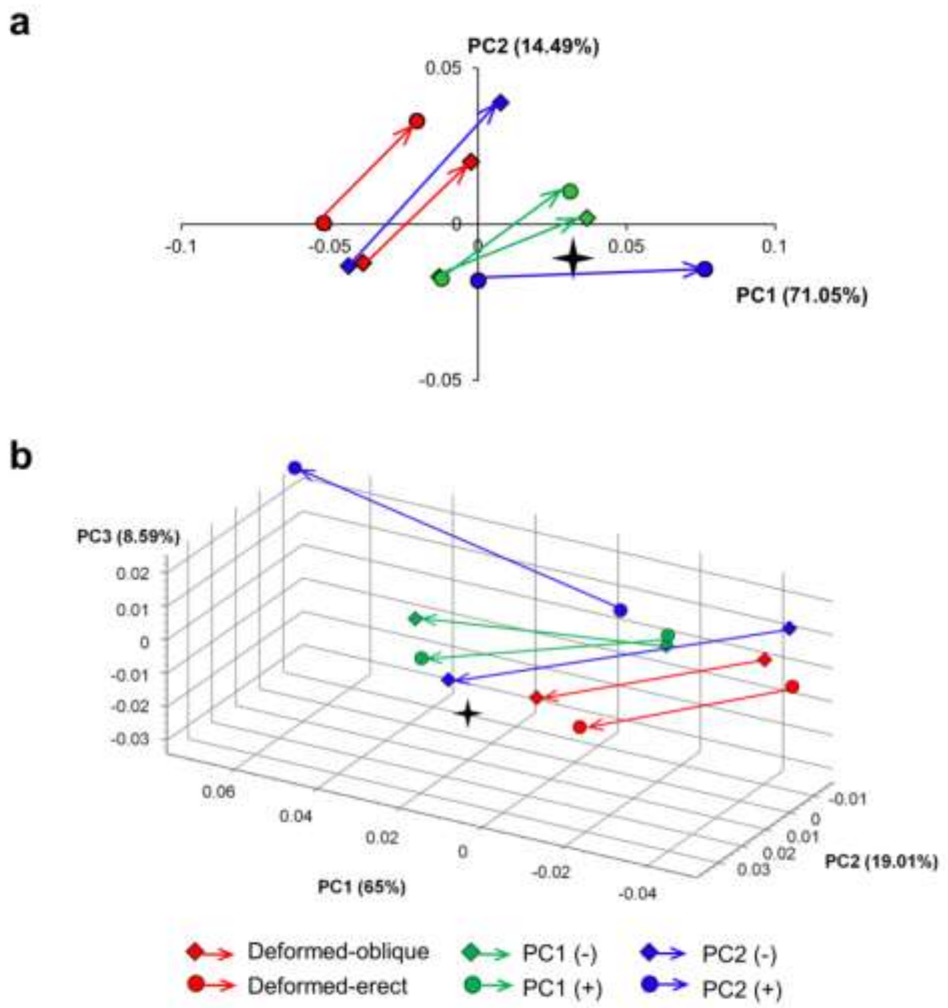

Figure 5.16. Principal components analysis of 43 craniofacial landmarks representing changes in size and shape among FE models producing 350 N and 700 N of bite force at I1 and left M1 respectively. a) PC1 vs. PC2, and b) PC1, PC2 and PC3. The star represents the mean undeformed reference model. Arrows represent the vector between I1 (beginning of the arrow) and left M1 (end of the arrow) biting simulations.

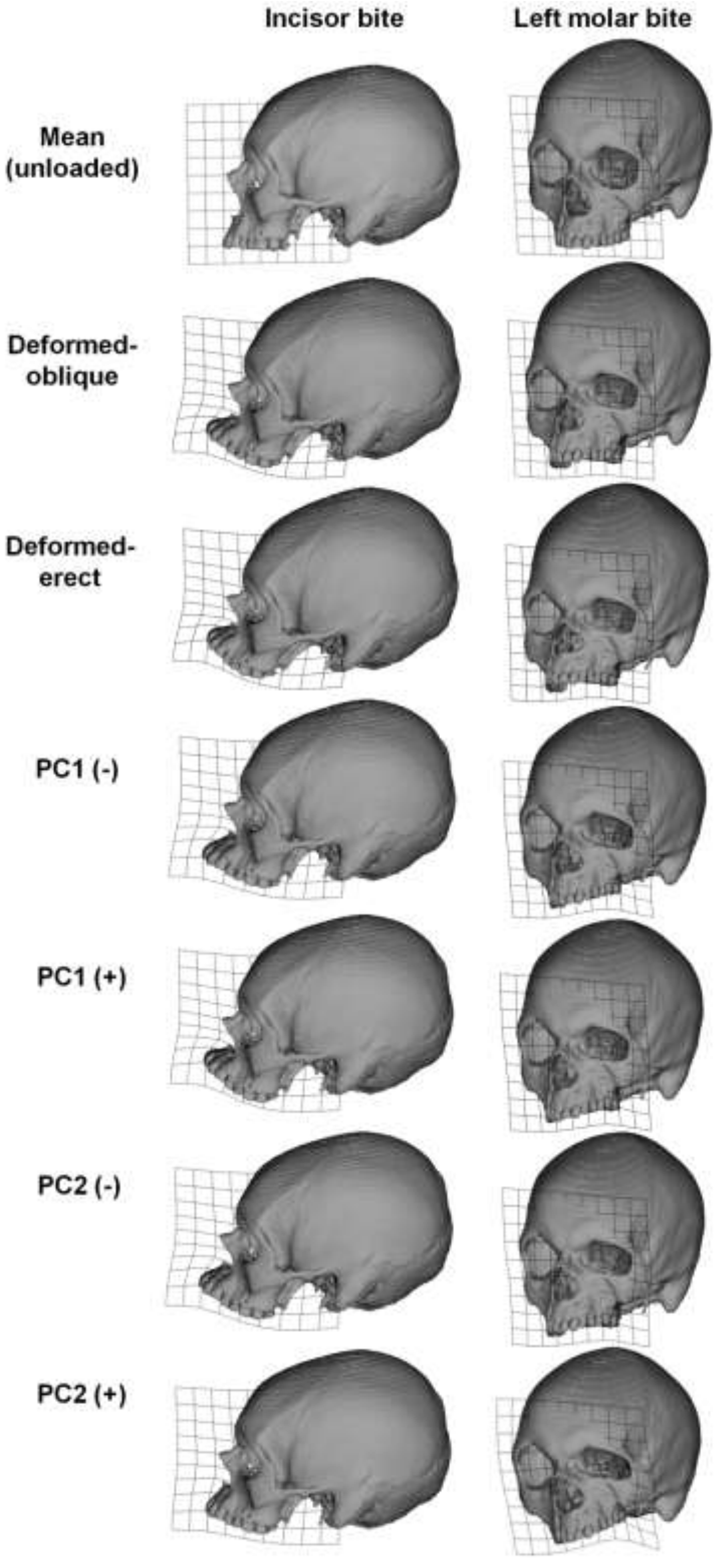

Figure 5.17. Changes in model size and shape under I1 and left M1 biting simulations using model specific muscle forces. Grids have been sited to visualise deformations of key structures. Surface warpings have been magnified 750 and 1000 times for I1 and left M1 biting simulations respectively.

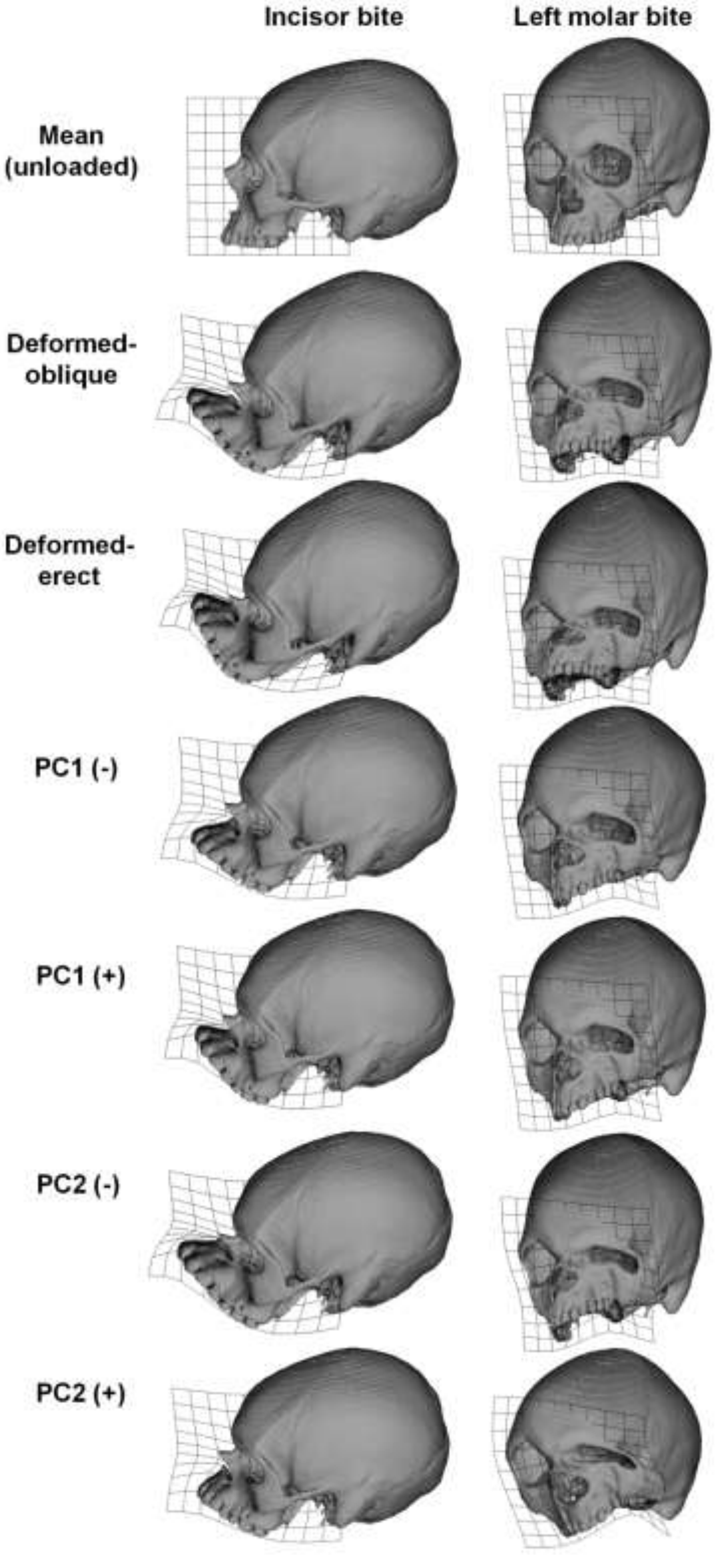

Figure 5.18. Changes in model size and shape under I1 and left M1 biting simulations using 2000 N of total muscle force. Grids have been sited to visualise deformations of key structures. Surface warpings have been magnified 750 and 1000 times for I1 and left M1 biting simulations respectively.

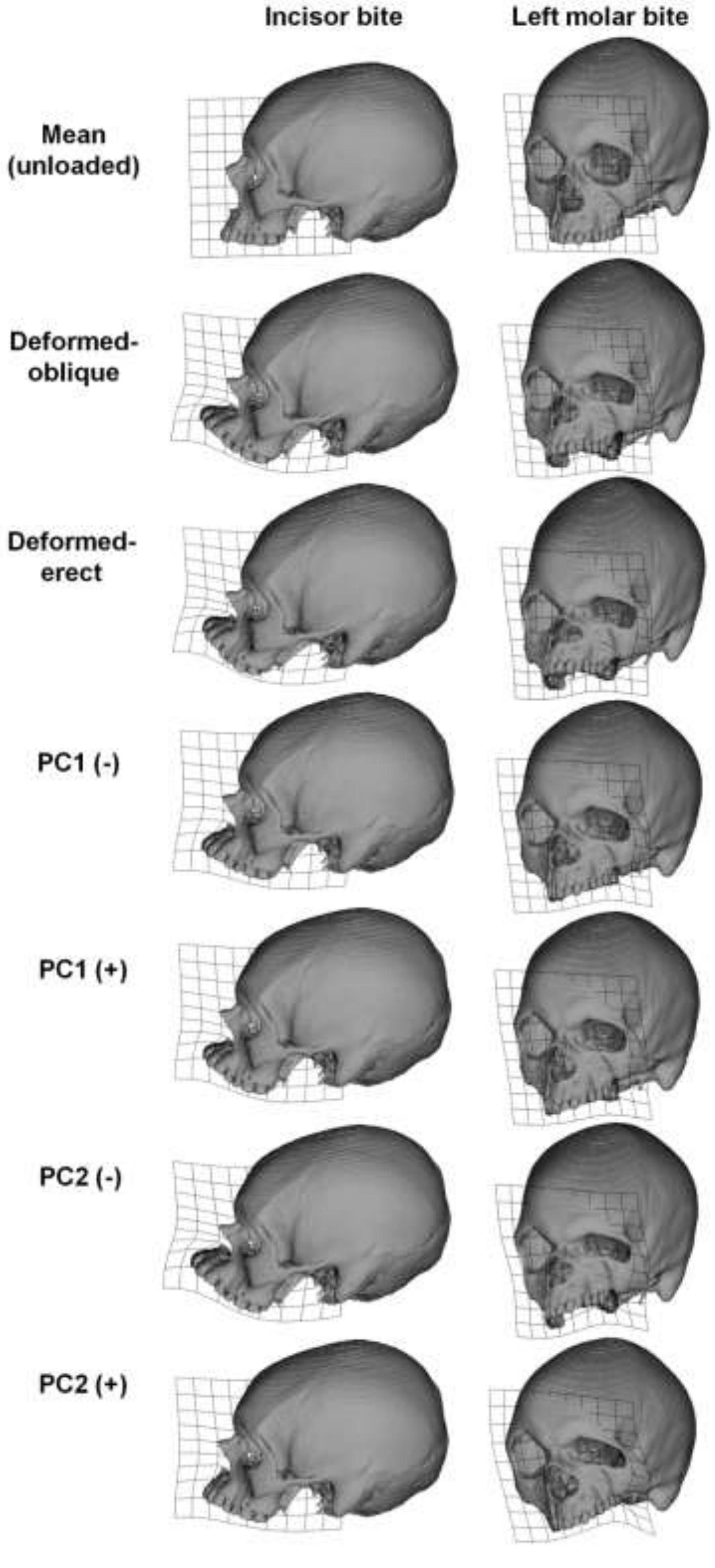

Figure 5.19. Changes in model size and shape under 350 N of I1 and 700 N of left M1 bite force. Grids have been sited to visualise deformations of key structures. Surface warpings have been scaled 750 and 1000 times for I1 and left M1 biting simulations respectively.

5.3.4.2. Association between facial form and model deformation

The PLS showed that there is a strong association between face shape and the mode of model deformation under identical muscle loads under each bite. The first pair of SWs from the I1 biting simulation explain 76%, and from the molar, 90% of the covariance among blocks. The second SWs of I1 biting explains 12% of the covariance, while SW2s of M1 biting explains only 5% (Table 5.5).

For I1 and left M1 bites respectively, 24.33% and 26.82% of the total variance in facial form is represented by the first SW of facial form (Table 5.5). These are the proportions of the total variance in facial form that relate to the differences in deformation represented by SW1 of that same block. The second and third SWs of facial form from both biting scenarios account for similar proportions of the total variance in facial form and a considerable proportion of the total variance remains to be explained by higher order SWs. Since only the first one or two SWs account for an appreciable proportion of the covariance among blocks, this means that while facial form shows a relatively strong association with the mode and extent of deformation, not all aspects of facial form variation impact on biting performance.

Conversely, for I1 and left M1 bites respectively, 73.94% and 87.44% of the total variance in large scale model deformation is represented by the first SW of deformation (Table 5.5). Very much smaller proportions are accounted for by the remaining SWs. This means that deformation in response to biting is strongly determined by facial form. Indeed, the proportions of the total variance explained by the singular warps closely parallel the proportions of total covariance explained by each. Since everything except form was kept constant in each biting simulation (the deformations are in relation to the undeformed mean), these last results indicate that differences in modes of deformation are completely explained by differences in facial form.

Table 5.5. Partial least squares of face form and model deformation results.

Bite point	SW	SV	Proportion of total covariance	Correlation (r)	% of face form variance explained by SW	% of model deformation variance explained by SW
I1	SW1	0.001655	0.77	0.97	24.33	73.94
	SW2	0.000660	0.12	0.99	29.62	9.34
	SW3	0.000431	0.05	0.94	21.88	5.89
	SW4	0.000371	0.04	0.96	13.55	6.85
	SW5	0.000258	0.02	0.99	10.63	3.98
LM1	SW1	0.002638	0.90	0.97	26.82	87.44
	SW2	0.000636	0.05	0.97	26.23	5.14
	SW3	0.000439	0.02	0.91	18.88	3.84
	SW4	0.000294	0.01	0.92	15.79	2.02
	SW5	0.000237	0.01	0.96	12.29	1.55

The plots of singular warps (Figures 5.20 to 5.23) show the very strong associations between the scores of specimens on the first singular warps of the facial form and deformation blocks. The positive limit of the distribution is occupied by specimen PC2(+) and the negative by the deformed erect individual (reflecting PC2 scores in Figure 5.15; the PCA of deformations under identical muscle loads).

The associations represented by these plots are visualised in Figures. 5.20 to 5.23. The pair of inset diagrams of the facial form block show how form covaries with the mode of deformation shown in the pair of insets of the cranial deformation block. The warpings of the cranium undergoing deformation under loading and the superimposed transformation grids have been magnified 1000 times because the deformations from FEA are very small. These warpings are all calculated with respect to the means. As such they are symmetric about the mean; moving away from the mean in one direction on any SW results in the opposite mode of deformation from that when moving in the opposite direction. In the warpings representing modes of deformation from biting, the 1000x magnification of warping results in one direction representing what one might expect from the loadcase (actual model deformation, magnified 1000 times) and the other direction, the opposite. Thus, for example, in Figure 5.20 incisor biting causes the alveolus and lower face to be deformed dorsally and this is clear from the inset of deformation in the positive quadrant. However, less deformation than the mean is represented in the negative quadrant by the opposite warping, which is not to be interpreted as the opposite (ventral) deformation, but rather as less than the mean deformation.

In all warpings, facial form shows a marked asymmetric component that contributes to differences in deformation among models. The other aspects of morphology contributing to model deformation, as shown by the first SWs, are largely related to the form of the lower face; the least prognathic, smallest individuals, PC1(-) and PC2(+) show the least degrees of deformation at the alveolar process level in both I1 (Figure 5.20) and LM1 (Figure 5.21) biting simulations. The remaining individuals, with a more prognathic maxilla undergo greater dorsal deformation of the maxilla with flexion at the level of the nasal notch during I1 bites (Figure 5.20). These same individuals, on the other hand, show less deformation of (particularly posterior) maxilla and of the orbit during left M1 biting (Figure 5.21). These findings are consistent with the predicted strains and large scale model deformations presented earlier.

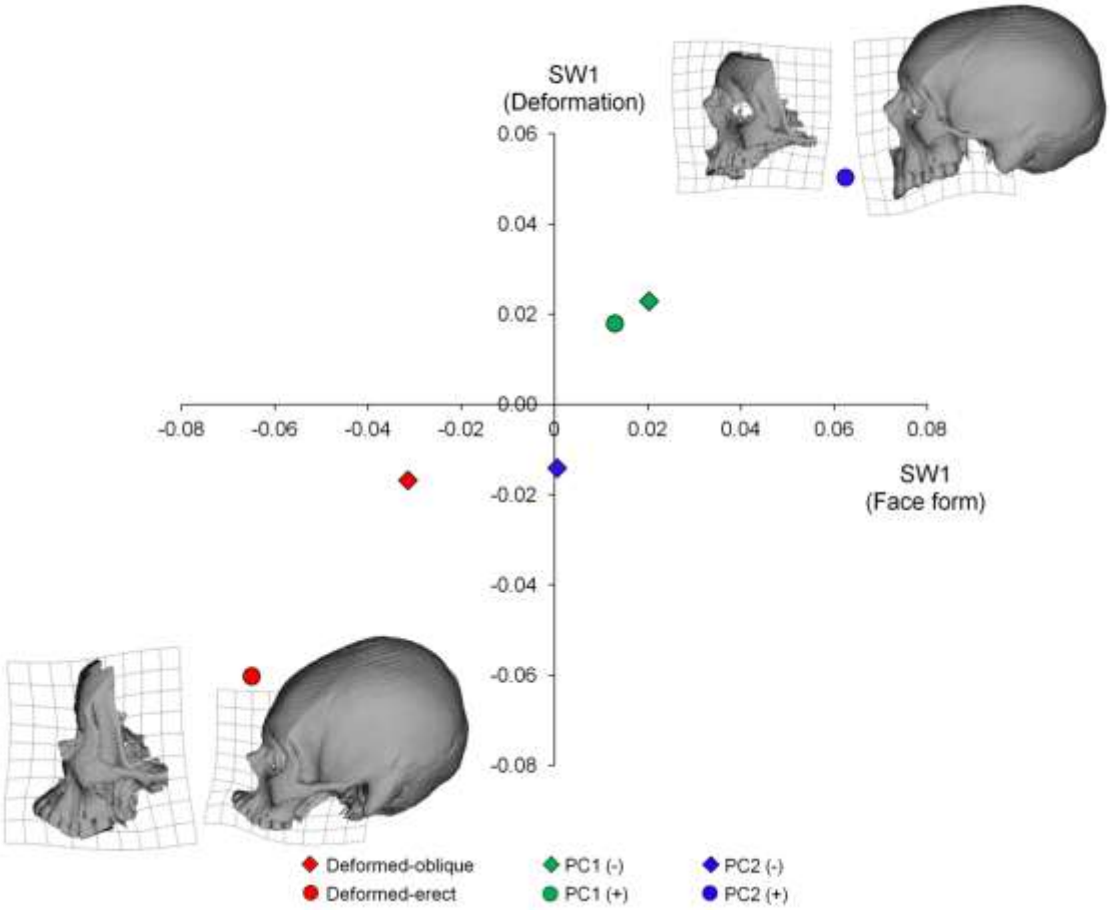

Figure 5.20. Partial least squares analysis of facial form vs. model deformation under I1 biting, first pair of SWs. The pairs of warpings at the extremes of the distributions are with respect to the mean of facial form (left) and model deformation (right). The warpings have been magnified five (face form) and 1000 (model deformation) times to facilitate visualisation.

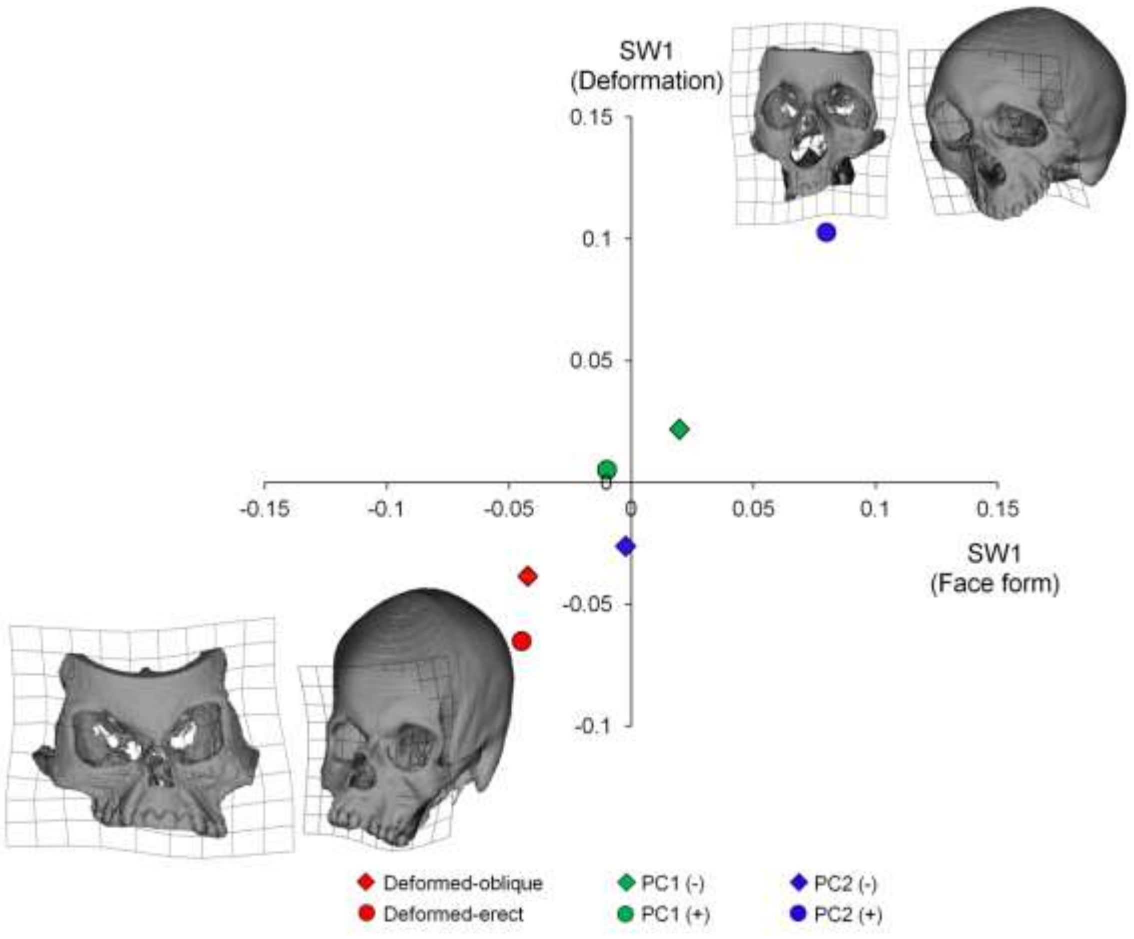

Figure 5.21. Partial least squares analysis of facial form vs. model deformation under left M1 biting, first pair of SWs. The pairs of warpings at the extremes of the distributions are with respect to the mean of facial form (left) and model deformation (right). The warpings have been magnified five (face form) and 1000 (model deformation) times to facilitate visualisation.

The second SWs explain 12% of the covariance among facial form and cranial deformation in the I1 biting simulation but only 5% in the M1 biting simulation. Plots of these second SWs are presented in Figures 5.22 and 5.23 respectively. For I1 biting (Figure 5.22), the second singular warps associate larger faces with greater degrees of facial prognathism with greater degrees of dorsal deformation of the anterior face. The facial warping is marked because the second SW from this analysis explains the greatest proportion of the total covariance with facial form.

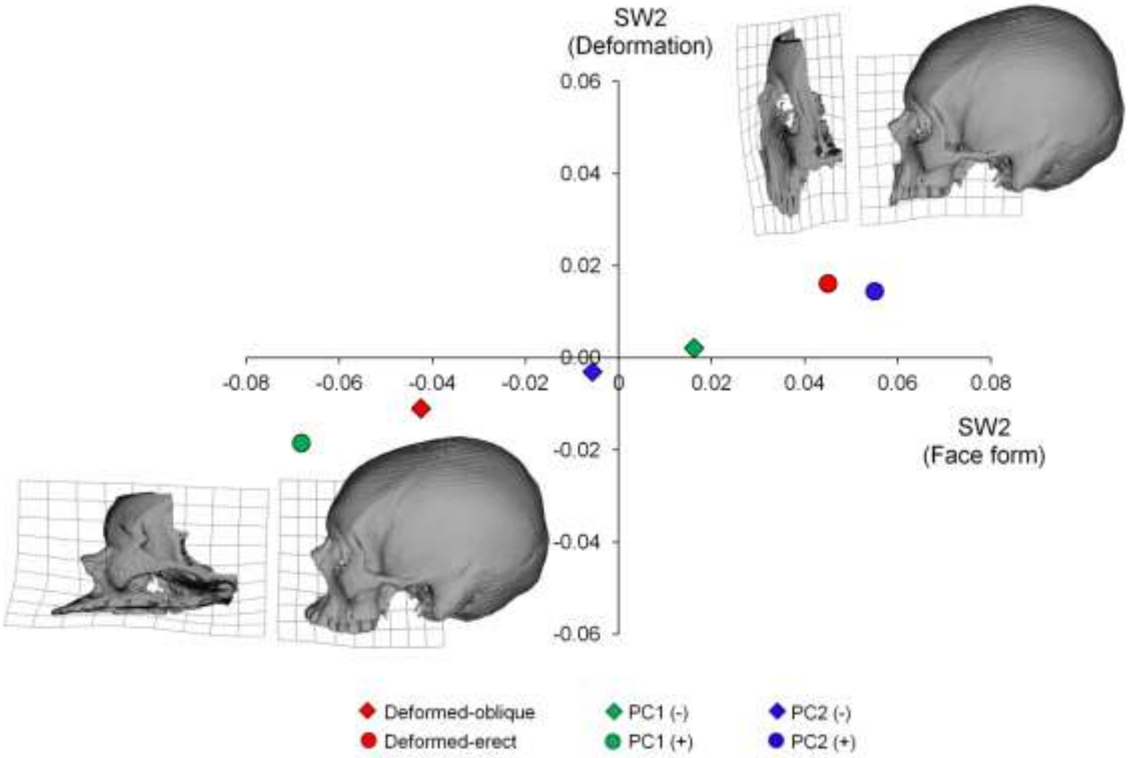

Figure 5.22. Partial least squares analysis of facial form vs. model deformation under I1 biting, second pair of SWs. The pairs of warpings at the extremes of the distributions are with respect to the mean of facial form (left) and model deformation (right). The warpings have been magnified five (face form) and 1000 (model deformation) times to facilitate visualisation.

For M1 biting (Figure 5.23), SW2 associates relatively small wide and short faces (positive scores) with an albeit very small degree of deformation of the posterior maxilla, when compared to SW1. As noted above this accounts for only 5% of the covariance between facial form and cranial deformation.

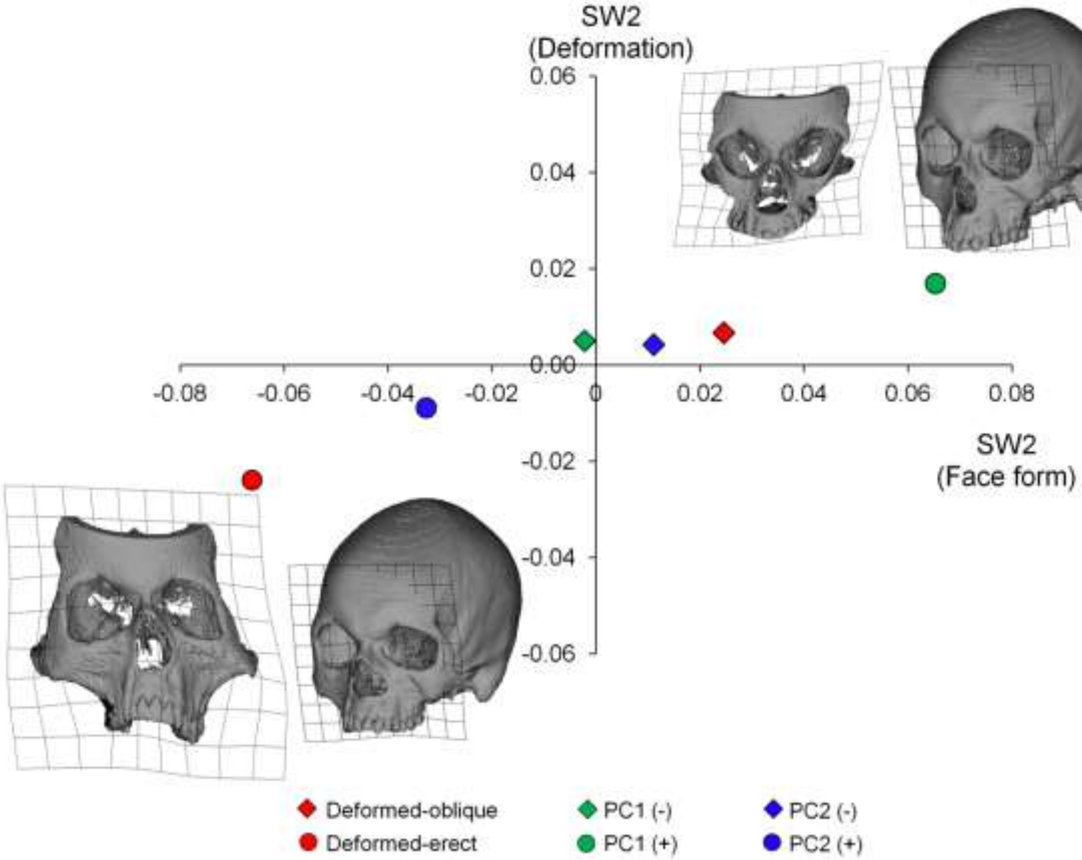

Figure 5.23. Partial least squares analysis of facial form vs. model deformation under left M1 biting, second pair of SWs. The pairs of warpings at the extremes of the distributions are with respect to the mean of facial form (left) and model deformation (right). The warpings have been magnified five (face form) and 1000 (model deformation) times to facilitate visualisation.

5.4. Discussion.

The present study aimed to assess the effects of morphological variations of the human cranium on mechanical performance during static incisor and molar bites. Finite element models of human crania showing different morphologies were constructed. The predicted strains, bite forces, TMJ reaction forces and large scale deformations were compared to test the central hypothesis that there is no relationship between cranial form and masticatory system performance parameters. This was tested under three loading conditions: (1) model specific muscle force magnitudes, (2) identical muscle force magnitudes among individuals and (3) identical bite force magnitudes among individuals.

The sample comprised CT scans of living individuals with no known pathologies impacting on craniofacial form or function and two artificially deformed crania from an archaeological population that present extreme, culturally induced, morphological variations. Cranial form and system performance parameters show sufficient covariation to falsify the central hypothesis, that there is no relationship between cranial form and masticatory system performance parameters. Taking into account strain magnitudes as well as distributions, the differences in performance among models under the same bites are of similar magnitude to the differences among bites, as assessed by strain contour maps (Figures 5.8 to 5.13), Procrustes size and shape analyses (Figures. 5.14 to 5.16) and visualisations of large scale deformations (Figures 5.17 to 5.19). However focussing on the modes of deformation alone shows consistency in strain distributions and large scale deformations (I1 and left M1 bites group) within biting simulations.

The deformed crania are, as expected, morphological outliers whether the cranium, or to a lesser extent the face, are considered (PCAs of Figures 5.6 and 5.7). They also possess the largest faces (Table 5.2). Interestingly however, the most unusual cranium in terms of its strain distributions as visualised in the contour maps and large scale deformations, especially in simulated molar biting, is that labelled PC2(+). This possesses the smallest, least prognathic, relatively most narrow and tall maxilla.

These results have implications for understanding how human masticatory system morphological variation impacts on cranial performance during biting. The findings and conclusions of this study are discussed in more detail below.

Deformed vs. non deformed crania

The deformed crania have undergone severe modifications of the normal development of the neurocranium, but this practice also impacts facial form (Cheverud et al., 1992; Cheverud and Midkiff, 1992; Manríquez et al., 2006; Khonsari et al., 2013). The findings of this study confirm this; in the PCA of facial form (Figure 5.7), artificially deformed crania show distinctive facial form in PC2.

Despite the differences in face morphology between deformed and non-deformed crania, their strain maps, bite forces and large scale deformations are less distinctive than one of the living individuals, PC2(+), which also differs from the remaining individuals in the face form analysis (Figure 5.7). This suggests that not all aspects of form impact on the response of the craniofacial skeleton to loading and this is borne out by the PLS analyses of face form vs. cranial deformation (Figures 5.20 to 5.23) where not all of the variance in facial form is associated with variance in deformation.

The results of the present study indicate that artificial cranial deformations do not result in particularly unusual cranial performance under simulated bites, with moderate effects on strains, large scale deformations, bite forces and bite force production efficiencies (bite force/muscle force). The pronounced asymmetries in the faces of the deformed crania appear to be a significant driver of the differences they show with respect to the living individuals. The artificially induced deformations of the cranium and face appear to be insufficiently large to alter performance markedly. However, it is important to note that under identical muscle loads, the deformed erect individual showed a considerably higher reaction force at the TMJs (Table 5.4). In this case, the predicted high values of TMJ reaction force suggest that a skull with such characteristics might not be able to function under high muscle loads without the risk of TMJ damage. Further studies of pathological findings in populations practising artificial cranial deformation are suggested to understand the effects of cranial deformation on TMJ function and dysfunction.

Artificial deformation of the neurocranium impacts on the attachment area of the temporalis muscle and so might have an effect on muscle force production and lever arms. However, the studies of Chapter 4 show that quite large perturbations of muscle forces impact on strain magnitudes but minimally on the spatial distribution of strains over the cranium and especially the face. Thus it is plausible that neurocranial deformation has little impact on biting and cranial performance because any impact on muscle force production (especially of the temporalis) has little effect on the modes of cranial deformation under different bites.

However, it may be that the impact of neurocranial deformation on facial form and so biting performance and deformation is minimised by the underlying mechanisms that modulate craniofacial growth, adapting it to its mechanical environment. Thus, bite forces and forces from muscle action modulate craniofacial growth remodelling via functional matrices (Moss, 1962; Moss, 1997). Any perturbations of morphogenesis (such as through neurocranial binding) on the face might then be compensated by the action of these functional matrices which act to maintain functional form. The existence of such compensatory mechanisms is expected given the broad range of vital functions maintained by the different parts of the skull: encephalon and nerve support, sensory functions, feeding and breathing. At the same time, the parts of the cranium show modular but integrated behaviour during development (van der Klaauw, 1948-1952; Cheverud, 1982; Lieberman et al., 2002; Goswami, 2006), this modularity and subsequent integration is thought to constrain phenotypic variation (Martínez-Abadías et al., 2009).

The process by which a phenotype develops consistently in a species despite environmental and genetic alterations is known as canalisation (Waddington, 1942; Alberch, 1980). Both phenotypic canalisation and modularity are evident in the sample of this study, particularly when considering the distinctive neurocranial morphology of the deformed individuals vs. their less distinctive facial form. This in agreement with the study on the morphological variations of artificially deformed crania by Martínez-Abadías et al. (2009). These authors found lower covariation between the calvarium and the face compared to that between the calvarium and the base. In other words, while the plasticity of the neurocranium becomes evident under the deforming forces, the development of the face, which is integrated with the neurocranium but not directly affected by the deforming appliance, is canalised. Thus, neurocranium and face behave as somewhat distinct modules but they are not entirely independent. Further studies carried out to test the hypothesis of functional modularity of the neurocranium and face will help to understand this relationship.

Studies in animal models have shown that during development, variation and canalisation are not necessarily antagonistic processes (Zelditch et al., 2004; Hallgrímsson et al., 2006). The degree of morphological variation increases when the time between the appearance of the variant traits and the occurrence of the canalisation mechanism is large (Zelditch et al., 2004). In the case of the human cranium, the face matures later than the neurocranium

(Bastir et al., 2006). Yet, supported by the presence of normally worn teeth, the deformed individuals in the present study do not present signs of marked functional impairment derived from the cranial deformation. As mentioned above, it may well be that masticatory system loading canalises facial morphogenesis as has been suggested by Moss (1962) in the functional matrix hypothesis. Since such loading would likely impact the face to a much greater degree than the neurocranium, this hypothesis also predicts that their morphogenesis is relatively independent. This is considered in more detail below.

Face morphology and mechanical performance

Functional loading of the facial skeleton during biting is a well recognised factor modulating cranial development in primates (Moss, 1962; Herring and Lakars, 1981; Demes and Creel, 1988; Zelditch et al., 2004; Kupczik et al., 2009). The jaws act as a lever system, the form of which impacts on force output by organising the relative positions of muscles, bite point and TMJs (Hylander, 1975; Herring, 1993; Spencer, 1998). Despite variations in facial morphology and loading conditions, the results of the present study show a consistent pattern of strain distribution among individuals. These resemble the results of other FEA studies of human and non-human primates (Gross et al., 2001; Kupczik et al., 2009; Strait et al., 2009; Wroe et al., 2010; Ross et al., 2011; Szwedowski et al., 2011; Fitton et al., 2012; Jansen van Rensburg et al., 2012). High strains are localised to five key areas: masseter and medial pterygoid insertions, the skeleton closely related to the biting tooth, the mandibular fossae and, depending on bite location, the compact-bone structures surrounding facial cavities that form the facial buttresses (Donat et al., 1998; Linnau et al., 2003). Strains in these regions mainly vary in magnitude rather than distribution. From the results of this study, and particularly the PLS analyses it is clear that the degree of subnasal prognathism, and the form of the alveolar process and dental arch are the main modes of variation that impact on the mode of model deformation in biting simulations.

The importance of maxillary form in determining the mechanical performance of masticatory system performance in humans is well known. Thus, during evolution, there has been a decrease in masticatory muscle CSA and hence potentially bite force. However bite force has to some degree been maintained by shortening and relocating the jaws more posteriorly (Demes and Creel, 1988; Lieberman, 1998; Trinkaus, 2003). The models in the present study illustrate how such variations in prognathism impact on biting performance. The two individuals with the least prognathic and narrowest maxillae, namely PC1(-) and particularly PC2(+), show the highest bite forces and lowest muscle CSAs. For I1 and M1 bites, these individuals show small dorso-ventral and medio-lateral deformations of the alveolar process. But under M1 bites the deformation is larger at upper facial levels and particularly at the orbit (see the visualisations of the PCAs of model deformation and PLSs), irrespective of the loading conditions. During M1 biting, the more prognathic, wider maxillae deform more in the buccal direction at the alveolar process, causing upper facial structures such as the orbits and the nasal cavities to deform less compared to the less prognathic individuals. Thus, the deformation of the alveolar process during M1 bites appears to limit strains in other facial structures in a similar way to that which has been proposed for the rostrum in mammals (Thomason and Russell, 1986; Rafferty et al., 2003; Lieberman, 2008). On the other hand, orthognathic faces have a more advantageous muscle/bite moment arm ratio, producing high I1 bite force with a relatively low muscle force input. They also show the lowest TMJ reaction forces.

Considering the latter, the morphology of orthognathic individuals seems best able to withstand high anterior dental loads, since the maxilla produces a high bite force with the lowest facial strains. However, as noted earlier in the analysis of model deformations, during M1 bites the deformation is larger in these individuals in superior parts of the face (particularly the orbit). This suggests that during high-force molar bites a larger, broader, buccally inclined maxilla offers greater resistance to deformation (SW1s from molar biting; Figure 5.21). During high-force unilateral M1 bites, TMJ reaction forces in the balancing side can be large relative to the working side in all the individuals. Considering the results of I1 and M1 bites, no individual manifests a morphology that simultaneously offers a particularly advantageous muscle/bite moment arm ratio, balanced working/balancing side TMJ reaction forces while deforming minimally.

The relationship between cranial morphology and mechanical performance

Morphological variation in the modern human craniofacial skeleton is associated with several factors including population history, geography, climate and diet (Strand Viðarsdóttir et al., 2002; Lieberman, 2008; Noback et al., 2011; Smith, 2011; von Cramon-Taubadel, 2011, 2013). Von Cramon-Taubadel (2011) showed that the shape of the mandible is significantly correlated with diet. The maxilla-palate complex is also correlated with diet, but not significantly so when controlling for the effects of population history. On the other hand neurocranial form does not appear to correlate with diet but with population history, climate and geography. Correlation between climate and the 3D geometry of the nasal cavity has also been noted (Noback et al., 2011), while cranial metric traits appear to correlate with geography but not with climate (Betti et al., 2009). Craniofacial form is therefore related to diverse factors, to different extents and different regions manifest morphological adaptations to masticatory system loadings. The findings of the PLS analyses concur in that they emphasise the primary role of maxillary form in relation to facial skeletal performance during biting.

Thus, variations in maxillary form are particularly strongly associated with variations in cranial performance in biting simulations. This is not surprising since the maxilla physically interacts with the mandible through occlusion. It is also directly related to adjacent facial regions, such as the orbits. It therefore has to adapt to masticatory loads applied via the mandible while maintaining anatomical and functional relationships with other craniofacial regions through functional matrices (Moss, 1962; Moss, 1997) whereby mechanical loadings induce strains and so adaptation. Thus, stronger morphological covariation between the maxilla and the mandible has been found in non-human extant primates than in humans. This has been attributed to the physical constraints on development in non-human primates imposed by large interlocking canines (Stelzer et al., 2013).

Dental occlusion in humans is believed to be a key factor in determining loading of the masticatory system and subsequent modulation and integration of facial growth. Normal occlusion, as in the individuals of the present study, can be achieved despite considerable variations in craniofacial morphology. Further studies in individuals with altered maxillomandibular relationships are necessary to assess the effects of occlusion on facial mechanics and form. An interesting model is presented by patients undergoing orthognathic surgery, who have previously developed an adult morphology with altered occlusion. The changes in morphology and lever arms potentially affect overall strain distributions, bite forces and TMJ reaction forces and so these individuals present an opportunity to study subsequent adaptation to these changes to the extent that such adaptations are still possible given the age at which surgery is undertaken. Additionally, our diet has become increasingly rich in processed food (Lieberman, 2008; Satia, 2010) and this is likely to impact on facial development. Studies of secular change in populations with known dietary histories provide an interesting opportunity to further relate loading to morphogenesis using FEA. This is worth exploring in future work.

5.5. Conclusion

The results of the present study have shown that different craniofacial morphologies show associated differences in mechanical performance in terms of strain distributions and magnitudes, bite forces, TMJ reaction forces and large scale deformations. The hypothesis that there is no relationship between cranial form and masticatory system performance parameters is therefore falsified. However, this relationship is mostly related to a small number of features of form, the most significant of which is the degree of prognathism. The main differences among individuals were found in strain, bite force, TMJ reaction force and large scale deformation magnitudes, whereas strain distributions and modes of large scale deformation were more consistent. These findings are to a large degree independent of the presence of intentional cranial deformation. This may be because normal dental occlusion and maxilla-mandibular relationships are maintained among individuals, which results in maintenance of relatively normal loading histories and so morphogenesis. Therefore, as long as normal occlusion is maintained the development of cranial form is relatively unconstrained by mastication; it can vary quite considerably because of other factors such as population history or climate.

Chapter 6 : Concluding remarks

Among primates, the human masticatory apparatus shows distinctive features such as a vertically inclined face, chin, relatively small teeth and jaw-elevator muscles; features that have been proposed to relate to changes in diet during evolution (Teaford and Ungar, 2000; Trinkaus, 2003; Lieberman et al., 2004; Stedman et al., 2004; Taylor and Vinyard, 2013).

Variations in facial morphology among modern humans are thought to be the result of several factors including population history and geography, climate and diet (Strand Viðarsdóttir et al., 2002; Lieberman, 2008; Noback et al., 2011; Smith, 2011; von Cramon-Taubadel, 2011; von Cramon-Taubadel, 2013). However, among these only the form of the mandible (Nicholson and Harvati, 2006; von Cramon-Taubadel, 2011), and less markedly the maxilla (von Cramon-Taubadel, 2011) are believed to reflect masticatory behaviour.

At the individual level, masticatory system loadings are important for normal facial development and form the basis of the functional matrix hypothesis that concerns the regulation of facial growth via forces (Moss, 1962; Moss, 1997). Thus, knowing the relationship between skull form and masticatory performance is essential in understanding the role of mastication in skull morphogenesis. Furthermore, studies at all of the levels above, but particularly in different individuals and populations are relevant to understanding disorders affecting masticatory system form and function.

With such studies in mind this thesis investigated the impact of morphological variation on the biting performance of modern humans, particularly in terms of the response of the cranial skeleton to loading using finite element analysis (FEA). This is a technique that has been increasingly used to study the functional factors underlying primate development (Kupczik et al., 2009) and evolution (Strait et al., 2009; Wroe et al., 2010; Gröning et al., 2011b), and the response of the human cranium to biting (Gross et al., 2001; Jansen van Rensburg et al., 2012). However, before using FEA in this thesis, it was necessary to assess the extent to which an FEA model of a human cranium could produce valid results and better understand the impact of necessary approximations and simplifications on model performance.

The general hypothesis that this thesis tests is that there is no relationship between cranial morphology and certain parameters of biting performance; particularly skeletal deformations assessed as predicted strains and changes in model size and shape analyses.

Prior to testing this hypothesis, three studies were performed that aimed to validate and carry out sensitivity analyses of modelling and simulation approaches. The results of these studies were then applied in the building and loading of FE models of six human crania, including two individuals with artificial deformations of the neurocranium, to assess the relationship between cranial form and mechanical performance.

The main findings of each study are summarised below.

Validation of a voxel-based finite element model of a human cranium using digital speckle interferometry

This study carried out a number of experiments with modelling approaches to assess the validity of certain approximations and simplifications in FE model construction. Further, the sensitivity of an FE model of a human cranium to various simplifications was assessed.

To assess the validity of different FE models based on the same cadaveric cranium, the strains and bite forces predicted by each of them were compared with those measured experimentally in the actual specimen using an optical technique (digital speckle interferometry).

Model sensitivity was assessed by comparing FEA results among models built using different approaches to simplify model geometry and resolution: including or omitting cancellous bone and inner sinus walls, and increasing or reducing the number of elements.

The first hypothesis tested was that there are no differences in distribution, magnitude and direction between the strains predicted by FE models built using different segmentation approaches and those measured experimentally. In terms of the distributions of strain magnitudes as seen in the contour maps, this hypothesis is not falsified; predicted strain distributions as well as directions showed strong similarities to those experimentally measured. However, the model built without cancellous bone predicted strain magnitudes that were three to four times lower than the experimentally measured ones and those in the other models. The accuracy of reconstruction of inner sinus walls had a significant effect on strains in the frontal process of the maxilla. The effect of model resolution on strains was negligible over the limited range tested in this thesis.

The second hypothesis was that there are no differences between the bite forces predicted by FE models built using different segmentation approaches and those measured experimentally. This hypothesis was falsified. Bite forces produced by all models were larger than the reaction forces at the incisors measured during the experiment by 23-27%. However, among models the differences in predicted bite forces were less than 2% of the mean.

Model sensitivity to variations in modelling decisions, was also assessed in terms of resulting model deformation. The third hypothesis was that FE models of the same skull built using different segmentation approaches predict the same modes of large scale deformation. This hypothesis was not falsified. The general mode of deformation was consistent among models, and consisted of dorso-ventral displacement of the maxilla at the level of the nasal notch. The main differences occurred when inner sinus walls were not reconstructed. These models showed greater deformation of the nasal region and maxilla with an additional unilateral displacement of the nasal notch.

These results show that FE models of human crania built using approaches such as those depicted here are generally reliable in that they predict general modes of deformation. The models that best predict mode of deformation and so strain distributions in contour maps include reconstructed maxillary sinus medial walls. With regard to magnitudes of strain (and thus by extension modes of large scale deformation) filled in, solid models appear too stiff.

The results of these studies provide a frame of reference for building FE models of the cranium. Bearing in mind the potential error in predicting strain magnitudes, it is recommended that in studies where absolute rather than relative magnitudes are of importance further validation analyses are performed to ensure model reliability when a certain anatomical reconstruction approach is chosen.

Can muscle cross-sectional area be predicted from skull morphology?

This chapter comprised two studies assessing two aspects of the relationship between skull shape and muscle force. The aim of the first study was to assess the predictability of muscle cross-sectional area (CSA) from bony features. Two independent variables are studied: (1) the area enclosed by muscle markings on bone (referred to as muscle area) and (2) skull size. The hypothesis was that there is no relationship between muscle CSAs, muscle areas estimated using bony features, and skull size.

The aim of the second study was to assess the association between skull shape and muscle CSA. The hypothesis was that there is no association between skull shape and masticatory muscle CSAs.

The first hypothesis was not falsified. It was found that muscle CSA, an estimator of muscle force, has low predictability from bony proxies. Their use tends to result in overestimates of muscle CSAs. This is important for mechanical studies of the masticatory system in fossils or archaeological material where muscle CSA cannot be directly measured.

The second hypothesis, that there is no association between skull shape and muscle CSA, was also not falsified. The proportion of temporalis CSA showed the strongest association with skull, and particularly, facial shape but this was not significant after Bonferroni correction. The generally poor relationship between cranial shape and muscle CSAs suggests a limited effect of jaw-elevator muscle force on adult skull morphology. This contrasts with the findings of several previous studies (Weijs and Hillen, 1986; Hannam and Wood, 1989; van Spronsen et al., 1992) that have suggested such a link. The reasons for this discrepancy may well lie in the methods used in previous studies to assess skull morphology; these have relied on linear measurements and so have included size. Size has been noted to show a weak relationship with muscle CSAs but also shows an allometric relationship with skull shape (Rosas and Bastir, 2002). These correlations could have confounded previous studies. Alternatively sample size may have been inadequate in the present study. Further, more extensive morphometric analyses are called for to clarify the discrepancies between the findings of this and previous studies.

The effect of varying jaw-elevator muscle force on the finite element model of a human cranium

This sensitivity study assessed the effects of varying the relative force magnitudes among jaw-elevator muscles in the finite element model of a human cranium. This is important to understand how varying loading, e.g. using estimates of muscle force or particular levels of muscle activation impact on FE model performance. This is relevant where full muscle force data are not available.

One model of the human cranium was loaded with several combinations of muscle forces: homogenously and asymmetrically scaled force magnitudes, plus heterogeneously scaled forces (i.e. muscles forces on the same side activated to different degrees). The hypothesis was that there is no effect of varying the relative magnitudes of muscle forces during the same biting task on FEA results in terms of strain distribution and magnitude, bite force, TMJ reaction force and large scale model deformation.

This hypothesis was not falsified. As expected, total applied muscle force had a directly proportional effect on predicted strain magnitudes, bite forces and large scale deformations. However, despite varying the relative magnitudes of muscle activations, the spatial distribution of regions of high and low strain, as well as large scale deformation remained approximately constant among loadcases.

The effect on strains over the TMJ surface and the reaction forces of the most asymmetric (total muscle force per side) loadcases is to invert the ‘normal’ relationship between sides in terms of relative magnitudes of these quantities. These loadcases represent rather extreme loading conditions unlikely to be found during normal biting.

These results indicate that when strain distributions are of interest, the use of symmetric maximum muscle forces can be considered a reliable simplification approach to loading of FE models of the human cranium. When the magnitudes of strains and bite forces are of interest, physiologically meaningful values can only be attained by physiologically reasonable loadings.

The relationship between cranial form and masticatory system performance parameters.

The final chapter of this thesis addressed the main question of this thesis: what is the relationship between cranial form and masticatory function? The central hypothesis is that there is no relationship between cranial form and masticatory system performance parameters. The results of the previous studies provided a frame of reference for the construction of the FE models of six morphologically different crania, including two artificially deformed individuals. These models were used to simulate central incisor (I1) and first molar (M1) bites, and compared in terms of resulting strain distribution, magnitudes, bite forces and large scale model deformations. Three different loading scenarios were simulated, one aiming to assess cranial performance under their original loads, and two under equivalent muscle and bite forces.

The first hypotheses was that there are no differences in strain distributions, magnitudes, bite forces, TMJ reaction forces and large scale deformations among models loaded with maximal muscle forces estimated from their individual anatomies (CT scans for living and bony proxies for archaeological individuals).

The second hypothesis was that there are no differences in strain distributions, magnitudes, bite forces, TMJ reaction forces and large scale deformations among models loaded with identical muscle force magnitudes.

The third hypothesis was that there are no differences in strain distribution and magnitudes, and large scale deformations among models exerting the same bite force magnitudes.

The results of this study falsified the central hypothesis. Different craniofacial morphologies showed similar but not identical mechanical performance in terms of strain distributions and magnitudes, bite forces, TMJ reaction forces and large scale deformations, irrespective of the loading conditions and the presence or absence of artificial cranial deformation. The relationship between cranial form and FE model performance is mostly driven by features of the lower face, the most significant of which is the degree of prognathism. The main differences among individuals were found in strain, bite force, TMJ reaction force and large scale deformation magnitudes, whereas strain distributions and modes of large scale deformation were more consistent. Individuals with the least prognathic, narrow maxillae showed the highest bite forces, the lowest strains and TMJ reaction forces during I1 bites and the highest strains during M1 bites. The models of these individuals also were deformed the most at the orbits during M1 bites. These findings are independent of the presence of intentional cranial deformation. Despite the morphological differences among crania, all individuals had normal dental occlusion and maxillomandibular relationships are maintained, which may well have led to similar loading histories and hence, morphogenesis. This requires further investigation through ontogenetic studies.

Conclusions and directions for future research

The findings of this thesis provide novel insights into how to reliably build and load FE models of the human cranium in terms of (1) model geometry and resolution and (2) applied jaw-elevator muscle forces. The FE models of the human cranium that included simplifications of bone internal anatomy and muscle loadings performed reasonably in terms of estimating strain distributions and large scale model deformations but impacted on magnitudes. As expected, total muscle force also impacts on strain and bite force magnitudes, in a predictable way. Temporomandibular joint reaction forces behaved as reported in the literature except when applied forces were unrealistically asymmetric. Thus strain distributions and large scale deformations can be predicted with more reliability than magnitudes of strains and reaction forces. To achieve accurate prediction of these, not only are physiologically accurate muscle loadings required but the internal anatomy of the craniofacial skeleton needs to be very accurately reproduced. This is difficult with current computing and manpower resources.

The FE models of six morphologically different crania were built to test the general hypothesis that there is no relationship between cranial form and masticatory system performance parameters. This hypothesis was falsified. However, features of the lower face principally impact or masticatory performance; the most significant of which is the form of the maxilla.

Additionally, and when previous studies on the validity and sensitivity of craniofacial structures to modelling approaches are considered (Ross et al., 2005; Kupczik et al., 2007; Szwedowski et al., 2011; Wood et al., 2011; Fitton et al., 2012), the results of this thesis suggest that FEA is a reliable method to investigate parameters of masticatory performance in primates. However, FEA reliability is rather low in predicting strain magnitudes. Further studies are needed to assess the extent to which this conclusion applies in other species.

The relationships found in this thesis between facial form and masticatory system performance suggest that, when the limitations are borne in mind, FEA-based studies can be usefully applied used to questions relating to normal and pathological functioning and pathogenesis of disorders of the masticatory system, as well as the impact of specific treatments. Furthermore, FEA appears to be a reliable tool to be applied to the study of the functional basis of skull evolution and morphogenesis.

References

AIELLO, L., DEAN, C. & CAMERON, J. 1990. *An introduction to human evolutionary anatomy,* London, Academic Press.

ALBERCH, P. 1980. Ontogenesis and morphological diversification. *American Zoologist,* 20**,** 653-667.

ANDERSON, M. J. 2001. A new method for non-parametric multivariate analysis of variance. *Austral Ecology,* 26**,** 32-46.

ANDERSON, P. S. L., BRIGHT, J. A., GILL, P. G., PALMER, C. & RAYFIELD, E. J. 2012. Models in palaeontological functional analysis. *Biology Letters,* 8**,** 119-122.

ANTÓN, S. 1990. Neandertals and the anterior dental loading hypothesis: A biomechanical evaluation of bite force production. *Kroeber Anthropological Society Papers***,** 67-76.

ANTÓN, S. 1999. Macaque masseter muscle: internal architecture, fiber length and cross-sectional area. *International Journal of Primatology,* 20**,** 441-462.

ANTÓN, S. C. 1989. Intentional cranial vault deformation and induced changes of the cranial base and face. *American Journal of Physical Anthropology,* 79**,** 253-267.

ANTÓN, S. C. 1994. *Masticatory muscle architecture and bone morphology in primates.* University of California, Berkeley.

ANTÓN, S. C. 1996. Tendon-associated bone features of the masticatory system in Neandertals. *Journal of Human Evolution,* 31**,** 391-408.

BARAK, M. M., GEIGER, S., CHATTAH, N. L.-T., SHAHAR, R. & WEINER, S. 2009. Enamel dictates whole tooth deformation: a finite element model study validated by a metrology method. *Journal of Structural Biology,* 168**,** 511-520.

BARAK, M. M., LIEBERMAN, D. E. & HUBLIN, J.-J. 2011. A Wolff in sheep's clothing: Trabecular bone adaptation in response to changes in joint loading orientation. *Bone,* 49**,** 1141-1151.

BARTON, E. R. 2012. Mechanical signal transduction: divergent communication and the potential consequences for masticatory muscle. *Seminars in Orthodontics,* 18**,** 2-9.

BASTIR, M., ROSAS, A. & O'HIGGINS, P. 2006. Craniofacial levels and the morphological maturation of the human skull. *Journal of Anatomy,* 209**,** 637-654.

BEHRENTS, R. G., CARLSON, D. S. & ABDELNOUR, T. 1978. *In vivo* analysis of bone strain about the sagittal suture in *Macaca mulatta* during masticatory movements. *Journal of Dental Research,* 57**,** 904-908.

BENAZZI, S., KULLMER, O., GROSSE, I. R. & WEBER, G. W. 2012. Brief communication: Comparing loading scenarios in lower first molar supporting bone structure using 3D finite element analysis. *American Journal of Physical Anthropology,* 147, 128-134.

BENAZZI, S., STANSFIELD, E., MILANI, C. & GRUPPIONI, G. 2009. Geometric morphometric methods for three-dimensional virtual reconstruction of a fragmented cranium: the case of Angelo Poliziano. *International Journal of Legal Medicine,* 123, 333-344.

BETTI, L., BALLOUX, F., AMOS, W., HANIHARA, T. & MANICA, A. 2009. Distance from Africa, not climate, explains within-population phenotypic diversity in humans. *Proceedings of the Royal Society B: Biological Sciences,* 276, 809-814.

BHAT, M. & ENLOW, D. H. 1985. Facial variations related to headform type. *The Angle Orthodontist,* 55, 269-280.

BLANKSMA, N. & VAN EIJDEN, T. 1995. Electromyographic heterogeneity in the human temporalis and masseter muscles during static biting, open\ close excursions, and chewing. *Journal of Dental Research,* 74, 1318-1327.

BOOKSTEIN, F. L. 1984. A statistical method for biological shape comparisons. *Journal of Theoretical Biology,* 107, 475-520.

BOOKSTEIN, F. L. 1989. Principal warps: thin-plate splines and the decomposition of deformations. *IEEE Transactions on Pattern Analysis and Machine Intelligence,* 11, 567-585.

BOOKSTEIN, F. L. 1991. *Morphometric tools for landmark data: geometry and biology,* Cambridge, University Press.

BOOKSTEIN, F. L. 2012. Geometric Morphometrics and Finite Element Analysis: First Results from a Joint Formalism for Modeling Strain. *In:* BREITENECKER, F. & TROCH, I. (eds.) *7th Vienna Conference on Mathematical Modelling.* Vienna University of Technology.

BREKELMANS, W., POORT, H. & SLOOFF, T. 1972. A new method to analyse the mechanical behaviour of skeletal parts. *Acta Orthopaedica,* 43, 301-317.

BRIGHT, J. A. 2012. The Importance of Craniofacial Sutures in Biomechanical Finite Element Models of the Domestic Pig. *PLoS ONE,* 7, e31769.

BRIGHT, J. A. & GRÖNING, F. 2011. Strain accommodation in the zygomatic arch of the pig: a validation study using digital speckle pattern interferometry and finite element analysis. *Journal of Morphology,* 272, 1388-1398.

BRIGHT, J. A. & RAYFIELD, E. J. 2011. The Response of Cranial Biomechanical Finite Element Models to Variations in Mesh Density. *The Anatomical Record: Advances in Integrative Anatomy and Evolutionary Biology,* 294, 610-620.

BUGAIGHIS, I., O'HIGGINS, P., TIDDEMAN, B., MATTICK, C., ALI, O. B. & HOBSON, R. 2010. Three-dimensional geometric morphometrics applied to the study of children with cleft lip and/or palate from the North East of England. *The European Journal of Orthodontics,* 32**,** 514-521.

CARTER, D. R. & CALER, W. E. 1985. A cumulative damage model for bone fracture. *Journal of Orthopaedic Research,* 3**,** 84-90.

CLARKE, L., VELTHUIZEN, R., CAMACHO, M., HEINE, J., VAIDYANATHAN, M., HALL, L., THATCHER, R. & SILBIGER, M. 1995. MRI segmentation: methods and applications. *Magnetic Resonance Imaging,* 13**,** 343-368.

CORTI, M., AGUILERA, M. & CAPANNA, E. 2001. Size and shape changes in the skull accompanying speciation of South American spiny rats (Rodentia: *Proechimys* spp.). *Journal of Zoology,* 253**,** 537-547.

COURANT, R. 1943. Variational methods for the solution of problems of equilibrium and vibrations. *Bulletin of the American Mathematical Society,* 49**,** 23.

COWIN, S. C. 2001. The false premise of Wolff's law. *In:* COWIN, S. C. (ed.) *Bone biomechanics handbook.* Second ed. Boca Raton: CRC press

COX, P. G., FAGAN, M. J., RAYFIELD, E. J. & JEFFERY, N. 2011. Finite element modelling of squirrel, guinea pig and rat skulls: using geometric morphometrics to assess sensitivity. *Journal of Anatomy,* 219**,** 696-709.

CREATH, K. & SLETTEMOEN, G. Å. 1985. Vibration-observation techniques for digital speckle-pattern interferometry. *Journal of the Optical Society of America A,* 2**,** 1629-1636.

CURREY, J. D. 1988. The effect of porosity and mineral content on the Young's modulus of elasticity of compact bone. *Journal of Biomechanics,* 21**,** 131-139.

CURREY, J. D. 2003. How well are bones designed to resist fracture? *Journal of Bone and Mineral Research,* 18**,** 591-598.

CURREY, J. D. 2006. *Bones: structure and mechanics,* Princeton, University Press.

CURTIS, N. 2011. Craniofacial biomechanics: an overview of recent multibody modelling studies. *Journal of Anatomy,* 218**,** 16-25.

CURTIS, N., JONES, M. E. H., EVANS, S. E., O'HIGGINS, P. & FAGAN, M. J. 2013. Cranial sutures work collectively to distribute strain throughout the reptile skull. *Journal of The Royal Society Interface,* 10.

CURTIS, N., WITZEL, U., FITTON, L., O'HIGGINS, P. & FAGAN, M. 2011. The mechanical significance of the temporal fasciae in *Macaca fascicularis*: an investigation using finite element analysis. *The Anatomical Record,* 294**,** 1178-1190.

CHEN, G., SCHUETZ, M. & PEARCY, M. 2010. Mechanobiology of bone development and computational simulations. *In:* BRONNER, F., FARACH-CARSON, M. C. & ROACH, H. I. (eds.) *Bone and development.* London: Springer.

CHEVERUD, J. M. 1982. Phenotypic, genetic, and environmental morphological integration in the cranium. *Evolution,* 36**,** 499-516.

CHEVERUD, J. M., KOHN, L. A. P., KONIGSBERG, L. W. & LEIGH, S. R. 1992. Effects of fronto-occipital artificial cranial vault modification on the cranial base and face. *American Journal of Physical Anthropology,* 88**,** 323-345.

CHEVERUD, J. M. & MIDKIFF, J. E. 1992. Effects of fronto-occipital cranial reshaping on mandibular form. *American Journal of Physical Anthropology,* 87**,** 167-171.

DE CLERCK, H., DERMAUT, L. & TIMMERMAN, H. 1990. The value of the macerated skull as a model used in orthopaedic research. *The European Journal of Orthodontics,* 12**,** 263-271.

DECHOW, P. C., NAIL, G. A., SCHWARTZ-DABNEY, C. L. & ASHMAN, R. B. 1993. Elastic properties of human supraorbital and mandibular bone. *American Journal of Physical Anthropology,* 90**,** 291-306.

DELAIRE, J. 1997. Maxillary development revisited: relevance to the orthopaedic treatment of Class III malocclusions. *The European Journal of Orthodontics,* 19**,** 289-311.

DEMES, B. 1987. Another look at an old face: biomechanics of the Neandertal facial skeleton reconsidered. *Journal of Human Evolution,* 16**,** 297-303.

DEMES, B. & CREEL, N. 1988. Bite force, diet, and cranial morphology of fossil hominids. *Journal of Human Evolution,* 17**,** 657-670.

DIGIROLAMO, D. J., KIEL, D. P. & ESSER, K. A. 2013. Bone and skeletal muscle: neighbors with close ties. *Journal of Bone and Mineral Research,* 28**,** 1509-1518.

DONAT, T. L., ENDRESS, C. & MATHOG, R. H. 1998. Facial fracture classification according to skeletal support mechanisms. *Archives of Otolaryngology—Head & Neck Surgery,* 124**,** 1306.

DOUGLAS-AKINWANDE, A. C., BUCKWALTER, K. A., RYDBERG, J., RANKIN, J. L. & CHOPLIN, R. H. 2006. Multichannel CT: Evaluating the Spine in Postoperative Patients with Orthopedic Hardware1. *Radiographics,* 26**,** S97-S110.

DRYDEN, I. & MARDIA, K. 1993. Multivariate shape analysis. *Sankhyā: The Indian Journal of Statistics, Series A***,** 460-480.

DRYDEN, I. & MARDIA, K. 1998. *Statistical shape analysis.,* Chichester, Wiley.

DUMONT, E., GROSSE, I. & SLATER, G. 2009. Requirements for comparing the performance of finite element models of biological structures. *Journal of Theoretical Biology,* 256**,** 96-103.

DUMONT, E. R., PICCIRILLO, J. & GROSSE, I. R. 2005. Finite-element analysis of biting behavior and bone stress in the facial skeletons of bats. *The Anatomical Record Part A: Discoveries in Molecular, Cellular, and Evolutionary Biology,* 283**,** 319-330.

DUNCAN, R. & TURNER, C. 1995. Mechanotransduction and the functional response of bone to mechanical strain. *Calcified Tissue International,* 57**,** 344-358.

EL HADDIOUI, A., BRAVETTI, P. & GAUDY, J.-F. 2007. Anatomical study of the arrangement and attachments of the human medial pterygoid muscle. *Surgical and Radiologic Anatomy,* 29**,** 115-124.

ERIKSEN, E. F. 2010. Cellular mechanisms of bone remodeling. *Reviews in Endocrine and Metabolic Disorders,* 11**,** 219-227.

ERIKSSON, P.-O. & THORNELL, L.-E. 1983. Histochemical and morphological muscle-fibre characteristics of the human masseter, the medial pterygoid and the temporal muscles. *Archives of Oral Biology,* 28**,** 781-795.

ESCOUFIER, Y. 1973. Le traitement des variables vectorielles. *Biometrics***,** 751-760.

ETHIER, C. R. & SIMMONS, C. A. 2007. *Introductory biomechanics: from cells to organisms,* Cambridge, University Press.

FAGAN, M. 1992. *Finite element analysis: theory and practice,* Harlow, Longman.

FAGAN, M. J., CURTIS, N., DOBSON, C. A., KARUNANAYAJE, J. H., KUPCZIK, K., MOAZEN, M., PAGE, L., PHILLIPS, R. & O'HIGGINS, P. 2007. Voxel-based finite analysis - Working directly with MicroCT scan data. *Journal of Morphology,* 268**,** 1071.

FARELLA, M., PALUMBO, A., MILANI, S., AVECONE, S., GALLO, L. & MICHELOTTI, A. 2009. Synergist coactivation and substitution pattern of the human masseter and temporalis muscles during sustained static contractions. *Clinical Neurophysiology,* 120**,** 190-197.

FARIAS GOMES, S., CUSTODIO, W., FAOT, F., DEL BEL CURY, A. & RODRIGUES GARCIA, R. 2010. Masticatory features, EMG activity and muscle effort of subjects with different facial patterns. *Journal of Oral Rehabilitation,* 37**,** 813-819.

FERRARIO, V., SFORZA, C., COLOMBO, A. & CIUSA, V. 2000. An electromyographic investigation of masticatory muscles symmetry in normo-occlusion subjects. *Journal of Oral Rehabilitation,* 27**,** 33-40.

FERRIER, J., ROSS, S. M., KANEHISA, J. & AUBIN, J. E. 1986. Osteoclasts and osteoblasts migrate in opposite directions in response to a constant electrical field. *Journal of Cellular Physiology,* 129**,** 283-288.

FINK, B., GRAMMER, K., MITTEROECKER, P., GUNZ, P., SCHAEFER, K., BOOKSTEIN, F. L. & MANNING, J. T. 2005. Second to fourth digit ratio and face shape. *Proceedings of the Royal Society B: Biological Sciences,* 272**,** 1995-2001.

FISHMAN, E., MAGID, D., NEY, D., CHANEY, E., PIZER, S., ROSENMAN, J., LEVIN, D., VANNIER, M., KUHLMAN, J. & ROBERTSON, D. 1991. Three-dimensional imaging. *Radiology,* 181**,** 321-337.

FITTON, L., KUPCZIK, K., MILNE, N., FAGAN, M., O'HIGGINS, P. & O'HIGGINS, P. 2009. The role of sutures in modulating strain distribution within the skull of *Macaca fascicularis*. *American Journal of Physical Anthropology***,** 128-128.

FITTON, L., SHI, J., FAGAN, M. & O'HIGGINS, P. 2012. Masticatory loadings and cranial deformation in *Macaca fascicularis*: a finite element analysis sensitivity study. *Journal of Anatomy,* 221**,** 55-68.

FRIEß, M. & BAYLAC, M. 2003. Exploring artificial cranial deformation using elliptic Fourier analysis of procrustes aligned outlines. *American Journal of Physical Anthropology,* 122**,** 11-22.

FROST, H. M. 1973. *Bone modeling and skeletal modeling errors,* Springfield, Thomas.

FROST, H. M. 1987. Bone "mass" and the "mechanostat": a proposal. *The Anatomical Record,* 219**,** 1-9.

FROST, H. M. 1997. On our age-related bone loss: insights from a new paradigm. *Journal of Bone and Mineral Research,* 12**,** 1539-1546.

GARCÍA-MORALES, P., BUSCHANG, P. H., THROCKMORTON, G. S. & ENGLISH, J. D. 2003. Maximum bite force, muscle efficiency and mechanical advantage in children with vertical growth patterns. *The European Journal of Orthodontics,* 25**,** 265-272.

GAUDY, J.-F., ZOUAOUI, A., BRAVETTI, P., CHARRIER, J.-L. & GUETTAF, A. 2000. Functional organization of the human masseter muscle. *Surgical and Radiologic Anatomy,* 22**,** 181-190.

GAUDY, J.-F., ZOUAOUI, A., BRI, P., CHARRIER, J. & LAISON, F. 2002. Functional anatomy of the human temporal muscle. *Surgical and Radiologic Anatomy,* 23**,** 389-398.

GAUGHRAN, G. R. 1957. Fasciae of the masticator space. *The Anatomical Record,* 129**,** 383-400.

GINGERICH, P. D. 1979. The human mandible: lever, link, or both? *American Journal of Physical Anthropology,* 51**,** 135-137.

GONZÁLEZ, C. & WESTFALL, C. Cementerio Regimiento Chorrillos de Calama: Testimonios Funerarios Formativos en el Loa Medio, Región de Antofagasta. Actas del XVI Congreso de Arqueología Chilena, 9th-14th October 2006 2006 Valdivia, Chile. 95-105.

GOODALL, C. 1991. Procrustes methods in the statistical analysis of shape. *Journal of the Royal Statistical Society. Series B (Methodological)***,** 285-339.

GOSWAMI, A. 2006. Cranial modularity shifts during mammalian evolution. *The American Naturalist,* 168**,** 270-280.

GRÖNING, F., FAGAN, M. & O'HIGGINS, P. 2011a. The effects of the periodontal ligament on mandibular stiffness: a study combining finite element analysis and geometric morphometrics. *Journal of Biomechanics,* 44**,** 1304-1312.

GRÖNING, F., FAGAN, M. J. & O'HIGGINS, P. 2012. Modeling the human mandible under masticatory loads: which input variables are important? *The Anatomical Record,* 295**,** 853-863.

GRÖNING, F., LIU, J., FAGAN, M. & O'HIGGINS, P. 2009. Validating a voxel-based finite element model of a human mandible using digital speckle pattern interferometry. *Journal of Biomechanics,* 42**,** 1224-1229.

GRÖNING, F., LIU, J., FAGAN, M. J. & O'HIGGINS, P. 2011b. Why do humans have chins? Testing the mechanical significance of modern human symphyseal morphology with finite element analysis. *American Journal of Physical Anthropology,* 144**,** 593-606.

GROSS, M. D., ARBEL, G. & HERSHKOVITZ, I. 2001. Three-dimensional finite element analysis of the facial skeleton on simulated occlusal loading. *Journal of Oral Rehabilitation,* 28**,** 684-694.

GRÜNHEID, T., LANGENBACH, G. E., KORFAGE, J. A., ZENTNER, A. & VAN EIJDEN, T. M. 2009. The adaptive response of jaw muscles to varying functional demands. *The European Journal of Orthodontics,* 31**,** 596-612.

GUNZ, P. 2012. Evolutionary relationships among robust and gracile australopiths: an "evo-devo" perspective. *Evolutionary Biology***,** 1-16.

GUPTA, K., KNOELL, A. & GRENOBLE, D. 1973. Mathematical modeling and structural analysis of the mandible. *Artificial Cells, Blood Substitutes and Biotechnology,* 1**,** 469-479.

HACK, E. & SCHUMACHER, A. 2007. DSPI strain measurement on an externally reinforced bending beam: A comparison of step-by-step addition and pixel shift correlation. *Optics and Lasers in Engineering,* 45, 589-595.

HAGBERG, C. 1987. Assessment of bite force: a review. *Journal of Craniomandibular Disorders: Facial & Oral Pain,* 1, 162.

HAGBERG, C., AGERBERG, G. & HAGBERG, M. 1985. Regression analysis of electromyographic activity of masticatory muscles versus bite force. *European Journal of Oral Sciences,* 93, 396-402.

HALAZONETIS, D. J. 2004. Morphometrics for cephalometric diagnosis. *American Journal of Orthodontics and Dentofacial Orthopedics,* 125, 571-581.

HALL, B. K. 2005. *Bones and cartilage: developmental and evolutionary skeletal biology,* San Diego, Academic Press.

HALLGRÍMSSON, B., BROWN, J. J. Y., FORD-HUTCHINSON, A. F., SHEETS, H. D., ZELDITCH, M. L. & JIRIK, F. R. 2006. The brachymorph mouse and the developmental-genetic basis for canalization and morphological integration. *Evolution & Development,* 8, 61-73.

HAMMER, Ø., HARPER, D. & RYAN, P. 2012. PAST: paleontological statistics software package for education and data analysis. Paleontol Electron 4 (art. 4): 9. *Paleontologia Electronica,* 4, 9.

HANNAM, A. & WOOD, W. 1989. Relationships between the size and spatial morphology of human masseter and medial pterygoid muscles, the craniofacial skeleton, and jaw biomechanics. *American Journal of Physical Anthropology,* 80, 429-445.

HANNAM, A. G. & MCMILLAN, A. S. 1994. Internal organization in the human jaw muscles. *Critical Reviews in Oral Biology & Medicine,* 5, 55-89.

HART, R. T., HENNEBEL, V. V., THONGPREDA, N., VAN BUSKIRK, W. C. & ANDERSON, R. C. 1992. Modeling the biomechanics of the mandible: a three-dimensional finite element study. *Journal of Biomechanics,* 25, 261-286.

HARVATI, K. 2003. Quantitative analysis of Neanderthal temporal bone morphology using three-dimensional geometric morphometrics. *American Journal of Physical Anthropology,* 120, 323-338.

HENNESSY, R. J. & STRINGER, C. B. 2002. Geometric morphometric study of the regional variation of modern human craniofacial form. *American Journal of Physical Anthropology,* 117, 37-48.

HERRING, S. W. 1985. The ontogeny of mammalian mastication. *American Zoologist,* 25, 339-350.

HERRING, S. W. 1993. Functional morphology of mammalian mastication. *American Zoologist,* 33, 289-299.

HERRING, S. W. & LAKARS, T. C. 1981. Craniofacial development in the absence of muscle contraction. *Journal of Craniofacial Genetics and Developmental biology,* 1, 341-357.

HIDALGO, J., SCHIAPPACASSE, V., NIEMEYER, H., ALDUNATE, C. & SOLIMANO, I. (eds.) 1989. *Culturas de Chile: prehistoria, desde sus orígenes hasta los albores de la conquista*: Editoria Andrés Bello.

HOH, J. F. Y. 2002. `Superfast' or masticatory myosin and the evolution of jaw-closing muscles of vertebrates. *Journal of Experimental Biology,* 205, 2203-2210.

HORGAN, T. & GILCHRIST, M. 2003. The creation of three-dimensional finite element models for simulating head impact biomechanics. *International Journal of Crashworthiness,* 8, 353-366.

HRENNIKOFF, A. 1941. Solution of problems of elasticity by the framework method. *Journal of Applied Mechanics,* 8, 169-175.

HUANG, C. & OGAWA, R. 2010. Mechanotransduction in bone repair and regeneration. *The FASEB Journal,* 24, 3625-3632.

HUMAN TISSUE ACT. *2004* [Online]. Available: http://www.legislation.gov.uk/ukpga/2004/30/contents [Accessed 26th September 2013].

HYLANDER, W. L. 1975. The human mandible: lever or link? *American Journal of Physical Anthropology,* 43, 227-242.

HYLANDER, W. L. & JOHNSON, K. R. 1997. *In vivo* bone strain patterns in the zygomatic arch of macaques and the significance of these patterns for functional interpretations of craniofacial form. *American Journal of Physical Anthropology,* 102, 203-232.

HYLANDER, W. L., JOHNSON, K. R. & PICQ, P. G. 1991. Masticatory-stress hypotheses and the supraorbital region of primates. *American Journal of Physical Anthropology,* 86, 1-36.

IVASKA, J. 2012. Unanchoring integrins in focal adhesions. *Nature Cell Biology,* 14, 981-983.

JANSEN VAN RENSBURG, G. J., WILKE, D. N. & KOK, S. 2012. Human skull shape and masticatory induced stress: Objective comparison through the use of non-rigid registration. *International Journal for Numerical Methods in Biomedical Engineering.*

JILKA, R. L. 2003. Biology of the basic multicellular unit and the pathophysiology of osteoporosis. *Medical and Pediatric Oncology,* 41, 182-185.

JIMENEZ, P., MARTINEZ-INSUA, A., FRANCO-VAZQUEZ, J., OTERO-CEPEDA, X. L. & SANTANA, U. 2012. Maxillary changes and occlusal traits in crania with artificial fronto-occipital deformation. *American Journal of Physical Anthropology,* 147**,** 40-51.

KARSENTY, G. 1999. The genetic transformation of bone biology. *Genes & Development,* 13**,** 3037-3051.

KENDALL, D. G. 1977. The diffusion of shape. *Advances in Applied Probability***,** 428-430.

KENDALL, D. G. 1984. Shape manifolds, procrustean metrics, and complex projective spaces. *Bulletin of the London Mathematical Society,* 16**,** 81-121.

KENT, J. T. 1994. The complex Bingham distribution and shape analysis. *Journal of the Royal Statistical Society. Series B (Methodological)***,** 285-299.

KEYAK, J., MEAGHER, J., SKINNER, H. & MOTE, C. 1990. Automated three-dimensional finite element modelling of bone: a new method. *Journal of Biomedical Engineering,* 12**,** 389-397.

KHONSARI, R. H., FRIESS, M., NYSJÖ, J., ODRI, G., MALMBERG, F., NYSTRÖM, I., MESSO, E., HIRSCH, J. M., CABANIS, E. A. M., KUNZELMANN, K. H., SALAGNAC, J. M., CORRE, P., OHAZAMA, A., SHARPE, P. T., CHARLIER, P. & OLSZEWSKI, R. 2013. Shape and volume of craniofacial cavities in intentional skull deformations. *American Journal of Physical Anthropology,* 151**,** 110-119.

KILIARIDIS, S., GEORGIAKAKI, I. & KATSAROS, C. 2003. Masseter muscle thickness and maxillary dental arch width. *The European Journal of Orthodontics,* 25**,** 259-263.

KILIARIDIS, S. & KÄLEBO, P. 1991. Masseter muscle thickness measured by ultrasonography and its relation to facial morphology. *Journal of Dental Research,* 70**,** 1262-1265.

KILIARIDIS, S., MEJERSJÖ, C. & THILANDER, B. 1989. Muscle function and craniofacial morphology: a clinical study in patients with myotonic dystrophy. *The European Journal of Orthodontics,* 11**,** 131-138.

KITAGAWA, Y., MITERA, K., OGASAWARA, T., NOJYO, Y., MIYAUCHI, K. & SANO, K. 2004. Alterations in enzyme histochemical characteristics of the masseter muscle caused by long-term soft diet in growing rabbits. *Oral Diseases,* 10**,** 271-276.

KLINGENBERG, C., WETHERILL, L., ROGERS, J., MOORE, E., WARD, R., AUTTI-RÄMÖ, I., FAGERLUND, Å., JACOBSON, S., ROBINSON, L. & HOYME, H. 2010. Prenatal alcohol exposure alters the patterns of facial asymmetry. *Alcohol,* 44**,** 649-657.

KLINGENBERG, C. P. 2009. Morphometric integration and modularity in configurations of landmarks: tools for evaluating a priori hypotheses. *Evolution & Development,* 11**,** 405-421.

KLINGENBERG, C. P. 2011. MorphoJ: an integrated software package for geometric morphometrics. *Molecular Ecology Resources,* 11**,** 353-357.

KNOELL, A. 1977. A mathematical model of an *in vitro* human mandible. *Journal of Biomechanics,* 10**,** 159-166.

KOHN, L. A. P., LEIGH, S. R., JACOBS, S. C. & CHEVERUD, J. M. 1993. Effects of annular cranial vault modification on the cranial base and face. *American Journal of Physical Anthropology,* 90**,** 147-168.

KOOLSTRA, J. & TANAKA, E. 2009. Tensile stress patterns predicted in the articular disc of the human temporomandibular joint. *Journal of Anatomy,* 215**,** 411-416.

KOOLSTRA, J. & VAN EIJDEN, T. 2005. Combined finite-element and rigid-body analysis of human jaw joint dynamics. *Journal of Biomechanics,* 38**,** 2431-2439.

KOOLSTRA, J., VAN EIJDEN, T., WEIJS, W. & NAEIJE, M. 1988. A three-dimensional mathematical model of the human masticatory system predicting maximum possible bite forces. *Journal of Biomechanics,* 21**,** 563-576.

KORFAGE, J., KOOLSTRA, J., LANGENBACH, G. & VAN EIJDEN, T. 2005. Fiber-type composition of the human jaw muscles—(part 1) origin and functional significance of fiber-type diversity. *Journal of Dental Research,* 84**,** 774-783.

KORIOTH, T. W. P., WALDRON, T. W., VERSLUIS, A. & SCHULTE, J. K. 1997. Forces and moments generated at the dental incisors during forceful biting in humans. *Journal of Biomechanics,* 30**,** 631-633.

KUPCZIK, K. 2008. Virtual biomechanics: basic concepts and technical aspects of finite element analysis in vertebrate morphology. *Journal of Anthropological Sciences,* 86**,** 193-198.

KUPCZIK, K., DOBSON, C., CROMPTON, R., PHILLIPS, R., OXNARD, C., FAGAN, M. & O'HIGGINS, P. 2009. Masticatory loading and bone adaptation in the supraorbital torus of developing macaques. *American Journal of Physical Anthropology,* 139**,** 193-203.

KUPCZIK, K., DOBSON, C., FAGAN, M., CROMPTON, R., OXNARD, C. & O'HIGGINS, P. 2007. Assessing mechanical function of the zygomatic region in macaques: validation and sensitivity testing of finite element models. *Journal of Anatomy,* 210**,** 41-53.

LANGENBACH, G. & HANNAM, A. 1999. The role of passive muscle tensions in a three-dimensional dynamic model of the human jaw. *Archives of Oral Biology,* 44**,** 557-573.

LANGENBACH, G. E. & VAN EIJDEN, T. M. 2001. Mammalian feeding motor patterns. *American Zoologist,* 41**,** 1338-1351.

LENGSFELD, M., SCHMITT, J., ALTER, P., KAMINSKY, J. & LEPPEK, R. 1998. Comparison of geometry-based and CT voxel-based finite element modelling and experimental validation. *Medical Engineering & Physics,* 20**,** 515-522.

LIEBERMAN, D. E. 1998. Sphenoid shortening and the evolution of modern human cranial shape. *Nature,* 393**,** 158-162.

LIEBERMAN, D. E. 2008. Speculations about the selective basis for modern human craniofacial form. *Evolutionary Anthropology: Issues, News, and Reviews,* 17**,** 55-68.

LIEBERMAN, D. E. 2011. *The evolution of the human head,* Harvard, University Press.

LIEBERMAN, D. E., KROVITZ, G. E., YATES, F. W., DEVLIN, M. & ST. CLAIRE, M. 2004. Effects of food processing on masticatory strain and craniofacial growth in a retrognathic face. *Journal of Human Evolution,* 46**,** 655-677.

LIEBERMAN, D. E., MCBRATNEY, B. M. & KROVITZ, G. 2002. The evolution and development of cranial form in *Homo sapiens*. *Proceedings of the National Academy of Sciences,* 99**,** 1134-1139.

LINNAU, K. F., STANLEY JR, R. B., HALLAM, D. K., GROSS, J. A. & MANN, F. A. 2003. Imaging of high-energy midfacial trauma: what the surgeon needs to know. *European Journal of Radiology,* 48**,** 17-32.

LIU, J., SHI, J., FITTON, L. C., PHILLIPS, R., O'HIGGINS, P. & FAGAN, M. J. 2012. The application of muscle wrapping to voxel-based finite element models of skeletal structures. *Biomechanics and Modeling in Mechanobiology,* 11**,** 35-47.

LOVEJOY, C. O., MCCOLLUM, M. A., RENO, P. L. & ROSENMAN, B. A. 2003. Developmental biology and human evolution. *Annual Review of Anthropology***,** 85-109.

MANNS, A., MIRALLES, R. & PALAZZI, C. 1979. EMG, bite force, and elongation of the masseter muscle under isometric voluntary contractions and variations of vertical dimension. *The Journal of Prosthetic Dentistry,* 42**,** 674-682.

MANRÍQUEZ, G., GONZÁLEZ-BERGÁS, F. E., SALINAS, J. C. & ESPOUEYS, O. 2006. Deformación intencional del cráneo en poblaciones arqueológicas de Arica, Chile: análisis preliminar de morfometría geométrica con uso de radiografías craneofaciales. *Chungará (Arica),* 38**,** 13-34.

MARINESCU, R., DAEGLING, D. J. & RAPOFF, A. J. 2005. Finite-element modeling of the anthropoid mandible: The effects of altered boundary conditions. *The*

Anatomical Record Part A: Discoveries in Molecular, Cellular, and Evolutionary Biology, 283, 300-309.

MARTÍNEZ-ABADÍAS, N., PASCHETTA, C., AZEVEDO, S., ESPARZA, M. & GONZÁLEZ-JOSÉ, R. 2009. Developmental and genetic constraints on neurocranial globularity: insights from analyses of deformed skulls and quantitative genetics. *Evolutionary Biology,* 36, 37-56.

MARTÍNEZ-ABADÍAS, N., ESPARZA, M., SJØVOLD, T., GONZÁLEZ-JOSÉ, R., SANTOS, M., HERNÁNDEZ, M. & KLINGENBERG, C. P. 2012. Pervasive genetic integration directs the evolution of human skull shape. *Evolution.*

MCELHANEY, J. H., FOGLE, J. L., MELVIN, J. W., HAYNES, R. R., ROBERTS, V. L. & ALEM, N. M. 1970. Mechanical properties of cranial bone. *Journal of Biomechanics,* 3, 495-511.

MCNAMARA, J. 1975. Functional adaptations in the temporomandibular joint. *Dental Clinics of North America,* 19, 457.

MEREDITH, N., SHERRIFF, M., SETCHELL, D. & SWANSON, S. 1996. Measurement of the microhardness and Young's modulus of human enamel and dentine using an indentation technique. *Archives of Oral Biology,* 41, 539-545.

METZGER, K. A., DANIEL, W. J. & ROSS, C. F. 2005. Comparison of beam theory and finite-element analysis with *in vivo* bone strain data from the alligator cranium. *The Anatomical Record Part A: Discoveries in Molecular, Cellular, and Evolutionary Biology,* 283, 331-348.

MIDDLETON, J., JONES, M. & WILSON, A. 1996. The role of the periodontal ligament in bone modeling: the initial development of a time-dependent finite element model. *American Journal of Orthodontics and Dentofacial Orthopedics,* 109, 155-162.

MILNE, N. & O'HIGGINS, P. 2012. Scaling of form and function in the xenarthran femur: a 100-fold increase in body mass is mitigated by repositioning of the third trochanter. *Proceedings of the Royal Society B: Biological Sciences,* 279, 3449-3456.

MIRALLES, R., HEVIA, R., CONTRERAS, L., CARVAJAL, R., BULL, R. & MANNS, A. 1991. Patterns of electromyographic activity in subjects with different skeletal facial types. *The Angle Orthodontist,* 61, 277-284.

MISCH, C. E., QU, Z. & BIDEZ, M. W. 1999. Mechanical properties of trabecular bone in the human mandible: implications for dental implant treatment planning and surgical placement. *Journal of Oral and Maxillofacial Surgery,* 57, 700-706.

MITTEROECKER, P. & GUNZ, P. 2009. Advances in geometric morphometrics. *Evolutionary Biology,* 36, 235-247.

MOAZEN, M., CURTIS, N., O'HIGGINS, P., EVANS, S. E. & FAGAN, M. J. 2009. Biomechanical assessment of evolutionary changes in the lepidosaurian skull. *Proceedings of the National Academy of Sciences,* 106**,** 8273-8277.

MOORE, C. A., SMITH, A. & RINGEL, R. L. 1988. Task-specific organization of activity in human jaw muscles. *Journal of Speech, Language and Hearing Research,* 31**,** 670.

MOSS, M. L. 1962. The functional matrix. *Vistas in Orthodontics.* Philadelphia: Lea & Febiger.

MOSS, M. L. 1968. A theoretical analysis of the functional matrix. *Acta Biotheoretica,* 18**,** 195-202.

MOSS, M. L. 1997. The functional matrix hypothesis revisited. 1. The role of mechanotransduction. *American Journal of Orthodontics and Dentofacial Orthopedics,* 112**,** 8-11.

NETTER, F. H. 2006. *Atlas of human anatomy,* Philadelphia, Saunders.

NEUBAUER, S., GUNZ, P. & HUBLIN, J. J. 2009. The pattern of endocranial ontogenetic shape changes in humans. *Journal of Anatomy,* 215**,** 240-255.

NEWTON, J., YEMM, R., ABEL, R. & MENHINICK, S. 1993. Changes in human jaw muscles with age and dental state. *Gerodontology,* 10**,** 16-22.

NICHOLSON, E. & HARVATI, K. 2006. Quantitative analysis of human mandibular shape using three-dimensional geometric morphometrics. *American Journal of Physical Anthropology,* 131**,** 368-383.

NOBACK, M. L., HARVATI, K. & SPOOR, F. 2011. Climate-related variation of the human nasal cavity. *American Journal of Physical Anthropology,* 145**,** 599-614.

O'CONNOR, C. F., FRANCISCUS, R. G. & HOLTON, N. E. 2005. Bite force production capability and efficiency in Neandertals and modern humans. *American Journal of Physical Anthropology,* 127**,** 129-151.

O'HIGGINS, P. 2000. The study of morphological variation in the hominid fossil record: biology, landmarks and geometry. *Journal of Anatomy,* 197**,** 103-120.

O'HIGGINS, P., COBB, S. N., FITTON, L. C., GRÖNING, F., PHILLIPS, R., LIU, J. & FAGAN, M. J. 2011. Combining geometric morphometrics and functional simulation: an emerging toolkit for virtual functional analyses. *Journal of Anatomy,* 218**,** 3-15.

O'HIGGINS, P. & DRYDEN, I. L. 1993. Sexual dimorphism in hominoids: further studies of craniofacial shape differences in Pan, Gorilla and Pongo. *Journal of Human Evolution,* 24**,** 183-205.

O'HIGGINS, P., FITTON, L. C., PHILLIPS, R., SHI, J., LIU, J., GRÖNING, F., COBB, S. N. & FAGAN, M. J. 2012. Virtual functional morphology: novel approaches to the study of craniofacial form and function. *Evolutionary Biology,* 39**,** 521-535.

O'HIGGINS, P. & MILNE, N. 2013. Applying geometric morphometrics to compare changes in size and shape arising from finite elements analyses. *Hystrix, the Italian Journal of Mammalogy,* 24**,** 126-132.

OLSEN, B. R., REGINATO, A. M. & WANG, W. 2000. Bone development. *Annual Review of Cell and Developmental Biology,* 16**,** 191-220.

ÖSTERLUND, C., THORNELL, L. E. & ERIKSSON, P. O. 2011. Differences in fibre type composition between human masseter and biceps muscles in young and adults reveal unique masseter fibre type growth pattern. *The Anatomical Record: Advances in Integrative Anatomy and Evolutionary Biology,* 294**,** 1158-1169.

OXNARD, C. & O'HIGGINS, P. 2009. Biology Clearly Needs Morphometrics. Does Morphometrics Need Biology? *Biological Theory,* 4**,** 84-97.

PAL, N. R. & PAL, S. K. 1993. A review on image segmentation techniques. *Pattern Recognition,* 26**,** 1277-1294.

PANAGIOTOPOULOU, O., KUPCZIK, K. & COBB, S. N. 2011. The mechanical function of the periodontal ligament in the macaque mandible: a validation and sensitivity study using finite element analysis. *Journal of Anatomy,* 218**,** 75-86.

PARR, W., WROE, S., CHAMOLI, U., RICHARDS, H., MCCURRY, M., CLAUSEN, P. & MCHENRY, C. 2012. Toward integration of geometric morphometrics and computational biomechanics: new methods for 3D virtual reconstruction and quantitative analysis of finite element models. *Journal of Theoretical Biology,* 301**,** 1-14.

PEARSON, O. M. & LIEBERMAN, D. E. 2004. The aging of Wolff's "law": ontogeny and responses to mechanical loading in cortical bone. *American Journal of Physical Anthropology,* 125**,** 63-99.

PENIN, X., BERGE, C. & BAYLAC, M. 2002. Ontogenetic study of the skull in modern humans and the common chimpanzees: neotenic hypothesis reconsidered with a tridimensional Procrustes analysis. *American Journal of Physical Anthropology,* 118**,** 50-62.

PEREZ, S. I. 2007. Artificial cranial deformation in South America: a geometric morphometrics approximation. *Journal of Archaeological Science,* 34**,** 1649-1658.

PETERSON, J. & DECHOW, P. C. 2003. Material properties of the human cranial vault and zygoma. *The Anatomical Record Part A: Discoveries in Molecular, Cellular, and Evolutionary Biology,* 274A**,** 785-797.

PHAM, D. L., XU, C. & PRINCE, J. L. 2000. Current methods in medical image segmentation 1. *Annual Review of Biomedical Engineering,* 2**,** 315-337.

POLIACHIK, S. L., BAIN, S. D., THREET, D., HUBER, P. & GROSS, T. S. 2010. Transient muscle paralysis disrupts bone homeostasis by rapid degradation of bone morphology. *Bone,* 46**,** 18-23.

PRENTICE, A. 2001. The relative contribution of diet and genotype to bone development. *Proceedings of the Nutrition Society,* 60**,** 45-52.

PREUSCHOFT, H. & WITZEL, U. 2002. Biomechanical investigations on the skulls of reptiles and mammals. *Senckenbergiana Lethaea,* 82**,** 207-222.

PRUIM, G., DE JONGH, H. & TEN BOSCH, J. 1980. Forces acting on the mandible during bilateral static bite at different bite force levels. *Journal of Biomechanics,* 13**,** 755-763.

PRUM, G., TEN BOSCH, J. & DE JONGH, H. 1978. Jaw muscle EMG-activity and static loading of the mandible. *Journal of Biomechanics,* 11**,** 389-395.

RAADSHEER, M., VAN EIJDEN, T., VAN GINKEL, F. & PRAHL-ANDERSEN, B. 1999. Contribution of jaw muscle size and craniofacial morphology to human bite force magnitude. *Journal of Dental Research,* 78**,** 31-42.

RAFFERTY, K. L., HERRING, S. W. & MARSHALL, C. D. 2003. Biomechanics of the rostrum and the role of facial sutures. *Journal of Morphology,* 257**,** 33-44.

RAYFIELD, E. J. 2005. Using finite-element analysis to investigate suture morphology: A case study using large carnivorous dinosaurs. *The Anatomical Record Part A: Discoveries in Molecular, Cellular, and Evolutionary Biology,* 283**,** 349-365.

RAYFIELD, E. J. 2007. Finite element analysis and understanding the biomechanics and evolution of living and fossil organisms. *Annual Review of Earth and Planetary Sciences,* 35**,** 541-576.

RAYFIELD, E. J. 2011. Strain in the ostrich mandible during simulated pecking and validation of specimen-specific finite element models. *Journal of Anatomy,* 218**,** 47-58.

REAZ, M. B., HUSSAIN, M. & MOHD-YASIN, F. 2006. Techniques of EMG signal analysis: detection, processing, classification and applications. *Biological Procedures Online,* 8**,** 11-35.

REED, D. A., PORRO, L. B., IRIARTE-DIAZ, J., LEMBERG, J. B., HOLLIDAY, C. M., ANAPOL, F. & ROSS, C. F. 2011. The impact of bone and suture material properties on mandibular function in Alligator mississippiensis: testing theoretical phenotypes with finite element analysis. *Journal of Anatomy,* 218**,** 59-74.

REES, J. 2001. An investigation into the importance of the periodontal ligament and alveolar bone as supporting structures in finite element studies. *Journal of Oral Rehabilitation,* 28**,** 425-432.

REMMLER, D., OLSON, L., EKSTROM, R., DUKE, D., MATAMOROS, A., MATTHEWS, D. & ULLRICH, C. G. 1998. Pre-surgical CT/FEA for craniofacial distraction: I.: Methodology, development, and validation of the cranial finite element model. *Medical Engineering & Physics,* 20**,** 607-619.

RICHMOND, B. G., WRIGHT, B. W., GROSSE, I., DECHOW, P. C., ROSS, C. F., SPENCER, M. A. & STRAIT, D. S. 2005. Finite element analysis in functional morphology. *The Anatomical Record Part A: Discoveries in Molecular, Cellular, and Evolutionary Biology,* 283**,** 259-274.

ROBBINS, D. H. & WOOD, J. L. 1969. Determination of mechanical properties of the bones of the skull. *Experimental Mechanics,* 9**,** 236-240.

ROBLING, A. G. & TURNER, C. H. 2002. Mechanotransduction in bone: genetic effects on mechanosensitivity in mice. *Bone,* 31**,** 562-569.

ROHLF, F. J. & CORTI, M. 2000. Use of two-block partial least-squares to study covariation in shape. *Systematic Biology,* 49**,** 740-753.

RÖHRLE, O., DAVIDSON, J. B. & PULLAN, A. J. 2012. A physiologically based, multi-scale model of skeletal muscle structure and function. *Frontiers in physiology,* 3.

RÖHRLE, O. & PULLAN, A. J. 2007. Three-dimensional finite element modelling of muscle forces during mastication. *Journal of Biomechanics,* 40**,** 3363-3372.

ROSAS, A. & BASTIR, M. 2002. Thin-plate spline analysis of allometry and sexual dimorphism in the human craniofacial complex. *American Journal of Physical Anthropology,* 117**,** 236-245.

ROSS, C. F., BERTHAUME, M. A., DECHOW, P. C., IRIARTE-DIAZ, J., PORRO, L. B., RICHMOND, B. G., SPENCER, M. & STRAIT, D. 2011. *In vivo* bone strain and finite-element modeling of the craniofacial haft in catarrhine primates. *Journal of Anatomy,* 218**,** 112-141.

ROSS, C. F., PATEL, B. A., SLICE, D. E., STRAIT, D. S., DECHOW, P. C., RICHMOND, B. G. & SPENCER, M. A. 2005. Modeling masticatory muscle force in finite element analysis: sensitivity analysis using principal coordinates analysis. *The Anatomical Record Part A: Discoveries in Molecular, Cellular, and Evolutionary Biology,* 283**,** 288-299.

ROWLERSON, A., RAOUL, G., DANIEL, Y., CLOSE, J., MAURAGE, C.-A., FERRI, J. & SCIOTE, J. J. 2005. Fiber-type differences in masseter muscle associated with different facial morphologies. *American Journal of Orthodontics and Dentofacial Orthopedics,* 127**,** 37-46.

RUBIN, C., RECKER, R., CULLEN, D., RYABY, J., MCCABE, J. & MCLEOD, K. 2004. Prevention of postmenopausal bone Loss by a low-magnitude, high-frequency mechanical stimuli: a clinical trial assessing compliance, efficacy, and safety. *Journal of Bone and Mineral Research,* 19**,** 343-351.

RUBIN, C., TURNER, A. S., MALLINCKRODT, C., JEROME, C., MCLEOD, K. & BAIN, S. 2002. Mechanical strain, induced noninvasively in the high-frequency domain, is anabolic to cancellous bone, but not cortical bone. *Bone,* 30**,** 445-452.

RUBIN, C., XU, G. & JUDEX, S. 2001. The anabolic activity of bone tissue, suppressed by disuse, is normalized by brief exposure to extremely low-magnitude mechanical stimuli. *The FASEB Journal,* 15**,** 2225-2229.

RUBIN, C. T. 1984. Skeletal strain and the functional significance of bone architecture. *Calcified Tissue International,* 36**,** S11-S18.

RUBIN, C. T. & LANYON, L. E. 1985. Regulation of bone mass by mechanical strain magnitude. *Calcified Tissue International,* 37**,** 411-417.

RUFF, C., HOLT, B. & TRINKAUS, E. 2006. Who's afraid of the big bad Wolff?:"Wolff's law" and bone functional adaptation. *American Journal of Physical Anthropology,* 129**,** 484-498.

SAITO, T., OHNUKI, Y., YAMANE, A. & SAEKI, Y. 2002. Effects of diet consistency on the myosin heavy chain mRNAs of rat masseter muscle during postnatal development. *Archives of Oral Biology,* 47**,** 109-115.

SATIA, J. A. 2010. Dietary acculturation and the nutrition transition: an overview. *Applied Physiology, Nutrition, and Metabolism,* 35**,** 219-223.

SCIOTE, J. J., HORTON, M. J., ROWLERSON, A. M., FERRI, J., CLOSE, J. M. & RAOUL, G. 2012. Human masseter muscle fiber type properties, skeletal malocclusions, and muscle growth factor expression. *Journal of Oral and Maxillofacial Surgery,* 70**,** 440-448.

SCIOTE, J. J. & MORRIS, T. J. 2000. Skeletal muscle function and fibre types: the relationship between occlusal function and the phenotype of jaw-closing muscles in human. *Journal of Orthodontics,* 27**,** 15-30.

SCOTT, J. H. 1957. Muscle growth and function in relation to skeletal morphology. *American Journal of Physical Anthropology,* 15**,** 197-234.

SCHINDLER, H. J., RUES, S., TÜRP, J. C., SCHWEIZERHOF, K. & LENZ, J. 2005. Activity patterns of the masticatory muscles during feedback-controlled simulated clenching activities. *European Journal of Oral Sciences,* 113**,** 469-478.

SCHMID, J. & MAGNENAT-THALMANN, N. 2008. MRI bone segmentation using deformable models and shape priors. *Medical Image Computing and Computer-Assisted Intervention*, 119-126.

SCHUMACHER, G.-H. 1961. *Funktionelle morphologie der kaumuskulatur,* Jena, G. Fischer.

SCHWARTZ-DABNEY, C. L. & DECHOW, P. C. 2003. Variations in cortical material properties throughout the human dentate mandible. *American Journal of Physical Anthropology,* 120, 252-277.

SELLERS, W. I. & CROMPTON, R. H. 2004. Using sensitivity analysis to validate the predictions of a biomechanical model of bite forces. *Annals of Anatomy-Anatomischer Anzeiger,* 186, 89-95.

SHI, J., CURTIS, N., FITTON, L. C., O'HIGGINS, P. & FAGAN, M. J. 2012. Developing a musculoskeletal model of the primate skull: Predicting muscle activations, bite force, and joint reaction forces using multibody dynamics analysis and advanced optimisation methods. *Journal of Theoretical Biology,* 310, 21-30.

SIGAL, I. A., HARDISTY, M. R. & WHYNE, C. M. 2008. Mesh-morphing algorithms for specimen-specific finite element modeling. *Journal of Biomechanics,* 41, 1381-1389.

SKINNER, M. M., GUNZ, P., WOOD, B. A. & HUBLIN, J.-J. 2008. Enamel-dentine junction (EDJ) morphology distinguishes the lower molars of Australopithecus africanus and Paranthropus robustus. *Journal of Human Evolution,* 55, 979.

SLEMENDA, C. W., CHRISTIAN, J. C., WILLIAMS, C. J., NORTON, J. A. & JOHNSTON, C. C. 1991. Genetic determinants of bone mass in adult women: A reevaluation of the twin model and the potential importance of gene interaction on heritability estimates. *Journal of Bone and Mineral Research,* 6, 561-567.

SLICE, D. E. 2007. Geometric morphometrics. *Annual Review of Anthropology,* 36, 261-281.

SMITH, H. F. 2011. The Role of Genetic Drift in Shaping Modern Human Cranial Evolution: A Test Using Microevolutionary Modeling. *International Journal of Evolutionary Biology,* 2011, 11.

SMITH, N. B. & WEBB, A. 2010. *Introduction to medical imaging: physics, engineering and clinical applications,* Cambridge, University Press.

SNEATH, P. H. 1967. Trend-surface analysis of transformation grids. *Journal of Zoology,* 151, 65-122.

SONNESEN, L. & BAKKE, M. 2005. Molar bite force in relation to occlusion, craniofacial dimensions, and head posture in pre-orthodontic children. *The European Journal of Orthodontics,* 27, 58-63.

SPENCER, M. & DEMES, B. 1993. Biomechanical analysis of masticatory system configuration in Neandertals and Inuits. *American Journal of Physical Anthropology,* 91**,** 1-20.

SPENCER, M. A. 1998. Force production in the primate masticatory system: electromyographic tests of biomechanical hypotheses. *Journal of Human Evolution,* 34**,** 25-54.

SPOOR, C. F., ZONNEVELD, F. W. & MACHO, G. A. 1993. Linear measurements of cortical bone and dental enamel by computed tomography: applications and problems. *American Journal of Physical Anthropology,* 91**,** 469-484.

STÅL, P., ERIKSSON, P.-O., SCHIAFFINO, S., BUTLER-BROWNE, G. & THORNELL, L.-E. 1994. Differences in myosin composition between human oro-facial, masticatory and limb muscles: enzyme-, immunohisto-and biochemical studies. *Journal of Muscle Research and Cell Motility,* 15**,** 517-534.

STEDMAN, H. H., KOZYAK, B. W., NELSON, A., THESIER, D. M., SU, L. T., LOW, D. W., BRIDGES, C. R., SHRAGER, J. B., MINUGH-PURVIS, N. & MITCHELL, M. A. 2004. Myosin gene mutation correlates with anatomical changes in the human lineage. *Nature,* 428**,** 415-418.

STELZER, S., GUNZ, P. & SPOOR, F. 2013. Morphological integration of upper and lower jaws in extant hominids. *Third Annual Meeting of the European Society for the Study of Human Evolution.* Vienna, Austria.

STOHLER, C. 1986. A comparative electromyographic and kinesiographic study of deliberate and habitual mastication in man. *Archives of Oral Biology,* 31**,** 669-678.

STRAIT, D. S., WANG, Q., DECHOW, P. C., ROSS, C. F., RICHMOND, B. G., SPENCER, M. A. & PATEL, B. A. 2005. Modeling elastic properties in finite-element analysis: How much precision is needed to produce an accurate model? *The Anatomical Record Part A: Discoveries in Molecular, Cellular, and Evolutionary Biology,* 283**,** 275-287.

STRAIT, D. S., WEBER, G. W., NEUBAUER, S., CHALK, J., RICHMOND, B. G., LUCAS, P. W., SPENCER, M. A., SCHREIN, C., DECHOW, P. C. & ROSS, C. F. 2009. The feeding biomechanics and dietary ecology of Australopithecus africanus. *Proceedings of the National Academy of Sciences,* 106**,** 2124-2129.

STRAND VIÐARSDÓTTIR, U., O'HIGGINS, P. & STRINGER, C. 2002. A geometric morphometric study of regional differences in the ontogeny of the modern human facial skeleton. *Journal of Anatomy,* 201**,** 211-229.

SWEENEY, H. L. & HOUDUSSE, A. 2010. Structural and functional insights into the myosin motor mechanism. *Annual Review of Biophysics,* 39**,** 539-557.

SZWEDOWSKI, T. D., FIALKOV, J. & WHYNE, C. M. 2011. Sensitivity analysis of a validated subject-specific finite element model of the human craniofacial skeleton. *Proceedings of the Institution of Mechanical Engineers, Part H: Journal of Engineering in Medicine,* 225**,** 58-67.

TANAKA, E., DETAMORE, M. & MERCURI, L. 2008. Degenerative disorders of the temporomandibular joint: etiology, diagnosis, and treatment *Journal of Dental Research,* 87**,** 296-307.

TANNE, K., MIYASAKA, J., YAMAGATA, Y., SACHDEVA, R., TSUTSUMI, S. & SAKUDA, M. 1988. Three-dimensional model of the human craniofacial skeleton: method and preliminary results using finite element analysis. *Journal of Biomedical Engineering,* 10**,** 246-252.

TAYLOR, A. B. & VINYARD, C. J. 2013. The relationships among jaw-muscle fiber architecture, jaw morphology, and feeding behavior in extant apes and modern humans. *American Journal of Physical Anthropology,* 151**,** 120-134.

TEAFORD, M. F. & UNGAR, P. S. 2000. Diet and the evolution of the earliest human ancestors. *Proceedings of the National Academy of Sciences,* 97**,** 13506-13511.

THOMASON, J. J. & RUSSELL, A. P. 1986. Mechanical factors in the evolution of the mammalian secondary palate: A theoretical analysis. *Journal of Morphology,* 189**,** 199-213.

THOMPSON, D. W. 1942. *On growth and form,* Cambridge, University Press.

THROCKMORTON, G. S. 1985. Quantitative calculations of temporomandibular joint reaction forces—II. The importance of the direction of the jaw muscle forces. *Journal of Biomechanics,* 18**,** 453-461.

THROCKMORTON, G. S. & THROCKMORTON, L. S. 1985. Quantitative calculations of temporomandibular joint reaction forces—I. The importance of the magnitude of the jaw muscle forces. *Journal of Biomechanics,* 18**,** 445-452.

TRINKAUS, E. 2003. Neandertal faces were not long; modern human faces are short. *Proceedings of the National Academy of Sciences,* 100**,** 8142-8145.

TURNER, C. 1998. Three rules for bone adaptation to mechanical stimuli. *Bone,* 23**,** 399-407.

TURNER, C., FORWOOD, M. & OTTER, M. 1994. Mechanotransduction in bone: do bone cells act as sensors of fluid flow? *The FASEB Journal,* 8**,** 875-878.

UEDA, H. M., ISHIZUKA, Y., MIYAMOTO, K., MORIMOTO, N. & TANNE, K. 1998. Relationship between masticatory muscle activity and vertical craniofacial morphology. *The Angle Orthodontist,* 68**,** 233-238.

VAN DER KLAAUW, C. J. 1948-1952. Size and position of the functional components of the skull. *Archives Néerlandaises de Zoologie,* 9**,** 1-159.

VAN EIJDEN, T. 1990. Jaw muscle activity in relation to the direction and point of application of bite force. *Journal of Dental Research,* 69**,** 901-905.

VAN EIJDEN, T. 1991. Three-dimensional analyses of human bite-force magnitude and moment. *Archives of Oral Biology,* 36**,** 535-539.

VAN EIJDEN, T., KOOLSTRA, J. & BRUGMAN, P. 1995. Architecture of the human pterygoid muscles. *Journal of Dental Research,* 74**,** 1489-1495.

VAN EIJDEN, T., KORFAGE, J. & BRUGMAN, P. 1997. Architecture of the human jaw-closing and jaw-opening muscles. *The Anatomical Record,* 248**,** 464-474.

VAN SPRONSEN, P., WEIJS, W., VALK, J., PRAHL-ANDERSEN, B. & VAN GINKEL, F. 1989. Comparison of jaw-muscle bite-force cross-sections obtained by means of magnetic resonance imaging and high-resolution CT scanning. *Journal of Dental Research,* 68**,** 1765-1770.

VAN SPRONSEN, P., WEIJS, W., VALK, J., PRAHL-ANDERSEN, B. & VAN GINKEL, F. 1991. Relationships between jaw muscle cross-sections and craniofacial morphology in normal adults, studied with magnetic resonance imaging. *The European Journal of Orthodontics,* 13**,** 351-361.

VAN SPRONSEN, P., WEIJS, W., VALK, J., PRAHL-ANDERSEN, B. & VAN GINKEL, F. 1992. A comparison of jaw muscle cross-sections of long-face and normal adults. *Journal of Dental Research,* 71**,** 1279.

VAN SPRONSEN, P. H. 2010. Long-face craniofacial morphology: cause or effect of weak masticatory musculature? *Seminars in Orthodontics,* 16**,** 99-117.

VERRUE, V., DERMAUT, L. & VERHEGGHE, B. 2001. Three-dimensional finite element modelling of a dog skull for the simulation of initial orthopaedic displacements. *The European Journal of Orthodontics,* 23**,** 517-527.

VITTI, M. & BASMAJIAN, J. V. 1977. Integrated actions of masticatory muscles: simultaneous EMG from eight intramuscular electrodes. *The Anatomical Record,* 187**,** 173-189.

VON CRAMON-TAUBADEL, N. 2011. Global human mandibular variation reflects differences in agricultural and hunter-gatherer subsistence strategies. *Proceedings of the National Academy of Sciences,* 108**,** 19546-19551.

VON CRAMON-TAUBADEL, N. 2013. Evolutionary insights into global patterns of human cranial diversity: population history, climatic and dietary effects. *Journal of Anthropological Sciences,* 91**,** 1-36.

WADDINGTON, C. H. 1942. Canalization of development and the inheritance of acquired characters. *Nature,* 150**,** 563-565.

WALTIMO, A. & KÖNÖNEN, M. 1993. A novel bite force recorder and maximal isometric bite force values for healthy young adults. *European Journal of Oral Sciences,* 101**,** 171-175.

WANG, K., ARIMA, T., ARENDT-NIELSEN, L. & SVENSSON, P. 2000. EMG–force relationships are influenced by experimental jaw-muscle pain. *Journal of Oral Rehabilitation,* 27**,** 394-402.

WANG, Q., SMITH, A. L., STRAIT, D. S., WRIGHT, B. W., RICHMOND, B. G., GROSSE, I. R., BYRON, C. D. & ZAPATA, U. 2010. The global impact of sutures assessed in a finite element model of a macaque cranium. *The Anatomical Record: Advances in Integrative Anatomy and Evolutionary Biology,* 293**,** 1477-1491.

WANG, Q., WOOD, S. A., GROSSE, I. R., ROSS, C. F., ZAPATA, U., BYRON, C. D., WRIGHT, B. W. & STRAIT, D. S. 2012. The role of the sutures in biomechanical dynamic simulation of a macaque cranial finite element model: implications for the evolution of craniofacial form. *The Anatomical Record: Advances in Integrative Anatomy and Evolutionary Biology.*

WARNER, S. E., SANFORD, D. A., BECKER, B. A., BAIN, S. D., SRINIVASAN, S. & GROSS, T. S. 2006. Botox induced muscle paralysis rapidly degrades bone. *Bone,* 38**,** 257-264.

WEBER, G. W., BOOKSTEIN, F. L. & STRAIT, D. S. 2011. Virtual anthropology meets biomechanics. *Journal of Biomechanics,* 44**,** 1429-1432.

WEIJS, W. & HILLEN, B. 1984. Relationship between the physiological cross-section of the human jaw muscles and their cross-sectional area in computer tomograms. *Acta Anatomica,* 118**,** 129-138.

WEIJS, W. & HILLEN, B. 1985a. Cross-sectional areas and estimated intrinsic strength of the human jaw muscles. *Acta Morphologica Neerlando-Scandinavica,* 23**,** 267-274.

WEIJS, W. & HILLEN, B. 1986. Correlations between the cross-sectional area of the jaw muscles and craniofacial size and shape. *American Journal of Physical Anthropology,* 70**,** 423-431.

WEIJS, W. A. & HILLEN, B. 1985b. Physiological cross-section of the human jaw muscles. *Cells Tissues Organs,* 121**,** 31-35.

WITZEL, U., PREUSCHOFT, H. & SICK, H. 2004. The role of the zygomatic arch in the statics of the skull and its adaptive shape. *Folia Primatologica,* 75**,** 202-218.

WOLFF, J. 1892. *Das gesetz der transformation der knochen,* Berlin, Quarto.

WOOD, S. A., STRAIT, D. S., DUMONT, E. R., ROSS, C. F. & GROSSE, I. R. 2011. The effects of modeling simplifications on craniofacial finite element models: The alveoli (tooth sockets) and periodontal ligaments. *Journal of Biomechanics,* 44**,** 1831-1838.

WROE, S., FERRARA, T. L., MCHENRY, C. R., CURNOE, D. & CHAMOLI, U. 2010. The craniomandibular mechanics of being human. *Proceedings of the Royal Society B: Biological Sciences,* 277**,** 3579-3586.

YANG, L. & ETTEMEYER, A. 2003. Strain measurement by three-dimensional electronic speckle pattern interferometry: potentials, limitations, and applications. *Optical Engineering,* 42**,** 1257-1266.

YANG, L., ZHANG, P., LIU, S., SAMALA, P. R., SU, M. & YOKOTA, H. 2007. Measurement of strain distributions in mouse femora with 3D-digital speckle pattern interferometry. *Optics and Lasers in Engineering,* 45**,** 843-851.

YOSHIKAWA, T., MORI, S., SANTIESTEBAN, A., SUN, T., HAFSTAD, E., CHEN, J. & BURR, D. B. 1994. The effects of muscle fatigue on bone strain. *Journal of Experimental Biology,* 188**,** 217-233.

ZELDITCH, M. L., LUNDRIGAN, B. L. & GARLAND, T. 2004. Developmental regulation of skull morphology. I. Ontogenetic dynamics of variance. *Evolution & Development,* 6**,** 194-206.

ZELDITCH, M. L., SWIDERSKI, D. L. & SHEETS, H. D. 2012. *Geometric morphometrics for biologists: a primer,* San Diego, Elsevier Academic Press.

ZIENKIEWICZ, O. C., TAYLOR, R. L. & ZHU, J. Z. 2005. *The finite element method: its basis and fundamentals,* Burlington, Butterworth-Heinemann.

Appendix

The following tables present data referenced in Chapters 3 and 5 of this thesis.

Table A.1. Description of sample from Chapter 3. Centroid size is calculated using the 59 landmarks listed in Table 3.1.

No.	ID	Sex	Age (years)	Centroid size (mm)	Muscle cross sectional areas (mm^2)						Muscle areas on bone (mm^2)			
					Temporalis		Masseter		Medial pterygoid		Temporalis		Masseter	
					Left	Righ	Left	Right	Left	Right	Left	Right	Left	Right
1	Female-29y	F	29	483.45	505.20	530.02	451.70	489.73	271.51	250.99	848.44	872.58	692.65	821.36
2	Female-34y	F	34	510.36	495.06	473.72	519.76	501.91	389.82	361.84	767.45	718.88	749.86	710.02
3	Female-36y	F	36	498.57	401.52	522.81	342.78	360.13	325.42	324.05	616.50	703.99	797.95	866.34
4	Female-40y	F	40	511.64	528.82	493.74	445.03	435.65	426.34	399.11	769.26	704.00	696.74	685.35
5	Female-49Ay	F	49	507.11	581.99	548.67	388.02	411.86	241.30	211.99	980.02	1194.11	851.99	1003.65
6	Female-49By	F	49	483.68	462.44	476.37	436.75	421.47	321.14	294.76	794.00	781.38	702.98	638.61
7	Female-51y	F	51	486.51	462.49	468.41	462.82	457.90	287.92	254.87	732.42	830.71	708.48	813.78
8	Female-54y	F	54	493.26	527.39	546.49	541.50	614.12	328.06	350.73	897.14	916.64	614.27	720.49
9	Female-55y	F	55	476.10	433.80	459.12	396.87	417.11	244.17	243.00	814.37	775.33	797.28	562.94
10	Female-61y	F	61	483.98	387.24	408.49	374.29	339.22	278.81	291.54	761.73	613.57	672.06	609.31
11	Female-86y	F	86	468.55	447.33	445.83	291.62	304.58	204.98	210.46	864.53	858.45	582.53	597.14
12	Male-38y	M	38	493.97	487.50	445.31	522.16	467.43	311.87	287.86	719.67	677.38	649.28	928.99
13	Male-39y	M	39	498.82	538.84	469.47	474.52	480.60	332.09	360.61	870.09	918.29	934.40	810.77
14	Male-42y	M	42	509.94	567.89	559.75	561.54	569.09	353.97	365.00	807.63	706.37	790.02	809.03
15	Male-43y	M	43	493.40	454.10	461.27	362.32	335.16	335.16	317.53	718.65	713.05	979.94	968.59
16	Male-46y	M	46	493.81	508.62	526.65	564.81	610.07	386.60	415.11	613.30	872.06	558.19	618.98
17	Male-47Ay	M	47	501.64	383.12	381.09	408.22	406.44	244.15	255.49	586.10	608.23	666.43	853.34
18	Male-47By	M	47	532.65	583.01	649.48	511.17	566.32	332.52	316.97	1062.56	1004.23	851.66	992.03
19	Male-62y	M	62	502.21	563.61	574.54	474.99	446.34	401.28	324.43	888.24	919.61	851.07	887.29
20	Male-72y	M	72	516.44	566.35	537.26	517.52	565.03	420.12	437.75	916.27	995.11	768.64	782.64

Table A.2.Principal strain magnitudes (in µstrains) under I1 (left and right) bite at 51 craniofacial points derived from sample in Chapter 5.

LM	Deformed-oblique				Deformed-erect				PC1(-)				PC1(+)				PC2(-)				PC2(+)			
	Own force		2000 N		Own force		2000 N		Own force		2000 N		Own force		2000 N		Own force		2000 N		Own force		2000 N	
	ε1	ε3	ε1	ε3	ε1	ε3	ε1	ε3	ε1	ε3	ε1	ε3	ε1	ε3	ε1	ε3	ε1	ε3	ε1	ε3	ε1	ε3	ε1	ε3
1	0.94	-0.51	2.09	-1.14	1.15	-0.90	2.61	-1.99	1.21	-1.01	2.49	-2.09	1.92	-2.30	4.10	-4.55	1.91	-2.26	4.78	-5.59	0.74	-0.47	1.68	-1.11
2	18.25	-31.71	40.74	-70.96	60.67	-152.77	135.50	-341.26	31.62	-88.47	56.97	-159.37	60.25	-160.68	108.69	-289.10	54.82	-176.69	134.64	-434.48	40.76	-134.74	85.75	-282.87
3	14.47	-32.07	32.33	-71.70	9.21	-23.98	20.56	-53.49	2.07	-1.55	3.77	-2.80	6.14	-8.62	10.90	-15.34	47.21	-29.07	119.24	-72.14	2.00	-1.14	4.21	-2.41
4	171.31	-141.83	383.10	-317.34	317.50	-362.85	708.79	-810.78	97.91	-89.47	175.14	-159.94	499.51	-175.94	890.73	-313.78	183.44	-157.92	439.56	-379.62	72.86	-54.97	151.59	-117.09
5	0.46	-0.82	1.03	-1.88	0.47	-0.76	1.06	-1.76	0.20	-0.43	0.37	-0.82	0.51	-0.52	0.82	-0.78	0.29	-0.38	0.62	-0.88	0.10	-0.25	0.21	-0.49
6	24.56	-29.90	54.61	-66.83	17.53	-34.72	39.12	-77.69	17.25	-13.23	30.32	-23.88	16.06	-26.24	28.02	-47.70	33.43	-37.77	83.58	-90.86	39.71	-16.64	80.50	-34.02
7	20.59	-17.95	46.02	-40.37	13.82	-36.04	30.76	-80.26	15.74	-6.57	25.85	-11.20	12.52	-8.70	20.31	-16.42	9.12	-5.49	27.28	-13.27	68.50	-23.63	125.36	-43.52
8	121.79	-373.03	272.23	-833.82	94.37	-270.88	211.22	-606.31	88.90	-220.88	164.01	-407.50	157.83	-487.13	281.01	-867.48	161.51	-487.00	386.37	-1165.16	83.89	-231.09	180.59	-497.85
9	39.44	-23.26	88.10	-51.96	5.58	-12.07	12.45	-26.99	49.09	-18.89	84.53	-33.08	13.17	-19.70	23.42	-34.85	4.37	-2.81	10.58	-6.83	16.82	-9.39	34.11	-18.59
10	13.85	-8.00	30.62	-17.83	22.05	-20.43	49.22	-45.65	18.35	-7.94	34.49	-15.56	9.94	-12.73	17.59	-22.33	11.91	-9.33	29.78	-18.91	37.76	-12.93	80.26	-27.45
11	23.71	-48.25	53.66	-107.91	26.78	-83.47	59.68	-186.08	46.33	-148.60	80.41	-258.25	31.23	-79.75	53.07	-134.07	29.14	-93.33	77.46	-248.06	52.78	-129.67	93.89	-231.27
12	51.47	-29.74	114.29	-65.88	96.88	-47.73	216.59	-106.54	48.50	-22.46	85.54	-41.17	38.76	-34.76	67.35	-62.13	74.53	-37.89	190.57	-94.05	140.32	-52.95	266.57	-101.37
13	169.52	-62.99	376.22	-139.93	347.41	-123.62	777.13	-276.54	446.32	-148.97	786.68	-262.60	477.69	-163.27	823.18	-281.31	429.91	-148.67	1117.51	-386.39	451.67	-166.31	835.20	-307.50
14	60.13	-39.76	137.51	-90.97	55.59	-130.17	124.82	-292.33	86.83	-68.63	152.54	-122.36	145.41	-60.38	255.09	-105.72	142.02	-67.52	367.36	-173.07	157.53	-81.54	273.19	-149.95
15	51.27	-146.85	117.46	-336.60	56.97	-76.48	128.71	-174.02	48.50	-140.54	99.89	-289.31	44.58	-134.31	93.64	-282.16	53.32	-155.59	124.23	-361.59	40.50	-112.93	84.81	-238.39
16	53.31	-24.26	123.01	-55.64	111.34	-179.61	250.94	-405.80	185.13	-71.21	336.11	-133.00	138.80	-76.22	242.00	-169.01	114.71	-139.91	297.33	-350.06	131.13	-49.81	237.00	-90.33
17	34.98	-85.06	78.72	-191.08	87.60	-69.75	196.12	-154.82	103.12	-318.18	181.70	-560.83	85.31	-186.03	140.97	-302.46	94.88	-232.86	246.44	-605.92	99.72	-255.13	186.19	-474.37
18	2.13	-3.89	4.82	-8.80	27.46	-9.79	62.18	-22.13	16.67	-43.54	30.54	-78.79	9.15	-14.13	17.63	-22.27	5.72	-15.97	14.73	-41.13	17.26	-45.70	33.94	-90.67
19	4.22	-2.97	9.71	-6.92	8.33	-5.38	19.04	-12.36	4.54	-10.02	8.96	-20.22	1.62	-1.11	3.84	-2.97	6.32	-11.36	15.65	-27.57	12.08	-15.93	25.05	-35.16
20	22.42	-39.67	49.80	-88.64	12.43	-32.50	27.84	-72.89	29.32	-18.14	51.03	-32.15	21.13	-21.36	37.57	-37.99	24.50	-35.20	62.89	-87.90	18.43	-7.81	37.03	-16.17
21	14.62	-22.32	32.37	-51.11	6.50	-14.76	14.60	-33.59	27.83	-10.25	35.82	-15.18	5.04	-10.50	11.95	-29.87	14.98	-36.13	38.46	-79.87	32.84	-13.22	64.39	-26.97
22	104.38	-331.35	233.95	-742.79	159.76	-488.73	357.73	-1094.36	155.31	-455.24	286.60	-840.37	178.91	-540.66	318.17	-961.82	169.51	-498.51	406.02	-1194.14	108.20	-301.32	231.11	-643.95
23	28.48	-16.33	63.21	-36.53	34.93	-22.79	78.37	-51.01	35.36	-15.28	64.97	-27.92	114.70	-42.26	205.45	-75.58	5.26	-12.09	12.74	-29.38	5.22	-2.58	9.41	-5.03
24	16.82	-16.19	37.60	-37.76	29.05	-11.55	65.33	-26.11	16.40	-6.86	30.57	-13.03	30.96	-19.03	55.11	-32.67	16.95	-12.97	40.93	-27.10	32.46	-10.86	65.69	-21.67
25	24.94	-48.36	56.17	-106.19	24.38	-51.86	52.15	-111.35	50.20	-132.42	74.96	-197.86	35.24	-106.58	52.76	-159.42	33.89	-102.07	96.46	-292.18	60.02	-182.03	118.23	-358.02
26	57.97	-41.35	128.40	-93.10	64.39	-27.11	142.16	-60.57	78.91	-28.58	128.30	-47.04	101.13	-35.84	163.41	-59.26	66.69	-24.33	179.55	-63.89	103.97	-36.28	212.28	-74.13
27	291.07	-107.03	639.66	-235.28	417.47	-142.27	915.72	-312.13	419.99	-147.40	669.85	-234.99	401.09	-150.66	641.18	-240.78	428.91	-164.85	1178.33	-452.62	289.95	-103.32	590.37	-210.36
28	39.65	-43.74	86.45	-95.01	63.35	-105.47	140.00	-232.68	75.36	-80.65	118.55	-129.89	64.71	-40.89	98.03	-66.72	39.67	-25.36	116.60	-69.44	202.21	-110.17	412.74	-227.99
29	45.48	-131.01	99.78	-287.58	57.00	-136.91	126.10	-302.63	53.53	-122.20	94.76	-228.69	68.51	-192.20	127.98	-358.84	39.51	-91.75	93.90	-208.89	50.77	-143.26	128.47	-361.32
30	24.96	-12.26	50.52	-26.01	162.45	-104.89	357.53	-233.67	197.21	-124.61	302.62	-194.94	89.85	-89.08	169.41	-174.46	92.05	-108.87	244.31	-251.61	58.39	-20.88	114.48	-41.82
31	41.19	-108.25	91.27	-240.11	110.44	-40.75	246.17	-90.61	91.41	-245.64	145.47	-391.23	59.02	-74.45	91.38	-106.34	31.60	-75.32	91.47	-220.97	63.49	-151.02	130.38	-309.51
32	4.77	-9.49	10.48	-20.87	15.78	-11.38	35.48	-25.59	3.33	-5.40	4.91	-7.13	12.76	-13.24	21.97	-17.62	30.12	-11.82	71.35	-27.62	4.11	-8.78	8.29	-16.88
33	3.98	-1.96	8.57	-4.23	9.43	-7.49	20.82	-16.36	2.60	-4.78	4.08	-7.45	5.88	-3.51	12.14	-7.56	18.81	-17.03	44.73	-40.98	12.10	-16.25	30.37	-40.33
34	10.10	-17.26	22.56	-38.05	5.57	-15.40	12.34	-34.04	10.67	-6.43	17.15	-11.28	7.60	-12.10	12.51	-22.90	23.27	-7.47	66.54	-21.14	6.30	-12.13	17.37	-43.50
35	3.32	-4.58	7.67	-10.24	4.06	-9.08	9.10	-20.47	4.01	-2.41	8.43	-4.91	2.49	-4.04	5.51	-8.64	1.43	-4.13	3.46	-9.99	1.78	-3.28	4.46	-8.32
36	3.87	-2.63	8.92	-6.12	9.72	-5.91	22.17	-13.53	3.64	-5.51	8.04	-11.76	2.34	-2.69	6.17	-6.80	2.91	-7.12	7.08	-17.35	8.79	-12.82	18.98	-27.54
37	4.65	-10.58	10.54	-25.76	7.56	-4.02	13.91	-8.37	13.69	-5.64	12.83	-6.89	32.68	-14.35	48.30	-22.45	14.18	-5.41	50.07	-18.58	33.24	-11.72	69.22	-24.02
38	2.69	-5.66	5.80	-12.63	6.09	-10.02	13.53	-22.29	2.20	-3.62	3.87	-7.51	2.67	-3.08	3.73	-6.23	2.62	-6.11	6.42	-14.65	1.95	-5.05	4.70	-11.68
39	4.67	-2.80	10.10	-6.06	9.47	-6.63	20.87	-14.59	2.54	-4.28	4.89	-8.34	2.94	-4.96	6.44	-10.42	3.83	-10.82	9.28	-26.23	4.63	-6.95	11.59	-17.28
40	66.83	-59.43	149.48	-132.97	42.72	-61.63	95.38	-137.42	45.14	-136.55	78.46	-237.34	19.66	-49.19	32.92	-81.55	47.01	-38.33	123.01	-99.35	131.54	-82.14	237.95	-149.21
41	45.25	-52.95	102.02	-120.06	106.80	-93.88	239.76	-209.61	27.26	-69.21	47.34	-117.88	31.95	-77.90	49.20	-117.90	47.45	-105.93	122.42	-272.85	86.61	-230.00	158.78	-422.13
42	37.77	-19.99	83.80	-43.67	113.28	-160.98	253.18	-359.58	128.12	-69.75	223.37	-121.41	100.02	-50.94	168.54	-84.70	130.48	-87.78	343.22	-236.13	176.30	-138.15	319.56	-251.33
43	55.87	-47.95	122.24	-104.93	29.34	-55.01	63.81	-119.23	53.10	-128.04	79.55	-190.54	90.26	-62.23	139.23	-95.85	94.94	-66.60	267.97	-188.45	32.95	-83.54	64.41	-162.39
44	78.62	-41.66	172.17	-91.54	107.55	-139.34	235.64	-304.69	113.90	-182.17	175.85	-280.59	53.57	-140.29	78.32	-190.35	66.14	-94.50	187.20	-271.64	14.97	-32.34	27.29	-62.19
45	66.83	-47.92	145.81	-104.44	162.97	-212.38	356.44	-464.12	100.84	-111.00	153.58	-165.48	139.02	-93.19	213.77	-139.82	102.56	-101.43	290.86	-289.32	166.94	-114.08	336.66	-228.07
46	161.88	-55.55	359.85	-123.82	241.40	-86.04	538.85	-192.15	72.78	-37.51	144.56	-77.73	173.85	-71.15	303.90	-125.34	71.71	-26.08	162.60	-61.79	28.19	-29.91	64.56	-63.11
47	58.63	-65.40	131.30	-146.72	28.13	-28.52	63.09	-64.07	88.46	-65.34	168.65	-128.92	80.15	-55.20	140.09	-96.69	29.57	-31.64	57.92	-72.95	41.90	-55.56	88.90	-114.60
48	128.62	-76.34	284.79	-169.88	122.94	-59.86	276.50	-134.50	57.10	-43.96	114.68	-91.51	134.86	-62.06	236.61	-109.57	79.87	-61.27	175.49	-136.29	59.50	-85.77	128.60	-184.47
49	134.23	-37.08	305.28	-84.92	209.10	-59.52	475.08	-134.89	34.65	-21.56	64.46	-44.35	95.29	-48.39	155.04	-81.36	31.66	-13.05	79.40	-28.91	36.41	-40.27	86.05	-93.93
50	51.34	-48.03	119.21	-110.63	36.32	-18.72	84.55	-43.45	81.29	-55.18	147.83	-102.15	82.03	-46.46	130.43	-75.38	34.34	-52.69	73.63	-115.65	30.05	-24.09	70.98	-53.42
51	104.11	-65.74	236.00	-151.10	98.33	-40.22	223.39	-90.99	65.07	-24.13	116.07	-41.96	102.52	-58.95	179.25	-100.83	61.73	-71.82	143.24	-167.31	34.57	-33.48	79.96	-78.37

Table A.3.Principal strain magnitudes (in µstrains) under left M1 bite at 51 craniofacial points derived from sample in Chapter 5.

	Deformed-oblique				Deformed-erect				PC1(-)				PC1(+)				PC2(-)				PC2(+)			
LM	Own force		2000 N		Own force		2000 N		Own force		2000 N		Own force		2000 N		Own force		2000 N		Own force		2000 N	
	ε1	ε3	ε1	ε3	ε1	ε3	ε1	ε3	ε1	ε3	ε1	ε3	ε1	ε3	ε1	ε3	ε1	ε3	ε1	ε3	ε1	ε3	ε1	ε3
1	2.46	-1.80	5.34	-3.84	3.33	-2.51	3.33	-2.51	1.90	-1.69	3.52	-3.06	3.20	-3.21	6.06	-5.92	2.21	-2.16	5.54	-5.33	1.22	-1.04	1.22	-1.04
2	24.47	-63.36	54.83	-141.73	96.25	-253.46	96.25	-253.46	21.30	-65.47	38.30	-117.11	40.70	-118.67	73.64	-213.51	43.94	-140.62	108.23	-347.08	17.45	-57.05	17.45	-57.05
3	7.10	-5.48	15.79	-12.19	2.01	-4.46	2.01	-4.46	0.47	-0.37	0.85	-0.68	0.87	-0.49	1.54	-0.86	9.03	-14.39	21.63	-31.11	0.11	-0.20	0.11	-0.20
4	13.71	-16.77	30.44	-37.43	18.12	-13.46	18.12	-13.46	10.44	-6.91	18.62	-13.02	2.98	-8.79	5.29	-15.54	10.37	-17.25	25.49	-43.20	11.26	-6.45	11.26	-6.45
5	0.17	-0.41	0.36	-0.88	1.18	-2.23	1.18	-2.23	0.72	-0.53	1.29	-1.00	0.54	-0.19	0.97	-0.33	0.97	-0.76	2.42	-1.90	1.36	-1.09	1.36	-1.09
6	19.28	-19.46	42.77	-43.48	35.63	-55.31	35.63	-55.31	13.29	-5.66	22.65	-9.72	16.01	-16.44	27.46	-29.78	24.39	-17.74	63.11	-43.89	39.30	-17.59	39.30	-17.59
7	111.08	-36.93	248.08	-82.47	176.45	-62.22	176.45	-62.22	118.43	-38.61	213.86	-69.73	139.23	-47.15	244.20	-82.74	163.13	-50.13	402.02	-123.55	162.46	-55.83	162.46	-55.83
8	51.61	-58.46	115.54	-130.58	142.09	-401.61	142.09	-401.61	46.82	-112.29	85.96	-206.47	66.09	-158.51	116.59	-279.68	51.36	-113.85	123.62	-268.41	16.63	-26.40	16.63	-26.40
9	17.29	-26.43	38.63	-59.07	71.20	-214.42	71.20	-214.42	96.60	-253.74	179.07	-471.15	95.28	-251.28	168.96	-445.27	13.39	-32.26	34.62	-85.18	70.11	-180.07	70.11	-180.07
10	6.77	-8.11	15.00	-18.21	9.67	-16.21	9.67	-16.21	16.43	-41.06	30.26	-75.88	5.25	-7.23	9.79	-13.15	9.99	-22.83	22.55	-49.45	47.06	-138.14	47.06	-138.14
11	25.74	-83.04	57.25	-184.80	100.40	-287.17	100.40	-287.17	58.66	-170.54	103.47	-299.06	62.88	-109.78	111.44	-189.05	66.45	-193.27	168.90	-491.88	78.81	-144.20	78.81	-144.20
12	67.51	-40.06	150.18	-88.98	204.36	-131.20	204.36	-131.20	59.42	-54.80	107.02	-102.22	53.24	-60.61	93.94	-108.99	92.07	-61.33	231.57	-149.25	158.97	-81.26	158.97	-81.26
13	205.21	-74.83	456.01	-166.29	715.09	-253.51	715.09	-253.51	340.95	-114.15	593.18	-198.67	435.01	-149.42	746.82	-256.52	400.26	-138.64	1045.58	-362.07	476.70	-175.96	476.70	-175.96
14	23.44	-23.75	53.29	-52.84	129.50	-324.87	129.50	-324.87	42.74	-45.77	73.25	-81.85	117.76	-46.43	205.73	-80.61	141.38	-64.89	366.39	-167.08	44.32	-55.74	44.32	-55.74
15	13.73	-34.66	33.07	-85.08	132.75	-113.47	132.75	-113.47	36.36	-19.01	40.99	-32.54	34.16	-17.93	24.57	-26.10	18.83	-42.45	43.82	-88.44	50.42	-21.99	50.42	-21.99
16	86.11	-35.51	196.04	-80.52	241.61	-346.71	241.61	-346.71	135.63	-50.99	241.96	-89.75	138.83	-48.56	221.53	-83.11	130.22	-155.29	335.48	-387.67	334.52	-118.58	334.52	-118.58
17	35.90	-26.34	80.93	-59.85	185.03	-107.50	185.03	-107.50	94.13	-291.03	165.12	-510.72	77.29	-160.06	126.61	-255.99	80.31	-179.33	210.79	-475.95	117.15	-281.78	117.15	-281.78
18	0.99	-1.17	2.11	-2.54	101.26	-36.11	101.26	-36.11	18.52	-46.90	34.81	-85.91	10.79	-20.17	23.94	-36.69	67.23	-20.37	163.02	-49.37	28.48	-78.98	28.48	-78.98
19	1.70	-1.77	3.98	-4.07	14.62	-8.96	14.62	-8.96	7.71	-3.72	14.21	-6.25	1.57	-3.10	3.56	-6.36	4.21	-7.12	10.73	-17.37	5.60	-10.30	5.60	-10.30
20	17.26	-30.26	38.31	-67.61	21.19	-55.94	21.19	-55.94	12.21	-10.05	20.15	-17.79	9.22	-13.89	16.72	-25.00	17.29	-30.70	44.22	-75.76	1.28	-2.64	1.28	-2.64
21	15.33	-12.76	33.16	-28.97	28.44	-9.77	28.44	-9.77	40.40	-13.50	56.07	-18.78	34.97	-11.71	50.16	-17.29	28.59	-15.90	84.20	-43.68	38.83	-15.30	38.83	-15.30
22	35.92	-114.83	81.00	-258.87	141.05	-430.09	141.05	-430.09	37.62	-108.90	71.01	-205.88	22.96	-69.81	40.40	-122.91	35.93	-104.23	83.36	-241.60	16.70	-45.17	16.70	-45.17
23	5.24	-11.85	11.93	-27.17	13.58	-28.02	13.58	-28.02	15.22	-20.96	29.41	-40.34	10.76	-14.81	19.06	-25.49	2.39	-2.78	5.76	-6.83	5.64	-7.02	5.64	-7.02
24	11.98	-32.40	27.68	-74.80	20.09	-21.51	20.09	-21.51	6.53	-9.67	12.40	-18.33	10.74	-23.00	17.79	-38.41	16.51	-35.29	36.97	-78.28	18.16	-12.06	18.16	-12.06
25	16.39	-51.18	35.79	-111.53	73.76	-153.04	73.76	-153.04	54.79	-143.95	83.00	-218.10	38.31	-115.31	57.70	-174.00	33.58	-101.55	97.14	-292.60	70.58	-217.85	70.58	-217.85
26	38.55	-17.74	84.26	-39.58	120.20	-43.37	120.20	-43.37	64.14	-23.59	97.86	-36.01	90.53	-31.07	142.85	-49.04	53.47	-18.70	148.98	-51.93	105.29	-36.65	105.29	-36.65
27	245.19	-89.95	536.85	-197.01	861.71	-293.54	861.71	-293.54	373.90	-131.38	585.04	-205.54	343.65	-128.99	538.77	-202.17	378.93	-145.34	1057.63	-405.45	258.08	-92.02	258.08	-92.02
28	39.44	-40.73	85.98	-88.15	126.86	-225.48	126.86	-225.48	70.45	-72.62	109.51	-115.06	65.15	-41.10	98.83	-67.33	42.48	-28.21	123.13	-76.05	218.21	-100.01	218.21	-100.01
29	51.62	-149.34	113.53	-328.58	134.88	-328.21	134.88	-328.21	56.13	-144.59	100.70	-271.00	74.11	-211.14	137.86	-392.35	45.59	-103.81	108.98	-238.88	62.18	-165.09	62.18	-165.09
30	20.07	-14.65	41.03	-33.20	330.90	-220.13	330.90	-220.13	177.50	-112.92	266.55	-173.48	90.60	-89.54	171.00	-175.53	87.69	-110.94	232.63	-256.26	43.23	-16.33	43.23	-16.33
31	39.95	-105.44	88.56	-233.99	235.97	-86.78	235.97	-86.78	79.05	-211.02	122.85	-328.01	56.90	-61.64	88.96	-85.15	29.01	-68.15	85.21	-203.63	51.57	-117.00	51.57	-117.00
32	5.72	-11.08	12.56	-24.46	32.99	-23.05	32.99	-23.05	2.57	-5.57	3.13	-4.74	18.96	-10.95	35.74	-16.30	29.92	-11.25	71.06	-26.43	2.50	-3.83	2.50	-3.83
33	5.64	-2.69	12.33	-5.86	22.29	-21.11	22.29	-21.11	7.04	-3.16	13.90	-6.48	7.18	-5.90	14.31	-11.63	24.40	-22.61	58.39	-54.58	21.76	-26.78	21.76	-26.78
34	14.74	-40.23	32.70	-89.24	50.31	-146.69	50.31	-146.69	25.53	-68.93	47.60	-128.48	29.40	-86.57	53.68	-158.32	17.99	-55.50	40.19	-123.91	43.44	-121.88	43.44	-121.88
35	5.08	-10.33	11.14	-22.89	13.58	-26.07	13.58	-26.07	2.59	-7.99	4.59	-14.05	5.59	-11.18	10.96	-21.13	2.50	-6.71	6.10	-16.30	2.67	-7.23	2.67	-7.23
36	1.52	-1.65	3.57	-3.77	17.13	-11.84	17.13	-11.84	3.66	-4.05	7.85	-8.87	4.95	-4.40	10.67	-9.61	2.48	-5.46	6.08	-13.31	8.45	-7.47	8.45	-7.47
37	29.30	-9.77	62.59	-20.88	73.45	-24.43	73.45	-24.43	66.72	-24.42	109.39	-40.18	78.81	-30.56	130.08	-50.87	59.83	-21.05	160.30	-56.43	79.73	-27.90	79.73	-27.90
38	5.84	-6.58	12.55	-14.43	13.15	-21.67	13.15	-21.67	3.68	-4.51	5.48	-7.99	5.70	-4.93	8.75	-9.21	3.53	-6.25	8.70	-15.06	2.34	-5.46	2.34	-5.46
39	6.38	-3.62	13.97	-7.90	23.40	-16.28	23.40	-16.28	5.10	-6.09	9.37	-11.53	5.11	-9.51	10.26	-18.49	4.68	-13.58	11.35	-32.94	6.71	-10.51	6.71	-10.51
40	68.72	-65.83	153.63	-147.06	112.48	-172.86	112.48	-172.86	48.76	-145.64	85.58	-254.71	44.63	-35.06	81.22	-59.96	49.21	-34.81	128.46	-91.28	130.26	-70.69	130.26	-70.69
41	79.61	-39.00	178.20	-87.83	248.64	-183.18	248.64	-183.18	28.74	-70.26	47.88	-119.29	29.64	-71.45	45.20	-107.12	37.02	-81.07	97.26	-212.84	84.43	-218.73	84.43	-218.73
42	45.06	-40.25	100.03	-88.06	252.17	-359.08	252.17	-359.08	133.60	-84.70	233.46	-148.67	104.92	-79.41	176.34	-133.68	129.10	-84.01	339.69	-226.49	192.78	-200.12	192.78	-200.12
43	57.05	-49.93	124.83	-109.21	70.68	-137.97	70.68	-137.97	57.59	-142.08	87.46	-215.19	91.93	-63.84	142.18	-98.37	95.03	-67.27	268.21	-190.16	42.78	-112.27	42.78	-112.27
44	70.17	-40.99	153.46	-90.42	229.65	-289.94	229.65	-289.94	112.72	-174.84	173.71	-267.15	52.34	-132.52	76.34	-175.96	64.67	-83.47	183.33	-244.43	11.00	-25.52	11.00	-25.52
45	71.35	-53.77	155.91	-117.22	358.96	-471.71	358.96	-471.71	105.58	-126.03	162.24	-192.83	139.96	-97.01	215.47	-146.68	105.32	-108.33	297.56	-306.04	169.47	-121.80	169.47	-121.80
46	183.31	-65.15	407.55	-144.71	398.33	-154.61	398.33	-154.61	43.80	-70.74	92.13	-141.92	180.36	-77.25	315.43	-134.85	106.48	-48.57	246.15	-107.43	94.78	-108.23	94.78	-108.23
47	61.06	-61.56	136.53	-137.88	54.40	-57.02	54.40	-57.02	71.85	-77.27	140.43	-142.05	107.46	-51.17	187.63	-89.38	39.85	-37.92	81.43	-88.30	121.24	-95.10	121.24	-95.10
48	166.67	-91.80	369.26	-203.83	111.34	-77.38	111.34	-77.38	92.52	-224.32	179.34	-425.38	161.20	-59.48	281.98	-104.36	78.12	-54.54	165.02	-120.42	133.63	-256.68	133.63	-256.68
49	70.88	-15.85	163.82	-37.10	301.02	-92.06	301.02	-92.06	27.62	-32.30	51.95	-64.47	98.76	-39.83	160.48	-65.86	18.31	-29.35	36.90	-54.66	46.91	-60.71	46.91	-60.71
50	48.40	-55.19	112.30	-126.42	90.64	-50.40	90.64	-50.40	50.99	-37.93	97.16	-71.28	98.83	-46.12	159.62	-74.76	39.05	-55.77	84.87	-122.98	39.80	-21.37	39.80	-21.37
51	62.41	-51.55	140.69	-117.15	110.69	-66.83	110.69	-66.83	49.93	-21.76	92.22	-38.23	49.62	-38.75	80.63	-64.53	42.07	-42.24	92.52	-98.08	32.82	-29.91	32.82	-29.91

Table A.4.Principal strain magnitudes (in µstrains) under right M1 bite at 51 craniofacial points derived from sample in Chapter 5.

LM	Deformed-oblique				Deformed-erect				PC1(-)				PC1(+)				PC2(-)				PC2(+)			
	Own force		2000 N		Own force		2000 N		Own force		2000 N		Own force		2000 N		Own force		2000 N		Own force		2000 N	
	ε1	ε3	ε1	ε3	ε1	ε3	ε1	ε3	ε1	ε3	ε1	ε3	ε1	ε3	ε1	ε3	ε1	ε3	ε1	ε3	ε1	ε3	ε1	ε3
1	2.49	-1.97	5.72	-4.58	1.59	-1.30	3.55	-3.01	2.28	-1.84	4.54	-3.66	2.27	-2.61	4.76	-5.21	1.75	-2.32	4.33	-5.74	1.38	-0.82	2.94	-1.34
2	20.56	-57.85	45.91	-129.18	49.05	-133.14	109.54	-297.31	21.60	-50.27	39.92	-90.43	38.86	-116.96	70.52	-211.32	44.18	-147.19	108.13	-362.17	20.82	-67.07	43.29	-197.53
3	5.71	-7.47	12.84	-16.78	3.28	-1.29	7.46	-2.92	0.38	-0.48	0.74	-0.93	1.08	-0.69	1.90	-1.21	9.39	-11.09	24.73	-25.28	0.11	-0.16	0.26	-0.41
4	10.93	-12.83	24.56	-29.00	9.31	-15.84	21.01	-36.19	8.53	-8.29	15.21	-15.63	2.57	-6.88	4.51	-12.03	17.73	-15.81	41.60	-37.93	15.97	-7.89	31.59	-23.48
5	0.41	-0.67	0.94	-1.53	0.53	-1.19	1.26	-2.75	0.42	-0.66	0.81	-1.28	0.27	-0.12	0.60	-0.24	0.34	-0.55	0.75	-1.29	1.43	-1.10	3.11	-2.39
6	18.41	-24.01	40.87	-53.67	13.22	-26.05	29.48	-58.30	4.84	-6.47	8.62	-12.60	9.97	-15.73	17.31	-29.15	25.02	-32.19	62.81	-76.85	13.72	-10.22	26.20	-19.02
7	20.76	-11.59	46.30	-26.05	7.01	-4.12	15.65	-9.20	44.27	-16.19	77.63	-28.55	33.31	-11.31	54.92	-18.72	32.68	-10.20	86.38	-26.91	65.92	-22.85	119.76	-38.59
8	38.57	-117.93	86.15	-263.37	29.43	-84.97	66.06	-190.70	16.66	-41.60	31.39	-78.23	21.31	-64.10	37.71	-113.30	43.37	-131.31	101.32	-306.87	4.44	-10.34	11.63	-29.35
9	4.10	-3.38	9.08	-7.55	1.33	-2.85	2.94	-6.34	17.03	-27.59	33.59	-56.98	5.23	-10.22	9.21	-18.00	0.83	-0.89	1.96	-2.08	23.11	-31.74	50.61	-82.58
10	10.72	-23.48	24.02	-52.76	6.53	-8.61	14.54	-19.24	8.31	-7.52	16.60	-15.55	7.84	-16.17	13.77	-28.40	9.36	-22.57	19.94	-47.63	24.45	-8.77	51.64	-22.65
11	15.56	-49.56	34.82	-110.37	40.45	-120.63	90.17	-269.09	54.93	-169.10	96.13	-295.82	30.90	-78.63	52.02	-131.53	34.66	-109.88	91.71	-290.18	61.75	-148.01	112.88	-148.73
12	26.77	-11.05	59.33	-24.39	68.48	-26.67	153.16	-59.58	48.80	-17.34	85.02	-30.24	32.03	-18.15	54.17	-31.30	56.76	-21.74	148.54	-56.52	119.89	-46.61	217.71	-64.86
13	133.45	-49.43	295.54	-109.60	329.69	-116.84	737.47	-261.37	387.05	-129.00	678.11	-226.02	389.86	-133.20	666.84	-227.80	385.06	-132.89	1009.09	-348.25	419.37	-154.12	766.88	-302.17
14	63.02	-43.19	143.93	-98.70	51.73	-128.72	116.12	-289.05	84.88	-60.69	148.83	-107.52	144.38	-57.47	253.25	-100.46	135.22	-62.89	351.30	-162.29	168.71	-73.49	295.78	-123.46
15	61.27	-176.05	139.83	-401.80	57.02	-80.12	128.93	-182.41	54.78	-158.90	111.11	-322.17	47.95	-143.22	99.65	-297.89	58.27	-168.83	135.93	-392.64	42.93	-122.02	90.56	-266.04
16	56.96	-25.82	131.31	-59.26	103.57	-168.88	233.53	-381.74	171.94	-65.14	311.43	-121.20	130.37	-77.86	229.17	-175.01	107.81	-135.72	280.20	-339.16	97.58	-39.95	165.35	-57.63
17	36.49	-87.71	82.14	-197.03	76.76	-57.99	171.84	-128.72	93.99	-289.18	164.91	-507.51	78.06	-163.87	128.18	-263.09	92.12	-225.74	239.64	-588.28	85.22	-220.35	155.23	-404.90
18	2.33	-4.13	5.29	-9.34	25.58	-9.27	57.96	-21.06	12.98	-33.47	23.69	-59.41	7.11	-10.77	14.91	-17.68	4.62	-13.06	11.50	-33.73	14.52	-39.76	28.34	-75.97
19	6.00	-4.29	13.77	-9.91	9.61	-6.85	21.80	-15.56	5.82	-7.27	11.10	-15.08	2.14	-1.77	4.72	-4.08	9.55	-14.78	23.44	-35.75	17.94	-25.74	37.66	-55.82
20	19.58	-29.26	43.42	-65.33	11.74	-21.46	26.07	-48.16	18.45	-8.44	30.81	-14.06	18.11	-15.71	31.80	-27.45	24.79	-24.88	64.59	-64.04	19.55	-9.05	37.86	-15.34
21	135.70	-44.01	301.24	-97.70	115.31	-36.15	256.94	-80.56	148.70	-49.10	254.17	-83.92	137.85	-43.77	232.42	-73.67	67.53	-27.75	179.47	-73.12	111.88	-36.73	231.81	-75.27
22	49.84	-80.70	111.15	-181.73	69.12	-197.37	155.10	-443.02	46.70	-112.11	86.36	-210.91	44.57	-104.79	78.85	-185.73	62.58	-155.75	149.40	-368.51	16.51	-24.63	34.44	-56.96
23	76.15	-202.61	169.88	-452.02	38.12	-139.78	84.92	-311.26	72.00	-187.77	132.97	-345.58	68.31	-177.68	121.02	-315.43	21.29	-61.41	53.44	-154.56	19.99	-30.86	42.79	-10.52
24	6.95	-11.25	15.97	-27.20	17.91	-43.93	39.57	-97.55	11.38	-27.09	20.52	-48.69	12.18	-28.56	22.09	-50.54	8.29	-18.65	17.02	-38.14	140.81	-435.49	302.34	-719.45
25	37.61	-120.52	83.07	-266.21	51.49	-83.05	112.74	-181.07	80.55	-209.79	130.55	-339.12	36.35	-87.26	59.17	-128.59	56.11	-168.29	151.35	-454.36	82.93	-221.74	167.40	-403.93
26	66.85	-54.37	148.48	-122.43	74.77	-47.91	166.10	-107.85	76.85	-42.06	131.26	-80.95	108.50	-54.38	179.89	-96.99	73.13	-34.41	192.48	-85.36	104.61	-48.45	216.85	-117.65
27	288.31	-105.52	633.67	-231.93	401.58	-136.98	880.25	-300.34	335.69	-118.86	515.29	-182.72	409.44	-153.88	656.24	-246.60	366.82	-141.07	1027.97	-395.00	286.80	-102.59	583.09	-187.79
28	62.97	-90.10	138.62	-198.66	56.38	-111.78	124.33	-246.70	51.71	-68.23	82.14	-112.47	46.05	-26.86	65.29	-41.68	31.84	-29.86	94.23	-77.19	64.54	-68.32	124.64	-142.30
29	15.28	-35.34	32.27	-73.67	24.58	-51.26	53.65	-111.30	116.39	-37.14	202.70	-64.65	11.93	-24.00	26.39	-56.44	19.99	-33.02	49.42	-73.06	55.20	-26.22	79.96	-31.65
30	91.48	-30.50	197.89	-66.16	205.20	-95.52	452.70	-212.10	216.01	-85.11	340.98	-127.51	55.34	-32.11	106.21	-67.63	85.47	-72.44	235.94	-173.03	176.38	-66.30	359.76	-112.17
31	17.51	-23.83	38.65	-51.68	145.37	-51.48	324.47	-114.76	77.26	-207.26	119.73	-321.40	54.31	-59.30	83.16	-80.07	21.06	-39.98	63.87	-133.41	73.98	-175.59	152.99	-396.58
32	4.07	-3.72	9.34	-8.46	18.84	-6.89	42.27	-15.47	21.89	-21.82	45.48	-42.92	14.59	-8.01	33.97	-17.19	34.86	-14.34	82.72	-33.55	73.69	-27.31	158.86	-56.67
33	1.66	-1.79	3.53	-3.93	6.83	-4.76	15.13	-10.32	15.66	-8.27	29.89	-15.81	4.47	-3.20	9.76	-7.13	8.19	-7.14	19.11	-16.91	8.75	-15.15	22.29	-39.90
34	22.23	-8.05	50.39	-18.23	25.64	-8.50	57.66	-19.11	72.92	-26.74	131.58	-48.25	47.45	-20.41	81.10	-35.71	52.36	-16.75	136.93	-43.57	81.36	-30.47	149.90	-56.08
35	6.15	-6.00	14.20	-13.74	3.99	-8.88	9.07	-20.01	7.18	-4.12	14.15	-8.10	3.06	-4.95	5.98	-10.22	1.73	-3.78	4.16	-9.20	2.40	-3.81	5.55	-9.40
36	5.49	-3.76	12.61	-8.67	11.11	-6.94	25.21	-15.74	8.40	-8.80	16.73	-17.70	5.56	-5.34	12.29	-11.76	3.78	-9.38	9.16	-22.76	13.88	-15.45	29.79	-33.07
37	16.13	-47.71	36.99	-109.46	16.39	-46.96	37.61	-107.78	23.35	-64.35	47.40	-131.02	20.51	-56.76	40.01	-111.25	18.74	-56.23	40.05	-120.56	8.92	-28.27	20.13	-65.72
38	4.15	-12.82	9.38	-28.94	7.40	-12.12	16.59	-27.01	4.13	-10.91	8.30	-21.72	2.74	-6.07	5.72	-12.65	2.27	-6.44	5.37	-15.13	3.50	-9.83	7.66	-22.23
39	2.25	-2.63	4.82	-5.77	6.94	-5.79	15.36	-12.72	4.17	-5.38	8.27	-10.72	2.96	-3.87	6.60	-8.55	2.80	-7.68	6.74	-18.62	3.05	-5.30	7.66	-15.33
40	66.97	-59.66	149.76	-133.38	50.05	-80.12	111.72	-178.66	52.31	-156.81	91.60	-274.49	21.89	-53.15	36.44	-88.11	48.11	-37.26	125.79	-97.19	132.64	-80.17	240.26	-175.75
41	41.82	-59.59	94.35	-134.94	100.87	-79.60	226.52	-177.64	24.97	-63.23	43.25	-107.25	30.23	-74.08	46.21	-111.44	45.05	-100.71	116.61	-260.21	78.80	-209.36	141.87	-444.24
42	40.06	-22.76	88.88	-49.27	117.45	-175.39	262.57	-391.99	130.54	-73.32	227.83	-127.76	99.97	-56.78	167.98	-94.16	133.22	-95.34	349.88	-254.92	177.34	-142.20	321.78	-279.10
43	58.99	-51.91	129.14	-113.60	34.00	-62.58	74.08	-135.89	78.50	-201.26	126.23	-324.22	90.82	-46.33	140.48	-69.33	94.95	-67.81	268.04	-191.47	47.42	-74.64	98.37	-84.31
44	129.32	-57.00	285.76	-125.66	101.25	-115.14	221.70	-250.87	103.84	-155.38	157.60	-231.68	50.52	-140.16	66.51	-187.87	66.20	-97.82	186.72	-278.33	34.87	-50.01	67.85	-75.91
45	71.85	-59.04	157.04	-129.09	163.68	-215.33	358.01	-470.66	118.61	-169.08	186.15	-271.83	142.66	-105.78	220.28	-162.36	100.55	-95.11	285.94	-273.90	175.62	-136.54	355.13	-272.71
46	76.57	-32.37	169.18	-72.28	136.91	-53.53	305.55	-119.61	52.31	-41.47	110.05	-89.15	170.79	-64.08	298.30	-112.10	36.43	-12.87	65.29	-24.14	46.21	-47.10	107.54	-94.64
47	61.34	-70.66	137.52	-158.72	34.71	-28.62	77.69	-64.21	48.97	-48.94	99.69	-99.78	95.96	-50.99	166.97	-89.11	35.78	-26.24	69.88	-54.53	41.52	-45.34	88.23	-95.41
48	50.94	-51.07	113.12	-114.96	87.19	-52.89	197.59	-119.85	47.16	-51.30	99.23	-109.51	142.20	-51.33	247.88	-90.33	54.83	-45.55	112.85	-98.98	54.32	-75.20	117.82	-156.81
49	150.95	-61.94	343.48	-141.75	144.02	-47.19	330.47	-108.46	37.64	-78.22	73.51	-151.54	98.95	-35.16	160.62	-57.46	28.90	-27.20	69.40	-57.34	83.76	-216.01	181.46	-596.08
50	57.89	-43.92	134.11	-100.98	46.40	-21.40	108.00	-49.66	70.27	-55.05	133.27	-103.69	117.43	-54.83	192.59	-90.22	36.03	-50.86	77.16	-110.86	189.47	-111.33	410.18	-250.30
51	102.50	-81.71	233.98	-188.25	58.93	-21.89	138.20	-50.73	65.27	-105.68	125.70	-205.04	72.12	-31.85	119.35	-54.18	73.77	-72.79	168.33	-165.26	153.13	-241.04	321.99	-714.76